

# **Preparation of the exploitation of the Cherenkov Telescope Array:**

LST analysis and prospects for the studies of  
the Large Magellanic Cloud

María Isabel Bernardos Martín

## DOCTORAL DISSERTATION IN PHYSICS

This research was done under the supervision of Dr. Carlos José Delgado with the financial support of the ... within a total duration of 4 years from April 1st 2016 to April 1st 2020.

*First release, April 2020*

# Resumen

La Red de Telescopios Cherenkov (Cherenkov Telescope Array (CTA) en inglés) es un proyecto que tiene como objetivo la construcción de un observatorio para la observación de rayos gamma de muy alta energía. Estará compuesto de alrededor de 100 telescopios de imagen de radiación Cherenkov atmosférica (Imaging Atmospheric Cherenkov Telescopes (IACTs) en inglés), de tres tipos (tamaño pequeño, mediano y grande), repartidos en dos emplazamientos, en los hemisferios Norte y Sur, con el propósito de poder cubrir todo el cielo. CTA ha sido diseñado con el objetivo de abarcar un rango de energías desde los 20 GeV hasta los 300 TeV, con una resolución energética y espacial sin precedentes, que le permitirán alcanzar una sensibilidad un orden de magnitud mayor que la actual generación de instalaciones que emplean la técnica de los IACTs.

Esta tesis está dedicada a dos frentes relativos a la preparación de CTA: La puesta en marcha del primer telescopio grande de CTA, el Large Size Telescope (LST); y el estudio de la emisión de rayos  $\gamma$  en la Gran Nube de Magallanes (Large Magellanic Cloud (LMC) en inglés) con el objetivo de hacer predicciones de los resultados esperables que se obtendrán tras las observaciones con CTA de esta galaxia, tanto relativo a fuentes astrofísicas de rayos  $\gamma$ , como a una posible detección de señal de aniquilación de materia oscura.

La primera parte de la tesis se centra en el primer prototipo de LST, instalado en el emplazamiento Norte de CTA en la isla de La Palma, cuya primera luz tuvo lugar en Diciembre de 2018. Durante el trabajo de esta tesis, he participado en varias tareas relativas a la puesta en marcha del telescopio. Principalmente, me he dedicado al desarrollo de las herramientas de software para el análisis de los datos del LST, durante su tiempo de operación en solitario. La observación con un solo telescopio Cherenkov requiere de unas técnicas de reconstrucción de eventos específicas, por ello, ha sido necesario desarrollar todo un paquete de herramientas dedicado al LST1, como complemento al software oficial de CTA. Este software ha sido desarrollado y verificado utilizando simulaciones de Monte Carlo especialmente producidas para el LST y, posteriormente, ha podido ser aplicado con éxito a los datos reales recogidos con el LST1 a lo largo de las tres campañas de toma de datos de la Nebulosa del Cangrejo que tuvieron lugar entre Noviembre de 2019 y Febrero de 2020. En el capítulo 4 se presentó una descripción completa de la cadena de análisis, y se muestran sus resultados aplicada a simulaciones y a los datos reales del LST1. Además, he

desarrollado un método alternativo para el cálculo de los parámetros de Hillas de las imágenes de cascadas Cherenkov, que no requiere la aplicación previa de un método de limpieza (o ‘cleaning’) de las imágenes, y permite recuperar información de cascadas con pocos fotones. Los resultados de este método comparados con el método tradicional, aplicado tanto a simulaciones como a datos reales son presentados también en este capítulo. Además, como trabajo complementario, he participado en algunas tareas relativas a la puesta en marcha de la cámara del LST1, cuya estructura mecánica y parte de la electrónica han sido diseñadas y construidas en el CIEMAT. Los apéndices B, C y D están dedicados a estas tareas, que consistieron en una caracterización de los Application-Specific Integrated Circuits (ASICs) del nivel L1 del sistema de trigger del telescopio, y a la calibración del de dicho sistema de trigger. La segunda parte de esta tesis está dedicada a una caracterización de la emisión en rayos  $\gamma$  de la LMC a las energías observables por CTA. El estudio detallado de esta galaxia, con más de 300 horas de observación asignadas, es uno de los principales proyectos científicos de CTA. Para poder hacer una estimación de los resultados científicos que se obtendrán con este proyecto, ha sido necesario hacer una recopilación de la información obtenida por otros telescopios (tanto en rayos  $\gamma$  como en otras longitudes de onda) de la LMC con el objetivo de construir un modelo de emisión extrapolado a las energías de CTA. El modelo de emisión construido contiene fuentes conocidas de rayos  $\gamma$ , como Nebulosas de Viento de púlsar (Pulsar Wind Nebulae (PWNe)) o remanentes de supernova (Supernova Remnants (SNRs)) detectadas por otros telescopios (H.E.S.S. y Fermi-LAT), una emisión difusa de rayos  $\gamma$  producida por la interacción de rayos cósmicos con el medio interestelar, y una población sintética de PWNe producida con el objetivo de estimar el número de nuevas fuentes de este tipo que podrán ser detectadas por CTA. Este modelo de emisión ha sido utilizado para realizar simulaciones de las observaciones con CTA de la región de la LMC, que después se han ajustado al modelo utilizando un método de máxima verosimilitud para obtener estimaciones de la sensibilidad de CTA a la detección de las diferentes fuentes. El modelo de emisión y los resultados de este ajuste han sido utilizados posteriormente, como un fondo sobre el que estudiar de las posibilidades de CTA para detectar una señal de materia oscura producida por la aniquilación de partículas pesadas que interactúan débilmente (Weak Interacting Massive Particles (WIMPs)) en la LMC. La descripción del modelo de emisión desarrollado y de las técnicas de simulación y ajuste, así como los resultados obtenidos están contenidos en el capítulo 5 de esta tesis.

A modo de introducción y puesta en contexto de la temática de la tesis, los tres primeros capítulos están dedicados al estado-del-arte de la astrofísica de rayos  $\gamma$  (capítulo 1), las técnicas de detección y actual generación de telescopios de rayos  $\gamma$  (capítulo 2), y a una descripción detallada de CTA (capítulo 3).

# Abstract

The Cherenkov Telescope Array (CTA) is an ambitious project to build an observatory for the detection of very high energy  $\gamma$ -rays. It will be integrated by around 100 Imaging Atmospheric Cherenkov Telescopes (IACTs), in three sizes (small, medium, large), situated in two locations, one for each hemisphere, to cover the full sky. CTA has been designed to achieve an energy range from 20 GeV to 300 TeV, with energy and angular resolution without precedents, which will allow reaching sensitivities one order of magnitude better than the current generation of IACT facilities. This thesis is dedicated to two subjects relative to the preparation of CTA for operation: The commissioning of the first Large Size Telescope (LST) of CTA; and the study of the very high energy emission from the Large Magellanic Cloud (LMC) at the energy range of CTA, to make predictions on the expected results that will be obtained from the survey of this galaxy, relative both to astrophysical  $\gamma$ -ray sources and to the detection of a possible signal from Dark Matter (DM) annihilation.

The first part of the thesis is focused on the prototype of the LST, installed in the CTA North site, in La Palma island, which first shower detection occurred in December 2018. During the time of this thesis, I have participated in several tasks relative to the commissioning of the LST1, mainly related to the development of the software tools for the analysis of the telescope data during its single telescope operations. Observations with a single IACT require dedicated event reconstruction techniques, thus, a specific tool package has been developed for LST1, as a complement to the official CTA software. The analysis chain has been developed and verified using Monte Carlo simulations specially produced for the LST1, and afterward, it has been successfully applied to real data taken during the three observation campaigns of the Crab Nebula, which took place between November 2019 and February 2020. In chapter 4 I describe the analysis tools, together with the results when applied to simulations and real data from the Crab campaigns. Besides, I have developed an alternative method for the calculation of the Hillas parameters of Cherenkov showers, which do not require a cleaning method of the shower images, allowing to recover information from showers with a low number of photons. The results of this method, compared to the traditional method which performs a tailcuts cleaning, applied both to simulations and to real data are also presented in this chapter. As a complementary work, I have participated in some activities related to the commissioning of the LST1 camera, which mechanical structure and some parts of the electronics were designed and produced at CIEMAT.

Appendices B, C and D are dedicated to these tasks, consisting on a characterization of the Application-Specific Integrated Circuits (ASICs) for the L1 trigger system, and its calibration.

The second part of the thesis is dedicated to a characterization of the  $\gamma$ -ray emission of the LMC at the energies observable by CTA. A deep survey of this galaxy, with more than 300 hours of assigned observation time, is one of the Key Science Projects (KSPs) of CTA. To perform an estimation of the future scientific products which will be provided by this survey, it has been necessary to collect the results obtained by other telescopes ( $\gamma$ -rays and other wavelengths) of the LMC, to build an emission model extrapolated to the energy range of CTA. The emission model produced is composed by known  $\gamma$ -ray sources, such as Pulsar Wind Nebulae (PWNe) and Supernova Remnants (SNRs) detected by other telescopes (H.E.S.S. and Fermi-LAT), a diffuse  $\gamma$ -ray emission produced by Cosmic Rays (CRs) interacting with the Interstellar Medium (ISM), and a synthetic population of PWNe produced with the purpose of estimate the number of new of such sources that will be detected by CTA. This emission model has been used to simulate observations of the region of interest of the LMC with CTA, which afterward has been fitted to the model with a maximum likelihood method to obtain estimations on the sensitivity to the detection of the different sources. The emission model and the results of this fitting have been used then as a background for the study of the possibilities of CTA to detect a DM signal produced by the annihilation of Weak Interacting Massive Particles (WIMPs). The description of the emission model developed, the analysis and simulation techniques, and the results obtained are presented in chapter 5.

As an introduction and to provide context for this thesis, the first three chapters are dedicated to the State-of-the-Art of  $\gamma$ -ray Astrophysics (chapter 1), detection techniques and current generation of  $\gamma$ -ray instruments (chapter 2) and a detailed description of CTA (chapter 3).

# Contents

<b>1</b>	<b>Introduction to <math>\gamma</math>-Ray Astronomy .....</b>	<b>13</b>
<b>1.1</b>	<b>Cosmic-ray physics .....</b>	<b>14</b>
<b>1.2</b>	<b>Acceleration mechanisms .....</b>	<b>16</b>
1.2.1	Electric field acceleration .....	16
1.2.2	Stochastic acceleration .....	17
1.2.3	Diffusive Shock Acceleration .....	19
<b>1.3</b>	<b>Production of <math>\gamma</math>-rays .....</b>	<b>20</b>
1.3.1	Bremsstrahlung .....	21
1.3.2	Inverse Compton scattering .....	21
1.3.3	Synchrotron emission .....	23
1.3.4	Curvature radiation .....	23
1.3.5	Matter-Antimatter annihilation .....	24
1.3.6	Hadronic collisions .....	24
<b>1.4</b>	<b><math>\gamma</math>-ray Absorption mechanisms .....</b>	<b>25</b>
1.4.1	Interaction with electrons: Compton effect .....	25
1.4.2	Pair production processes .....	25
1.4.3	The Extragalactic Background Light .....	26
<b>1.5</b>	<b>Dark Matter and <math>\gamma</math>-rays: WIMP annihilation .....</b>	<b>27</b>
<b>1.6</b>	<b><math>\gamma</math>-ray sources .....</b>	<b>31</b>
1.6.1	Galactic sources .....	31
1.6.2	Extragalactic sources .....	37
1.6.3	Potential Dark Matter annihilation emission sources .....	42
<b>2</b>	<b>Detection of <math>\gamma</math>-rays .....</b>	<b>45</b>
<b>2.1</b>	<b>Space detectors .....</b>	<b>46</b>
2.1.1	Compton detectors .....	47
2.1.2	Pair production detectors .....	47

<b>2.2</b>	<b>Extensive Air Showers</b>	<b>49</b>
2.2.1	Electromagnetic Showers .....	50
2.2.2	Hadronic showers .....	52
2.2.3	Electronic showers .....	53
<b>2.3</b>	<b>Cherenkov radiation</b>	<b>54</b>
<b>2.4</b>	<b>Ground-based detectors</b>	<b>57</b>
2.4.1	Particle detectors .....	57
2.4.2	Atmospheric Cherenkov Telescopes .....	57
<b>3</b>	<b>The Cherenkov Telescope Array .....</b>	<b>63</b>
<b>3.1</b>	<b>Introduction</b>	<b>63</b>
<b>3.2</b>	<b>CTA Requirements and Performance</b>	<b>64</b>
<b>3.3</b>	<b>CTA Telescopes</b>	<b>68</b>
3.3.1	Large Size Telescope (LST) .....	68
3.3.2	Medium Size Telescope (MST) .....	72
3.3.3	Small Size Telescope (SST) .....	73
<b>3.4</b>	<b>Reconstruction and Analysis tools</b>	<b>75</b>
3.4.1	Monte Carlo simulations .....	76
3.4.2	Low level analysis: ctapipe .....	78
3.4.3	Science analysis: ctools .....	79
<b>4</b>	<b>Analysis chain of Single Telescope data and sensitivity calculation for the LST1 .....</b>	<b>81</b>
<b>4.1</b>	<b>Introduction</b>	<b>81</b>
<b>4.2</b>	<b>The LST1 analysis chain overview</b>	<b>81</b>
4.2.1	Calibration .....	82
4.2.2	Image cleaning and parameterization .....	84
4.2.3	Reconstruction of energy and source position .....	85
4.2.4	$\gamma$ -hadron separation .....	86
<b>4.3</b>	<b>Sensitivity of the LST1</b>	<b>87</b>
4.3.1	Reweighting .....	88
4.3.2	Cut optimization .....	90
4.3.3	Expected LST1 Performance .....	90
<b>4.4</b>	<b>Expectation-Maximization method for Hillas Parameters...</b>	<b>93</b>
4.4.1	The Expectation-Maximization algorithm .....	93
4.4.2	Comparison of EM without cleaning and tailcuts cleaning .....	97

<b>4.5 Results on real data</b>	<b>100</b>
4.5.1 Analysis of Crab Campaigns with Expectation-Maximization method for Hillas Parameterization .....	102
<b>4.6 Summary and conclusion</b>	<b>104</b>
<b>5 Characterization of the Large Magellanic Cloud at TeV energies and prospects on Dark Matter detection for CTA</b>	<b>113</b>
<b>5.1 Introduction</b>	<b>113</b>
<b>5.2 Emission Model</b>	<b>114</b>
5.2.1 Diffuse emission .....	115
5.2.2 Point Sources .....	117
5.2.3 PWNe population in the LMC .....	120
<b>5.3 Simulations and Analysis method</b>	<b>122</b>
5.3.1 Region of Interest and Observational strategy .....	122
5.3.2 Simulation parameters .....	123
5.3.3 Fitting method .....	124
<b>5.4 Results</b>	<b>126</b>
5.4.1 Point sources .....	126
5.4.2 Population of PWNe .....	126
5.4.3 Diffuse Emission .....	127
<b>5.5 Dark Matter annihilation in the LMC</b>	<b>129</b>
5.5.1 Dark Matter profile in the LMC .....	130
5.5.2 $\gamma$ -ray spectrum .....	132
5.5.3 Results on DM sensitivity curves .....	132
5.5.4 Effect of the diffuse emission on the DM sensitivity curves .....	133
<b>5.6 Summary and conclusions</b>	<b>136</b>
<b>6 Conclusiones</b> .....	<b>139</b>
<b>7 Conclusions</b> .....	<b>143</b>
<b>A The L1 Trigger System of the LST1</b> .....	<b>147</b>
<b>A.1 Introduction</b>	<b>147</b>
<b>A.2 Pixel Level: L0 trigger decision</b>	<b>148</b>
A.2.1 Majority trigger .....	148
A.2.2 Sum trigger .....	149
A.2.3 Camera Level: L1 trigger decision .....	149

A.2.4	Array Level trigger decision .....	150
-------	------------------------------------	-----

## **B Characterization of analogue ASIC for L1 trigger decision**

**151**

<b>B.1</b>	<b>Introduction</b>	<b>151</b>
<b>B.2</b>	<b>Quality control test</b>	<b>152</b>
B.2.1	Test DAC .....	153
B.2.2	Voltage Test: Rate scan .....	153
B.2.3	Test Adder Channels .....	153
B.2.4	Analog Offset test .....	153
B.2.5	Digital Offset test .....	153
<b>B.3</b>	<b>Characterization of the ASIC</b>	<b>154</b>
B.3.1	Rate Scan Fit .....	154
B.3.2	Gain .....	154
B.3.3	Offset .....	156
B.3.4	Noise .....	157
<b>B.4</b>	<b>Characterization: Summary and discussion</b>	<b>158</b>

## **C Calibration method for the L1 analog trigger system of LST camera**

**163**

<b>C.1</b>	<b>Introduction</b>	<b>163</b>
<b>C.2</b>	<b>L1 transfer function calibration</b>	<b>163</b>
C.2.1	Calibration algorithm .....	164
C.2.2	Calibration result .....	164

## **D Time calibration for implementation of the trigger distribution in the backplane network of LST camera**

**167**

<b>D.1</b>	<b>Introduction</b>	<b>167</b>
<b>D.2</b>	<b>Time calibration procedure</b>	<b>167</b>
<b>D.3</b>	<b>Time calibration setup and tests</b>	<b>169</b>

## **E Random Forests**

**171**

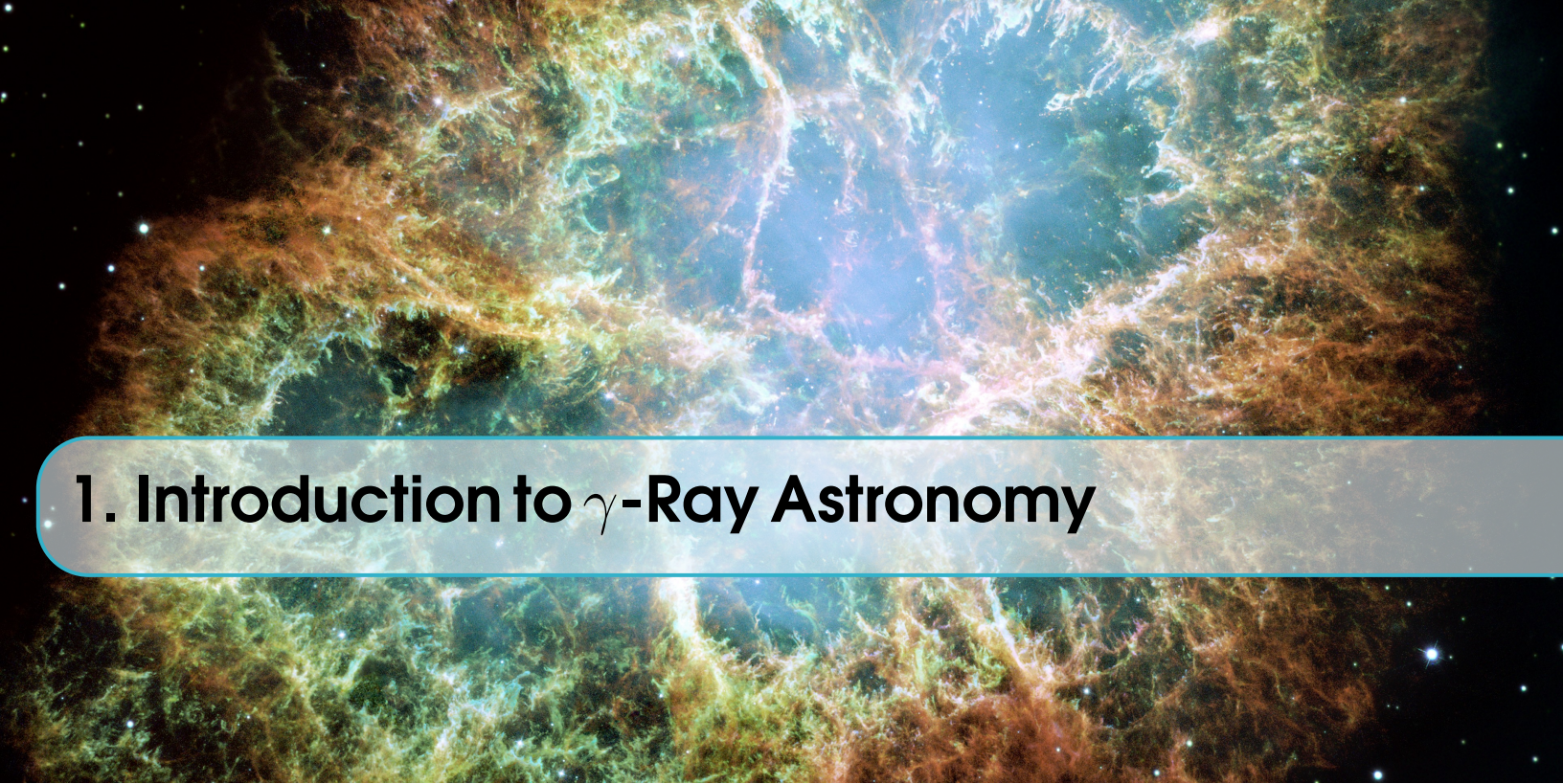
<b>E.1</b>	<b>Introduction</b>	<b>171</b>
<b>E.2</b>	<b>Gini Index</b>	<b>171</b>
<b>E.3</b>	<b>Random Forests in cta-lstchain</b>	<b>172</b>
E.3.1	Random Forest parameters .....	172

E.3.2	Random Forest features .....	173
-------	------------------------------	-----

## **F Evolution of LST1 camera uniformity ..... 175**

<b>F.1</b>	<b>Introduction</b>	<b>175</b>
<b>F.2</b>	<b>Distribution of centroids of Hillas ellipses for standard analysis</b>	<b>175</b>
<b>F.3</b>	<b>Distribution of centroids of Hillas ellipses for Expectation-Maximization analysis</b>	<b>175</b>





# 1. Introduction to $\gamma$ -Ray Astronomy

During many centuries humanity has looked towards the skies and wondered about the mysteries of the universe. At first, with the naked eye, our ancestors measured the movements of astronomical objects and used them as calendars and guidance. We can say that modern Astronomy was born with the invention of the optical telescope by Galileo in 1609 AD. However, we were looking only to a small part of the universe, studying the stars just through the visible light they were emitting. Like an incomplete symphony where we can only listen to the melody of one instrument, our knowledge of the physics of the cosmos was purely limited to the thermal emission. It was not until the first half of the XX century that we could start talking about the *multiwavelength* astronomy with the first infrared, radio, ultraviolet and X-ray observations. The most energetic part of the electromagnetic spectrum,  $\gamma$ -rays, was first detected in the 1960s. Along with the multiwavelength astronomy, other messengers from the sky were discovered: In 1912 the Austrian physicist Victor Hess found that the puzzling source of high levels of ionizing radiation in the atmosphere was actually charged particles coming from space. These particles were later named Cosmic Rays (CRs) by Millikan, and as will be explained later, their origin was thought to be closely related to the origin of  $\gamma$ -rays. The emission of this high energy radiation (above 100 keV), and the origin of such energetic particles as CRs were, could not be explained through thermal processes, thus other physical phenomena came into play, mostly involving interactions of relativistic particles.

The Astroparticle physics field studies the relation between  $\gamma$ -rays and CRs, combining astrophysics and particle physics, and includes other cosmic messengers, like neutrinos, to face unresolved problems like the origin and acceleration mechanisms of CRs, towards the completion of the cosmic symphony that is the Universe.

This chapter will be an overview of the basic concepts of CR and  $\gamma$ -ray physics, their production, acceleration and absorption, and their known sources of emission in the

universe.

## 1.1 Cosmic-ray physics

CRs are relativistic charged particles arriving at the atmosphere from outer space. Their origin and the mechanisms that accelerate them to reach such high energies are still being debated. However, arguments are pointing towards them being accelerated in very violent events in the universe, such as supernova explosions. Several measurements strongly support that galactic CRs are in fact accelerated in Supernova Remnants (SNRs) [1], [2], [3]. As they are charged particles, they suffer from the effects of the magnetic fields (both interstellar and Earth magnetic fields) which divert their trajectories and make very difficult to trace back their original direction. Nevertheless, they can interact with the medium close to their sources producing  $\gamma$ -rays through processes such as Inverse Compton (IC) scattering or neutral pion decay. Observing  $\gamma$ -rays, which travel in straight lines from their origin, can provide information on how and where do CRs are produced and interact with the medium.

The composition of CRs arriving to the Earth is mainly protons (86%), alpha particles (11%), electrons (2%) and other heavy nuclei (1%). We can distinguish between two types of cosmic-rays: Those reaching the Earth unaltered from their source, known as *primary CRs*; and those resulting from inelastic collisions of the primary CRs with the Interstellar Medium (ISM), called *secondary CRs*.

The spectrum of CRs is shown in figure 1.1. Mostly, it can be described as a piecewise Power Law with a spectral index  $\gamma$  that changes along different regions of the spectrum [4]:

$$\frac{dN(E)}{dE} \propto E^{-\gamma} \quad (1.1)$$

Where  $N$  is the flux of CRs and  $E$  is the energy. The different regimes that can be observed are:

- From few keV to less than 10 GeV: CRs are produced locally in solar flares and coronal mass ejections from the Sun [5], with a spectral index  $\sim 5$  [6].
- Up to the *knee* (below  $10^6$  GeV): CRs follow a simple power law with spectral index  $\gamma \sim 2.7$ . In this region CRs are considered to have a galactic origin, accelerated in SNRs.
- From the *knee* to the *second knee* (at  $10^8$  GeV) the spectral index becomes  $\sim 3.1$ . From the *knee* until the *ankle* there is a transition from galactic dominated CRs to extragalactic dominated.
- Between the *second knee* (at  $10^8$  GeV) and the *ankle* the spectral index is  $\sim 3.3$ .
- Energies above the *ankle* ( $\sim 10^9$  GeV): CRs coming from extragalactic sources are predominant, with a hardening in the spectrum back to an index  $\sim 2.7$ . At such high energies, particles are no more confined by galactic magnetic fields so they travel with their trajectories almost unperturbed [7], allowing to estimate

their direction. These kind of very energetic CRs can be produced in Active Galaxy Nuclei (AGN), Gamma Ray Bursts (GRBs), radio galaxy lobes and the intra-cluster medium in galaxy clusters [8].

- At energies above  $\sim 4 - 5 \times 10^{10}$  GeV a strong suppression is observed, interpreted as the GZK cutoff, which sets a theoretical upper limit on the energy carried by CRs from distant sources.

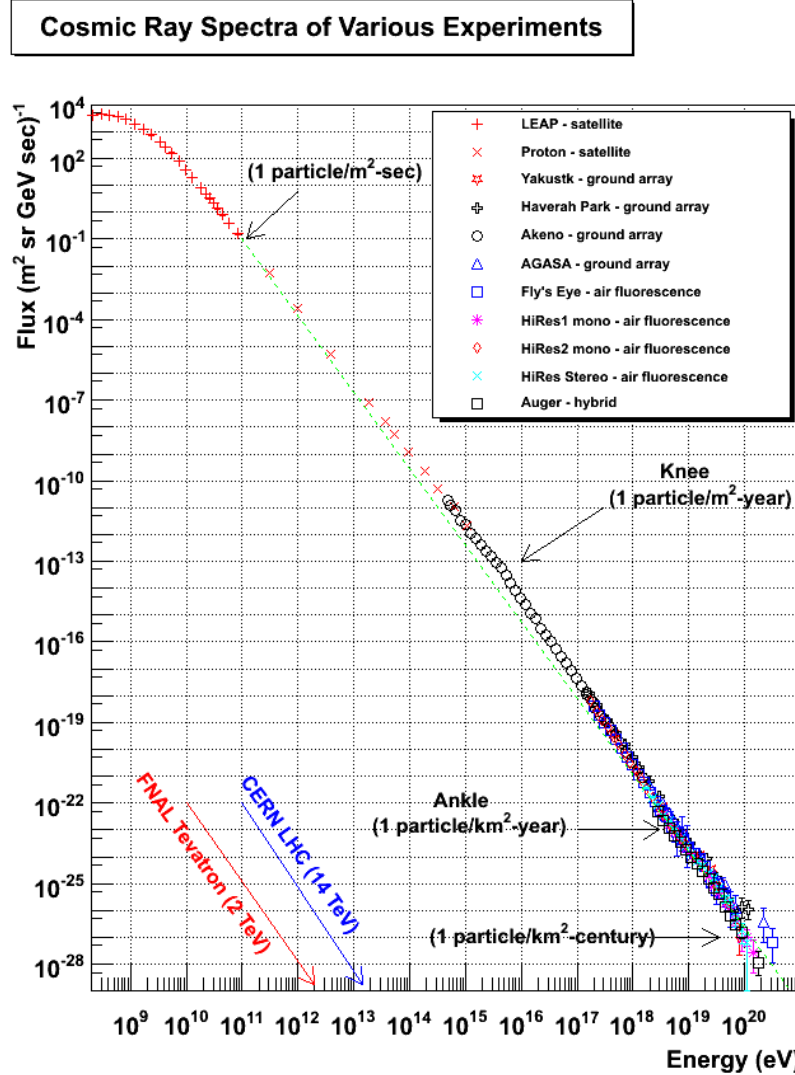


Figure 1.1: CR spectrum from [9] built with data from several experiments. Red and blue lines represent the energy spectrum covered by Tevatron and LHC accelerators. Green line shows the fit to a power law with spectral index 2.7.

As already mentioned, it is possible to differentiate two CR origins: galactic CR and extragalactic CR. Below the *knee*, CRs are produced in galactic accelerators (SNRs) and their maximum energy can be considered a limit on the acceleration that

is possible to gain from this kind of objects. CRs with energies above the *ankle* are thought to come from extragalactic sources and so, their higher acceleration must come from different phenomena, more violent and energetic (AGN, GRBs, etc.). The Larmor radius defines the curved trajectory of charged particles moving perpendicular to a magnetic field. The "Hillas condition" [10] sets a minimum requirement for the accelerators to reach certain energies, stating that a necessary condition to accelerate particles to ultrahigh-energy is that of confinement, meaning that they can stay in the acceleration region as long as their Larmor radius is smaller than the size of the accelerator. For energies over the *ankle*, the Larmor radius starts to become larger than galactic scales, hence extragalactic CRs propagate almost linearly and unaffected by the galactic magnetic field, while galactic (less energetic) CRs propagate diffusively through the ISM. Figure 1.2 shows the Hillas diagram, where different source classes are presented as a function of their characteristic size and magnetic field strength. The transition in the spectrum between galactic and extragalactic accelerators, although still not well understood, can be explained by the effect of the galactic magnetic field in the trajectories of CRs, and the effect of galactic wind termination shocks as a re-acceleration process [4].

The chemical composition of galactic CRs is very similar to that of the Solar System (see figure 1.3), suggesting a similar origin (stellar interiors) but with some discrepancies in certain elements. The most noticeable difference regards Li, Be, and B, and to a lesser extent sub iron elements Mn, Cr, V, Ti, and Se. The abundances of these elements are small in stars because they are rapidly consumed by nuclear reactions, but they are present in secondary CRs due to *spallation* of carbon and oxygen nuclei [11] and other abundant heavy nuclei as Fe and Ni [12].

## **1.2 Acceleration mechanisms**

Acceleration mechanisms take place in astrophysical plasmas which in general consists of thermal plasma components: a magnetic field, and non-thermal distributions of fast particles. Within the plasma, turbulence and plasma waves take place, having an important role in particle acceleration. The mechanisms that accelerate CRs to the huge energies observed, that can reach up to  $10^{20}$  eV are still a topic of debate and research in the high energy astrophysics field. Several particle acceleration mechanisms are proposed to explain the CR spectrum, which should be able to achieve the highest energies measured for CRs, reproduce the spectral shape of a power law with an index  $\sim 2.7$ , and recover the abundances of elements measured [13], [14], [15].

### **1.2.1 Electric field acceleration**

Electric fields parallel to magnetic fields can accelerate charged particles and can arise during magnetic field reconnection (the breaking and reconnecting of oppositely magnetic field lines in a plasma). Because ideal Magnetohydrodynamics (MHD) of plasmas require the parallel component of electric field to be null  $E_{\parallel} = 0$ , non-ideal MHD effects are needed to explain the development of  $E_{\parallel} \neq 0$ , such as resistivity or

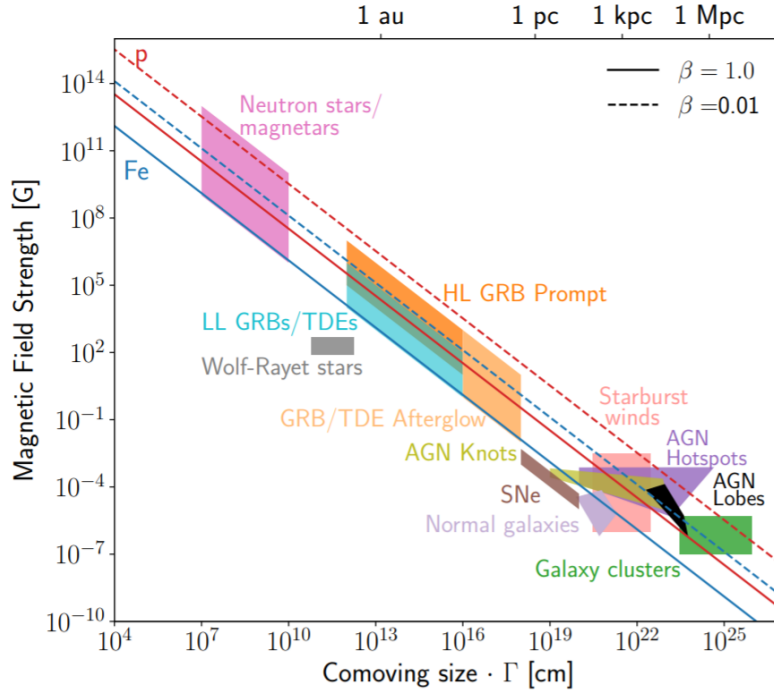


Figure 1.2: Hillas diagram, from [8]. Source classes as a function of their characteristic radius  $R$ , given as the comoving size of the source times the Lorentz factor  $\Gamma$ , and the magnetic field  $B$  in the comoving frame of the source. Solid (dashed) lines indicate the product of  $B \times R$  beyond which confinement of protons (red) and iron (blue) nuclei with energy  $10^{20}$  eV is possible.

inertial effects on Alfvén waves (a type of MHD wave where ions oscillate in response to a restoring force provided by an effective tension on the magnetic field lines) [15]. This kind of acceleration is believed to take place in the magnetic reconnection of the Earth's magnetotail, accelerating auroral electrons; Also, reconnection in pulsar gaps (see section 1.6.1) could produce this kind of acceleration which involve large oscillations in  $E_{\parallel}$ .

### 1.2.2 Stochastic acceleration

Stochastic acceleration is also known as *Second Order Fermi acceleration* or simply *Fermi process*. This idea was developed by Enrico Fermi in 1949 [16] as a mechanism to explain the acceleration of galactic CRs. The basic concept is that particles can gain velocity after being reflected several times by randomly moving magnetized clouds in the ISM. Fermi showed that after a characteristic time  $\tau_{esc}$ , the spectrum of the accelerated particles would follow a power law. If the particle is moving with a pitch angle  $\theta$  (the angle between the particle velocity vector and the local magnetic field), the gain in energy after a collision with a cloud moving with velocity  $V$  will be

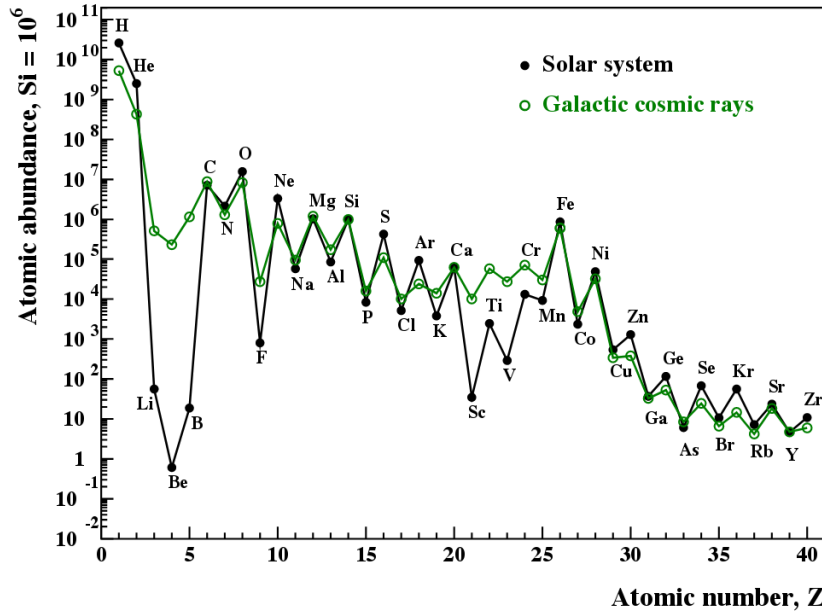


Figure 1.3: Abundances of elements of galactic CRs compared to the Solar System, from [12].

[17]:

$$\Delta E = E \left[ \frac{2V \cos\theta}{c^2} + 2 \left( \frac{V}{c} \right)^2 \right] \quad (1.2)$$

Where  $E$  is the energy of the particle before the collision. Between collisions the particle will be moving inside a plasma and will suffer scattering due to hydrodynamic waves. The total gain in energy has to be averaged over a set of random  $\theta$  angles. The probability of a collision is proportional to the relative velocities of the particle ( $v$ ) and the cloud ( $V$ ). If  $v \approx c$  the probability of a head-on collision  $P \propto 1 + (V/c)\cos\theta$  is slightly higher than the probability of head-tail collision  $P \propto 1 - (V/c)\cos\theta$  (see figure 1.4) hence the total gain in energy, averaged in all  $\theta$  angles between 0 and  $\pi$ , will be positive:

$$\left\langle \frac{\Delta E}{E} \right\rangle = \frac{8}{3} \left( \frac{V}{c} \right)^2 \quad (1.3)$$

Being the increase in energy *second order* proportional to  $V/c$ . However, this process cannot be the main source of particle acceleration: the velocities of interstellar clouds in the ISM are too low ( $V/c \simeq 10^{-4}$ ), the mean free path of CRs in the ISM is too high (the number of collisions would be  $\sim 1\text{yr}^{-1}$ ) and the particles should be injected in the acceleration region with already high velocities (this is known as the *injection problem* and it is present in every acceleration mechanism).

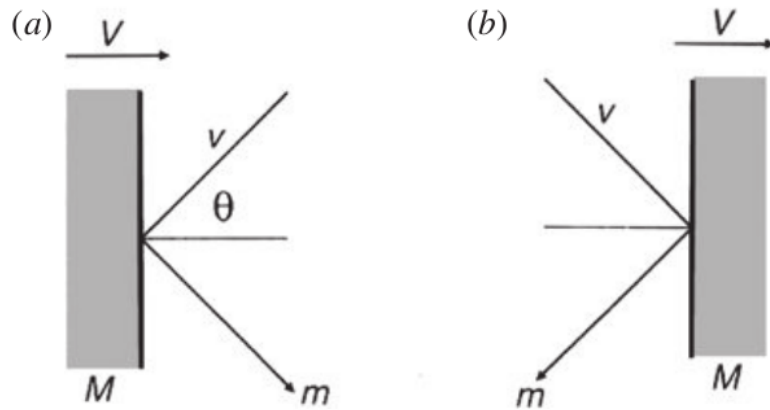


Figure 1.4: Collision of a particle of mass  $m$  with velocity  $v$  against a cloud of mass  $M$  and velocity  $V$ . *a)* head-on. *b)* head-tail. From [17].

### 1.2.3 Diffusive Shock Acceleration

The most popular acceleration mechanism in astrophysical plasmas, which is believed to take place in SNRs (the best candidates for galactic CR production) is known as Diffusive Shock Acceleration (DSA) or *First Order Fermi acceleration*. This mechanism revisits the original idea formulated by Fermi of particles colliding with randomly moving ‘magnetic mirrors’ in the ISM, but with all the collisions happening always head-on. For example, when two clouds are approaching each other and the particle bounces back and forth [15]. This process can happen in the presence of strong supersonic shock waves propagating through a diffuse medium, like those produced after a Supernova (SN) explosion (see figure 1.5). A flux of relativistic particles is assumed to exist on both sides of the shock, moving much faster than the latter. Each time a particle crosses to one side or the other, their velocity becomes isotropic in the frame of reference of the moving fluid. Since on every crossing the particle encounters gas moving towards it at a velocity proportional to the shock velocity ( $V$ ), which for a fully ionized plasma composed by monoatomic perfect gas is  $\sim 3/4V$  [17], it will receive a boost in energy of the order  $\sim V/c$ . That is why this process is called *first order* in counterpart to the classical second order Fermi acceleration where the energy gain in each collision is proportional to  $\sim (V/c)^2$ . DSA is able to predict a spectral index of  $\sim 2$ , very close to the observed for galactic CRs. Also, it is the only acceleration mechanism efficient enough to transfer the observed amount of energy in SNRs to particles. On the other hand, it exists an upper limit on the maximum energy that a particle can gain through DSA which is set to  $\sim 10^{14}$  eV [18], so is still not enough to explain the full CR spectrum, which reaches up to  $\sim 10^{20}$  eV.

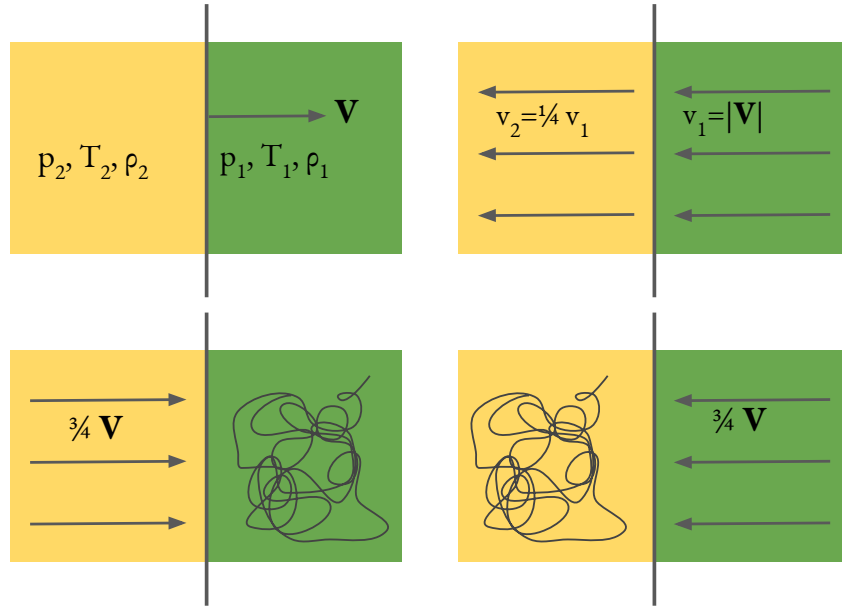


Figure 1.5: Scheme of the *Diffuse shock acceleration*, inspired by [17]. *Upper left*: Observer frame. A diffusive shock is propagating at velocity  $V$ . *Upper right*: the frame where the shock front is at rest. The velocities of the gas in both sides of the front, assuming it is fully ionized, have a ratio of 4. *Lower left*: the frame of reference where the upstream gas is at rest, the distribution of velocities of the high energy particles is isotropic. *Lower right*: the same case as previous, but in the reference frame of the downstream gas.

### 1.3 Production of $\gamma$ -rays

Although CRs have been known for more than a century, it is difficult to make conclusions about their origin and acceleration mechanisms. As they are charged particles, their trajectories are deflected while traveling through the ISM, hence their incoming direction does not point towards the source of origin. Nevertheless, CRs can interact with the medium producing  $\gamma$ -rays through several mechanisms, which reach the Earth undeflected, offering a way to indirectly study CR origin, acceleration, and diffusion in the ISM. When we talk about radiation production, we can distinguish between two main mechanisms which involve very different physical phenomena: thermal and non-thermal processes. A large fraction of the low energy radiation emitted by stars or interstellar dust is produced by thermal processes following a black body spectrum. To produce radiation as energetic as  $\gamma$ -rays a temperature of the order of  $10^{10}$  K would be needed, which was only reachable in the Big Bang conditions. Therefore, to understand the production of  $\gamma$ -rays we must study the so-called *non-thermal universe*, where radiation is produced by interactions of relativistic particles moving in electromagnetic fields. In general,  $\gamma$ -rays are produced in two kinds of

scenarios: leptonic emission (produced mainly by electrons) and hadronic emission (produced mainly by protons). Which one of those is dominant in astrophysical particle accelerators is still a subject of debate and will be commented in section 1.6 about  $\gamma$ -ray sources. In this section a summary of the different  $\gamma$ -ray production mechanisms (see figure 1.6) is given.

### 1.3.1 Bremsstrahlung

From the German ‘braking radiation’, the bremsstrahlung process occurs when a charged particle is decelerated by the electric field produced by an atomic nucleus. While their trajectory is deflected, the particle emits electromagnetic radiation with amplitude proportional to the magnitude of the deceleration suffered. The differential cross section for a particle of charge  $e$ , mass  $m$ , carrying an energy  $E_e$  to radiate a photon between energies  $E_\gamma$  and  $E_\gamma + dE$ , when interacting with the Coulomb field is:

$$\sigma(E_e, E_\gamma) dE_\gamma = 4\alpha Z^2 r_e^2 \frac{dE_\gamma}{E_\gamma} F(E_e, \nu) \quad (1.4)$$

Where:

$$F(E_e, \nu) = [1 + (1 - \nu)^2 - \frac{2}{3}(1 - \nu)] \left[ \ln \left( \frac{2E_e}{m_e c^2} \frac{1 - \nu}{\nu} \right) - \frac{1}{2} \right] \quad (1.5)$$

Being  $\alpha$  the fine structure constant and  $\nu = E_\gamma/E_e$  the fractional energy carried by the photon [19]. From equations 1.4 and 1.5 it can be seen that the acceleration suffered by the particle is  $\propto Ze^2/m$ , then while any charged particle can suffer bremsstrahlung, it is going to be much more efficient for electrons than for protons which have a higher mass. The photons emitted will have a continuum spectrum with energies of the same order of the particle, which for cosmic electrons in gas is going to be a power-law [20]. Bremsstrahlung is mainly efficient under high-density conditions. It takes place in gaseous nebulae that contain ionized gas, such as SNRs, and in the intracluster medium of galaxy clusters [21].

### 1.3.2 Inverse Compton scattering

IC scattering is the inelastic interaction where a relativistic charged particle transfers a considerable amount of energy to a photon. In the frame of reference of the electron, the photon will suffer an ‘energy boosting’ [20]. The energy of the scattered particle is  $E = \Gamma mc^2$ , where  $\Gamma$  is the Lorentz factor, and we can define the parameter  $\alpha = h\nu/mc^2$ , where  $\epsilon = h\nu$  is the initial energy of the photon. We can differentiate between two regimes depending on the initial energy of the photon:

- *Thomson regime*: For low values of  $\alpha$ , particle recoil can be neglected and the energy of the photon after the scattering will be:

$$E_\gamma \simeq \frac{4}{3}\epsilon\gamma^2 \quad (1.6)$$

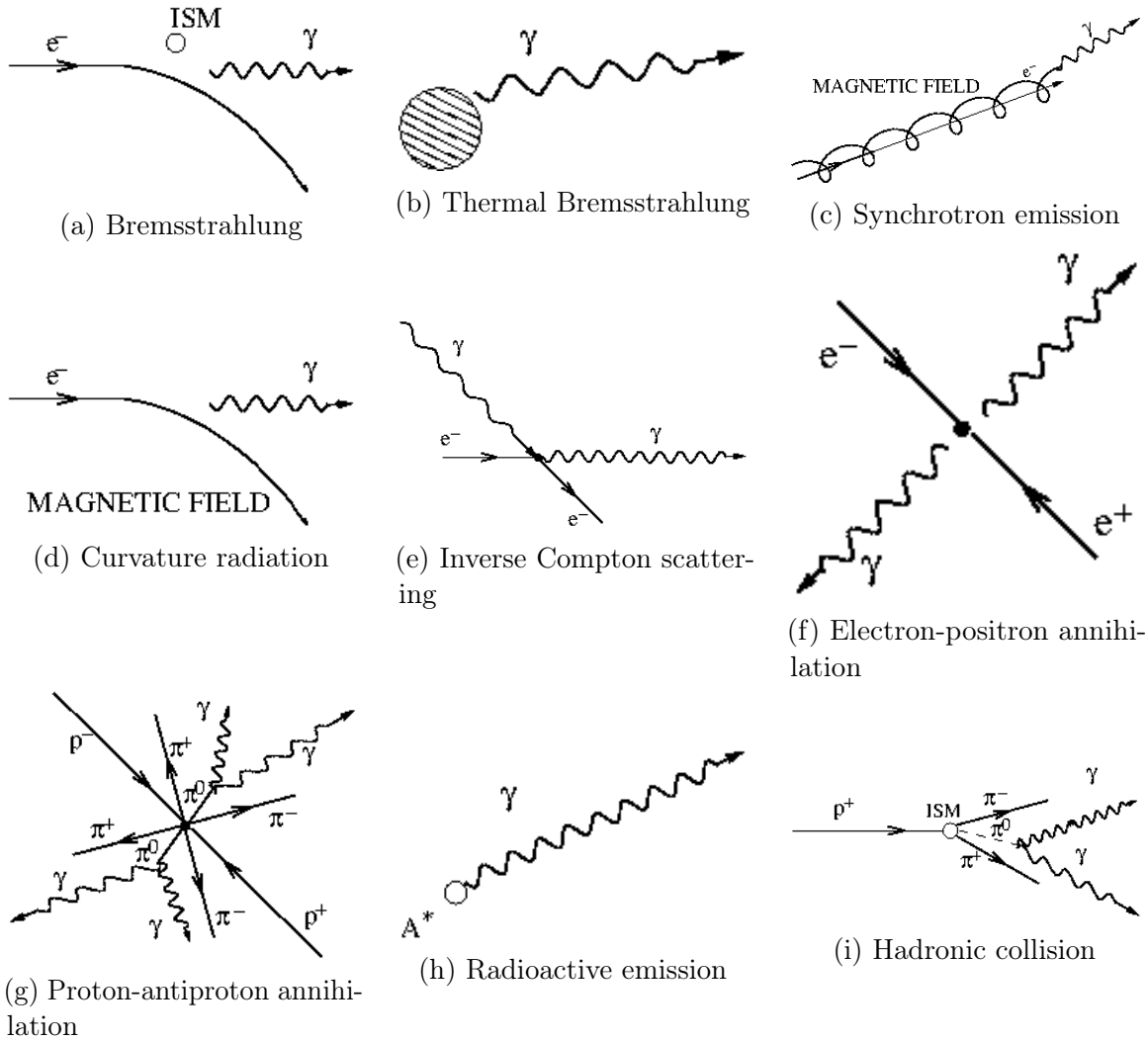


Figure 1.6: Diagrams of the different  $\gamma$ -ray production processes. Figures extracted from [22].

- *Klein-Nishina regime:* For large values of  $\alpha$ , particle recoil is significant and in this case the energy of the photon after the interaction is:

$$E_\gamma \simeq \frac{1}{2} E \quad (1.7)$$

Photons from the Cosmic Microwave Background (CMB) are typical targets for IC scattering, together with synchrotron photons or photons thermally emitted by astrophysical sources. This mechanism is predominant in Very High Energy (VHE)  $\gamma$ -ray emitters, like in the jets of AGN and TeV blazars. The spectrum of the photons boosted by this process will follow a power law related to that of the population of

relativistic electrons in the medium ( $\propto E_e^{-\Gamma_e}$ ):

$$\frac{dN_\gamma}{dE} \propto E^{-\frac{(\Gamma_e+1)}{2}} \quad (1.8)$$

### 1.3.3 Synchrotron emission

Synchrotron emission is produced when a charged particle is moving in a magnetic field. The particle will follow a spiral path, with constant velocity along the field lines, while being accelerated towards the center of its orbit. The particle will suffer energy losses that for relativistic particles follow a continuum spectrum [20] with a critical frequency  $w_c$  at which the maximum power is emitted:

$$w_c = \frac{3eB}{2mc}\Gamma^2 \sin\phi \quad (1.9)$$

Where  $e$  and  $m$  are the charge and mass of the particle,  $B$  is the magnetic field,  $\Gamma$  is the Lorentz factor and  $\phi$  is the pitch angle between the directions of the magnetic field and the particle. The total energy loss is given by

$$-\frac{1}{c} \left( \frac{dE}{dt} \right) = \frac{2e^4}{3m^2c^4}\Gamma^2 B^2 \text{erg cm}^{-1} \quad (1.10)$$

Following 1.10, the power emitted is inversely proportional to the mass of the particle so it will be comparatively much more efficient for electrons than for protons.

Synchrotron radiation of ultra-relativistic particles is the most important contribution to the non-thermal universe (radio, X-rays...). According to 1.9 the production of High Energy (HE)  $\gamma$ -rays will require too high values of  $B$  and  $E_e$ , but regions emitting synchrotron radiation contain relativistic electrons capable of IC scattering [23], which will acquire much higher energies.

### 1.3.4 Curvature radiation

In presence of very strong magnetic fields, of the order of  $10^{11}$ - $10^{13}$  G, electrons and positrons will be forced to follow a trajectory parallel to the magnetic field lines. Since the lines are curved, with a curvature radius  $\rho_c$ , the particle will emit *curvature radiation* in the direction of movement, with a characteristic photon energy [24]:

$$E_c = \frac{3}{2}\Gamma^3 \frac{\hbar c}{\rho_c} \quad (1.11)$$

A typical environment where curvature radiation takes place are the surroundings of pulsars, due to the extremely high magnetic fields close to their surfaces. An electron with an energy of 10 TeV moving along a field line with a curvature of  $10^8$  cm, which is typical for pulsars, emits photons of energy  $\approx 2.5$  GeV [19].

### 1.3.5 Matter-Antimatter annihilation

Matter-antimatter pair annihilation processes can produce  $\gamma$ -rays. The most common case is electron-positron annihilation ( $e^-e^+ \rightarrow 2\gamma$ ). If the two particles are at rest, they produce  $\gamma$ -rays with energy equal to their masses (0.511 MeV). If the particles are thermalized but with low energies, such as the electrons of the ambient gas/plasma, they form the unstable state called positronium which can annihilate into 3 photons forming a continuum [25]. For relativistic particles interacting in-flight, the annihilation cross section is:

$$\sigma_A = \frac{\pi r_e^2}{\Gamma} [\ln(2\Gamma) - 1] \quad (1.12)$$

Where  $\Gamma = E_e/m_ec^2$  is the Lorentz factor of the positrons and  $r_e = e^2/m_ec^2 = 2.82 \times 10^{-13}$  cm is the classical radius of the electron. The result of the interaction is the emission of two photons with a continuum of energies. At very high energies, the cross section of equation 1.12 is quite low, leading to very high mean free paths and long lifetimes for the positrons, which typically will be affected by other processes before annihilating. Positrons can lose energy gradually without escaping the galaxy until the cross section is high enough and they annihilate [19].

Proton-antiproton annihilation can also produce  $\gamma$ -rays indirectly by the production of neutral pions  $\pi^0$  which decay into  $\gamma$ -rays later on [26]. In theory, antiprotons can be produced by interactions of protons with matter, but this process is much less efficient than the direct production of  $\pi_0$  mesons [20] so the production of  $\gamma$ -rays this way is considered marginal.

### 1.3.6 Hadronic collisions

While most of the processes described above were dominated by electron interactions (leptonic scenario), we now focus on the processes that constitute the hadronic contribution to the production of  $\gamma$ -rays, which are believed to be the dominant  $\gamma$ -ray production processes in SNRs and AGN.

Protons accelerated to relativistic energies in extreme environments, such as strong magnetic fields or jets, can collide with other hadrons producing mesons, kaons and hyperons. The most common interaction is the proton-proton collision to produce pions ( $\pi$  mesons):



With a threshold energy of the proton as the minimum kinetic energy the pair of protons must have in the collision to produce the meson:

$$E_p = 2m_{\pi^0}c^2 \left( 1 + \frac{m_{\pi^0}}{4m_p} \right) \simeq 280\text{MeV} \quad (1.14)$$

Where  $m_{\pi^0} = 134.97$  MeV is the mass of the  $\pi_0$ -meson and  $m_p = 938.27$  MeV is the mass of the proton [25].

Neutral pions  $\pi^0$  decay into  $\gamma$ -rays within a short lifetime  $\tau = 8.6 \cdot 10^{-17}$ s through the channels:

$$\pi^0 \rightarrow \gamma\gamma \quad (98.8\%) \quad (1.15)$$

$$\pi^0 \rightarrow e^-e^+\gamma \quad (1.2\%) \quad (1.16)$$

Then the energy of the photons emitted by the  $\pi^0$  peaks at  $E_\gamma = m_{\pi^0}c^2/2 \simeq 67.5$  MeV, but in the laboratory frame of reference, this energy depends on the energy of the  $\pi^0$  and the angle of the proton trajectory with respect to the  $\pi^0$  allowing the emitted  $\gamma$ -rays to reach very high energies. The collision of protons can also produce charged mesons, which can decay into neutrinos  $\nu_{e,\mu}$  with a spectrum similar to that of the photons [25]. Finding a correlation between  $\gamma$ -ray emission and astrophysical neutrinos from a certain source would be an unequivocal way to differentiate between leptonic and hadronic emission. Their spectrum shape and the lack of correlation with X-rays could be other ways to distinguish hadronic and leptonic emission.

## 1.4 $\gamma$ -ray Absorption mechanisms

Because  $\gamma$ -rays are very energetic, they can travel long distances without being altered. However some mechanisms can produce losses of energy in astrophysical  $\gamma$ -rays or their total absorption, altering the spectrum that is measured from Earth. These mechanisms can be divided into  $\gamma$ -matter interactions and  $\gamma - \gamma$  processes.

### 1.4.1 Interaction with electrons: Compton effect

Compton effect is produced when a photon is scattered by an electron, shifting the wavelength of the photon to lower energies. The shift in the wavelength goes like:

$$\lambda' - \lambda = \frac{h}{m_e c} (1 - \cos\theta) \quad (1.17)$$

Where  $\lambda'$  is the wavelength of the scattered photon,  $\lambda$  the wavelength of the incident photon and  $\theta$  is the scattering angle. In the standard ISM density of 1 atom per  $\text{cm}^{-3}$ , for distances of  $\sim 10$  kpc, the mean free path for photons of 1 MeV would be of 2 Mpc, thus the Compton effect is negligible. In hot dense plasmas, where densities are much higher, the effect can start to be important [19]. This effect is used in Compton  $\gamma$ -ray telescopes such as described in section 2.1.1.

### 1.4.2 Pair production processes

Pair production is the opposite process to pair annihilation, where two photons interact to produce a pair  $e^-e^+$ . This is the most common absorption mechanism for HE and

VHE photons. A  $\gamma$ -ray with energy  $\epsilon_1$  which collides with a target photon with energy  $\epsilon_2$  will produce a pair of particles of mass  $m$  if  $\epsilon_1$  is greater than a threshold energy:

$$\epsilon_t = \frac{2m^2c^4}{\epsilon_2(1 - \cos\theta)} \quad (1.18)$$

where  $\theta$  is the angle between the trajectories of the photons. In astrophysics, this process occurs when energetic photons traveling through the Universe encounter a radiation field, such as the CMB ( $\epsilon_t \approx 4 \times 10^{14}$ eV) or the light of stars ( $\epsilon_t \approx 4 \times 10^{11}$ ). Even though photon-photon collisions are not generally frequent, because the spatial density of the target photons is not very large ( $\approx 400 \text{ cm}^{-3}$  for the CMB radiation, and  $\approx 5 \times 10^{-3} \text{ cm}^{-3}$  for extragalactic starlight) the attenuation effect can be appreciated, specially for VHE photons coming from high redshifts. This process also occurs when  $\gamma$ -rays penetrate the atmosphere and are absorbed, leading to the production of Extensive Air Showers (EAS), which are the key for ground-based  $\gamma$ -ray detectors and will be covered in section 2.2.

### 1.4.3 The Extragalactic Background Light

The Extragalactic Background Light (EBL) is the accumulated radiation in the universe due to star formation processes and the emission from AGNs. It is a fundamental constituent of the universe that permeates it uniformly. The direct measurement of the EBL is a very difficult task, mainly because of the foreground light from the Solar System. Phenomenological approaches try to predict an EBL model based on galaxy formation and evolution during the history of the universe and several direct measurements have been done from the far infrared , to the optical, to set constraints on the density and spectrum of the EBL [27]. Besides the different proposed models, it is accepted that the energy density is characterized by two peaks, as seen in figure 1.7. The first peak, found at  $\sim 1\mu\text{m}$  is the stellar component and the second peak at  $\sim 100\mu\text{m}$  is the dust component, the light re-emitted by cosmic dust.

EBL photons are a typical target for  $\gamma$ -rays to produce pair production. The attenuation to the spectrum of a  $\gamma$ -ray source at the energy  $E$  follows the form:

$$F = F_0(E)e^{\tau(E,z)} \quad (1.19)$$

Where  $F$  is the observed flux and  $F_0$  the intrinsic spectrum of the  $\gamma$ -ray source,  $\tau$  is the optical depth which depends on the energy and the redshift  $z$  (as shown in figure 1.8). As a consequence of this dependence, for each energy there is a distance (redshift) at which the universe is optically thick to  $\gamma$ -rays when the optical depth is equal to 1. The spectrum of the  $\gamma$ -ray source will suffer a cutoff at the energy that reaches the threshold optical depth, which decreases rapidly with redshift. Observations of this effect in distant sources in the VHE range are very useful to characterize the EBL indirectly, comparing the expected spectrum to the measured one [29].

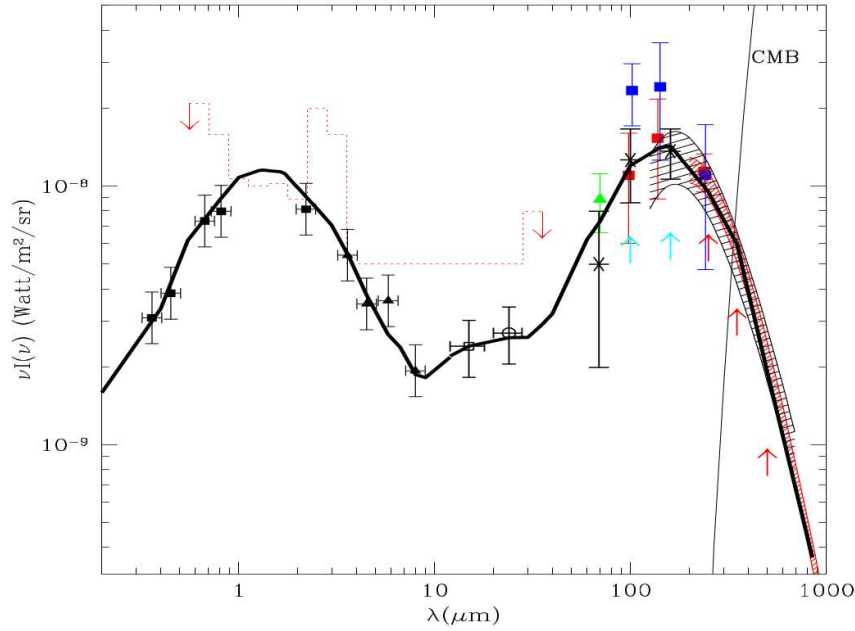


Figure 1.7: Best fit model prediction of the EBL energy density from [28] (thick black line).

## 1.5 Dark Matter and $\gamma$ -rays: WIMP annihilation

The nature of Dark Matter (DM) is one of the most important open questions in modern physics. Many probes suggest that the universe is composed of something more than the visible matter: From the Fritz Zwicky measurements on the velocity dispersion in the Coma galaxy cluster [30], and the rotation curves of high-luminosity spiral galaxies obtained by Vera Rubin [31], to the much more modern measurements of the CMB, by Planck [32], all of them point towards the existence of a non-baryonic type of matter which only interacts gravitationally with Standard Model (SM) particles. Cosmological simulations and cosmological probes such as Wilkinson Microwave Anisotropy Probe (WMAP) point to a hierarchical structure formation of the universe, where small structures were formed first and then merged to the larger. To accomplish for that model, if DM is formed by particles, they should be non-relativistic (Cold dark matter) which decoupled from the thermal equilibrium in the early universe. Hot dark matter models, where DM particles would be still largely relativistic (like neutrinos), would lead to large structures forming first and fragment out later [33]. With these assumptions, we can derive the number density evolution of DM particles today. In the early universe, DM and SM particles were in thermal equilibrium with the photon bath emitted in the Big Bang, and reactions of annihilation and formation of particles were taking place at the same rate. While the universe expanded, these reactions started to be slower than the rate of expansion, so these particles *decoupled* from the thermal bath. This is the moment of *freeze-out*. Before that, particles had

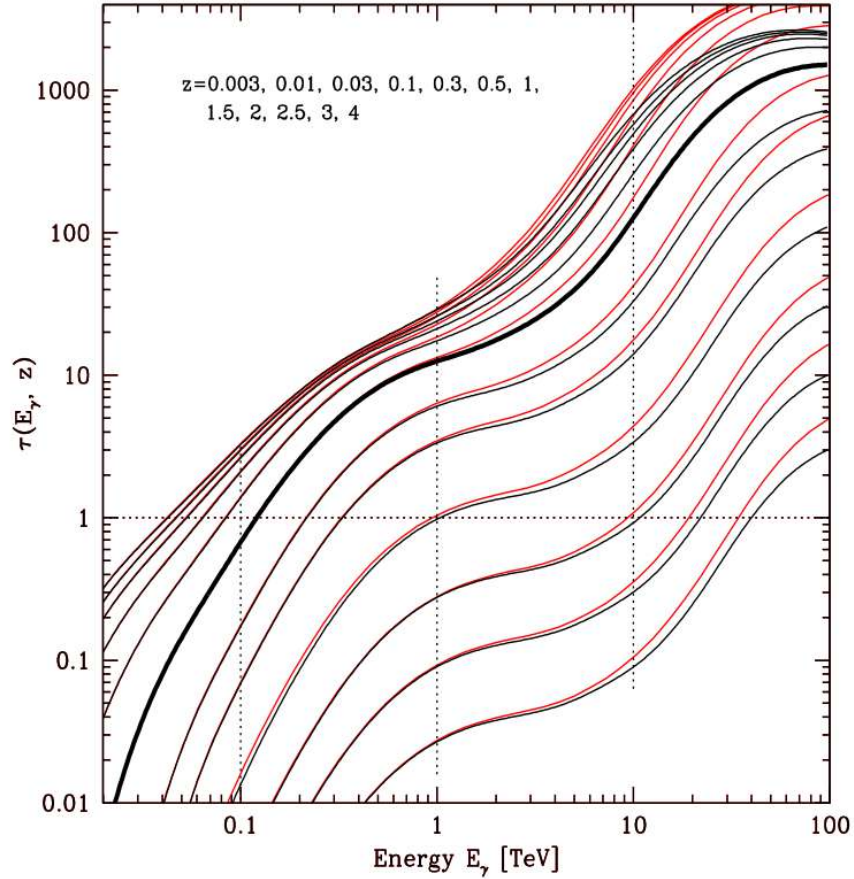


Figure 1.8: Optical depth due to photon-photon collision as a function of energy for different redshift values, from [28].

an equilibrium number density  $Y_{eq}$ , which evolves with time while the universe keeps expanding. For DM, and using the Boltzmann equation, the number density evolution  $dY/dx$  follow the equation:

$$\frac{dY}{dx} = -\frac{xs\langle\sigma v\rangle}{H(m)}(Y^2 - Y_{eq}^2) \quad (1.20)$$

Where  $m$  is the mass of the DM particle,  $x$  is the scaled time variable  $x = m/T$ , being  $T$  the temperature of the photon bath at the moment of freeze out,  $s$  is the total entropy density of the universe,  $Y$  is defined as the number density of DM rescaled to  $s$  ( $Y = n/s$ ) to account for the expansion of the universe,  $\langle\sigma v\rangle$  is the velocity averaged cross section for the reaction of DM particles annihilating into SM particles and  $H(m)$  is the Hubble rate (which defines the rate of expansion of the Universe) defined as  $H(x) = H(m)/x^2$ . While the annihilation rate of the particles is higher than the expansion rate of the universe ( $\Gamma \gg H$ ), the number density  $Y$  remains close

to  $Y_{eq}$ . After the moment of freeze-out  $x_f$  ( $\Gamma \ll H$ ), the number density will remain almost constant as shown in figure 1.9.

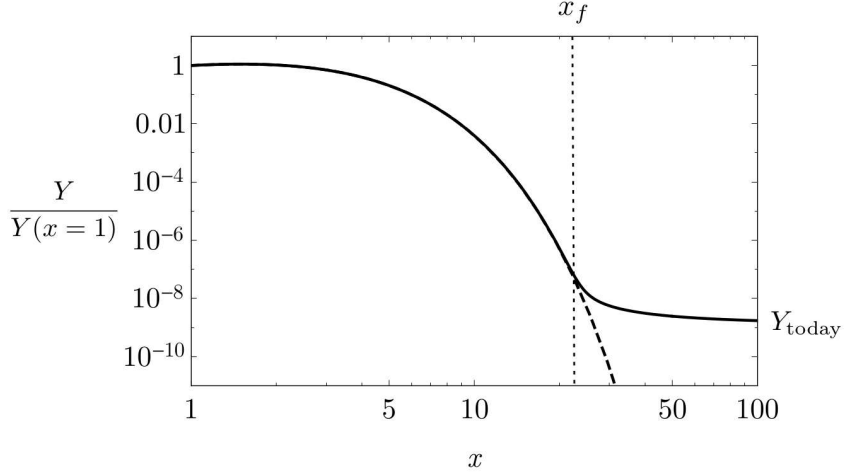


Figure 1.9: Evolution of Cold Dark Matter number density with time variable  $x$ ,  $x_f$  is the time of *freeze-out*, from [34].

Following the approach of [34], after freeze-out, the evolution of DM abundance can be written as:

$$\frac{dY}{dx} \approx -\frac{\lambda}{x^{n+2}}, \text{ where } \lambda = \frac{\langle \sigma v \rangle_0 s_0}{H(m)} \quad (1.21)$$

To define  $\lambda$  the dependency of the cross section and entropy with  $x$  was pulled out through the change of variables:  $\langle \sigma v \rangle = \langle \sigma v \rangle_0 x^{-n}$  and  $s = s_0 x^{-3}$ , where  $n$  is an exponent which depends on details of the particle physics model. Taking  $n=0$ , the DM abundance today would be  $\simeq x_f/\lambda$ . There is no SM particle which can explain the cosmic density of DM measured today  $\Omega_\chi$ , but if we consider a weak interacting particle in the weak mass regime ( $m_\chi \sim 100$  GeV), the correct DM density measured by Planck and WMAP arises naturally:

$$\Omega_\chi = \frac{m_\chi s_{today} Y_{today}}{\rho_{cr}} \rightarrow \Omega_\chi h^2 \sim \frac{10^{-26} cm^3/s}{\langle \sigma v \rangle} \simeq 0.1 \left( \frac{0.01}{\alpha} \right)^2 \left( \frac{m_\chi}{100 GeV} \right) \quad (1.22)$$

where  $\rho_{cr}$  is the critical density in the universe required for it to be at balance. This is called the ‘WIMP miracle’ for the theoretical Weak Interacting Massive Particles (WIMPs) which have some candidates within the Super Symmetry (SUSY) theory. Although the annihilation of these particles would be strongly suppressed after freeze-out, it can still occur in regions with high DM density. The products of this annihilation are pairs of SM particles that can be detected as an excess signal

in particle detectors, providing indirect evidence of the presence of DM. This way,  $\gamma$ -ray astrophysics can contribute to the indirect detection of DM signatures: Two DM particles can annihilate directly into a pair of  $\gamma$ -rays with a characteristic line spectrum with  $E_\gamma = m_\chi$  or they can annihilate into pairs of other SM particles which afterward decay giving out a continuum spectrum of  $\gamma$ -rays.

The differential flux of photons produced by DM annihilation is described as:

$$\frac{d\Phi}{dE} = \frac{1}{8\pi} \frac{\langle \sigma v \rangle}{m_\chi^2} \frac{dN_\gamma}{dE} \int_{\Delta\Omega} \int_{l.o.s} dl \rho^2(\vec{l}) \quad (1.23)$$

Where  $dN/dE$  is the spectrum of  $\gamma$ -rays from annihilation of a pair of dark matter particles,  $\langle \sigma v \rangle$  is the thermal velocity averaged annihilation cross section,  $m_\chi$  is the DM particle mass and  $\rho$  is the dark matter density profile. If DM particle is not its own antiparticle, equation 1.23 should be multiplied by a factor 1/2.

The first term of the equation comes from the already discussed particle physics, depends on the annihilation channel and the mass of the particle. The integral second term is known as the J-factor and is the integral over the line of sight and solid angle  $\Delta\Omega$  of the squared DM density profile ( $\rho$ ) and it dependent on the source. The most simple density profile for a dark matter halo that we can think of is a self-gravitating isothermal gas sphere, where:

$$\rho(r) \propto 1/r^2 \quad (1.24)$$

However, to address the actual physics of galaxy evolution, we need to rely on structure formation simulations which follow the initial DM density perturbations until the formation of current halos. From these simulations and from actual observations [35] we know that the DM density profile can be well reproduced as a six-parameters function of distance  $r$  from the center of the profile [36][37][35]:

$$\rho(r) = \frac{\rho_0}{\left(\frac{r}{r_s}\right)^\gamma \left[1 + \left(\frac{r}{r_s}\right)^\alpha\right]^{\frac{\beta-\gamma}{\alpha}}} \Theta(r_{max} - r) \quad (1.25)$$

Where  $\Theta$  is the Heaviside step function,  $r_s$  is the scale radius, and  $\rho_0$  is the characteristic density. These two last parameters depend on the specific DM halo. Setting  $(\alpha, \beta, \gamma) = (1, 3, 1)$  we retrieve the Navarro-Frenk-White profile [38]. Combinations of these parameters can be used to fit a possible DM signal to a specific profile. Other types of profiles have also been treated in the literature, such as the Einasto profile [39]. From 1.23, we can see that the best objects to search for a  $\gamma$ -ray signal will be those that are nearby and DM dense, so the J-factor would be sufficiently large relative to the background of  $\gamma$ -rays produced by ordinary matter interactions.

## 1.6 $\gamma$ -ray sources

In the previous section, the processes that produce  $\gamma$ -ray emission were introduced. In this section, the astrophysical objects where they take place are described. Two major classes of  $\gamma$ -ray emitters can be distinguished: galactic sources and extragalactic sources. At the end of the section, potential sources for DM annihilation signals will be also covered. Figure 1.10 show the current known population of VHE  $\gamma$ -ray sources based on the observations of the current generation of  $\gamma$ -ray detectors, either in space (*Fermi*-LAT) or ground based (the Major Atmospheric Gamma Imaging Cherenkov Telescopes (MAGIC), the High Energy Stereoscopic System (H.E.S.S.), the Very Energetic Radiation Imaging Telescope Array System (VERITAS) and the High-Altitude Water Cherenkov Observatory (HAWC)).

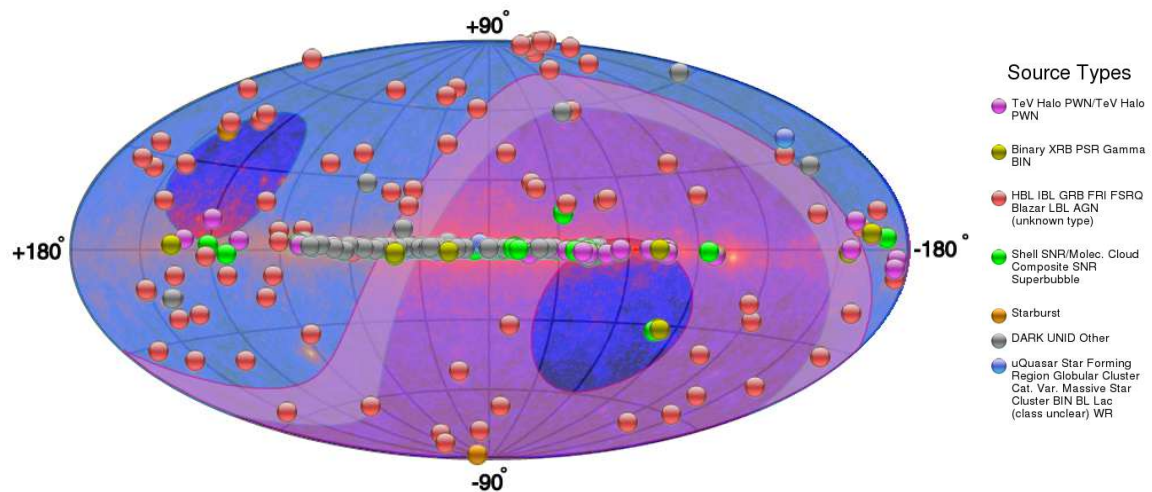


Figure 1.10: Full skymap from TeVCat[40] catalog as of July 2019, with all the detected TeV sources. In the background, the *Fermi*-LAT skymap is shown and the shadowed regions correspond to the MAGIC field of view (blue) and H.E.S.S. (pink).

### 1.6.1 Galactic sources

As shown in figure 1.10, the richest region in  $\gamma$ -ray sources is the galactic plane, meaning that the majority of detected emitters belong to our galaxy. In this section, the different characteristics of these sources will be described.

#### Pulsars

Pulsars are the most common type of  $\gamma$ -ray emitters known. When a massive star ( $< 8M_{\odot}$ ) suffers gravitational core collapse at the end of its life, the resulting object is a compact neutron star sustained by degeneracy pressure, where neutronization (the combination of protons and electrons) has taken place due to the extremely high pressures which lead to high densities ( $> 10^9 g/cm^3$ ). The neutron star comprises 1 - 2  $M_{\odot}$  in a radius of 10 - 14 km and as the angular momentum of the parent

rotating star is conserved, the much more compact neutron star will spin at extremely high velocities with periods that can go from milliseconds to a few seconds. This fast spin produces strong magnetic fields in their surroundings where electrons and positrons are accelerated by the electric field aligned with the magnetic field. When the magnetic fields are aligned with the line of sight from the Earth, we can detect a pulsed emission (mainly synchrotron and curvature radiation) with the period of the rotation of the neutron star. This object is what is called a pulsar. Pulsed emission has been detected broadband in the electromagnetic spectrum, from radio to  $\gamma$ -rays. It is generally accepted that the origin of the  $\gamma$ -ray emission from pulsars is due to curvature radiation, produced when relativistic electrons accelerated in gaps of the electromagnetic fields powered by the pulsar rotation, are trapped and propagate along the lines of the magnetic field [41]. However, the location of the gaps and the dominating acceleration mechanism are not well known and there are different models proposed (see figure 1.11).

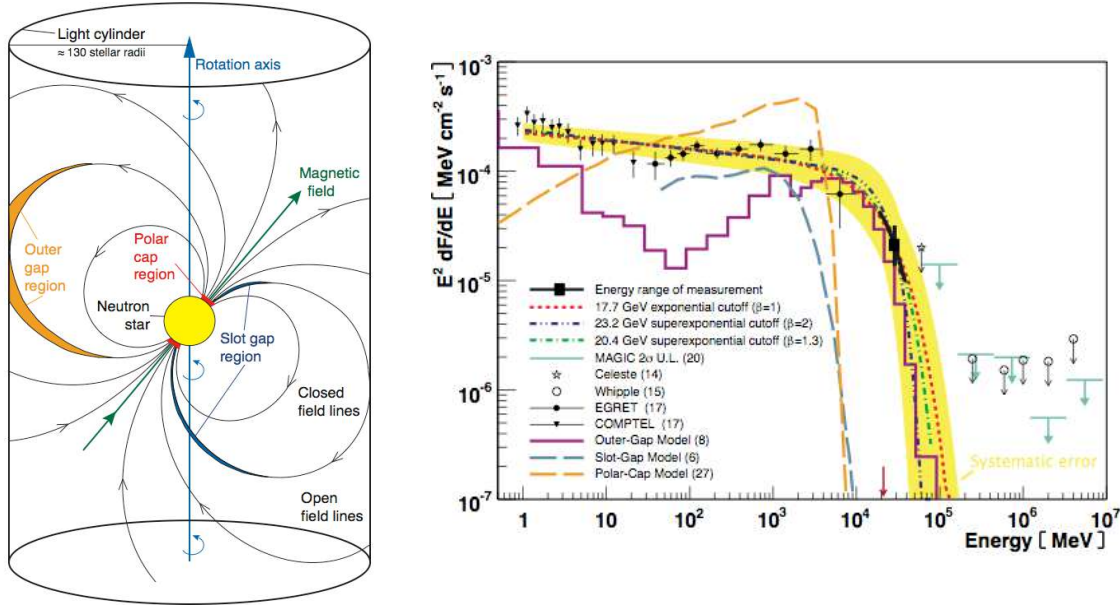


Figure 1.11: *Left:* Crab pulsar's magnetosphere where the location of the three models (Polar-Cap in red, Slot-Gap in blue and Outer-Gap in yellow) is shown. *Right:* Crab pulsar spectral cutoff. Figures from [41]

Combined observations of the Crab pulsar from the Imaging Compton Telescope (COMPTEL), the Energetic Gamma Ray Experiment Telescope (EGRET) [42], MAGIC [41], VERITAS [43] and *Fermi*-LAT [44] have shown that their spectrum follows a power law with a cutoff at energies over a few GeV (see figure 1.11). The detection of the pulsar emission at energies over 25 GeV by MAGIC ruled out the possibility of acceleration happening too close to the pulsar (as the Polar-Cap model assets) because the magnetic pair-production attenuation would provide a super-exponential cutoff at much lower energies to those observed. Currently, the

Outer-Gap model offers the best explanation of the observed Crab spectrum [45]. While pulsars are the most common  $\gamma$ -ray emitters, only two have been detected in the VHE range, up to TeV energies: the Crab and Vela pulsars [46].

### **Supernova Remnants**

Supernovae are the result of the evolution of a star, which suddenly becomes much brighter while shells of gas are expelled to the interstellar medium in an explosive event. They can be classified in different types by features in their spectrum, which also implies a different origin of the explosion. Type II supernovae show hydrogen emission lines, meaning they come from very massive stars ( $M > 8M_{\odot}$ ) with hydrogen in their outer layers. After burning lighter elements (H, He, etc.) into heavy nuclei, fusion reactions become inefficient and the imbalance between gravitational forces and pressure radiation lead to the collapse of the central core into a neutron star or a black hole in a violent reaction, expelling shells of material at high velocities. Type I supernovae do not present hydrogen lines, meaning they come from a hydrogen-poor star. They usually are produced by white dwarfs in binary systems that accrete material until reaching the Chandrasekhar limit [47] and suffer a thermonuclear explosion. Type I supernovae are classified in subtypes: Type Ia show Si lines in their spectra, whereas those without these lines are classified as Ib if they have He lines and Ic if not [48].

The structure of ejected material which is left in the surroundings of the parent star is the SNR. These structures can be classified in different types depending on their spectrum, but the most important feature to differentiate them is the presence (or not) of a shell. There are shell-type SNRs, in which the material in the surroundings is heated by the power of the shockwave during the SN explosion. The so-called *plerion* SNR or Pulsar Wind Nebula (PWN) do not present a shell. The result of the SN explosion is always a central pulsar and their emission is produced by the interaction between electrons ejected to the medium by the pulsar and its huge magnetic field. There is also a composite type of SNR where a plerion is surrounded by a shell and depending on the wavelength observed, they emit more like one type or the other [49]. Depending on the SNR type, the particle acceleration and  $\gamma$ -ray emission would have a different origin and features.

- **Shell-type remnants:** Shell-type remnants, commonly referred simply as SNRs, are the most popular candidates for CR acceleration. We know CRs can produce  $\gamma$ -rays via hadronic interactions with the gas and dust in the medium. For example, the production of pions and posterior pion decay would give rise to a spectrum with a characteristic peak at 67.5 MeV, if pions are at rest. A simple energetic argument is used to pose shell-type remnants as the main source of galactic CRs: As a rough estimation, if we assume that the typical total kinetic energy produced by a SN explosion is around  $E_{SN} \sim 10^{51}$  erg, with a SN rate in the galaxy of about one in 50-100 years, and a constant fraction  $\eta$  of the kinetic energy is transferred to hadrons, it can be shown that this fraction has to be of the order of the 10% to retrieve the approximated CR luminosity in the galaxy

$$L_{CR} \sim 2 \times 10^{41} \text{ erg/s.}$$

$$L_{CR} = \eta \cdot E_{SN} \cdot SN_{rate} = 0.1 \cdot 10^{51} \text{ erg} \cdot 50 \text{ yr}^{-1} \propto 10^{41} \text{ erg/s} \quad (1.26)$$

A more detailed analysis using real data of galactic SNR was done by [50] concluding that future  $\gamma$ -ray data can be used to constrain the amount of CR energy coming from SNR. However, there are still problems with proving this hypothesis because many of the  $\gamma$ -ray signatures coming from SNR have a leptonic origin rather than hadronic. Also, for SNRs to reproduce the full spectrum of CR, SNRs should be pevatrons (meaning they can accelerate CR to PeV energies) at some fraction of their lifetimes, to reach the region after the *knee*. Still, no SNR pevatron has been observed yet but high hopes are deposited in the next generation of  $\gamma$ -ray experiments [51].

- **Plerions or Pulsar Wind Nebulae.** As mentioned, PWN are powered by a central rotating pulsar which dissipates kinetic energy over time in the form of *spin down luminosity*. This energy is injected steadily into the surrounding nebula of ejected material that was formed during stellar evolution. To understand the features of the emission of Pulsar Wind Nebulae (PWNe), it is important to follow their evolution with time and how the period, spin-down luminosity and magnetic field changes [52]. A pulsar is formed in a SN explosion and the final state of the pulsar and its PWN will depend on how it interacts with the SNR. If the SNR expands outward freely, the pulsar will remain in the center, but if a reverse shock happens, reverberations between the PWN and the shock can produce instabilities which in the end will displace the pulsar from its original position, even being able to cross away from the SNR shell. Strong magnetic fields in pulsars create currents of particles of the surrounding nebula, producing pulsar winds. Electrons accelerated this way produce synchrotron radiation from radio to X-ray wavelengths. The wind starts decelerating when reaching the nebula radius, due to the more slowly expanding material, and thus a wind termination shock is formed. The TeV  $\gamma$ -ray emission from PWNe is explained as IC emission produced by the relativistic particles in the shocked wind interacting with the synchrotron photons. The Crab PWN was the first source detected of this type, associated with a SN explosion observed in 1054 CE, and has become a sort of standard candle for  $\gamma$ -ray astrophysics.
- **Composite remnants.** A rare type of SNR is a combination of the previous two, where a PWN is surrounded by a shell-type SNR. Usually, PWNe are considered young SNRs while shell-types are older systems. Composite SNRs could be an intermediate phase of evolution where the shell and the PWN evolve and interact together [53]. In these systems, the PWN formed in the interior of the SNR expands outwards and it can encounter the inward reverse shock of the SNR [54]. Some examples of this kind are SNRs W28, W44, and SNR G21.5-0.9, which is shown in figure 1.12.

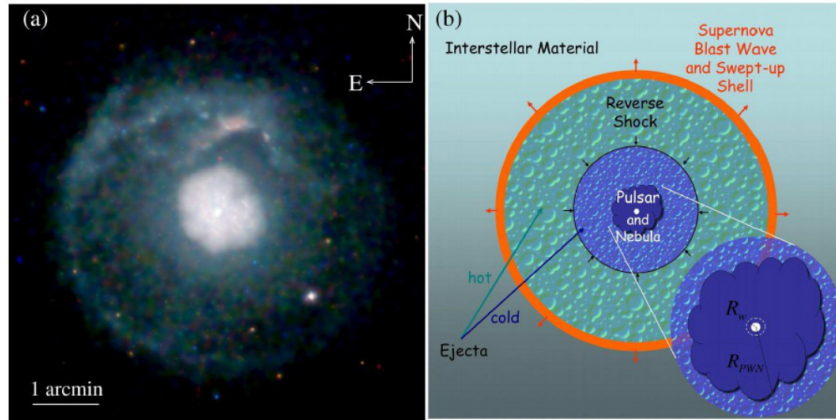


Figure 1.12: a): Chandra X-ray image of the composite SNR G21.5-0.9. b): Diagram of a PWN inside a SNR. Pictures from [54].

### $\gamma$ -ray binaries

$\gamma$ -ray binaries are systems composed of two objects orbiting each other: One is a compact object, such as a pulsar and the other can be an ordinary massive star big enough to reach the Roche lobe of the pulsar, with stellar winds connecting the two objects. Just a few objects ( $< 10$ ) of this kind have been detected in HE and VHE  $\gamma$ -rays very recently [55], and yet the exact mechanisms of the origin of their emission are unknown. There are two main explanations to the HE and VHE emission in  $\gamma$ -ray binaries. It can be produced by accretion energy released in the form of relativistic jets, or by the energy emitted by the pulsar in the form of pulsar winds in a similar way as in PWNe. The first case is denominated the *microquasar* scenario due to its similarities with AGN (also known as quasars) but emitting jets in a smaller scale. However, a variety of indirect evidence seems to favor the pulsar wind interpretation mainly based on the spectral similarities of the known binaries with the power of a pulsar spindown. Also the presence of strong magnetic fields and morphological characteristics of radio emission are similar features to those found in PWNe [56].

### Novae

Binary star systems are rather common objects in the universe. One of the stars can be more massive than the other, evolving faster and becoming a white dwarf while the second star can still be in its main sequence phase. If this happens, the white dwarf can start accreting material from the companion, building an accretion disk. The hydrogen-rich gas in the surface of the white dwarf starts heating the bottom layers, which become electron-degenerated, leading to a chain of thermonuclear explosions [57]. This event is known as "classical nova". When the companion star is a red giant, which has highly increased its volume, the system is called a *symbiotic binary system*. In this case, the interaction between the stellar wind of the red giant and the white dwarf surface expansion gives place to a favorable scenario for particle

acceleration. Both classical novae and symbiotic systems have been detected in HE  $\gamma$ -rays by *Fermi*-LAT [58], [59] although these results do not allow to differentiate between the different emission scenarios.

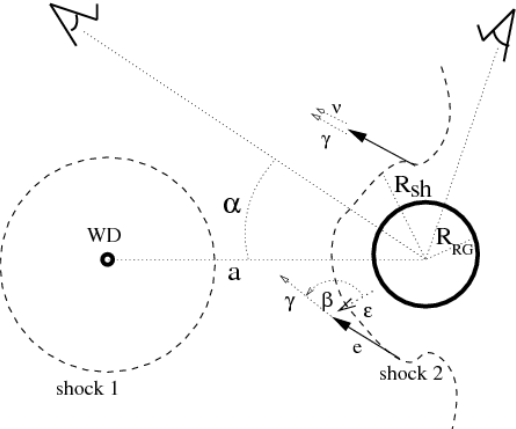
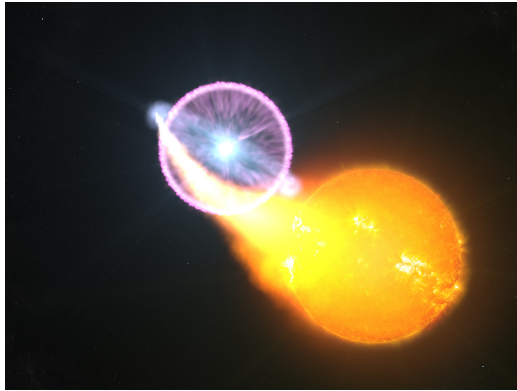


Figure 1.13: *Left:* Artist concept of a classical nova. Credits: NASA’s Goddard Space Flight Center/S. Wiessinger. *Right:* Diagram of the geometry of the symbiotic binary system V407 Cyg from [60]. The expanding shock (1) from the white dwarf partially overtakes the Red Giant (shock 2), producing particle acceleration through IC (leptonic scenario, with angle of interaction  $\beta$ ) and proton collisions with the red giant wind (hadronic scenario).

### The Galactic Center and the Fermi Bubbles

The Galactic Center (GC), which is the center of the Milky Way (MW), is a region of the sky situated at  $4^\circ$  longitude,  $2^\circ$  latitude, with a size of  $600 \times 300$  pc and at a distance of about 8 kpc. It is obscured by dust in the optical and ultraviolet range, but emission in infrared, radio, X-rays, and  $\gamma$ -rays reveals a prolific region full of energetic sources. Among many SNRs, PWNe and stellar clusters in HII regions, there is also a Super Massive Black Hole (SMBH), Sagittarius A\*, whose detection has been one of the major motivations for GC surveys. Many  $\gamma$ -ray experiments have surveyed the GC region (*Fermi*-LAT, MAGIC [61], H.E.S.S. [62], VERITAS [63]) and emission from HE to VHE bands has been detected. The main problem with this highly populated region is the difficulty of telling apart individual sources, making it a big challenge to identify the actual emission from Sgr A\* [64]. The high energy emission from Sgr A\* has its origin in the strong winds produced by the presence of an accretion disk surrounding the black hole, where the material is accelerated at very high energies [65].

Closely related to Sgr A\* might be the *Fermi bubbles*, two large  $\gamma$ -ray lobes that appear to be ejected from the center of the galaxy. They were discovered while searching for a  $\gamma$ -ray counterpart to the WMAP haze [66], which is a residual microwave emission that arises after subtracting all the other known emission components. They extend to  $55^\circ$  up and above the GC and are not symmetric, with an enhanced emission towards

the south-east side of the bubbles. With well-defined edges, a uniform power-law spectrum of index  $\sim 2$ , and a cocoon-like shape, they resemble jet-like structures [67]. Their origin is still under debate: They could be jets, outflows, or the result of accretion events from the black hole, winds from SN explosions, or the remnant of AGN activity in the MW in the past.

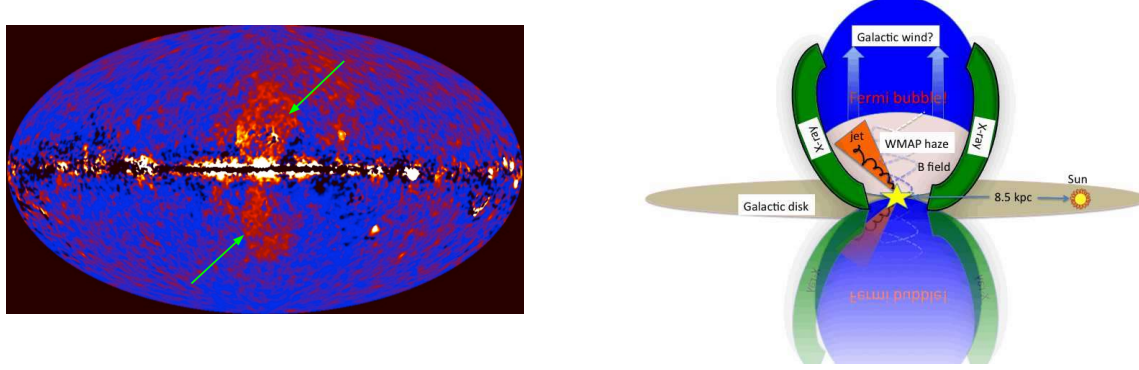


Figure 1.14: *Left:* The Fermi Bubbles as seen by *Fermi*-LAT after subtracting all the other known  $\gamma$ -ray components. Credits: NASA/DOE/Fermi LAR/D. Finkbeiner et al. *Right:* Schematic picture of Fermi Bubbles structure from [66].

### Globular Clusters

Globular clusters are compact gravitationally bounded stellar associations with spherical geometry that are distributed outside the galactic plane, forming a spherical halo around the galaxy. They are old highly evolved systems with many compact objects like neutron stars, white dwarfs, and pulsars even forming binary systems. Furthermore, the majority ( $\sim 80\%$ ) of Millisecond Pulsars (MSPs) (pulsars with a period of the order of milliseconds) detected up to date have been found in globular clusters. Since all the mentioned objects are well known  $\gamma$ -ray emitters, globular clusters have been observed and detected in  $\gamma$ -rays by *Fermi*-LAT [68] and H.E.S.S. [69]. Even pulsed  $\gamma$ -ray emission have been observed from individual MSPs [70], [71]. Two types of models of  $\gamma$ -ray emission have been discussed to happen in globular clusters, both related to MSPs. One takes place in MSPs magnetospheres, where  $\gamma$ -ray emission would be produced by curvature radiation. The second type of models involve IC scattering of electrons accelerated close to the MSP with optical, infrared or CMB photons [72].

#### 1.6.2 Extragalactic sources

While most of the  $\gamma$ -ray emission detected on Earth comes from the galactic plane, there is a big amount of individual sources outside our galaxy that produce HE radiation and allow the study of a new range of extragalactic phenomena. A big caveat for extragalactic sources is that the VHE range is suppressed by the EBL absorption, as described in section 1.4.

### Active Galactic Nuclei

AGN are the brightest steady sources of  $\gamma$ -rays in the universe and the most luminous known electromagnetic emitters. Known as *black-hole galaxies*, their strong emission is powered by infalling gas into a massive Black Hole (BH) located in the center. The BH attracts gas and material from the galaxy, forming an accretion disk, where matter loses angular momentum through turbulent processes in high viscosity regions and emits a huge amount of energy from ultraviolet to soft X-ray bands [73]. AGN can be classified in two broad types, according to their radio emission: *Radio-quiet* and *radio-loud*. Further observational classification depends strongly on the orientation angle, which can make AGN appear as spectroscopically completely different sources, depending on the region of the object that is showing. All AGN have a dusty tori, broad-line regions, narrow-line regions and strong blue/UV bump emissions from the accretion disk [74]. Depending on the angle, one or several of these regions will be observable and will show their particular features in the spectrum. Figure 1.15 show a scheme of AGNs taxonomy.

Radio-loud AGN, also known as *blazars*, are about three orders of magnitude brighter in radio band than their quiet counterparts. This radio emission is directly related to the presence of relativistic jets of plasma which carries a big part of the energy released during accretion and that afterward is emitted as radiation from radio to  $\gamma$ -rays [75]. They are associated with elliptical galaxies that have undergone recent mergers. On the contrary, radio-quiet galaxies do not show jets and so do not account for high energy non-thermal emission. Also, they are typically spiral galaxies in lower density regions [76]. Blazars are rare among AGN, accounting only for 10% of the total, but a large number of them have been detected in  $\gamma$ -rays, with more than 1500 sources detected at GeV energies, and more than 60 at TeV energies [74].

### Gamma Ray Bursts

GRBs are short and intense flashes of  $\gamma$ -ray emission coming isotropically from random directions in the sky. With a range of luminosities from  $10^{51}$  ergs/cm<sup>2</sup> to  $10^{52}$  ergs/cm<sup>2</sup> they are the brightest transient objects in the sky [78]. They can be classified by their duration, having two distinct populations: short GRBs, which last just a few seconds; and long GRBs which can last for a few minutes [79]. Long bursts are usually followed by afterglows in X-rays, optical, and radio which can last for several years after the event. The so-called *fireball* model is the generally accepted mechanism which drives GRB [80]. Since the observed emission of the bursts is not thermal, its origin must be the result of the conversion of a ultra-relativistic energy flow into radiation in an optically thin region. The energy flow could come from the kinetic energy of accelerated particles or electromagnetic Poynting flux. In this model, the process is ignited by an ‘inner engine’ which is not directly observed, but which activity can be characterized by the temporal structure of the bursts. The engine produces an explosive fireball of the size of the engine itself. There is an alternative model based on internal shocks, where the engine would produce wind and a long energy flow. About the nature of the phenomena producing GRBs, there exist an apparent difference

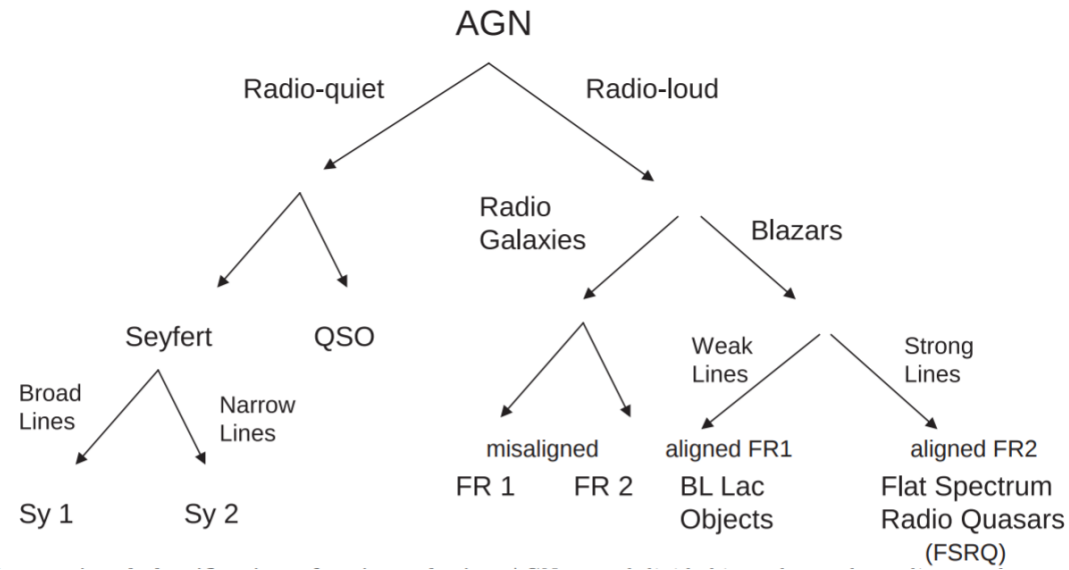
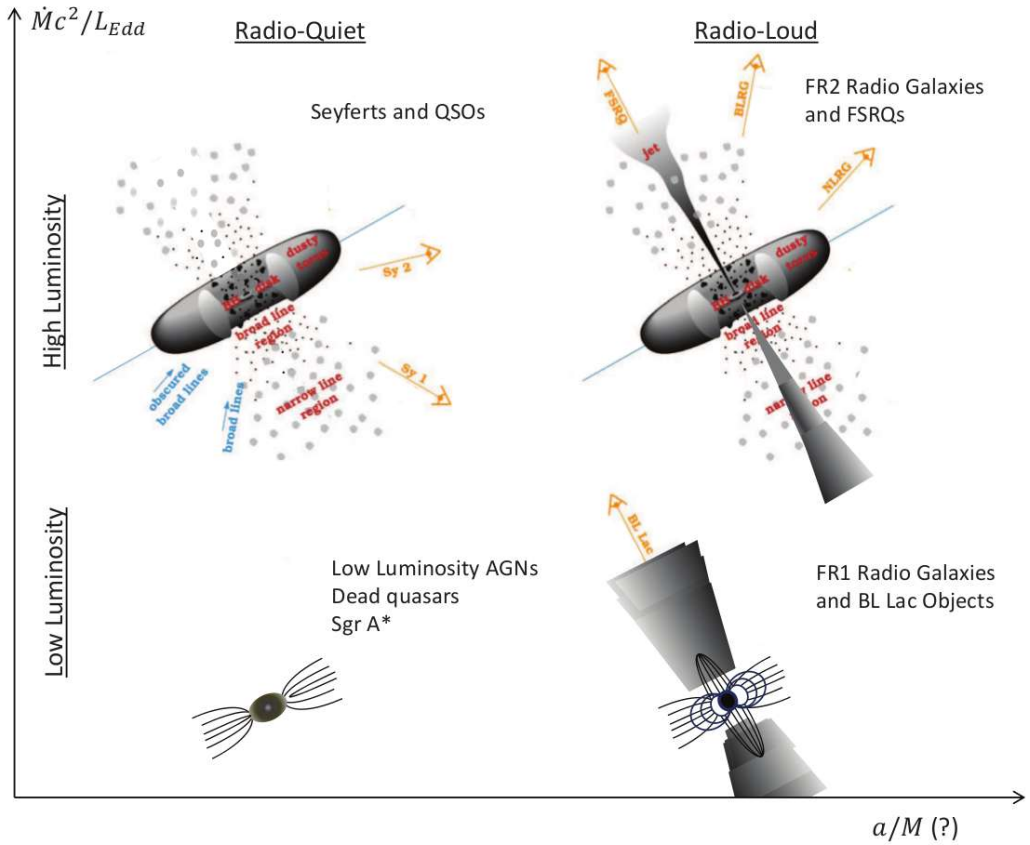


Figure 1.15: *Top:* AGN taxonomy as from [74]. In this scheme, the vertical axis represents the luminosity power in terms of the mass-accretion rate and horizontal axis represents the BH rotation. *Bottom:* Observational classification of active galaxies. QSO= quasi-stellar objects; Sy1(Sy2) = Seyfert 1(2); FR1(FR2)=Fanaroff-Riley 1(2). Pictures based on [77] and [74].

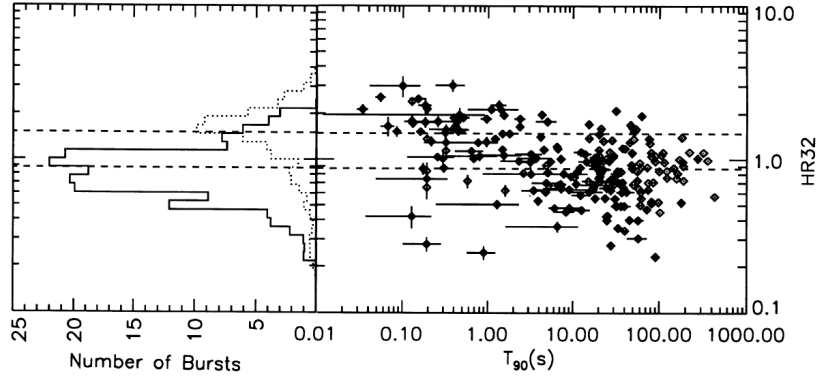


Figure 1.16: *Left:* Hardness ratios for the two duration classes of GRB. Solid lines corresponds to short GRBs, dashed line to long GRBs. *Right:* Hardness vs. duration plot, where duration  $T_{90}$  is defined as the time during which the cumulative counts  $> 25$  keV increase from 5% to 95% above background. Dashed lines correspond to the mean hardness ratio of the two classes. Figure from [79].

between the origin of short GRB and long GRB according to their hardness ratio (defined as the ratio of the flux in two separated bands) versus duration plot (see figure 1.16) [79].

These two populations in the hardness ratio vs. duration plot, together with rather significant spectral differences [81] and afterglow observations, suggest that long GRBs are closely related to star-forming regions, compatible with SN explosions of massive stars. Short GRBs on the other hand, could be related to more evolved regions and be the result of neutron star mergers, such as the recently detected gravitational wave event GW170817 by LIGO/VIRGO [82] which was also detected as a GRB by the Fermi Gamma-Ray Burst Monitor and later observed by *Fermi*-LAT [83]. Also recently MAGIC, which were specifically designed to observe such objects, detected the first event in the VHE range [84].

### Starburst galaxies

Starburst galaxies are those with a greatly enhanced star formation, whose Star Formation Rate (SFR) is considered to be out of equilibrium, consuming gas for star formation at very short timescales ( $< 1$  Gyr). Since the SFR is highly correlated with the SN explosion rate, it is expected that  $\gamma$ -ray emission detected from starburst galaxies has its origin in SNRs.

The production and transport of CRs in the ISM significantly affects the star formation, because CRs penetrate deep into molecular cloud cores (molecular clouds are dense gas regions where star formation takes place) catalyzing complex chemical reactions which can affect the initial conditions of star formation and evolution [85]. The conditions of the ISM in starburst galaxies are very different from MW [86]. The gas density is much higher and the high population of massive stars produces a huge amount of radiation, which is absorbed by dust and re-emitted in infrared. Magnetic fields are

also affected by the presence of such population. Thereby particles accelerated in the region will suffer strong losses of energy and faster cooling. Detection of  $\gamma$ -rays from starburst galaxies is a key probe to understand the efficiency of CR acceleration in SNRs and CR transport in different ISMs. The current generation of  $\gamma$ -ray telescopes have detected NGC253 and M82 starburst galaxies ([86], [87], [88]), which has been long predicted to emit  $\gamma$ -rays up to VHE range.

### **Galaxy clusters**

Galaxy clusters are the largest gravitationally bounded structures in the universe. They are mainly composed of DM (70-80% of the total mass) and their ordinary matter is composed of the galaxies and the filaments connecting them, plus a big amount of hot gas in the surroundings called the Intracluster Medium (ICM)[89]. In the standard paradigm of structure formation, clusters are formed by hierarchical mergers and accretion of smaller structures. Mergers are the most energetic phenomena to occur in the universe (they release  $10^{63}$ - $10^{64}$  ergs/Gyr) and they dissipate energy in the form of shocks which heat the gas or through large-scale ICM motions [90]. Part of the energy dissipated during this process is fused into particle acceleration to ultra-relativistic energies, thus they are a source of CR production. Radio observations of galaxy clusters prove the existence of non-thermal emission from synchrotron radiation processes in the ICM. Galaxy clusters can, therefore, be a source of HE photons which can be produced via leptonic scenario through IC scattering of CMB photons with ultra-relativistic electrons or hadronic scenario by neutral pion decay. Until recently,  $\gamma$ -ray experiments that tried to detect  $\gamma$ -ray signal from the closest galaxy clusters were only able to set upper limits [91], [92]. *Fermi*-LAT was able to report the detection of an extended  $\gamma$ -ray signal from the Coma cluster roughly correlated with the radio halo [93].

### **Neighbour galaxies**

The Local Group is the cluster of galaxies gravitationally bounded to the MW. They are the closest galaxies to be observed and their characteristics are expected to be similar to those of our galaxy. The second and third closest and spatially resolved galaxies (the first being the Canis Major dwarf galaxy) are the Large Magellanic Cloud (LMC) and the Small Magellanic Cloud (SMC). They are two irregular dwarf galaxies seen in the southern hemisphere, at a distance of 50 kpc [94]. They present a remarkable high star formation rate ( $\sim 0.2\text{yr}^{-1}$  for the LMC,  $0.3\text{yr}^{-1}$  for the SMC [95], compared to the  $0.68\text{yr}^{-1}$  to  $1.45\text{yr}^{-1}$  of the MW [96] in a much smaller volume.). They can produce  $\gamma$ -ray emission due to the interaction of CR with ISM. The first detection of a  $\gamma$ -ray diffuse signal from the LMC was made by EGRET [97], being the first normal galaxy outside the MW detected in  $\gamma$ -rays. The SMC was first detected in  $\gamma$ -rays by *Fermi*-LAT [98]. Further observations of the LMC from *Fermi*-LAT at HE [99], [100], [101] and H.E.S.S. [102], [103] at VHE revealed a complex structure of the diffuse emission and a population of very interesting individual sources comprising pulsars, SNRs, PWNe and  $\gamma$ -ray binaries. Since the LMC emission in  $\gamma$ -rays is one of

the main topics of this thesis, it will be extensively treated in chapter 5.

Apart from the before mentioned starburst galaxies M82 and NGC253, other close galaxies such as M31 and M33 have also been observed and detected in HE  $\gamma$ -rays by *Fermi*-LAT [104].

### **1.6.3 Potential Dark Matter annihilation emission sources**

In section 1.5 the production of  $\gamma$ -rays through WIMP annihilation or decay was described. In the search for this kind of signal, one can analyze which would be the best sources in the universe for an indirect search of DM. First of all, they must have a high amount of DM, given by the astrophysical parameter J-factor (integral term in eq. 1.23). Also, a low background of other  $\gamma$ -ray sources would permit to unequivocally identify the DM signal. Following these premises, indirect DM searches have been performed by  $\gamma$ -ray experiments in the most promising sources, described in this section.

#### **The Galactic Center**

In the present evolutionary stage of the universe, galaxies are believed to be embedded in DM halos which extend much more than the visible matter, the center of the galaxies being the location of higher DM density [105]. The center of the MW is therefore a promising target for DM searches. However, as explained in section 1.6.1, it is also a very populated region with many  $\gamma$ -ray sources which are even not fully resolved. This fact makes the GC a true challenge for disentangle a possible DM emission, needing a very good background modelling and control of the instrumental systematics [106]. Usually, DM searches in the GC tend to avoid the galactic plane region, observing a region with a lower background at expenses of having a weaker DM signal due to the lower density. The most constraining upper limits in the VHE energy range for the velocity averaged cross section  $\langle \sigma v \rangle$  in the GC have been established by H.E.S.S. [107]. Both *Fermi*-LAT and H.E.S.S. have accounted for a  $\gamma$ -ray excess coming from the GC of unknown origin which has been fitted with the most conventional DM models, but the results were not compatible enough to identify the excess with DM [108], [109].

#### **Dwarf Spheroidal Galaxies and Dark Clumps**

Following the standard model of cosmology, N-body simulations of the evolution of CDM since the Big Bang predicts a hierarchical structure formation where DM clusters into subhalos that merge into higher structures. The final picture at galactic scales, are galaxies embedded in a big DM halo, surrounded by a population of subhalos with mass inversely proportional to their number [110]. Simulations like Via Lactea II predict that the MW is surrounded by a large number of DM subhalos ( $\sim 50,000$ ). The heavier of these substructures are the so-called Dwarf Spheroidal Galaxies (DSphe). They are very faint galaxies (in optical) orbiting the MW. Many of the observed DSphe are strongly DM dominated, but have absent or very little star formation and no signal of ionized or neutral gas [111]. Smaller structures with no

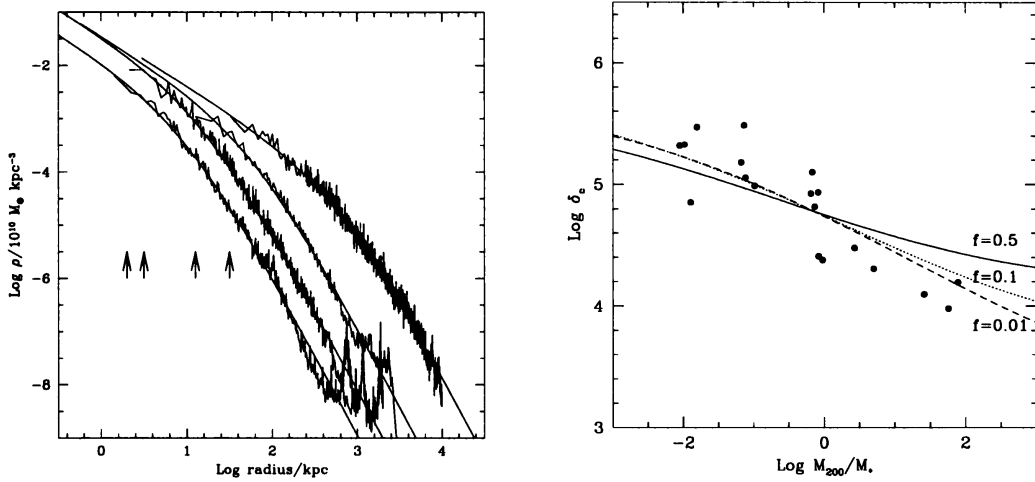


Figure 1.17: *Left:* Typical density profiles from Cold Dark Matter (CDM) halos obtained from N-body simulations. *Right:* Characteristic overdensity of halos as a function of mass. Masses are expressed in units of the current non linear mass corresponding to the standard biased CDM spectrum  $M_* = 3.3 M_\odot$ . Figures from [105].

emission at all are known as Dark Clumps. These objects are a perfect target for DM searches because no  $\gamma$ -ray signal is expected from them due to ordinary astrophysical processes. Any  $\gamma$ -ray detection would be an unequivocal signal of DM annihilation. The present generation of  $\gamma$ -ray experiments have widely studied these objects in the search for DM, not yet being successful at detection but setting very stringent upper limits on DM models using data from many DSphes ([112], [113], [114], [115], [116]).

### Galaxy Clusters

As has been mentioned before in section 1.6.2, galaxy clusters are mostly dominated by DM with a very high mass-to-light ratio. For this reason, they are good targets for indirect DM searches both for annihilation and decay. They are especially suitable for decaying DM since at large volumes the signal of decaying DM which is proportional to the first power of the density overshines the signal of annihilation [117].

Strong constraints for a wide number of models for DM annihilation and decay have been set by *Fermi*-LAT [118], [119] and H.E.S.S. [120], and also constraints on the decaying lifetime of DM were set by MAGIC [121].

### The Large Magellanic Cloud

The LMC has been considered a well promising target for DM searches due to its proximity and rather high J-factor ( $10^{20} J/\text{GeV}^2 \text{cm}^{-5}$ ). Kinematic studies of the LMC show that more than half of the LMC mass is forming a dark halo with a compact central bulge [122], [123].

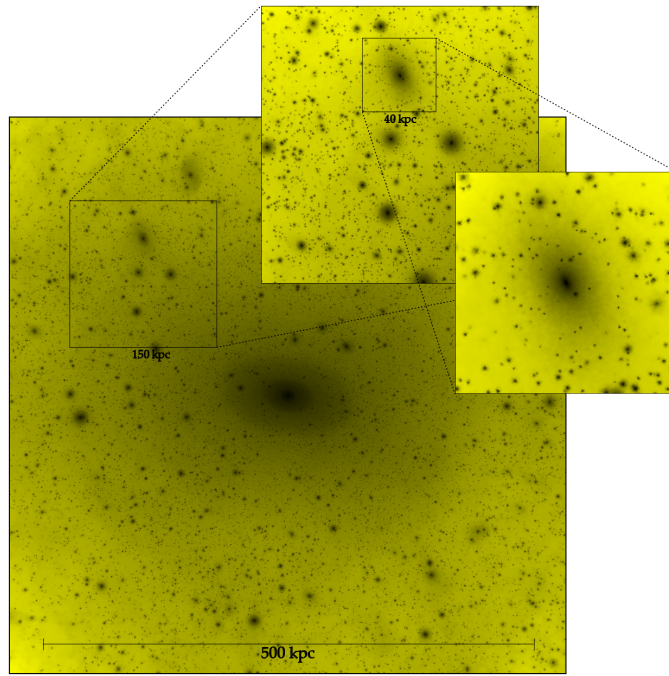
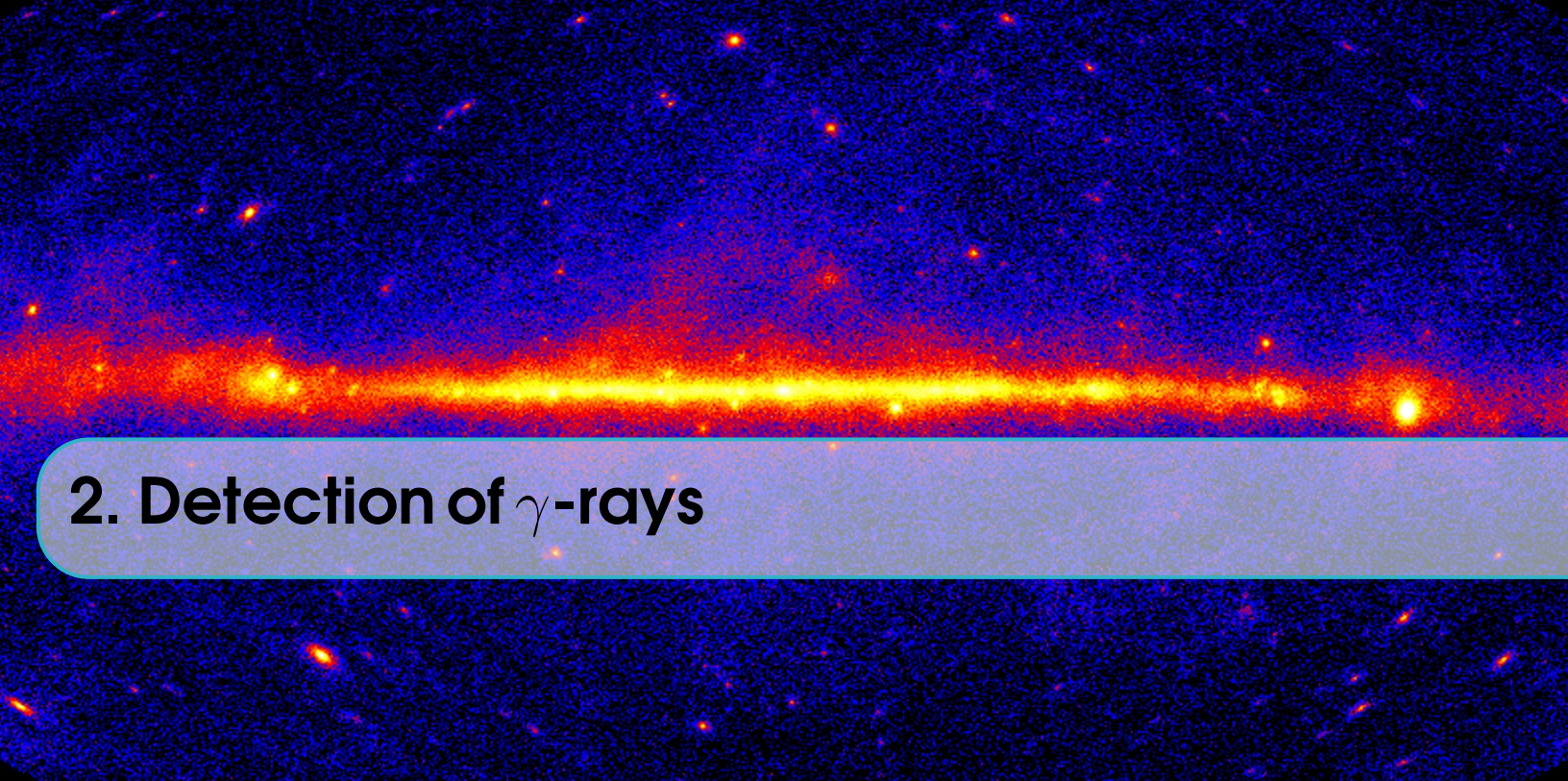


Figure 1.18: Results from *Via Lactea* N-body simulations of DM substructures. The picture show a projection of density squared in a  $566 \text{ kpc} \times 566 \text{ kpc} \times 566 \text{ kpc}$  region centered on the host halo at  $z = 0$ , from [110].

*Fermi*-LAT has used five years of data to set constraints on the DM annihilation signal from the LMC in the HE regime [124]. No limits has yet been set in the VHE range though.

As one of the main topics of this thesis, more on this subject will be extensively discussed in chapter 5.



## 2. Detection of $\gamma$ -rays

Discoveries in astronomy have always been directly related to technological advances of new instruments and observation techniques. The first astronomical telescope was developed by Galileo in the *XVII* century and it allowed him to observe for the first time the four brightest moons of Jupiter. Since then, and especially during the *XX* century, a broad new range of experiments, detectors, and telescopes have been built either on the ground or in space. Thanks to them, astronomers have observed the universe in every wavelength from radio to  $\gamma$ -rays. Furthermore, the recent field of multimessenger astronomy has started a new era, combining electromagnetic radiation with other cosmic messengers such as neutrinos and gravitational waves.

This chapter is dedicated to the technologies developed to detect  $\gamma$ -rays, from the history of first detectors, to the present generation and future of  $\gamma$ -ray observatories. Contrary to the visible light that Galileo received with his first telescope,  $\gamma$ -rays cannot be directly observed from Earth. The atmosphere absorbs most of the radiation coming from space, limiting the range of the spectrum that can be detected with ground-based detectors. As shown in figure 2.1, only visible and radio wavelengths reach the ground through the so-called *atmospheric windows*, hence  $\gamma$ -rays can be observed directly only from outside the atmosphere, with detectors in balloons or satellites. A description of different types of such detectors and their used techniques is given in section 2.1.

Another possibility is to take advantage of the interactions of  $\gamma$ -rays with particles in the atmosphere when they are absorbed. When a  $\gamma$ -ray or any cosmic particle hits an atmospheric atom, a large number of secondary particles are produced which suffer further interactions in a cascade reaction known as Extensive Air Showers (EAS). More on EAS and ground-based detectors can be found in sections 2.2 and 2.4 respectively.

Space detectors and ground-based detectors complement perfectly well, supplying the limitations of one another to cover the full  $\gamma$ -ray spectrum. Lower energy  $\gamma$ -

rays are abundant, but so are hadronic backgrounds (Cosmic Rays (CRs)). Space detectors are perfectly suited to study this part of the spectrum because besides their rather small collection areas ( $\sim 1\text{ m}^2$ ), they have very good background rejection. At higher energies, the  $\gamma$ -ray flux decay strongly and much higher collection areas are needed. Ground-based instruments detect the extended secondary products of  $\gamma$ -rays interacting in the atmosphere. They are designed to cover big areas, capturing even events from the highest energy  $\gamma$ -rays.

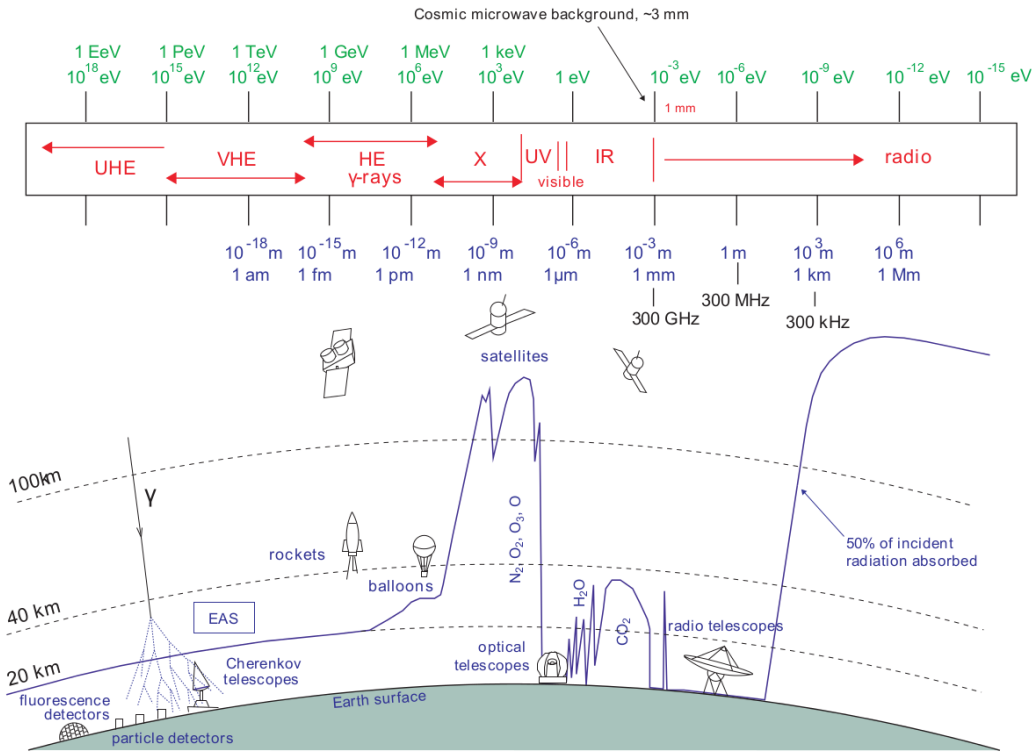


Figure 2.1: Atmospheric transparency for the whole electromagnetic spectrum, from [17]. The continuous line represents the height in the atmosphere where 50% of the light is absorbed.

## 2.1 Space detectors

Direct detection of  $\gamma$ -rays can only be done outside the atmosphere, with particle detectors mounted in high altitude balloons or satellites. The main advantage of this kind of detector is the extremely efficient background rejection, being relatively easy to veto charged cosmic particles and distinguish them from neutral  $\gamma$  photons. However, they are limited in the energy of the  $\gamma$ -rays they can observe, not being able to go much further 100 GeV (High Energy (HE) regime) because of the technical difficulties to have a large collection area. The collection area corresponds to the size

of the detector, which for space instruments is about  $1\ m^2$ , hindering the capture of Very High Energy (VHE) photons which flux decreases rapidly with energy. In this section, different types of space detectors are described.

### 2.1.1 Compton detectors

Compton scattering occurs when a photon transfers part of its energy to an electron. At the low end of the  $\gamma$ -ray energy range (from 20 keV to 30 GeV) this is the process that dominates interactions between light and matter, and Compton detectors are based on it. Usually, they count on two parts: In the first level, the interaction between the  $\gamma$  photon and an electron occurs inside a scintillator. The trajectory deviation of the photon is measured and then it is possible to reconstruct its original direction. Afterward, the photon travels to a second level where it is absorbed by a calorimeter and its energy is measured. The Imaging Compton Telescope (COMPTEL) instrument from the Compton Gamma Ray Observatory (CGRO) was operative between 1991 and 2000 and was able to do a survey of the galactic plane using this technique, detecting more than 60 sources (figure 2.2). Currently, the Imager on-Board the INTEGRAL Satellite (IBIS) [125] telescope [126] is the present representative of this kind of detectors.

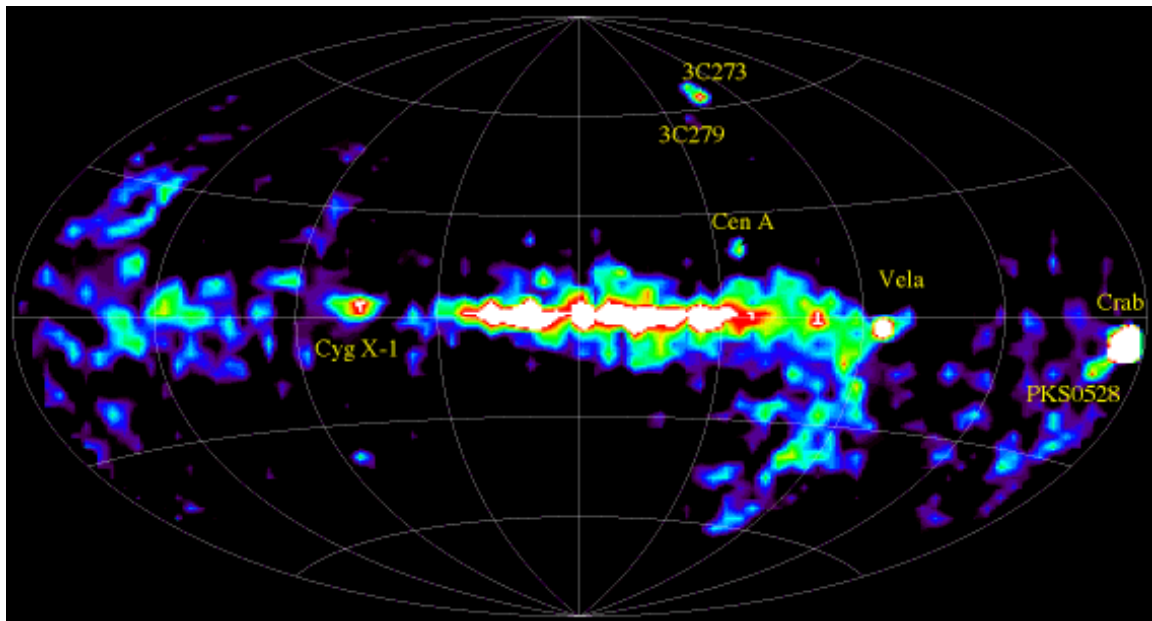


Figure 2.2: Skymap from COMPTEL source catalog. Credits to NASA.

### 2.1.2 Pair production detectors

A photon traveling with energy over twice the rest mass of the electron, passing close to a nucleus, has a high probability to undergo a pair production process, giving rise to an electron-positron pair. Pair production detectors account for different layers of

a heavy material where the interaction takes place, interleaved with a tracker material that measures the position of the resulting particles, being able to reconstruct the original direction of the  $\gamma$ -ray. A calorimeter measures the energy of the particles and an anti-coincidence detector acts as a veto for the background of charged particles (CRs) which can enter the detector. A very prolific instrument of this kind, still ongoing, is the Large Area Telescope (LAT) instrument, on the Fermi Gamma-Ray Telescope which is formerly described in the next section.

### The Fermi Gamma-ray Space Telescope

The Fermi Gamma-ray Space Telescope was launched in 2008 to perform a sky survey in the HE range. It follows a low Earth orbit, being able to observe the whole sky in 3 hours. It counts with two instruments: The LAT, which is the principal instrument for  $\gamma$ -ray detection, and the Gamma-Ray Burst Monitor (GBM), which is designed to detect Gamma Ray Bursts (GRBs).

- **The LAT:** This is the principal instrument of the Fermi telescope, a pair production  $\gamma$ -ray detector able to observe photons with energies from 20 MeV to more than 300 GeV [127]. It consists of 16 modular towers with 18 tungsten converter layers, where the pair production takes place and 16 dual silicon tracker planes which measure the trajectory of the  $e^\pm$  pair. The 16 calorimeter modules have 96 long, narrow CsI scintillators which measure the deposited energy. When any particle enters the detector, it first passes through an anticoincidence plastic scintillator where, if it is a charged particle, it will produce a flash of light, making it possible to distinguish it from true  $\gamma$ -ray events.
- **The GBM:** Complementary to the LAT, the GBM is destined to detect GRBs and quickly alert the main instrument to reposition towards their direction. It is sensible to X-rays and  $\gamma$ -rays in the range between 8 keV to 40 MeV. The detector includes 12 Sodium Iodine (NaI) scintillation detectors which cover the lower part of the spectrum (up to 1 MeV) and provide the burst trigger, and 2 Bismuth Germanate (BGO) scintillation detectors with an energy range from  $\sim 150$  keV to  $\sim 30$  MeV, aimed to overlap the LAT energy range.

The principal scientific goals of Fermi are the study of unidentified sources detected by previous instruments like Energetic Gamma Ray Experiment Telescope (EGRET); understanding the mechanisms of particle acceleration in Supernova Remnants (SNRs) and GRBs; studying the behavior of GRBs; performing indirect searches of Dark Matter (DM) and using  $\gamma$ -rays to probe the early universe and cosmic evolution of HE sources. During the more than 10 years of data taking up to date, the *Fermi*-LAT has been extremely prolific, launching several catalogs with thousands of sources. The 4FGL catalog is the last one released, based on the first 8 years of scientific data. It counts with 5065 detected sources above  $4\sigma$ , 1337 of which do not have a counterpart in other wavelengths. Some of the scientific highlights during its lifetime are the discovery of the Fermi Bubbles (see section 1.6.1); the detection of hadronic signals

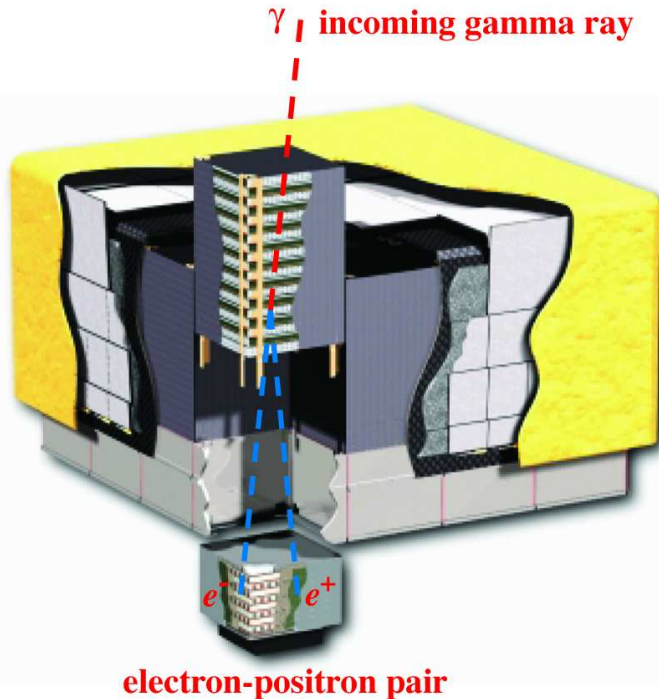


Figure 2.3: Schematic picture of the LAT from [127]. Dimensions are  $1.8 \text{ m} \times 1.8 \text{ m} \times 0.72 \text{ m}$ .

in SNRs [128]; the detection of the most luminous GRB ever observed GRB130427A [129] and the detection with the GBM of the GRB after the LIGO event GW170817 [130], among many more.

## 2.2 Extensive Air Showers

As explained at the beginning of this chapter, the atmosphere absorbs the totality of the  $\gamma$  radiation coming from space. Any  $\gamma$ -ray entering the atmosphere will interact with an atomic nucleus triggering the production of a cascade of particles known as EAS. Furthermore, not only  $\gamma$ -rays can produce EAS, but CRs too, being in fact the responsible for the majority of EAS happening in the atmosphere ( $> 99\%$ ). The products of these cascades, whether being secondary particles or Cherenkov radiation (see section 2.3), are the targets for ground-based  $\gamma$ -ray detectors. Depending on the type of detector, different techniques are required to reconstruct the energy and direction of the primary particle, and to distinguish between electromagnetic (produced by  $\gamma$ -rays) and hadronic (produced by CRs) showers. In this section, the characteristics and physical processes produced in the different types of EAS are described.

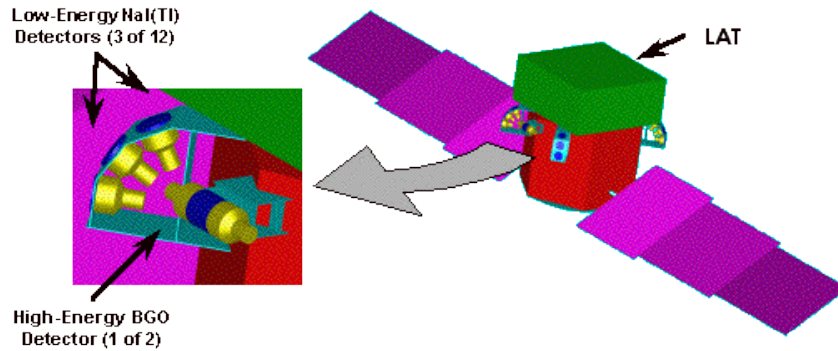


Figure 2.4: Schematic picture of the GBM integrated between the LAT and the shroud envelope of the Fermi’s spacecraft.

### 2.2.1 Electromagnetic Showers

When a primary  $\gamma$ -ray enters the atmosphere, it will produce a pair of  $e^\pm$  in the electric field of an atomic nucleus, typically after traversing one radiation length ( $\xi_0$  defined as the mean distance for a charged particle to reduce its energy by a factor  $e$  due to interactions with the medium), at about 20 km of altitude. This pair of particles, emitted in the forward direction will again interact with other atmospheric nuclei through bremsstrahlung, producing high energy photons. The result is a chain of pair production-bremsstrahlung processes, where a certain amount of energy is lost in each interaction until the high energy photons reach a critical energy  $E_c \sim 83$  MeV. When this happens, ionization and Compton scattering of electrons and positrons become dominant over bremsstrahlung so the production of high energy photons is reduced until the shower slowly dies. Since the angle of emission in all the processes is proportional to  $\propto m_e c/E$  rad, the shower will not spread too much laterally, from an axis pointing towards the primary direction [20].

To easily understand the evolution of the shower, it can be considered that it develops in discrete steps of one radiation length, just as in the model from [131]. The radiation length for the  $e^\pm$  pair is going to be close to the mean free path of photons of similar energy ( $\simeq 9/7\xi_0$ ) which for the air is  $36.7$  g cm $^{-2}$ . Defining the atmospheric thickness as  $R = \xi_0 \ln 2$ , the probability of a photon, electron, or positron of the shower to interact while traversing a longitude  $R$  will be  $\exp(-R/\xi_0) = 1/2$ . Since the distribution of energy in each step between the charged particles and the emitted high energy photon is considered symmetric, after traversing a thickness  $nR$ , the number of surviving  $e^\pm$  and photons will be  $2^n$ , and their mean energy  $E_\gamma/2^n$ , where  $E_\gamma$  is the energy of the primary  $\gamma$ -ray. When the energy reaches the critical energy  $E_c$ , the shower has reached the shower maximum, where the total number of particles is  $E_\gamma/E_c$ . The position of such a maximum is:

$$X_{max} = \frac{R}{\ln 2} \ln \frac{E_\gamma}{E_c} = \xi_0 \ln \frac{E_\gamma}{E_c} \quad (2.1)$$

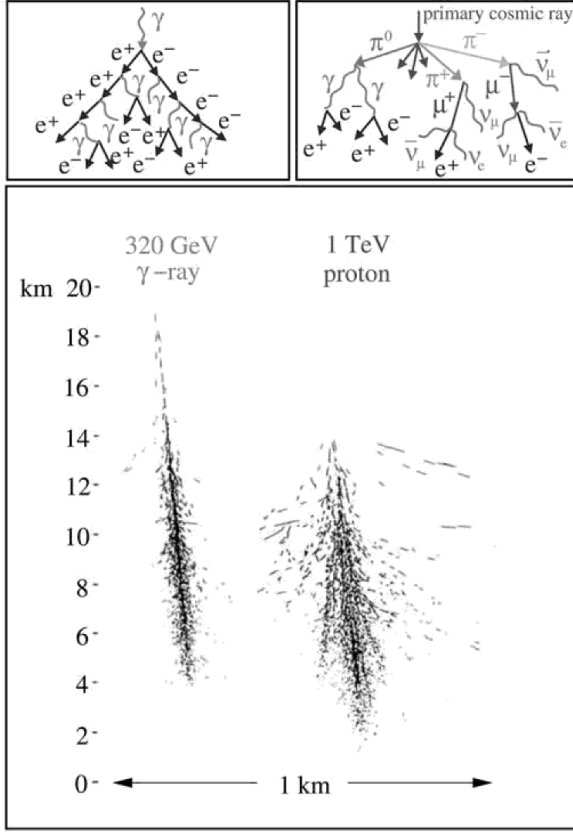


Figure 2.5: Montecarlo simulations of a 320 GeV  $\gamma$ -ray shower and a 1 TeV proton shower from [20]. The top panel show a schematic diagram of shower development with their secondary particles.

The shower maximum depends on the energy of the primary: higher energy photon showers penetrate more deeply in the atmosphere than lower energy showers, hence to lower the energy threshold of a ground-based detector it must be located at high altitudes. An analytical approach to shower development was carried out in [132]. The Greisen equation defines the number of electrons, positrons and photons in the shower before reaching the critical energy:

$$N_e(t) = 0.31 \left[ \log \frac{E_\gamma}{E_c} \right]^{-1/2} e^{T[1-(3/2)\log s]} \quad (2.2)$$

Where T is defined as the atmospheric depth expressed in radiation lengths, and s is the shower age parameter:

$$s = \frac{3T}{T + 2\ln \left[ \frac{E_\gamma}{E_c} \right]} \quad (2.3)$$

The age parameter  $s$  indicates the degree of development of the shower, being equal to 0 at first interaction, 1 in the shower maximum, and 2 in the dying point. While  $N_e$  describes the longitudinal distribution of the shower, the lateral distribution is given by the Nishimura-Kamata-Greisen function:

$$f(r) = \frac{\Gamma(4.5 - s)}{\Gamma(s)\Gamma(4.5 - s)} \frac{N_e}{2\pi r^2} \left[ \frac{r}{r_m} \right] \left( 1 + \frac{r}{r_m} \right)^{s-4.5} \quad (2.4)$$

Where  $r$  is the distance from the shower longitudinal axis and  $r_m$  is the Molière radius, characteristic from multiple scattering theory, and  $\Gamma$  is the gamma function.

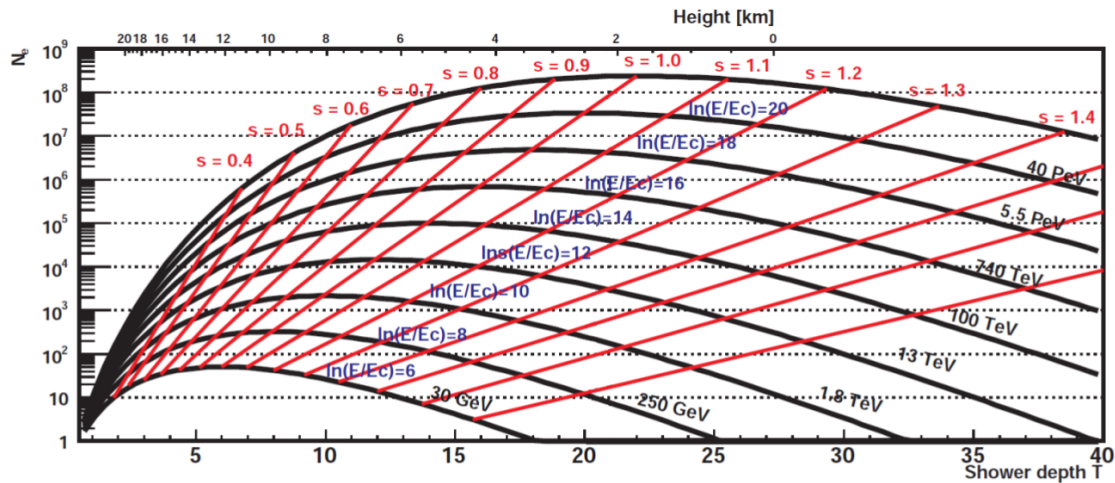


Figure 2.6: Longitudinal development of an electromagnetic shower in the Greisen approximation, from [133] and [134].

### 2.2.2 Hadronic showers

Hadronic showers are produced by CRs, mostly protons, colliding with atmospheric particles. Their development is substantially different from electromagnetic showers since they produce a vast number of secondary particles of different natures (see figure 2.5), mainly fragments of atomic nuclei, pions, and kaons, which end up decaying into muons and neutrinos. Hadronic showers have three components:

- **Hadronic core:** In the first interaction, a relativistic CR collides with a nucleus (O, N...) fragmenting it into smaller nucleons and transferring energy to them, which on their side keep colliding with other particles. They also produce charged mesons in each interaction ( $\pi$  and K mesons). Hadronic interactions will continue until the energy per nucleon becomes smaller than the pion production threshold around 1 GeV.

- **Electromagnetic component:** Around 90% of the particles generated in hadronic showers are pions, of which 1/3 are  $\pi^0$ . Neutral pions decay into two HE photons which generate pure electromagnetic showers. Charged K mesons can also decay into neutral pions through  $K^\pm \rightarrow \pi^\pm + \pi^0$ .
- **Muon and neutrino component:** Charged mesons decay into muons and neutrinos through  $\mu^\pm \rightarrow \nu_\mu(\bar{\nu}_\mu)$ . Muons traversing the atmosphere will only lose energy through ionization due to their long life and their small bremsstrahlung cross-section. They will decay into electrons/positrons and neutrinos through  $\mu^\pm \rightarrow e^\pm + \nu_e(\bar{\nu}_e)$  after a time of  $2.2 \cdot 10^{-8}$  s in their own reference frame, but due to their high Lorentz factor, time dilation can make them reach the ground level without decaying at all.

Despite their complexity, a model can be assumed to describe the evolution of hadronic showers, similar to the one for electromagnetic EAS. In the superposition model from [135] it is assumed that the shower induced by a nucleus of mass  $A$  and energy  $E_0$  is equivalent to  $A$  independent nuclei of energy  $E_0/A$ . The shower maximum in this case would be:

$$X_{max} \propto \xi_N \ln \left( \frac{E_0}{AE_c} \right) \quad (2.5)$$

Where  $E_c$  is the critical energy and  $\xi_N$  is defined as the mean path which reduces the number of relativistic charged particles by a factor  $1/e$  as they pass through matter. For a proton of 1 TeV is  $83 \text{ gcm}^{-2}$ . Because  $\xi_N$  is larger than the radiation length for photons  $\xi_0$ , the altitude of first interaction of hadronic showers is higher than for electromagnetic showers and they can penetrate deeper into the atmosphere. Furthermore, hadronic interactions can transfer considerable transverse momentum to the secondary products of the showers making them disperse laterally. Also, hadronic showers are more irregular and present large fluctuations. These features are used in detectors to distinguish between electromagnetic and hadronic induced showers.

### 2.2.3 Electronic showers

There exist a third type of EAS produced by cosmic electrons and positrons entering the atmosphere. The type of cascade produced is very similar to electromagnetic showers since the same processes take place: The electron/positron produces HE photons via bremsstrahlung while interacting in the electromagnetic field of atmospheric nuclei and those resulting photons produce  $e^\pm$  pairs. The main differences with electromagnetic showers have to do with the nature of the primary: Since it is a charged particle, interactions start just when it enters the atmosphere so the shower maximum is reached at higher altitudes. Also, it will be more affected by the deviations produced by the geomagnetic field of the Earth.

## 2.3 Cherenkov radiation

The Cherenkov radiation is a kind of electromagnetic radiation that is emitted when a charged particle travels through a dielectric medium at a velocity higher than the local speed of light. Many scientists during the XX observed that when a transparent material was placed in the neighborhood of strong radioactive sources, they emitted a faint bluish light. From 1934 to 1938 Pavel Alekseyevich Cherenkov carried out a series of exhaustive experiments to try to explain the causes of this effect, named after him, and was awarded the Nobel Prize in 1958 for his results.

Cherenkov radiation is a very important effect for ground-based  $\gamma$ -ray detectors because EAS, which produce a large number of relativistic charged particles, can produce this kind of radiation in the atmosphere. Characterization of the Cherenkov signal from EAS allows to trace back the nature of the primaries.

This effect can be explained through the reaction of the atoms of a material when a charged particle is traveling through it. For example, in the case of an electron traveling through a glass, if the electron has a slow velocity, along its trajectory the electric field of the particle will distort the atoms, attracting the positively charged nucleus and repelling the negative electrons (see figure 2.7 a). The medium becomes polarized around the position of the particle, each atom behaving like a dipole and producing a small electromagnetic pulse in the region of the glass. Since the distribution of dipoles is symmetric, the resulting field is null and no radiation will be emitted.

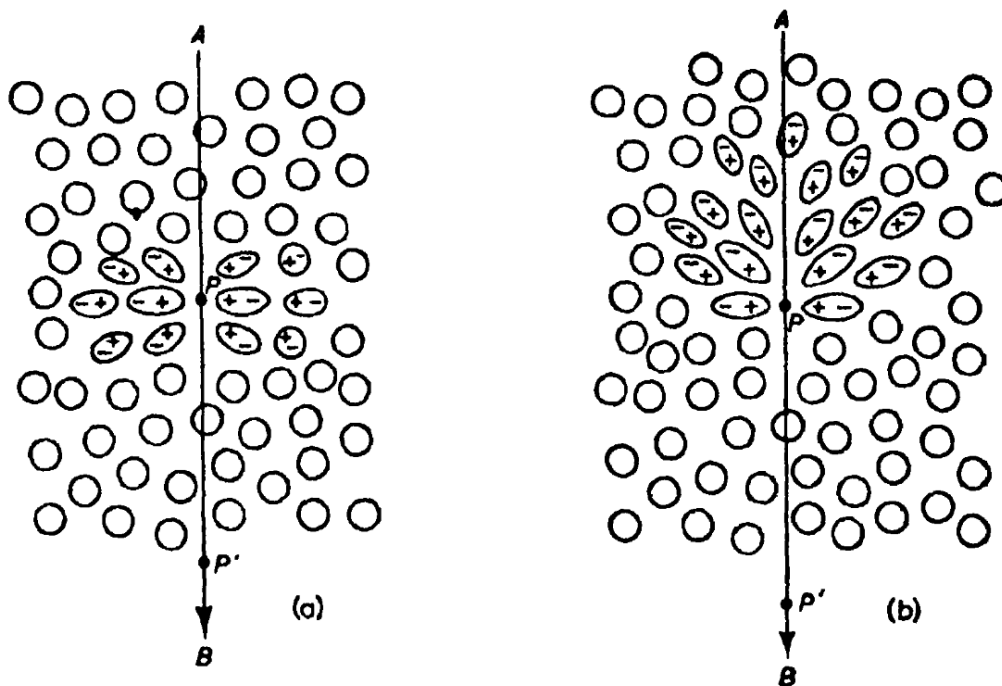


Figure 2.7: Polarization of a dielectric material at the passing of a charged particle by the point P at a) low velocity b) high velocity. Image from [136].

In the case when the electron travels almost at the velocity of light in the medium the resulting field is not symmetric anymore along the direction axis of the particle (see 2.7 b). The dipole field will be noticeable even at long distances and the electron will produce the emission of wavelets of radiation at each point of its trajectory. In general, those wavelets will interfere destructively so that the resulting intensity of the field will be zero. If the velocity of the electron is higher than the speed of light in the medium, the wavelets can be in phase and produce a global field visible in the distance, emitting radiation. Figure 2.8 shows a diagram of a Huygens construction of this effect. If a particle travels from A to B faster than the speed of light in the medium, it can travel that distance in the same amount of time that light will go from A to C, therefore when seen under an angle  $\theta$  all the waves emitted along the trajectory will be in phase and form a plane wave from B to C.

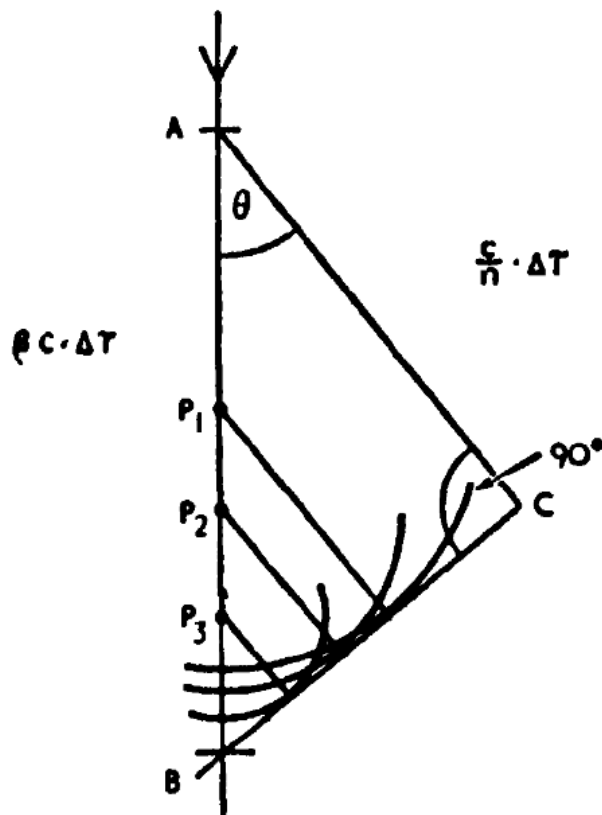


Figure 2.8: Diagram of Huygens construction showing coherence of waves emitted by a charged particle travelling faster than the speed of light in the medium, from [136].

The angle  $\theta$  is named Cherenkov angle and can be expressed as:

$$\cos \theta = \frac{1}{n\beta} + \frac{\hbar k}{2p} \left( 1 - \frac{1}{n^2} \right) \quad (2.6)$$

Where  $\beta = v/c$ ,  $k$  is the emitted photon momentum,  $p$  is the charged particle momentum and  $n$  is the refractive index of the medium. Since  $p \gg k$ , the expression can be simplified to:

$$\cos \theta = \frac{1}{n\beta} \quad (2.7)$$

The Cherenkov light produced by EAS in the atmosphere is emitted in the shape of a cone around the axis of the shower, leaving a ringlike signal in the ground. Because the refractive index of the atmosphere changes with altitude, the maximum angle will also vary and so the extension of the ring and the minimum energy required by a particle to produce Cherenkov radiation (when  $v = c/n$ ). The variation of the refractive index with altitude can be approximated by:

$$n(h) = 1 + n_0 e^{-\frac{h}{h_0}} \quad (2.8)$$

Where  $n_0$  is  $2.9 \times 10^{-4}$  and  $h_0 = 7.1$  km for an isothermal atmosphere. The minimum energy:

$$E_{min} = \frac{m_e c^2}{\sqrt{1 - \beta_{min}^2}} = \frac{m_e c^2}{\sqrt{1 - (1/n)^2}} \quad (2.9)$$

Hence, as a function of altitude:

$$E_{min} \approx \frac{m_0 c^2}{\sqrt{2n_0}} e^{-\frac{h}{2h_0}} \quad (2.10)$$

and the maximum angle  $\theta$ :

$$\theta_{max} = \sqrt{(2n_0)} e^{-\frac{h}{h_0}} \quad (2.11)$$

This dependency means that at higher altitudes, the maximum angle is lower, so the Cherenkov signal in the ground will be less spread. Also, the minimum energy lowers with altitude, meaning that more developed EAS will more likely produce Cherenkov light.

About the spectrum of Cherenkov light in the atmosphere, while it could go from infrared to ultraviolet, photons below 290 nm are absorbed by ozone ( $O_3$ ), and over 800 nm by  $H_2O$  and  $CO_2$ . Also it suffers Rayleigh dispersion and aerosol dispersion. As a result, the peak of the spectrum at a detection altitude of about 2 km is around 300 nm (blue light). The Cherenkov spectrum produced by a particle with charge  $z$  and velocity  $\beta$  is:

$$\frac{d^2N}{dxd\lambda} = \frac{2\pi\alpha z^2}{\lambda^2} \left( 1 - \frac{1}{\beta^2 n^2(\lambda)} \right) \quad (2.12)$$

## 2.4 Ground-based detectors

Ground-based detectors work capturing the products of EAS generated by primary  $\gamma$ -rays in the atmosphere. As explained in previous sections, EAS produce a cascade of particles that emit Cherenkov light. There are two main types of ground-based detectors: Particle detectors, which capture the particles produced in the shower, and Cherenkov detectors, which measure the Cherenkov light. Because both  $\gamma$ -rays and CRs produce showers, the biggest challenge for ground-based detectors is to differentiate the two kinds of events, being the background rejection less efficient than for space detectors. Proper knowledge of the differences in the development of electromagnetic and hadronic showers is crucial for this task. In general, ground-based instruments take advantage of very precise Monte Carlo (MC) simulations of EAS to find features in the signals which can help to do the  $\gamma$ /hadron separation.

### 2.4.1 Particle detectors

Particle detectors measure the particles and secondary photons produced by EAS. Because the shower maximum depends on the energy of the primary, as seen in equation 2.1, only  $\gamma$  rays with extremely high energies can produce showers that reach the ground. To lower the energy threshold of detectors is necessary to place them at high altitudes (over 2000 m). Different types of particles detectors are:

- **Particle counter matrices detectors** are classic particle detectors which record the arrival time and direction of particles to reconstruct the shower and eventually the primary characteristics. Examples of this kind of experiments are CASA-MIA [137], LHAASO-KM2 [138], Tibet-AS [139] and HEGRA [140].
- **Water Cherenkov detectors** consist of a large number of big water tanks where particles from the shower produce Cherenkov light. ARGO-YBJ [141] and HAWC [142] are examples of this kind of detector.

The advantage of particle detectors is that they can be extended over hundreds of square meters, covering a very wide field of view. Also, they can work anytime, even under daylight. In general, they cover the higher energy range, reaching energies of hundreds of TeV.

### 2.4.2 Atmospheric Cherenkov Telescopes

Atmospheric Cherenkov Telescopes detect the photons of Cherenkov light reaching the ground. Cherenkov photons produced by EAS in the atmosphere account for  $10^{-4}\%$  of the Night Sky Background (NSB) and they can be observed from the ground as flashes of around 10 ns. For that reason, unlike particle detectors, they require very clear and dark moonless nights, to differentiate Cherenkov photons from any background light. There are two types of atmospheric Cherenkov telescopes:

### Sampling detectors

They consist of a grid of counters which measure the Cherenkov light from EAS at ground level with low-gain Photomultiplier Tubes (PMTs). The direction of the primary can be determined by measuring the timing signals from the photons detected, and the energy is reconstructed from the lateral distribution of the Cherenkov light. The energy threshold for this type of detector is high, being suitable for the study of VHE and Ultra High Energy (UHE)  $\gamma$ -rays. For example, the minimum energy threshold of the Air shower Observation By angle Integrating Cherenkov Counters (AIROBICC) was 20 TeV [143]. For sampling detectors, differentiating  $\gamma$ -ray showers from hadronic is truly problematic, and currently they have been outperformed by Imaging Atmospheric Cherenkov Telescopes (IACTs).

### Imaging Atmospheric Cherenkov Telescopes (IACTs)

IACTs are the most prolific type of ground-based  $\gamma$ -ray detectors and their evolution is the key for the next generation of VHE  $\gamma$ -ray astrophysics. They work similar to optical telescopes, with a large mirror that focuses Cherenkov light into a camera, that records the images of the showers. Because Cherenkov light flashes are very short, cameras need to be very fast to take snapshots of just a few nanoseconds. Also, as the number of photons of the NSB is very high compared to the small number of Cherenkov photons, it is essential to have a very precise time correlation between camera pixels, given by state-of-the-art electronics, to reject random signals from NSB and get the time evolution of the showers.

The reconstruction of the energy and incident direction of the primary photon as well as the separation of  $\gamma$  and hadron events can be achieved through a parameterization of the shower images, based on the work done by Michael Hillas [144]. With this method, the moments of the observed light distribution in the camera, which for  $\gamma$ -rays looks like an ellipse (named Hillas ellipse), are used as parameters to characterize the shower, which subsequently allows distinguishing between  $\gamma$  and hadronic showers. The intensity of Cherenkov light in the image is directly proportional to the energy of the primary and the orientation of the ellipse can be used to reconstruct their direction of arrival. Several techniques are used to reconstruct the primary information from Hillas parameterization, most of them based on modern Machine Learning algorithms. A quantity named *gammaness* (or *hadroness*) is used to designate how likely is an event to be a  $\gamma$ -ray (or hadron). The closer to 1, the more  $\gamma$ -like (hadron-like) the event is. Another important reconstructed quantity is the denominated  $\theta^2$  angle, which is the square of the angle between the reconstructed source position and the true source position.

Other techniques make use of the entire information of the camera image, comparing pixel by pixel with a template generated by a semi-analytical model of shower development. A detailed summary on reconstruction methods for Cherenkov Telescopes can be found in [145] and [146]. Either of the techniques improves substantially when using stereoscopy, taking shower images with several telescopes at the same time. This not only improves the reconstruction power but also helps to reject the

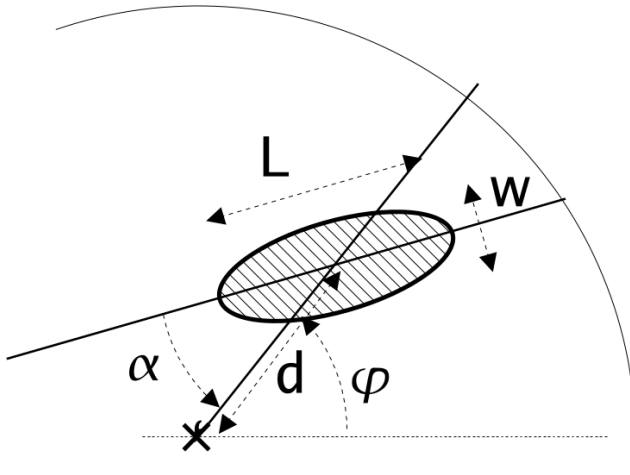


Figure 2.9: Geometrical definition of the Hillas parameters. L for Length (W for Width) is the RMS spread of light along the major(minor) axis of the image, it carries information of the longitudinal(lateral) development of the shower. Nominal distance  $d$  is the angular distance between the center of the camera and the image center of gravity. Angle  $\phi$  is the azimuthal angle of the image major axis and orientation angle  $\alpha$  is the angle between the major axis and the center of the camera. Figure from [145].

hadronic background very efficiently. When pointing the telescopes to a  $\gamma$ -ray source, in general, shower images from  $\gamma$  primaries will be oriented towards the position of the source in the cameras of all telescopes. Hadronic showers, which come from random directions in the sky, will point towards random directions in the camera, so they can be easily discarded.

The first telescope of this kind was the Whipple Observatory 10 m reflector [147], with a camera of 37 pixels. It started operations in 1968 but it was not until 1988 that they detected the first  $\gamma$ -ray source, the Crab Nebula. The first stereoscopic system was the High Energy Gamma Ray Astronomy (HEGRA) complex, with a total of six IACTs which worked together with other types of  $\gamma$ -ray detectors (the AIROBICC). The current generation of IACTs is formed by Major Atmospheric Gamma Imaging Cherenkov Telescopes (MAGIC) [148], High Energy Stereoscopic System (H.E.S.S.) [149] and Very Energetic Radiation Imaging Telescope Array System (VERITAS) [150] telescopes:

- **MAGIC:** The MAGIC telescopes are a set of two IACTs of 17 m diameter, located in the Roque de Los Muchachos Observatory at the island of La Palma, Spain. They are located at an altitude of 2200 m, separated by 85 m. The first telescope, MAGIC-I, started operations in single telescope mode in 2004, and in 2009 the second telescope, MAGIC-II was included, becoming a stereoscopic system. An upgrade was made during the years 2011-2012, to reduce differences

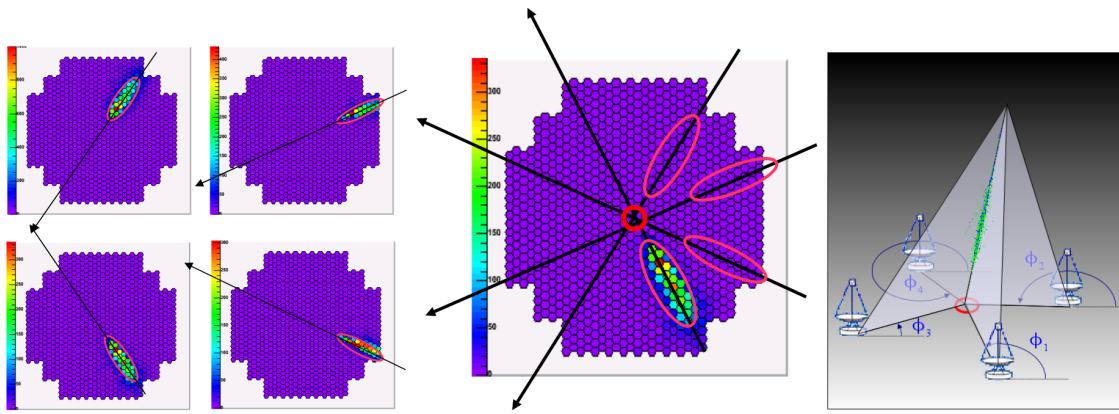


Figure 2.10: Geometric reconstruction of shower direction in stereo mode, from [146]. *Left and middle:* The shower image from 4 telescopes is combined to get the source position in the intersection of the main axis. *Right:* Intersection of the planes which contain the shower tracks and the telescopes give the shower Impact Parameter on the ground.

between both telescopes and improving the stereo performance. The lower energy threshold of MAGIC can reach 25 GeV when using the *sum trigger* setup, becoming the most sensitive IACT system below 300 GeV in the northern hemisphere. Due to their big size, the MAGIC telescopes are especially well suited to observe low energy events, which produce less Cherenkov photons and require bigger mirrors. This characteristic makes them especially ideal for observing high redshift Active Galaxy Nuclei (AGNs) and pulsars. Also, they were designed to be very lightweight, to be able to do a fast repositioning to follow up GRBs alerts. The MAGIC collaboration announced the first detection of a GRB in January 2019 [84]. During their fifteen years of operations the MAGIC telescopes have given prolific scientific results such as the detection in VHE of the Pulsar Wind Nebula (PWN) 3C 58, the one with the lowest luminosity and lowest flux ever detected in VHE  $\gamma$ -rays; the observation of  $\gamma$ -ray emission from a jet originated inside the event horizon of the central Black Hole (BH) of the galaxy IC 310; the detection of the galaxy PKS 1441+25, one of the two most distant galaxies detected at high energies; the detection of the Crab pulsar, located inside the well-known Crab PWN; the detection of  $\gamma$ -rays from a gigantic explosion occurred in the galaxy QSO B0218+357 thanks to gravitational lensing; and the tracing of the source (the active blazar XS 0506+056) of a very rare cosmic neutrino event detected by IceCube experiment on September 2017 [151].

- **H.E.S.S.:** An array of 5 telescopes located in Namibia, close to the Gamsberg mountain, being the only IACT observatory in the southern hemisphere. The first four telescopes, operational since 2004, have 12 m diameter and are arranged

in a square distribution. The second phase of the experiment consisted of a fifth telescope of 28m of diameter, sitting in the center of the square. It was inaugurated in 2012 and contributed to lower the energy threshold of the system. An update in the cameras of the small telescopes was performed during the years 2015-2016 improving the performance of the whole array. The energy range of H.E.S.S. goes from 30 GeV to 100 TeV, being the widest range of IACT observatories. Because it is located in the South, H.E.S.S. has been able to perform a galactic plane survey in VHE range, complementary to the HE survey done by *Fermi*-LAT (see picture 2.11). Some important scientific highlights of H.E.S.S. are the detection of the Vela pulsar and the colliding wind binary system Eta Carinae; the discovery of new SNRs in the galactic plane; the detection of VHE emission from the LMC P3 binary system discovered by *Fermi*-LAT, with a binary phase of  $\sim 0.3$ , being the most luminous binary system detected up to date; direct measures of the Extragalactic Background Light (EBL) spectral density thanks to the observations of a large number of AGN spectra, and observation of flares and variability in the AGNs Mrk 501 and 3C 279. A detailed summary of these topics among many more scientific highlights of H.E.S.S. can be found in [149].

- **VERITAS:** Is an array of four IACTs located in the Fred Lawrence Whipple Observatory in southern Arizona. They are 12 m diameter telescopes arranged in a diamond shape and their design is based on the original Whipple 10 m Telescope. The first light of the VERITAS prototype was in 2004 and the full array started operations in 2007. In 2012 the cameras PMTs were upgraded to high-quantum-efficiency PMTs. The total energy range goes from 85 GeV to 30 TeV. Among the most important scientific results from VERITAS are the detection of pulsed emission from the Crab pulsar; Regarding the observations of blazars (AGN), the detection of rapid variability in the blazar BL Lacertae, the detection of the high redshift blazar ( $z \sim 0.6$ ) PKS 1424+240 above 0.1 TeV, the discovery of the source VER J0521+211 and deep observations of the distant 1ES 0229+200 ( $z = 0.14$ ). Also, the survey of the Cygnus region which allowed to resolve new sources and contributed with new candidates of counterparts at TeV energies to *Fermi*-LAT sources. A summary on the most recent VERITAS highlights can be found in [150].

The future of ground-based  $\gamma$ -ray astronomy is in the hands of the Cherenkov Telescope Array (CTA), currently in construction. CTA will be a  $\gamma$ -ray observatory without precedents, as the result of combined efforts of scientists from all over the astroparticle physics community. It will have two locations, one observatory in the northern hemisphere, on the island of La Palma, Spain, and the other in the south, in the Atacama desert, Chile. This will allow full-sky observations, with a sensitivity one order of magnitude better than the current generation of IACT observatories (see figure 3.6). An extended summary on CTA can be found in chapter 3.

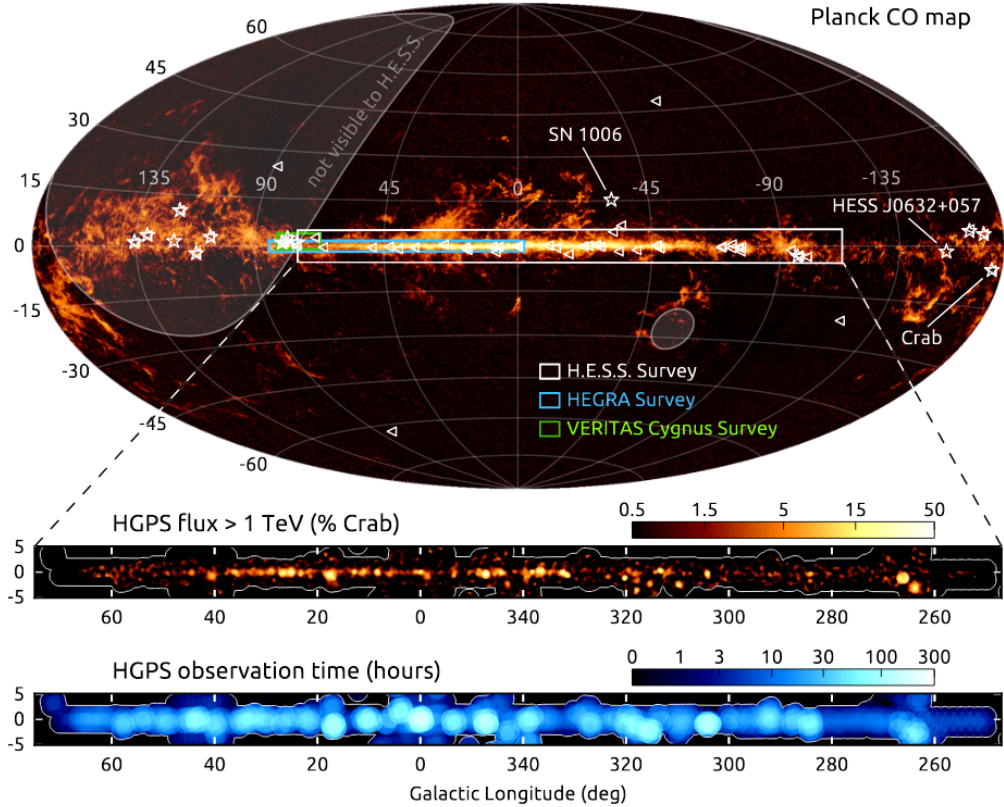


Figure 2.11: Illustration of the H.E.S.S. I galactic plane survey. The region surveyed is shown in the top panel as a white rectangle on top of the carbon monoxide gas sky map measured with the Planck satellite. Previous surveys from HEGRA and VERITAS are also represented. Triangles are sources detected at lower energies by *Fermi*-LAT and stars are galactic sources detected outside the survey region. Middle and lower panels show the observed flux and observation time. Picture from [149].



## 3. The Cherenkov Telescope Array

### 3.1 Introduction

The Cherenkov Telescope Array (CTA) [152] is the next-generation observatory for ground-based  $\gamma$ -ray astronomy. It is the result of the combination of efforts from all the  $\gamma$ -ray community, to push the field of Very High Energy (VHE) astrophysics to new limits. It will consist of two arrays of Imaging Atmospheric Cherenkov Telescopes (IACTs) located in the Northern hemisphere, in the Roque de los Muchachos Observatory, on the island of La Palma (Canary Islands, Spain) and in the Southern hemisphere, in the Paranal desert (Chile). With this configuration, CTA will be the first ground-based observatory to be able to observe the full sky. CTA will have five to ten times better sensitivity than current instruments in the broader energy range ever reached by IACTs facilities, from 20 GeV to 300 TeV. Its angular resolution down to 2 arcseconds, with a field of view of  $\sim 10^\circ$  will allow the observation of fine structures in extended  $\gamma$ -ray sources. Its energy resolution, with an uncertainty less than 10%, will make CTA able to study features in the sources spectra, such as lines and cutoffs, in great detail.

To reach such performance goals, CTA will count with around 100 telescopes in three sizes, each optimized for the observation in a specific spectral range. Large Size Telescopes (LSTs) have the bigger size, with a 32 m diameter mirror. They are optimal to observe the lowest part of the VHE spectrum covered by CTA ( $\sim$ 20 GeV to 3 TeV) where  $\gamma$ -rays are more abundant, so a small number of telescopes is enough, but the induced  $\gamma$ -ray showers emit a low number of Cherenkov photons, and large mirrors are required to collect the maximum number of photons. Medium Size Telescopes (MSTs) have an intermediate size, with a diameter of  $\sim 10$  m. They have the best performance at the range between  $\sim$ 100 GeV and 50 TeV. Small Size Telescopes (SSTs) have much smaller mirrors ( $\sim 4$  m), and a large number of them

will be installed to get big collection areas and be able to capture the highest energy photons (up to 300 TeV), which are very rare but produce huge amounts of Cherenkov light.

Thanks to the large number of telescopes, CTA will have great flexibility of operations, with different observation modes: with the full array for best sensitivity; using subarrays to observe several sources at the same time; and a divergent pointing mode where the field of view can be extended up to 20 deg.

In this chapter the main features of CTA are covered. A description of performance is given in section 3.2. In section 3.3 the three types of telescopes are described in detail. Section 3.4 is dedicated to CTA data analysis techniques and tools at different levels.

## **3.2 CTA Requirements and Performance**

The current generation of Cherenkov telescope observatories consists of arrays of 2 to 5 telescopes that reach sensitivities of about 1% of the Crab flux at the range of 0.1-1 TeV for 50h observation time. Their typical angular resolution is about 0.1°, but it can reach 0.02° for intense point sources of 20 to 30 arc seconds. The different types of telescopes will be spread over large areas, to reach a collection area of several km<sup>2</sup> [153]. The goal of CTA design is to advance the state-of-the-art in  $\gamma$ -ray astronomy, improving sensitivity, energy range, angular and timing resolution, and offering full sky coverage. The performance goals of CTA are shown in table 3.1. As a consequence of these goals, CTA will provide for two unique features: the ability to produce a deep survey of the fullVHE sky, potentially discovering hundreds of new sources; and the possibility to observe short timescale phenomena, such as flares and jets from black holes in the center of active galaxies or periodic emission of pulsars.

The final performance of CTA depends on the design of the telescopes, which will be discussed more deeply in the next sections, and also on the optimization of their arrangement in the two sites. To find the best configuration and estimate their performance, detailed Monte Carlo (MC) simulations were made [154], comprising simulations of shower development in the atmosphere, detector response, and event reconstruction. A deep study of these simulations [155] for different configurations of telescopes and sites came up with the final array layout illustrated in picture 3.1.

The baseline design for Southern observatory foresees 4 LSTs, 25 MSTs and 70 SSTs. It will be dedicated to the study of galactic sources that emit the most energetic  $\gamma$ -rays reaching the Earth. Because of their extremely low fluxes, it will cover a very large area ( $\sim 4$  km<sup>2</sup>), achieved thanks to the large number of SSTs, to capture as many events as possible.

The Northern observatory will mainly observe extragalactic sources and transient events from which only the less energetic photons reach the Earth due to absorption by the Extragalactic Background Light (EBL) (see section 1.4). Its final configuration will consist on 4 LSTs and 15 MSTs.

The performance of CTA has been evaluated for the observation of a point source located at the center of the field of view of telescope cameras. A set of metrics are

Diff. sensitivity (erg cm <sup>2</sup> s <sup>-1</sup> )	at 50 GeV at 1 TeV at 50 TeV	$8 \times 10^{-12}$ $2 \times 10^{-13}$ $3 \times 10^{-13}$ (S) / $3 \times 10^{-12}$ (N)
Collection area (m <sup>2</sup> )	at 1 TeV at 10 TeV	$> 10^4$ $> 10^6$ (S) / $> 5 \times 10^5$ (N)
Angular resolution	at 0.1 TeV $> 1$ TeV	0.1° 0.05°
Energy resolution	at 50 GeV $> 1$ TeV	$\leq 25\%$ $\leq 10\%$
Field of view	at 0.1 TeV at 1 TeV $> 10$ TeV	5° 8° 10°
Sensitivity in FoV	at 1 TeV flat out to at 1 TeV	$> 2.5$ ° 5" per axis
Repointing time	<0.1 TeV 0.1-10 TeV	20s (goal), 50s(max) 60s (goal), 90s (max)

Table 3.1: Performance goals for CTA observatories, adapted from [153]. Sensitivity given in 5 bins per energy. (N)= Northern site, (S) = Southern site.

taken into account: Effective collection area, residual Cosmic Ray (CR) background rate, angular resolution, and differential sensitivity. Usually they are calculated after applying  $\gamma$ -hadron separation cuts, using the quantities *gammaness* and  $\theta^2$  (defined in section 2.4.2), optimized to maximize the sensitivity for a set of typical observation times. An overview of the mentioned metrics for performance evaluation is the following:

- **Effective collection area:** The effective collection area describes the area of the upper atmosphere where an incident  $\gamma$ -ray would be detected if CTA would have a detection efficiency, after cuts, of 100%. The effective collection areas for the assumed point sources are shown in figure 3.2.
- **Residual cosmic-ray background rate:** The ability of CTA to reject background events due to showers produced by CRs instead of  $\gamma$ -rays is measured through the residual CR background rate. 99.9% of the showers reaching the telescopes are produced by CRs, so a good background rejection is mandatory for IACTs. In figure 3.3 the post-analysis resulting CR background rate per square degree vs reconstructed  $\gamma$ -ray energy is shown. The rate is integrated in

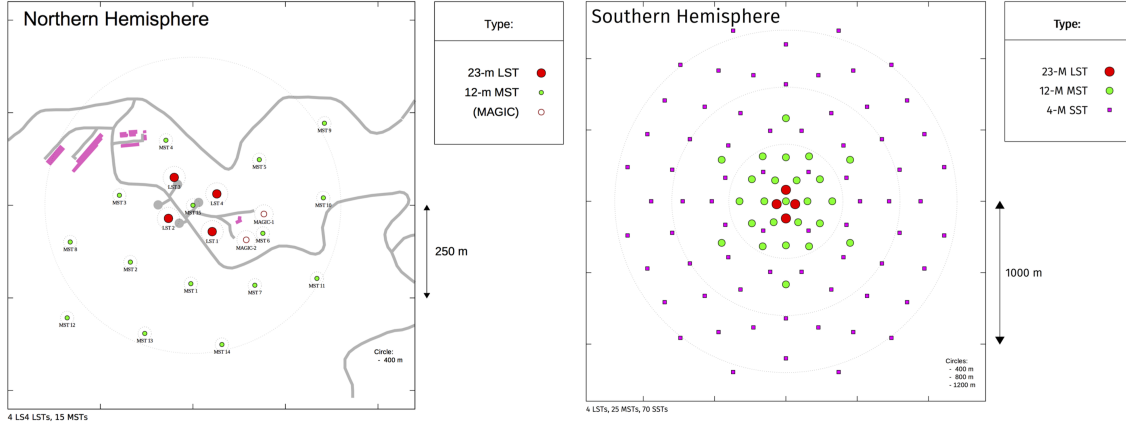


Figure 3.1: Array layout selected for CTA from [156]. Left is Northern site where also Major Atmospheric Gamma Imaging Cherenkov Telescopes (MAGIC) telescopes are located. Right is Southern location.

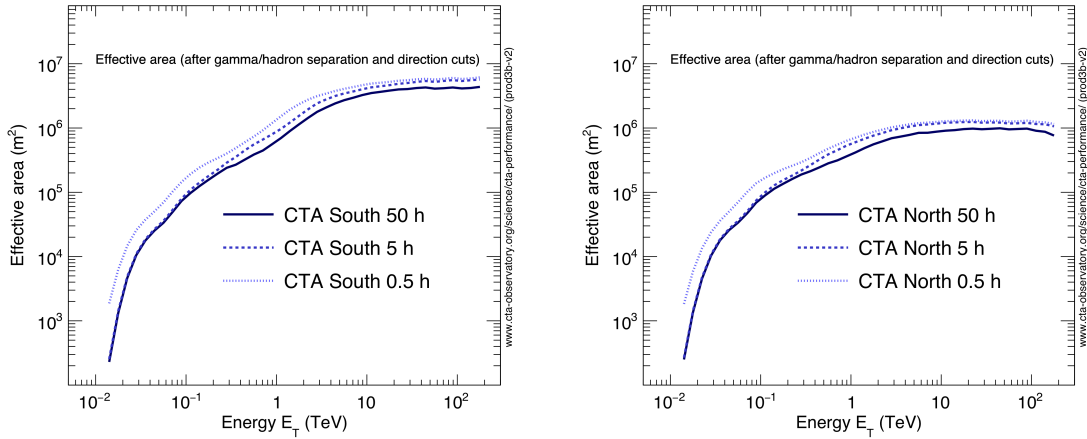


Figure 3.2: Effective collection area for point-like sources for CTA South(left) and CTA North (right) [156].

each bin, where five bins per decade have been taken. CTA background rejection capabilities allow to reject the majority of the background in the range 0.2-1.5 TeV, where the remaining background is due to CR electrons and positrons [157] which produce showers very similar to those produced by  $\gamma$ -rays (see section 2.2.3), making them an irreducible.

- **Angular resolution:** The angular resolution is defined as the angle within which 68% of reconstructed  $\gamma$ -rays fall, relative to their true direction. Figure 4.2 show the angular resolution vs. reconstructed energy optimized for best point-source sensitivity. It is possible to improve angular resolution at expenses of collection area for a better study of morphological features of bright sources.

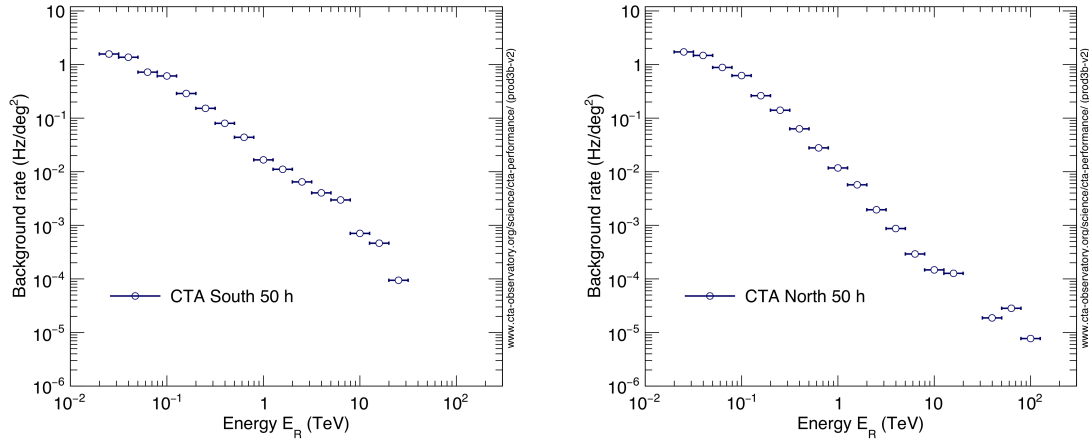


Figure 3.3: Residual cosmic-ray background rate vs reconstructed energy for CTA South(left) and CTA North (right) [156].

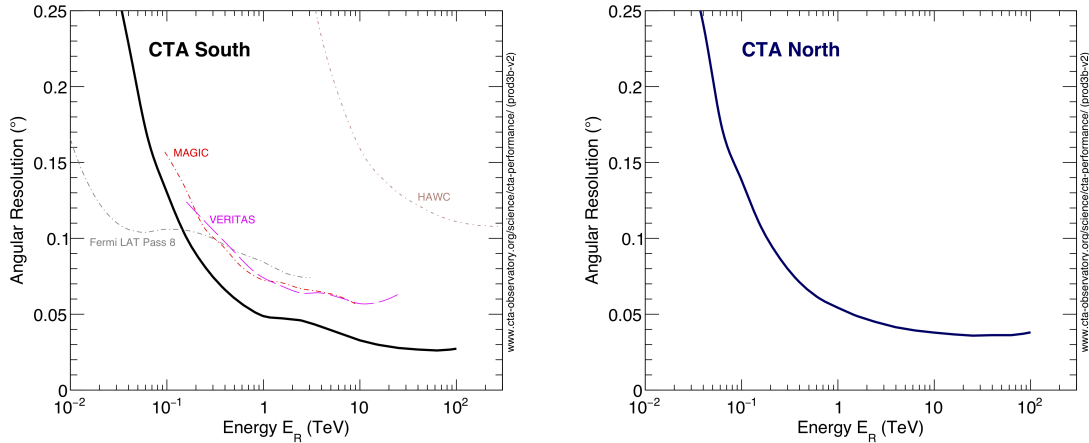


Figure 3.4: Angular resolution for CTA South compared to other experiments (left), and for CTA North (right) [156].

- **Energy resolution:** The energy resolution  $\Delta E/E$  is obtained from the distribution  $(E_{rec} - E_{true})/E_{true}$ , where  $E_{true}$  and  $E_{rec}$  are the true and reconstructed energies of  $\gamma$ -ray events. It is defined as the half-width of the interval around 0 which contains the 68% of the distribution. The energy resolution of CTA as a function of reconstructed energy is shown in figure 3.5. Note that for the range of 1-10 TeV the energy resolution is well below the required 10%.
- **Differential sensitivity:** The most important feature at evaluating the performance is the differential sensitivity, which indicates the minimum flux needed to detect a point-like source at  $5\sigma$  in 50 hours. The sensitivity is calculated in five energy bins per decade, where it is required that at least 10  $\gamma$ -rays are detected and the signal to background ratio is at least 1/20. The cuts in gammaness and

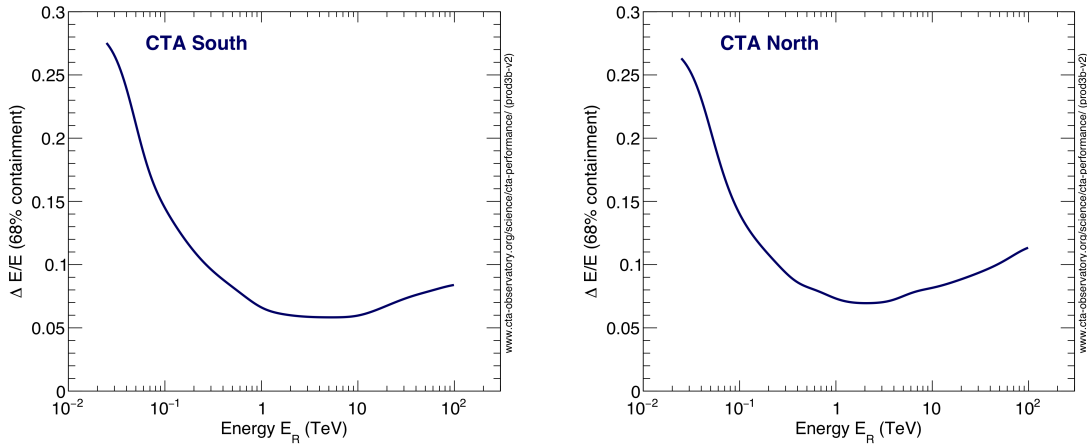


Figure 3.5: Energy resolution vs reconstructed energy for CTA South (left) and CTA North (right) [156].

source direction ( $\theta^2$ ) are optimized to improve this quantity. The differential sensitivity of CTA compared to that of other instruments for 50h observation time is shown in figure 3.6.

### 3.3 CTA Telescopes

While all telescopes share a basic design concept, they have particular features to accomplish the performance requirements for CTA. In general, the subsystems of IACTs are divided into the structure, optics, and camera. In this section an overview of these subsystems and the particularities of each of the three types of CTA telescopes is given.

#### 3.3.1 Large Size Telescope (LST)

The LST has been designed to reach an effective energy threshold down to 20-30 GeV. This energy range has a particular interest because it covers the barely explored gap between the highest energies detected by satellite experiments and the lowest by IACTs. The main science goals for LSTs are to observe high redshift Active Galaxy Nuclei (AGN), Gamma Ray Bursts (GRBs), pulsars and galactic transients. The prototype for the LSTs (LST1) was installed in the CTA North site, in La Palma island, in 2018.

A detailed description of LST subsystems can be found in [158], next sections offer a summary of each subsystem of the telescope, which consists of: the structure of the telescope, to support the optics, camera and driving system; the optics, composed by the 23 m diameter mirror which collects the Cherenkov light and focus it in the camera; and the camera, to record the Cherenkov photons coming from the showers.

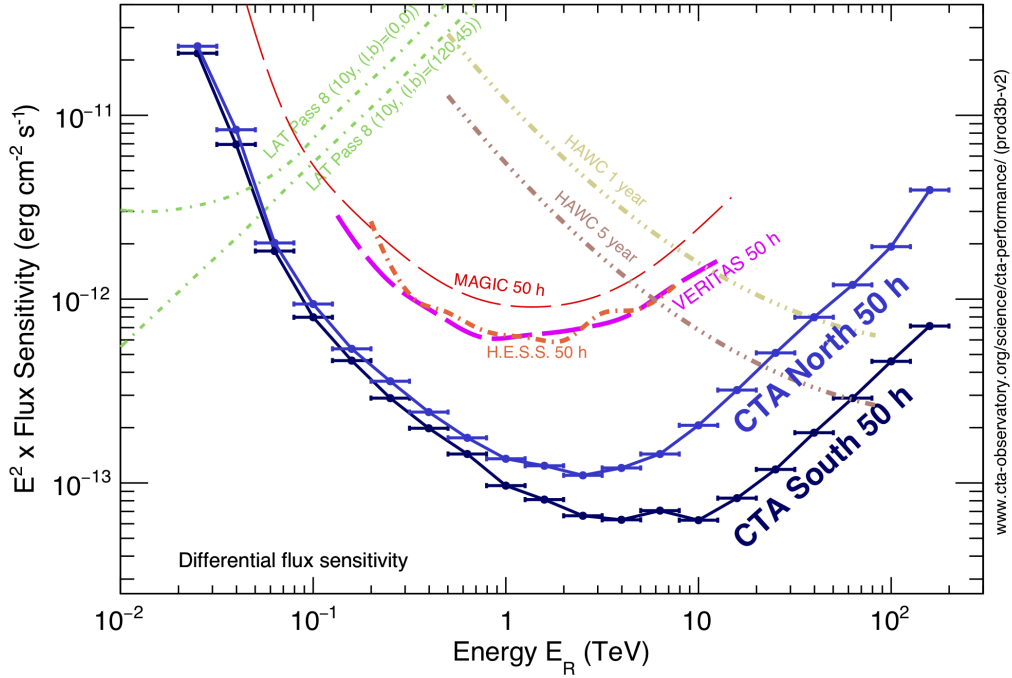


Figure 3.6: Differential sensitivity of CTA for 50 h observation compared to other  $\gamma$ -ray experiments, from [156].

### LST Structure

The structure of the telescope is divided into several parts: The azimuth system, the mirror support dish, the elevation system, the camera support structure, and the drive system. All parts of the structure are specially designed to make the telescope lightweight ( $\sim 100$  tons), to ensure fast repositioning in the case of a transient alert (mainly GRBs), being able to re-position to any part of the sky within 20 seconds. The azimuth system allows the telescope to turn around its vertical axis. It consists of a circular rail of 24 m diameter where six mobile bogies support the structure. The azimuth structure is a framed composition made of carbon fiber reinforced plastic (CFRP) and aluminum tubes. The mirror support dish is a double layer space frame made of CFRP tubes arranged in a tetrahedral structure, with a diameter of 23 m. The elevation system consists of a structure made in part of steel tubes, located in the backside of the dish, to help compensate the weight of the telescope and ensure the stiffness of the structure. The camera support structure, which holds the camera frame, consists of an arch with three curve sections on each arm, made of CFRP, and a total of 26 ropes to stiffen the structure. The drive system, designed to ensure a fast and precise repositioning, consists of 4 synchronous motors capable to supply a total mechanical power of 190 kW to move the structure in azimuthal axis and elevation. The different parts of the structure are shown in figure 3.7.

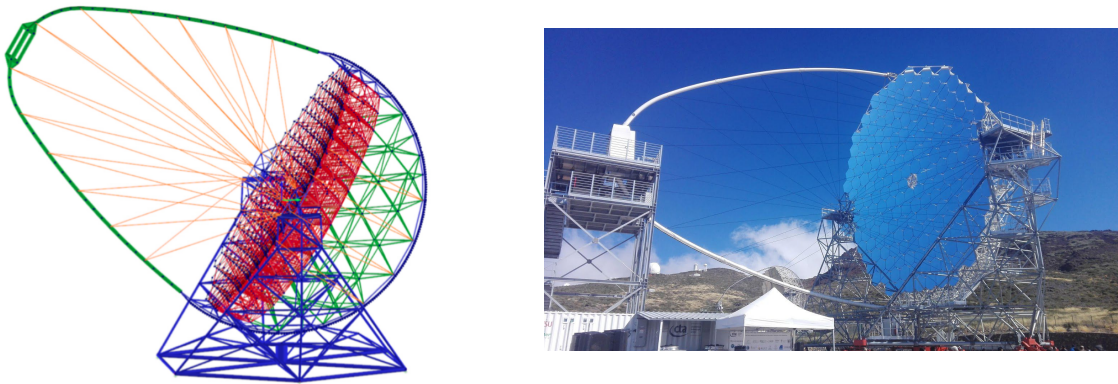


Figure 3.7: Left: Simplified diagram of the structures of LST without bogies, mirrors and camera. Azimuth substructure is blue color, the elevation system and the camera support structure are shown in green color and the mirror dish is red color, from [158]. Right: Photo of the first LST installed in CTA North site (Roque de los Muchachos Observatory, La Palma, Spain).

### LST Optics

The mirror of the telescope has a parabolic shape, to guarantee the isochronousity of the optics. It has 23 m diameter, 28 m of focal length and it is segmented in 198 hexagonal facets. The facets are manufactured using the cold slump technique consisting in producing a sandwich of an aluminum honeycomb structure between two glass sheets [159]. Mirrors are fixed to the telescope structure by three knots, two of them mounted on actuators to adjust each mirror panel in two directions. The *active mirror control* system controls these actuators to fine-tune the focal distance and focusing, to account for the possible deformations and bending of the telescope structure. Each mirror segment is equipped with an infrared laser, and two more lasers are mounted in the center of the disk, which constantly points to the left and right of the camera. The directional offset of the mirror facets can be estimated by taking pictures of the reflected spots on a target in front of the camera with a high-resolution IR CCD camera located in the center of the dish. The achievable positioning resolution can reach  $< 5\mu\text{m}$  [158].

### LST Camera

The camera focal plane instrumentation consists of 256 modules (sometimes also referred to as clusters) with seven Photomultiplier Tubes (PMTs) each, making a total of 1855 pixels. The PMTs are mounted with a 50 mm pitch, coupled to hexagonal light guides made of reflective material (3M ESR), to collect all the light arriving at the camera. The PMT model is Hamamatsu R11920-100-20, specially developed to reach high quantum efficiency (42%) and low after pulse rates, which go below 0.02 % above 4 photoelectrons. Each module with seven photodetectors has one readout system based on the Domino Ring Sampler version 4 (DRS4) [160]. The signal from the PMTs

is split into three branches: high and low gain ones, which are sampled at  $\mathcal{O}(\text{GS/s})$  in the DRS4 chips; and the trigger branch, which is feed into the Level 0 trigger Application-Specific Integrated Circuit (ASIC) [159]. A slow control board monitors the PMTs and controls the high voltage elevators. Analog backplanes are dedicated to trigger distribution along with the modules and clock signal propagation. The mechanical structure of the camera consists of several parts, shown in figure 3.8. The modules are inserted in the load-bearing structure from the front of the camera and connected to the backplane electronics on its rear part. The design of such a modular structure guarantees easy access to individual modules in case any repair is necessary, allowing to disconnect and extract one module without manipulating the rest of the camera. The load-bearing structure is mounted inside the tubular structure which holds the camera external walls, doors, and interfaces with the camera frame. In the front part of the camera, there is a window that can be covered by a shutter to avoid the entrance of sunlight during the day, to maximize the life of the PMTs. In the back part of the camera lies all the cabling and auxiliary electronics. The total dimensions of the camera are  $2.9 \times 2.9 \times 1 \text{ m}^3$  and the weight is less than 2000 kg. Since all the electronics are stored inside the camera, the structure was required to accomplish a series of requirements related to the exposure to environmental conditions such as the protection to the entrance of dust, water, and sunlight, and guarantee a stable temperature between  $20^\circ\text{C}$  and  $40^\circ\text{C}$  [161]. Temperature regulation is possible thanks to the water cooling system, based on cold plates and a temperature-controlled airflow cooling system. An access tower permits to intervene in the camera during day-time operations when the telescope rests in parking position, and also acts as an anchor in case of strong winds.

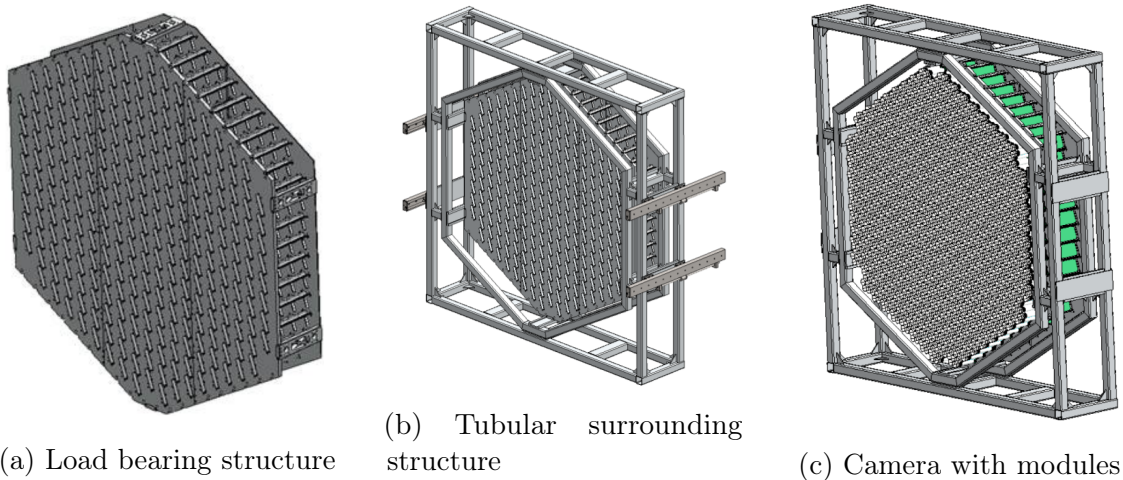


Figure 3.8: Different LST camera mechanical elements.

### 3.3.2 Medium Size Telescope (MST)

MSTs will cover the core energy range of CTA, from 100 GeV to  $\sim 10\text{TeV}$ . This is the usual range reached by current IACT generation, so the improvements in sensitivity will come from the large area covered and the better image reconstruction due to the larger number of telescopes (15 in the north, 25 in the south). The MST 12 m diameter mirror is a modified Davies-Cotton (DC) optical layout very similar to that of Very Energetic Radiation Imaging Telescope Array System (VERITAS) and High Energy Stereoscopic System (H.E.S.S.). The first prototype of this type, the Davies-Cotton MST (DC-MST) [162], was built in Adlershof, Germany. There are two different camera designs for DC-MST: *FlashCam* and *NectarCAM*, which characteristics will be discussed in this section. A detailed report of the status of the MSTs as of July 2019 can be found in [163]. A summary of the different parts of the telescopes is given in this section.

#### MST Structure

The structure of the MST can be seen in figure 3.9. The main mechanical structure of the telescope is a cylindrical tower of 1.8 m diameter and 20 mm wall thickness. The tower is connected on top to the head of the telescope, which contains the azimuth bearing to allow the telescope to rotate in the horizontal axis, and the drive assemblies. It is possible to access to the tower through a door at the base. All electrical cabinets are stored and distributed over three floors of the tower. A combination of ventilation and air conditioning system is used to keep the temperature within the cabinets operation range. The drive assemblies are designed to reach any object above 30° in elevation in less than 90 s. It is divided into the azimuth drive subassembly and two elevation drive subassemblies, mounted in the left and right of the telescope. To account for the possible sources of excitation, like wind gusts, which can lead to oscillations of the structure, an active vibration damping control is used to reduce their effect on the pointing accuracy of the telescope. The dish structure is designed to host the mirrors, and the camera support structure is attached to it [164].

#### MST Optics

The optical system of the DC-MST consists of a mirror segmented in 86 hexagonal facets of 1.2m length, providing an effective mirror area  $> 88 \text{ m}^2$ . The focal length of the telescope is 16 m. Different mirror technologies are being tested, all based on cold slumping techniques, with different layers of materials, coatings, and structures. A system of actuators forms the Active Mirror Control (AMC) system of the MST allowing to adjust the mirror position for focusing. The structure is stiff enough to make unnecessary to readjust the mirrors during observations to maintain the Point Spread Function (PSF). The AMC is used only for the initial mirror adjustment and for maintenance activities, or adjust the focal distance for specific observations.

#### MST Cameras

Two camera prototypes have been designed and tested in the structure installed in Adlershof and showers have been detected with both of them, as shown in picture



Figure 3.9: DC-MST prototype with FlashCam in Adlershof, from [165].

3.10. The first design named FlashCam has 1764 PMT-based pixels divided into 147 modules of 12 pixels each. It implements a fully-digital trigger and readout system operating at 250 MS/s which allows to define flexible trigger patterns relying on the digitized PMT signals. The readout system is designed for a dead-time-free operation with trigger rates up to 30 kHz. FlashCam uses only one gain channel, reducing the required bandwidth for data transfer. The second camera design named NectarCAM counts with 1855 pixels, divided into 256 groups of 7 modules. The camera mechanics and many auxiliary systems have been designed to be equivalent to the LST camera. The signal digitizing of NectarCAM relies on a dedicated Nectar ASIC which digitizes the PMT signals at sampling speeds of around 1 GHz. It implements a digital trigger based on the binary outputs of individual pixels after comparing their analog signals with a threshold (Level 0 trigger).

### 3.3.3 Small Size Telescope (SST)

The smaller telescopes, SSTs, will be the more numerous in the CTA layout, with more than 70 telescopes in the southern site. These telescopes are dedicated to detecting the highest energy  $\gamma$ -rays which in the majority of cases will come from the galactic

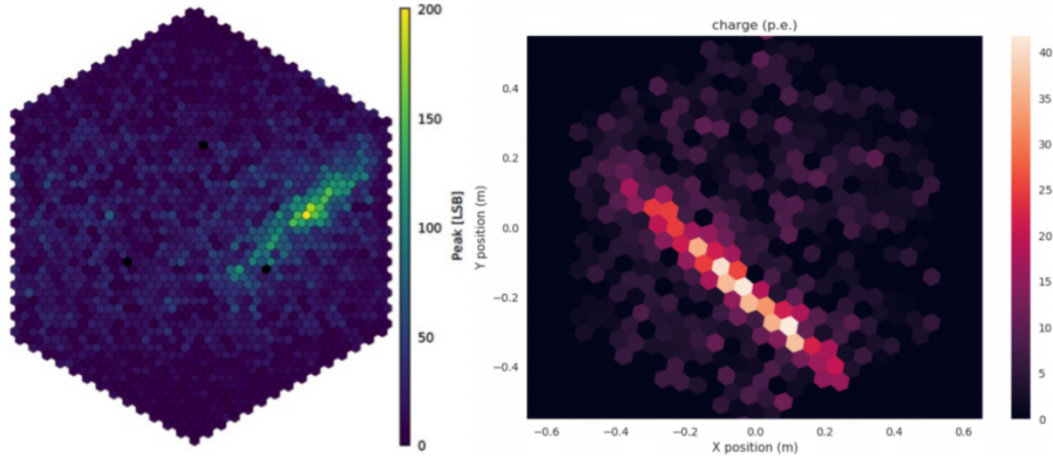


Figure 3.10: Left: DC-MST Showers obtained with FlashCam(*left*), Nectar-CAM(*middle*) and Schwarzschild-Couder MST (SC-MST) camera (*right*) prototypes, from [163].

plane. They need to be spread over a very large area, to catch as many  $\gamma$ -ray showers as possible, but they do not need large mirrors because VHE radiation produces a huge amount of Cherenkov light. They are designed to reach their peak sensitivity at energies greater than 10 TeV.

### SST Structure

The optical design of SSTs is based on a Schwarzschild-Couder (SC) double mirror configuration. A column raises from the base of the telescope and interfaces at the top with the azimuth fork. The fork sustains the elevation assembly, which is composed of the mirror dish, the counterweight, and the structure that sustains the two mirrors. The dish is designed to hold the segments of the primary mirrors, which can be individually controlled by actuators. A quadrupod is attached to the dish, which together with a central pole, is joint to the structure that supports the secondary mirror and also serves to counteract deformations due to gravity and wind. The structure for the monolithic secondary mirror accounts for three actuators and three lateral arms which support the transverse components of the weight of the mirror. The drive of the azimuth is located at the base of the column. A scheme of the structure can be found in picture 3.11. A detailed description of the SST structure design can be found in [166].

### SST Optics

The SC design of the SSTs is composed of two mirrors, one primary of 4.3 m diameter segmented in hexagonal tiles, and a monolithic secondary mirror of 1.8 m. The primary mirror tiles have been manufactured using a cold slumping replication process. The

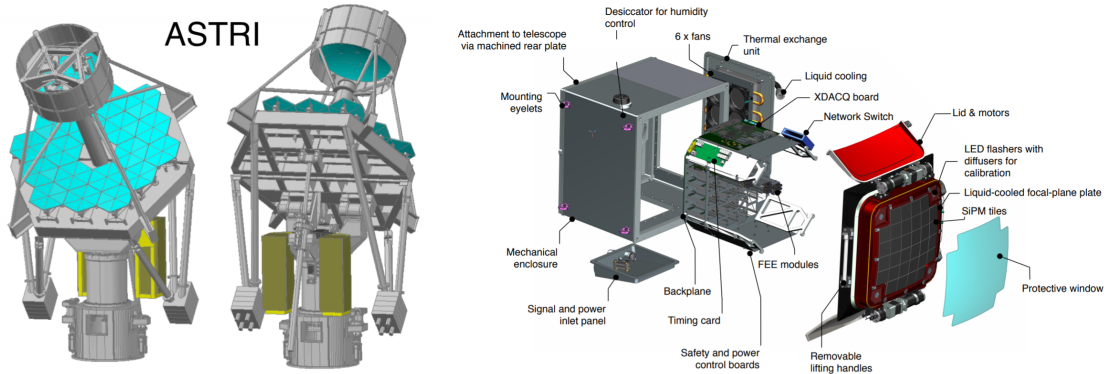


Figure 3.11: *Left:* General view of the SST structure and electromechanical subsystems, adapted from [166]. *Right:* CAD model of the Compact High-Energy Camera (CHEC) camera from [167]

secondary is made of a hemispherical thick glass shell thermally bent to 2.2 m radius of curvature. The focal length of the system is 2.15 m, f/0.5 and the field of view (FoV) reaches 10°. The advantages of a double mirror configuration are a better PSF over a large FoV and better correction of aberrations [168] than for single mirrors.

### SST Camera

The camera is composed of 2048 pixels made of Silicon Photomultiplier (SiPM), instrumented in 32 modules which contain 64 pixels of  $\sim 6 \times 6 \text{ mm}^2$ . The digitalization of the waveform is performed by Front-end electronics (FEE) based on TARGET ASICs [169] which also give the first trigger level, as the sum of four neighboring pixels. A backplane provides the power, clock, trigger, and data interface of the FEE. The trigger decision is formed in the backplane by combining trigger signals from all the FEE modules. In the camera structure, a lid protects the camera from the environment and a cooling system based on the circulation of chilled liquid through the camera focal plane plate and six internal fans, maintains a stable temperature. A diagram of the camera is shown in figure 3.11. A detailed description of the camera and results from its commissioning phase can be found in [167].

## 3.4 Reconstruction and Analysis tools

The best performance results from CTA relative to the current generation IACTs will come not only from the telescopes designs, but it is also very important to have solid software tools, accessible and user friendly, which will allow analyzing the forthcoming data. Also, especially during the initial phases of the development of the facility, to calculate the predicted sensitivity shown in section 3.2 it is necessary to produce precise and reliable simulations of the instrument response to the arrival of electromagnetic showers. In this section, the main software tools for the simulation and analysis of the different levels of CTA data are described.

### 3.4.1 Monte Carlo simulations

MC simulations are of great importance for the IACT technique, where the detection of  $\gamma$ -rays is indirect and it is necessary to reconstruct the primary parameters from the signal received at the telescopes. Detailed simulations of the development of the Extensive Air Showers (EAS) in the atmosphere, combined with simulations of the instrument response to the Cherenkov light produced by those EAS are used for two main purposes: Separation of  $\gamma$  and hadron showers and reconstruction of the shower direction and energy of the primary. For the former, since hadrons produce the majority of Cherenkov light which reach IACTs, it is necessary to characterize the particular differences between photon and hadron induced showers thanks to the MC simulations. For the latter, comparing the shower parameters to those of the simulated showers, and applying different reconstruction methods, like Multi-variate analysis (MVA), Machine Learning (ML) or Deep Learning (DL) among others, the characteristics of the primary particles can be reconstructed.

MC simulations consist of two phases: The first is the simulation of the EAS development in the atmosphere, tracking the particles created, the products of their interaction, and the amount of Cherenkov light produced. The second part consists of simulating the instruments, taking into account ray tracing, the optical features of the mirrors, the response of the electronics, etc.

For CTA, MC simulations have been performed using the programs **C**Osmic **R**ay **S**Imulations for **K**Ascade (CORSIKA), for the EAS simulation, and `sim_telarray`, for the telescopes response. These two software packages permit to configure a specific array of telescopes with their particular features and store only the information of the particles and light from the showers that fall in the surrounding of the telescopes. The current production of MC data, with the layout described in section 3.2, is the *prod3b-v2* which used CORSIKA version 6.9. In the next subsections, a brief description of CORSIKA and `sim_telarray` is given.

#### CORSIKA

CORSIKA is a detailed MC program to study the development of EAS in the atmosphere [170], originally developed for the Kascade experiment [171]. The showers can be initiated by different types of primary particles, such as photons, protons, or other heavier nuclei. The program treats every possible process taking place in the development of EAS to the present state of our knowledge. It takes into account the transport of particles through the atmosphere and their interactions with air molecules. The secondary particles produced are tracked along their trajectories and their parameters are stored when they reach an observation level, i.e. the stage of the shower that can be detected by an instrument. The main problem of the simulation of EAS is the extrapolation of hadronic interactions at the higher energies which cannot be probed in collision experiments. The secondary particles emitted in the extreme forward direction, which are not accessible by colliders, are precisely the more important in EAS development because they are the ones bringing the largest energy fraction to the atmosphere. The extrapolations must, therefore, rely on different

theoretical models. To study the systematics of such models, in CORSIKA there are five different hadronic interaction models available. For CTA prod3b-v2 the model used was QGSJET-II [172]. An example of three different types of showers simulated with CORSIKA is shown in picture 3.12.

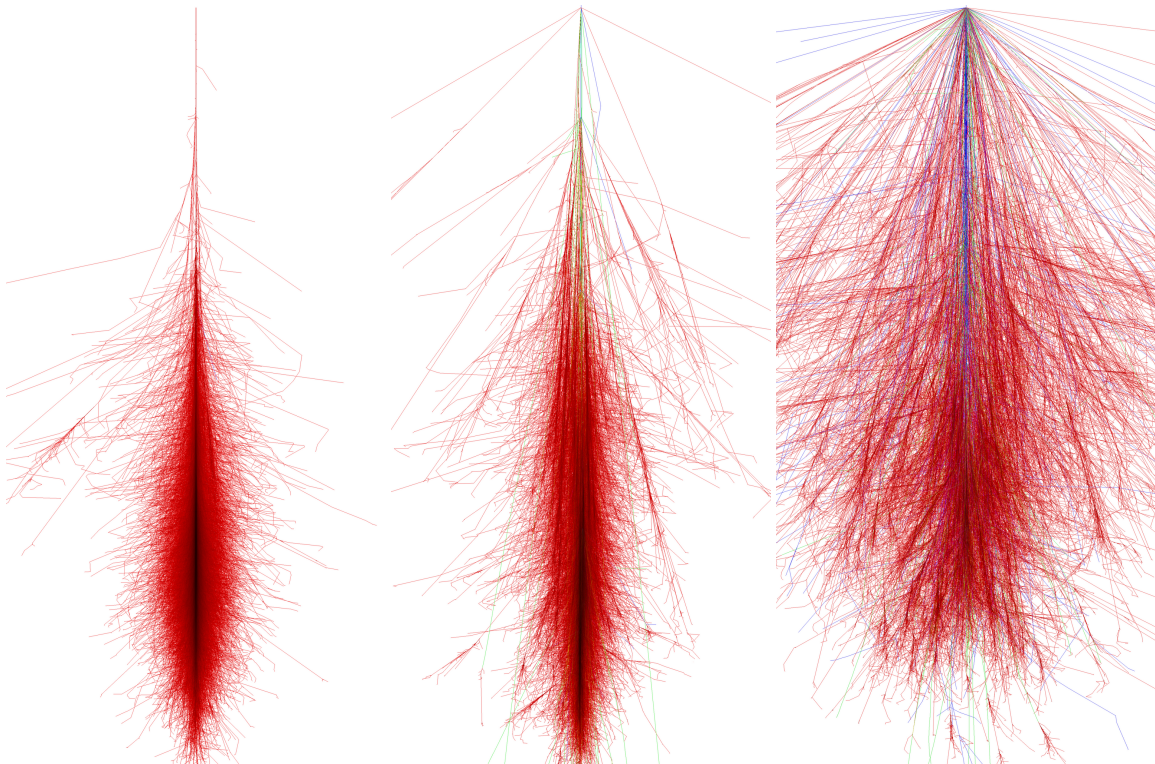


Figure 3.12: Photon (left), proton (center) and iron (right) produced showers for a primary energy of 1 TeV and  $0^\circ$  zenith angle, simulated with CORSIKA from [173].

### **sim\_telarray**

The second part of MC simulations is carried out by the program sim\_telarray [174], dedicated to the simulations of the detectors: Optical ray-tracing of photons, their registration by PMTs, the behavior of discriminators or comparators for trigger at pixel and telescope levels, and the digitalization of resulting signals. It was created for the High Energy Gamma Ray Astronomy (HEGRA) IACT system, and has been improved and made fully configurable to be used with any kind of IACT layouts.

The simulation of ray-tracing follows the trajectory of photons since they reach the mirrors of the telescopes and arrive at the camera pixels. The mirror optics are simulated taking into account the configured mirror morphologies, dish shapes, and segmentation. The shadowing of the camera structure can be also included in the simulation. The final step of the ray-tracing simulation is the angular acceptance of the pixels, which usually are equipped with Winston cones (light guides) to avoid gaps between neighboring pixels. From ray-tracing simulations, the PSF of the telescopes

Data level	Description
R0	Raw data from camera, or MC data
R1	Calibrated data
DL0	Data Volume Reduced Data
DL1	Calibrated image with Hillas parameters
DL2	Reconstructed shower parameters (Energy, direction and $\gamma$ -hadron separation)
DL3	Reduced data, sets of gamma-like events with associated Instrument Response Function (IRF) and technical data needed for science analysis
DL4	High level binned data products, like spectra, skymaps or light curves.
DL5	Legacy observatory data, like survey sky maps or source catalog.

Table 3.2: The different CTA data levels, based on [176] and [177]

can be calculated and hence can be used to optimize their designs. In the simulation of the photon detection by the PMTs, the fluctuations in quantum efficiency in each pixel are taken into account. As pixels are permanently exposed to Night Sky Background (NSB), the number of photons arriving at each pixel is fully configurable assuming a specific NSB spectrum. In the final simulation, the amplitude of the NSB signal is subtracted from the signal baseline. The afterpulsing produced by ions is also taken into account, which can produce pulses of large amplitude which enter in the readout window of the front-end electronics of the cameras. The trigger system simulation takes into account the switching behavior of discriminators or comparators, which can be configured to a specific logic (next-neighbor, pixel sectors...). The result from the pixel trigger system serves as input for the stereo level trigger, which usually requires that at least two telescopes trigger within a short time window. The final output of the `sim_telarray` simulation is a data container in a format as closest as possible as the real data format from the actual instruments, based on the `eventio` machine-independent format [175].

### 3.4.2 Low level analysis: `ctapipe`

The analysis of CTA data, goes through different steps before turning into a format with which real science can be done. A description of the different CTA data levels is given in table 3.2.

*Ctapipe* [176] is a framework for prototyping the low-level data processing algorithms for CTA. It is written in Python and its currently in development, still suffering large and rapid changes in structure and functionality. While is not yet the final code for CTA analysis and other alternatives are currently on development, *ctapipe* is the framework chosen for the low-level data analysis carried on in this thesis and so it is the one that will be described in this section.

The goal of *ctapipe* is to reduce R0 data, that is raw data directly out of telescope cameras or MC simulated data out from `sim_telarray` to DL2 data containing the reconstructed shower parameters. Raw data can be read with *ctapipe* thanks to specific *EventSource* classes, which depend on the type of the input file (simulated data, real data from each specific telescope, etc.). It is possible to loop over the events of the source container to perform different operations on them. The first part of the data analysis is typically the calibration of the signal, requiring the treatment of the

waveform signal in each pixel. *Ctapipe* performs the integration of the signal from the registered waveform using different types of integrators (*LocalPeakWindowSum*, *Full-WaveformSum...*) to calculate the total number of counts in the pixel and transform it to photoelectrons. The result is a camera image, where pixels contain the light from the shower and background. Different cleaning methods, like the two-level tailcuts cleaning, can be applied to subtract the background light and get the shower image. Afterward, the Hillas parameters can be calculated. Another function computes a linear fit to the extracted charge arrival times projected along the longitudinal axis of the Hillas ellipse, to extract the timing parameters. All these shower parameters are stored in the DL1 format, with the possibility to lose pixel-wise information and reduce the size of data files. For the reconstruction of the primary parameters, that is the energy, direction and particle type, there are currently two different algorithms implemented: a moment-based stereo reconstruction, which combines the Hillas parameters of different triggered telescopes geometrically to estimate the shower direction; and a template-based stereo reconstruction, which uses a fit of the full camera image to an expected image model to find the best fit shower axis, energy, and depth of maximum. Other methods using machine learning and deep learning techniques are also being explored but are not yet implemented in the main source code of *ctapipe*.

### 3.4.3 Science analysis: *ctools*

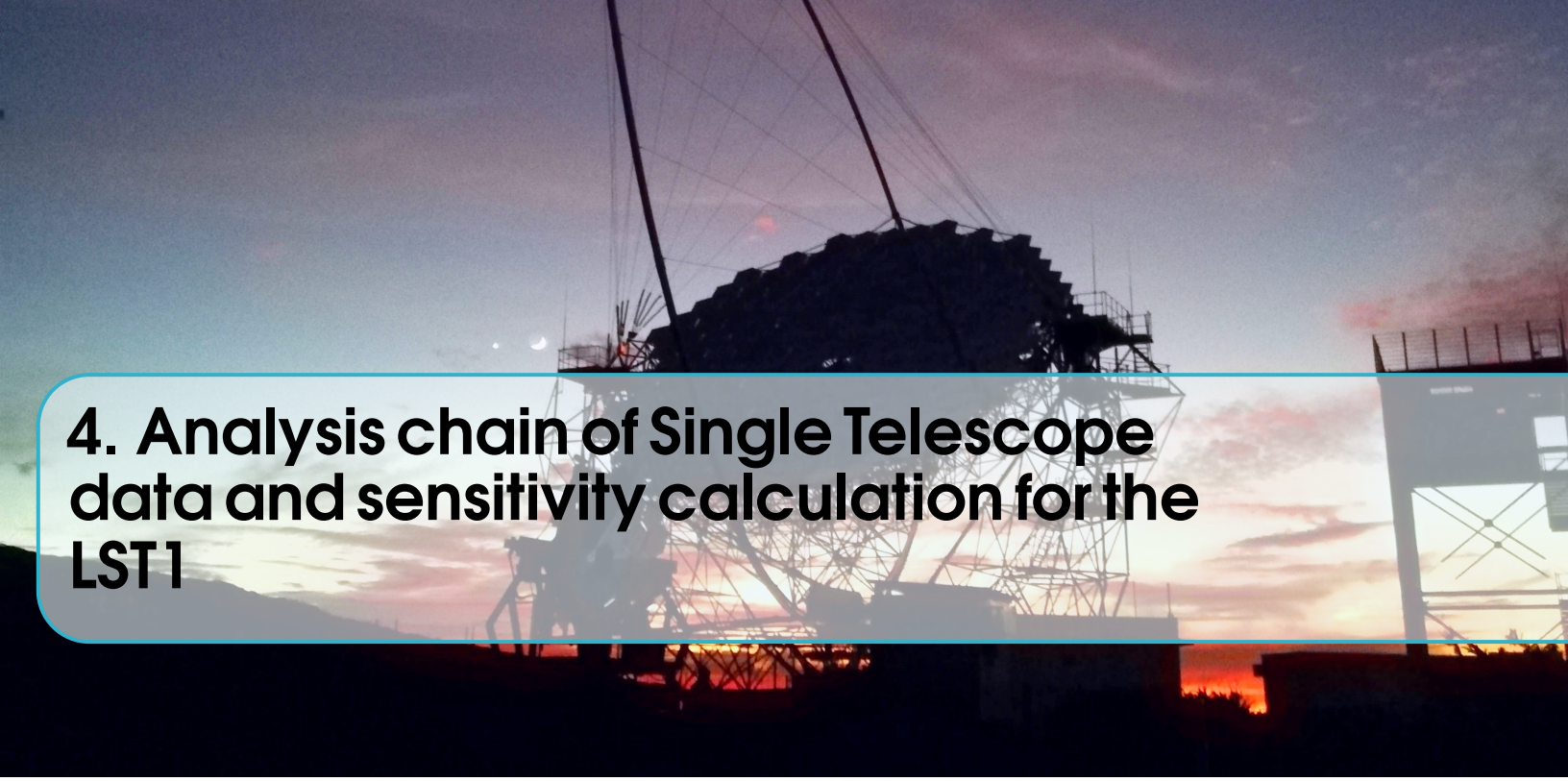
One of the proposed software packages for the scientific analysis of CTA data is *ctools*, based on *GammaLib* [178], a versatile toolbox for the scientific analysis of astronomical  $\gamma$ -ray data. It comprises a set of tools and python scripts with a command-line interface that allows interactive data analysis. It is possible also to create scripts and pipelines within Python using *ctools* functionalities. The data managed by *ctools* is at the level of DL3 and beyond, treating with observation events, skymaps, spectra, and so on. For the analysis of observation events, *ctools* includes the possibility of doing a binned (separating the data in energy bins) or unbinned analysis, and also it can stack the data of several observations to be analyzed together. A likelihood fitting can be performed to fit data to a given emission model, retrieving the best-fit parameters of spectral, spatial, and time components of the model of each emission source. Besides, *ctools* allow to perform simulations of observations, using a set of precomputed IRFs, to serve as *mock data* for the calculations of prospects of the future performance of CTA. Some of the most important tools of *ctools* that has been used in this thesis are:

- *ctobssim*: This tool produces simulations of event lists using the instrument characteristics specified by a given IRF and an input model. The model is composed of the individual models of each  $\gamma$ -ray source in the target FoV. Each model has a spatial component, given by the geometry of the source (point source, disk, gaussian, spatial map...), a spectral model describing the flux (it can be specific functions like power-law or log parabola, or a user-made spectrum where the flux per each energy is given in a file), and a time model,

describing the variability of the source with time. The model also should include an instrumental background model to simulate background events, which are misclassified proton events. As input, *ctobssim* requires a pointing direction, radius of the simulation region, time interval, energy interval, an IRF, and an input model. The result is an event list in fits format, which contains all the information of the observation in the header.

- *ctbin*: This tool creates a counts cube, with a certain number of energy bins, and fills it with events from an event list. It is possible to stack events from different observations in the same counts cube. The resulting cube can be used in further steps of the analysis, as the likelihood fitting.
- *ctlike*: Performs a maximum likelihood fitting of a model to binned or unbinned data. As input, it can take event lists or a count cube, and depending on the input it will perform a binned or unbinned likelihood fit. A joint likelihood fitting can be done for multiple observations, and the average response functions (exposure, PSF and background) can be precomputed using the tools *ctexpcube*, *ctpsfcube* and *ctbkgcube*. It is also possible to calculate the Test Statistics (TS) (which is a measure of the source significance) of a source. More details on the likelihood fitting with *ctools* will be given in chapter 5.
- *ctmodel*: This tool generates a 3D model cube which provides the predicted number of counts for an input model as a function of spatial coordinates and energy. As an input, it will require a counts cube, an event list, or an observation definition file and it will need the parameters of the cube, such as sky coordinates, projection method, energy binning, number of pixels, and pixel scale.
- *ctulimit*: Computes the upper flux limit for a specific source model. Starting from the maximum likelihood parameters, the tool will look for the flux that produces a decrease in the likelihood which corresponds to a given confidence level. By default, it is set at 95% confidence level, but it can be configured. The result is the differential flux upper limit for specified reference energy and the integrated flux in a certain energy range.

All the scientific tools for CTA are still in development, suffering improvements and changes every day to ensure their efficiency and reliability once the observatory is in full operation.



## 4. Analysis chain of Single Telescope data and sensitivity calculation for the LST1

### 4.1 Introduction

The first Large Size Telescope (LST) detected its first Cherenkov shower in December 2018 and is currently in commissioning phase. It is the first Cherenkov Telescope Array (CTA) telescope installed on-site (in La Palma island), and it is expected to be operating on its own until LST 2-4 are built. This means that LST1 needs a proper analysis chain in single operation mode, which differs in several aspects from the benchmark analysis tools of CTA (see section 3.4.2), which are prepared for stereo operations. Although single telescope observations present a big challenge, especially regarding source position reconstruction and  $\gamma$ -hadron separation, thanks to its mirror size and camera design, it is expected that LST1 performance will be competitive enough to provide interesting scientific results in the time operating alone.

This chapter covers a considerable amount of the work done during this thesis, which includes the development of the code for the single telescope analysis for LST1, the calculation of LST1 sensitivity based on Monte Carlo (MC) simulations, the development of a new technique for Hillas parameters calculation without cleaning, based on the Expectation-Maximization (EM) algorithm, and the application of the analysis chain to real LST1 data.

### 4.2 The LST1 analysis chain overview

The software for the single telescope analysis of LST1, named *cta-lstchain*, has been developed due to the necessity of specific tools for single telescope analysis, which are not included in *ctapipe*. It has been written as a python package that relies heavily on *ctapipe*, and it is structured in several modules containing functions destined to the different parts of the data reconstruction. The first version of *cta-lstchain* was

written by the author of this thesis and many contributors have joined the project over the last two years to improve and optimize the repository to its current version. At the moment, there is a full pipeline, which can perform the full analysis chain, from the raw data level (R0) to the reconstruction of the primary energy and direction, and the  $\gamma$ -hadron separation (level DL2), both for MC and real data. The analysis chain is divided into several steps, each of which can be executed through a python script which requires certain inputs and calls for the appropriate functions. All the configuration parameters of the different elements of the analysis are given through a configuration file, which can be edited by the user. The input of the analysis chain are the raw data files of LST1 events, which for MC data are the output files from *sim\_telarray* (see section 3.4.1), and for real data are *zfits* [179] files with an equivalent internal format as *simtel* files. The files contain the full information available per pixel, known as *waveform*, which is the digitized signal amplitude vs. time for every triggered event. Also, it includes MC information in the case of simulated data (such as the true energy, source position, number of simulated events, etc), or recorded information from the different telescope subsystems in the case of real data (such as time, pointing, trigger type, etc). Throughout the analysis chain, the shower images and image parameters are stored in containers designed in *cta-lstchain* specifically for LST1, which can be dumped into *pandas* DataFrames and saved in *hdf5* [180] files. The main steps of the analysis chain can be summarized as:

- **Calibration:** The waveforms of each pixel in the camera are integrated after pedestal subtraction, and converted to number of photoelectrons. Also, the arrival time of the light to each pixel is obtained.
- **Image cleaning and parameterization:** The images in the camera contain pixels with a signal from Night Sky Background (NSB), not related to the Cherenkov event, so a cleaning method must be applied to remove them. Afterward, the distribution of photons in the image is used to calculate the Hillas parameters.
- **Energy and direction reconstruction:** The energy and direction reconstruction of the triggered events are performed using a multidimensional regression technique based on Random Forests (RFs) ([181] or see appendix E). A set of simulated diffuse  $\gamma$  events are used to train the RFs.
- **$\gamma$ -hadron separation:** For the  $\gamma$ -hadron separation, a multidimensional RF classifier is used. Sets of simulated  $\gamma$  and proton events, which energies and directions have been reconstructed in the previous step, are used to train the classifier.

### 4.2.1 Calibration

In the calibration phase, the raw signal known as *waveform*, is integrated after pedestal subtraction, to obtain a total number of Analog to Digital Converter (ADC) counts per pixel, which afterward is multiplied by a factor to be converted in the number of photoelectrons. The different steps for calibration vary depending on the type of data

that is being analyzed: MC simulated or real data.

### Signal extraction

For every triggered event, the signal in each pixel is recorded in a window of 40 samples from the 4096 samples of the Domino Ring Sampler version 4 (DRS4). This signal contains counts not only from the Cherenkov light but also from background light from NSB and the intrinsic noise induced by the readout chain. Before integrating the signal, it is necessary to subtract this baseline, known as the pedestal. For simulated MC events the pedestal value for each pixel in the camera is already stored in the file, but for real data it is necessary to take special runs triggered randomly during observations, to obtain the values of the pedestal for each sample of the DRS4. In *cta-lstchain* a specific script is used to extract the pedestal values from these runs and store them in a *hdf5* file. Once the pedestal is subtracted from the signal, the peak in the waveform can be integrated. Typically, a window of a few samples around the maximum is used for the integration, which can be performed with one of the several integrators implemented in *ctapipe* [182]. These calibration steps are applied to the two gain channels of LST1 camera.

### Conversion to photoelectrons

Once the signal amplitude is extracted, it must be converted from ADC counts to photoelectrons through a calibration factor, which is different for each pixel and gain. For simulated MC data, these factors are stored in the file and the conversion can be done simply by multiplying the image in ADC counts by the factors. For real data, special calibration runs must be taken to calculate these factors. Calibration runs are taken using near-ultraviolet light pulses fired from the CaliBox [183], [184] located in the mirror dish. The calibration coefficients are obtained using the F-factor method [185], which assumes that the distribution of photoelectrons in a Photomultiplier Tube (PMT) follows a Poissonian statistics with mean  $N$  and root mean square (RMS)  $\sqrt{N}$ . The signal distribution, however, will deviate from Poissonian statistics due to an excess-noise factor  $F$ , which is different for each PMT and is measured in the laboratory. The relation between the relative widths of the two distributions can be written as:

$$F \cdot \frac{1}{\sqrt{N}} = \frac{\sigma_Q}{\langle Q \rangle} \quad (4.1)$$

Where  $\langle Q \rangle$  is the mean value of the pixel signal and  $\sigma_Q$  is its RMS. The calibration coefficients will come from the relation between the number of photoelectrons  $N$  and the mean pixel signal  $\langle Q \rangle$ . From 4.1, and taking into account that the signal must be pedestal corrected, the relation between number of photoelectrons  $N$  and the pixel charge  $\langle Q \rangle$  is:

$$\frac{N}{\langle Q \rangle} = F^2 \frac{\langle Q \rangle - \langle \text{ped} \rangle}{\sigma_Q^2 - \sigma_{\text{ped}}^2} \quad (4.2)$$

The values of  $\langle Q \rangle$ ,  $\sigma_Q$ ,  $\langle ped \rangle$  and  $\sigma_{ped}$  are calculated from a sufficiently large number ( $> 1000$ ) of calibration and pedestal events, using a specific script from *cta-lstchain*, which stores the resulting calibration coefficients in an *hdf5* file. For the LST1, the value of the  $F$  factor is 1.2, the mean value for all PMTs.

### 4.2.2 Image cleaning and parameterization

To extract information from the image of Cherenkov light recorded by the camera, it is necessary to get rid of the background light not belonging to the shower. This background light is usually related to fluctuations in the NSB. A cleaning method is used to eliminate all pixels which presumably do not contain light from the shower. The *clean* image is used later to perform the Hillas parameterization. Besides there exist several proposed cleaning algorithms in the literature [186], [187], [188], [189], for the time being in *cta-lstchain*, a classical two-level tailcuts cleaning is being applied (like the one used in [190]). This method requires only the information of the amount of light in pixels (already converted to photoelectrons) and compares it to two levels of thresholds in the following way:

- Pixels with number of photoelectrons over the highest threshold level  $Th_{high}$  are selected.
- If pixels selected in the previous step have at least one neighbor above the highest level threshold, those pixels are marked as core pixels from the shower.
- Neighbors of the core pixels with number of photoelectrons above the lower level threshold  $Th_{low}$  are selected as boundary pixels.
- The charge of not selected pixels is set to zero.

The standard values for the two levels used in *cta-lstchain* are  $Th_{high} = 6$  phe and  $Th_{low} = 3$  phe. Note that these values have not been yet fully optimized for the particular case of the LST1, and they can be changed easily in the configuration files. Optimization of the cleaning can lead to better performance, especially for those Cherenkov showers with a low number of photoelectrons, where information can be lost because of the cleaning. Using other information apart from the number of photoelectrons, like the arrival times of the signals to pixels, can help to improve the image parameterization. Low energy showers of  $\gamma$ s and hadrons are much more difficult to differentiate, for that reason, an image parameterization which highly depends on the settings of the cleaning parameters can be problematic when trying to lower the energy threshold of the telescope. In section 4.4 a method for image parameterization not requiring a previous cleaning is proposed as an alternative.

The Hillas parameterization of the shower image after cleaning (see section 2.4.2 and figure 2.9), is performed by a specific function from *ctapipe*. The resulting parameters are intensity (total number of photoelectrons in the shower), width, length, coordinates of ellipse center of gravity, azimuthal angle  $\phi$ , orientation angle  $\psi$ , and the third-order moments: *skewness*, which is a measure of the asymmetry of the distribution; and *kurtosis*, which is a measure of whether the distribution is peaked or flat relative to

a normal distribution. The calculation of the Hillas parameters with *ctapipe* only requires the image of the shower (i.e. the number of photoelectrons in each pixel) and the information of the camera geometry.

The time parameters, *time gradient* and *intercept* are also calculated as explained in section 3.4.2. The time gradient is especially important for single telescope analysis because they reflect the direction of development of the shower, which give information of the side of the ellipse where the source position is located in the camera frame.

Other parameters taken into account are the *leakage2*, which indicates the percentage of the shower that falls in the two outer pixel rings of the camera (image with large values of *leakag2* are heavily truncated); and the *number of islands*, which accounts for the number of separated groups of pixels in the image. A typical  $\gamma$ -ray shower will only have one island with elliptical form, but hadronic and heavier nuclei showers tend to produce messy light distributions with several islands of irregular shapes.

The calibration and image parameterization is performed in *cta-lstchain* using the scripts *lstchain\_data\_r0\_to\_dl1.py*, *lstchain\_mc\_r0\_to\_dl1.py*, for real or simulated data respectively. As it is reflected in the script names, these steps reduce the data level from raw R0 to DL1 (see table 3.2). In general, only the image parameters describing the shower are needed in further steps of the analysis, therefore, pixel-wise information is not needed. However, for testing and crosscheck purposes, *cta-lstchain* scripts offer the possibility to store DL1 data with the full images.

#### 4.2.3 Reconstruction of energy and source position

After the calibration and image parameterization, the image parameters are used to reconstruct the information of the primary particle. In *cta-lstchain* the first step is to reconstruct the energy and arrival direction of the event. The direction reconstruction is problematic in single telescope mode, because even knowing that the Hillas ellipse should point towards the source position in the camera frame, we do not know in which side of the ellipse is located (this is known as head-tail degeneracy). In stereo mode, the problem is solved because the source position will be in the cross point between the line which follows the semi-major axis of Hillas ellipses of all cameras, but for single telescope we must rely on other methods. In the case of *cta-lstchain* we make use of an observable known as *disp*. This is the vector going from the center of gravity of the ellipse to the source position. Originally, the magnitude of the *disp* vector was parameterized in terms of the elongation of the image, that is the ratio between *width* and *length*. The first parameterization was proposed by the Whipple collaboration [191]:

$$Disp = \xi \cdot \left( 1 - \frac{width}{length} \right) \quad (4.3)$$

Where  $\xi$  is a factor dependent on the amount of photoelectrons in the shower image (the *intensity* parameter). A more general parameterization was used for MAGIC-I

[192]:

$$Disp = A(intensity) + B(intensity) \cdot \frac{width}{length + \rho(intensity) \cdot leakage} \quad (4.4)$$

Where A, B and  $\rho$  are second order polynomial function parameters of  $\log(intensity)$ .

Instead of using a parameterization, in *cta-lstchain* the disp vector is directly reconstructed using a multivariate regression method adjusting the MC. The time parameters are very important to reconstruct this quantity because the Cherenkov light from the upper parts of the shower arrives before the light from later developed lower parts, giving rise to a time gradient in the shower image. The time gradient gives information on which side of the ellipse is pointing to the source position.

The method used in *cta-lstchain* for the reconstruction of these quantities, energy and disp, is based on a multidimensional regression technique relying on RFs. The RF is a supervised learning algorithm which uses an ensemble of several decision trees ([181], or see appendix E). In the basic analysis of *cta-lstchain*, the one carried on in this thesis, a source independent approach is used, where the knowledge of the position of the source is assumed to be unknown. For that reason, the RFs for energy and disp reconstruction are trained using a set of MC simulated  $\gamma$  events triggering the LST1, with diffuse arrival directions distributed in a  $5^\circ$  radius field of view (FoV). The simulated data is divided into two sets, for training and testing. The list of parameters used to train the RFs can be found in E. The trained RFs are used to reconstruct the desired values (energy and disp) in the test data. For energy reconstruction, the reconstructed quantity is  $\log_{10}(E)$ . In the case of the disp vector, the two components of the vector (*disp\_dx*, *disp\_dy*) are reconstructed using the same RF. The implementation of the RFs relies on the Python package *scikit-learn* [193], a machine learning package which offers a large number of tools for predictive data analysis. The class *RandomForestRegressor* is used for the energy and direction reconstruction. This class has a set of parameters that can be modified by the user to optimize the performance of the predictions. In *cta-lstchain* these parameters can be modified by a configuration file. The most relevant parameters and the values used to compute the performance results of the LST1 in this chapter are shown in table E.1.

#### 4.2.4 $\gamma$ -hadron separation

The primary particles of the majority of Cherenkov showers produced in the atmosphere are not  $\gamma$ -rays but cosmic hadrons. These events trigger the telescopes  $\sim 10^4$  times more than  $\gamma$ -rays, therefore it is necessary a very efficient background rejection method to discard hadronic showers and analyze only  $\gamma$  events. The methods for  $\gamma$ -hadron separation, in general, rely on the morphological differences between the showers produced by the two kinds of particles, including temporal information. This task is much more efficient in stereo mode because  $\gamma$ -ray showers which trigger different telescopes will produce images in the cameras with Hillas ellipses pointing towards

the source position, while hadronic showers will produce much less correlated images. In mono mode we can only rely on the morphological features of the images, knowing that hadronic shower images are much more extended, without a clear definite shape and with a higher number of islands than  $\gamma$  showers.

The task of  $\gamma$ -hadron separation is done in *cta-lstchain* with a RF classifier, which follows similar principles as the RF regressor of the previous section. Instead of calculating the value of a variable, it decides to which class each event belongs. In this case, it is only a two classes problem:  $\gamma$ s or hadrons. The best splitting criterion for classification is calculated in terms of the so-called Gini index (see E.2).

The training set for the  $\gamma$ -hadron classifier consists of two sets of MC simulated events, of diffuse  $\gamma$ s and protons with arrival directions coming from a  $10^\circ$  radius FoV. Usually in Imaging Atmospheric Cherenkov Telescopes (IACTs), the set of hadronic events used for training is taken from real background events recorded with the telescope when pointing to a direction in the sky without any  $\gamma$ -ray source, because the model used to simulate MC proton showers contains large uncertainties (see section 3.4.1). However, as by the time this thesis was written there were not enough real data from LST1 to build a big enough background data set, all the calculations have been done using MC simulations.

The parameters used for the splitting of the classifiers are the same from the ones used for the regressors (see E.3.2) but adding the reconstructed energies and disp vector. To do so, the original  $\gamma$  events set is split in a training set for the regressor, and a test set, to which the energy and disp vector are reconstructed. The regressors are also used to reconstruct the energy and disp vector of the set of proton events. Afterward, this new set of  $\gamma$  and proton events, with reconstructed energy and disp is divided again in a training and test set to build the RF classifier. The classifier is implemented using the *RandomForestClassifier* class from *scikit-learn*.

### 4.3 Sensitivity of the LST1

The sensitivity of a telescope is defined as the minimum flux of  $\gamma$ -rays over the background that should be recorded for a statistically significant detection. Using the simulated MC data and the analysis techniques explained in section 4.2 the differential sensitivity of LST1 in mono mode can be calculated. The sensitivity is computed for the detection of a point source after 50 hours of observations. To do so, we are using the Li&Ma method, extensively described in [194]. The significance of the detection of a source is a way to evaluate the statistical reliability of an observational result. A typical observation in  $\gamma$ -ray astronomy will consist of pointing to a region where it is supposed to exist a source, recording  $N_{on}$  counts in a time  $t_{on}$ . Then, to evaluate the background, a region without any source is observed, recording  $N_{off}$  counts in a time  $t_{off}$ . If the ratio between the observation time of the on and off regions is  $\alpha = t_{on}/t_{off}$  then the number of background photons in the on region is estimated by  $\hat{N}_B = \alpha N_{off}$  and the probable number of photons contributed by the source is  $N_S = N_{on} - \alpha N_{off}$ . The significance can be estimated in terms of the likelihood ratio method, which tests

the *null hypothesis*, where no source exists at all and all the excess counts detected in the on region are due to fluctuations in the background. In this case,  $N_{on}$  will follow a Poisson distribution with variance equal to that of the background  $\langle N_B \rangle$ . The likelihood ratio can be written as:

$$\lambda = \frac{L(X|E_0, \hat{T}_c)}{L(X|\hat{E}, \hat{T})} \quad (4.5)$$

Where  $X$  denote the observed data and  $(\hat{E}, \hat{T})$  are the maximum likelihood estimations of the unknown parameters. In the null hypothesis,  $E = E_0$  and  $T = \hat{T}_c$  are the parameters for the conditional maximum likelihood estimation. In our case, the unknown parameters will be  $N_S$ ,  $N_B$  wherein the null hypothesis  $N_S = 0$ . The maximum likelihood ratio has the form:

$$\lambda = \left[ \frac{\alpha}{1 + \alpha} \left( \frac{N_{on} + N_{off}}{N_{on}} \right) \right]^{N_{on}} \left[ \frac{1}{1 + \alpha} \left( \frac{N_{on} + N_{off}}{N_{off}} \right) \right]^{N_{off}} \quad (4.6)$$

If the null hypothesis is true, and  $N_{on}, N_{off} \gtrsim 10$ , by the theorem exposed in [194], the quantity  $-2\ln\lambda$  will asymptotically follow a  $\chi^2$  distribution with one degree of freedom. Therefore,  $\sqrt{(-2\ln\lambda)}$  is equivalent to the absolute value of a standard normal variable, so we can take it as the significance:

$$S = \sqrt{(-2\ln\lambda)} \quad (4.7)$$

Typically, detection is claimed when the significance  $S$  is equal to or higher than 5 ( $5\sigma$  detection). To calculate the sensitivity of LST1 we will find the number of excess counts over the background from a hypothetical source  $N_S$  that will lead to  $S = 5$ , assuming  $\alpha = 1/5$ , i.e. for  $t_{off}$  5 times longer than  $t_{on}$ . To perform this calculation, we need to estimate the number of background (proton) events ( $N_B = \alpha N_{off}$ ) that will remain after analyzing the data and doing the  $\gamma$ -hadron separation. The steps followed to obtain the final sensitivity are described in the next sections.

### 4.3.1 Reweighting

The MC simulations of Extensive Air Showers (EAS) used for this work follow a power law spectrum:

$$\frac{dN}{dE} = KE^a \quad (4.8)$$

with a spectral index  $a = -2$ . However, we want to give the sensitivity for the true spectrum of protons, and a realistic spectrum of  $\gamma$ -rays, typically, the Crab nebula.

We need to transform the distribution of simulated events from number of events per energy to a rate (events per unit time) per energy which follows the desired spectral shape. To this end, we will calculate a spectral weight  $w(E)$  for each event, which will depend on its true energy.

Suppose that  $N$  MC events have been generated in the energy range  $(E_1, E_2)$ , following the power law from 4.8, with isotropically distributed directions in a solid angle  $\Omega$  and impact parameters uniformly distributed in a circular area  $A$ , orthogonal to the incident direction of the particles. The quantity  $K$  will be:

$$K = \frac{N(a+1)}{E_2^{a+1} - E_1^{a+1}} \quad (4.9)$$

We want to change the shape of this spectrum, and get a new differential spectrum of the shape:

$$\frac{dF}{dE(E)} = \frac{dF}{dE(E_0)} \cdot f(E/E_0) \quad (4.10)$$

Where  $\frac{dF}{dE(E_0)}$  is a normalization factor referring to an arbitrary energy  $E_0$ , which should be between  $E_1$  and  $E_2$ , with units  $s^{-1}sr^{-1}m^{-2}TeV^{-1}$  and  $f$  is a function that satisfies  $f(E = E_0) = 1$ . In our case,  $f$  will simply be the new power law. To correct the  $dN/dE$  simulated spectrum to the desired power law, we should multiply it by  $(E/E_0)^{-a}$ , so it will become flat, and then by  $f(E/E_0)$  to get the correct form. Weighting by these two factors, the corrected number of MC events  $N'$  will be the integral:

$$N' = \int_{E_1}^{E_2} \left( \frac{E}{E_0} \right)^{-a} f(E/E_0) dE = \int_{E_1}^{E_2} KE_0^a f(E/E_0) dE \quad (4.11)$$

We need to transform the number of events to a rate (in Hz), in order to calculate the sensitivity, for a certain observation time. The total rate calculated in the energy range  $E_1, E_2$  will be:

$$R = \int_{E_2}^{E_1} \frac{dF}{dE} dEd\Omega dA \quad (4.12)$$

Therefore, the final weight  $w(E)$  for which the spectrum of each event should be multiplied is:

$$w(E) = \left( \frac{E}{E_0} \right)^{-a} \cdot f(E/E_0) \cdot \frac{N'}{R} \quad (4.13)$$

Where  $a = -2$  is the spectral index of the simulated events,  $E_0$  is taken as 1 TeV and  $f(E/E_0)$  would depend on the spectral shape to be reproduced. For  $\gamma$  events we take the spectrum of the Crab nebula measured by HEGRA [195]:

$$\left(\frac{dF}{dE}\right)_{Crab} = 2.83 \cdot 10^{-14} \left(\frac{E}{1TeV}\right)^{-2.62} GeV^{-1}cm^{-2}s^{-1} \quad (4.14)$$

And for protons, we use the results from the BESS spectrometer [196]:

$$\left(\frac{dF}{dE}\right)_{Crab} = 9.6 \cdot 10^{-9} \left(\frac{E}{1TeV}\right)^{-2.7} GeV^{-1}cm^{-2}s^{-1} \quad (4.15)$$

The values of the differential sensitivity will be given for a certain number of energy bins, therefore, we must calculate the number of weighted events in each energy bin and multiply them by the observation time. This will give us the quantities  $N_S$  and  $N_B$ . To calculate the sensitivity we only need  $N_B$ , which will be the number of weighted proton events divided by the factor  $\alpha = 1/5$ .

### 4.3.2 Cut optimization

To obtain the best possible sensitivity, instead of using all the weighted proton events, we use the two parameters *gammaness* and  $\theta^2$  to perform cuts that will reject the majority of the background.

*Gammaness* is a number between 0 and 1 assigned by the RF classifier to decide on the  $\gamma$ -hadron separation. Events close to 1 will be more  $\gamma$ -like, and events close to 0 will be more proton-like.  $\theta^2$  is the angle between the reconstructed direction of the event and the true assumed direction of the source. Events with a high  $\theta^2$  are most likely to be proton events, while  $\gamma$ s will have a  $\theta^2$  close to 0.

To optimize the cuts in these parameters, we define several bins in *gammaness* and  $\theta^2$ , calculate the number of weighted proton events left after the cuts in each bin, and then use this quantity as  $N_B$  for the sensitivity calculation. For each energy bin, we will select the combination of cuts that provides the best sensitivity. To ensure significant statistics, we require that after the cuts, at least 10 events of  $\gamma$ s and protons remain in the energy bin.

### 4.3.3 Expected LST1 Performance

The analysis methods described before were used to compute the expected performance of the LST1 in mono mode for the observation of a point source. In this section, the results on energy and angular resolution,  $\gamma$ -hadron separation and sensitivity are discussed.

#### Data

The data used for the analysis is a set of MC simulations produced specifically for the LST1 in the northern CTA site. The primaries produced were point-like  $\gamma$ s with an

	$\gamma$ (PS) offset = 0.4°	$\gamma$ diffuse	electron	proton
Energy Range	5 GeV - 50 TeV	5 GeV - 50 TeV	5 GeV - 5 TeV	10 GeV - 100 TeV
Viewcone	0 °	10°	10°	15 °
Core Range	1000 m	1000	1000 m	2500
Input Events	South: $3 \cdot 10^7$ North: $3 \cdot 10^7$	South: $5 \cdot 10^8$ North: $5 \cdot 10^8$	South: $6 \cdot 10^8$ North: $6 \cdot 10^8$	South: $5 \cdot 10^9$ North: $5 \cdot 10^9$
Triggered Events	South: $1.08 \cdot 10^6$ South: $9.60 \cdot 10^5$	South: $1.22 \cdot 10^6$ South: $1.11 \cdot 10^6$	South: $1.18 \cdot 10^6$ South: $1.04 \cdot 10^6$	South: $8.25 \cdot 10^5$ South: $8.10 \cdot 10^5$

Table 4.1: Summary of the MC production dedicated to the LST1

offset of 0.4° from the center of the camera, diffuse  $\gamma$ s, electrons <sup>1</sup>, and protons. The generation of particles was split in the North and South direction. The zenith angle was 20°, the spectral index of the particle spectra was -2. A summary of the main characteristics of the production is given in table 4.1.

After calibrating and parameterizing the data, using three sets of cleaning parameters to study the effect on cleaning in the analysis, the diffuse  $\gamma$  events were used to train the RF regressors. Then, a subset of diffuse  $\gamma$ s and proton events to which the energy and direction were reconstructed, were used to train the RF classifier for  $\gamma$ -hadron separation. The point source  $\gamma$ s, together with a subset of proton events as background, have been used to produce the performance results. Cuts in intensity  $> 300$  phe, leakage2  $< 0.2$ , width/length  $> 0.1$  and gammaness  $> 0.5$  were applied to the reconstructed events, to avoid bad reconstructions of Hillas parameters.

### Energy resolution

The energy resolution gives information on the error in the reconstruction of the energy. It is defined as the 68th percentile of the relative error  $\Delta E/E = (E_{reco} - E_{true})/E_{true}$ . If the relative error follows a normal distribution, the 68th percentile is equivalent to one  $\sigma$ . The results on energy resolution are shown in figure 4.1. The features used for the energy regression ordered by their importance can be seen in figure E.1.

### Angular resolution

The angular resolution is calculated similarly to the energy resolution, but in this case the relative error shown in figure 4.2 refers to the angular difference between the true direction of the source and the reconstructed direction. As can be seen in the left plot from figure 4.2, the majority of gamma events concentrate in low  $\theta^2$  angles, therefore, making cuts in this angle allows to discard background events. The features used for the disp vector regression ordered by their importance can be seen in figure E.1.

---

<sup>1</sup>Electrons are not included in the results presented in this thesis

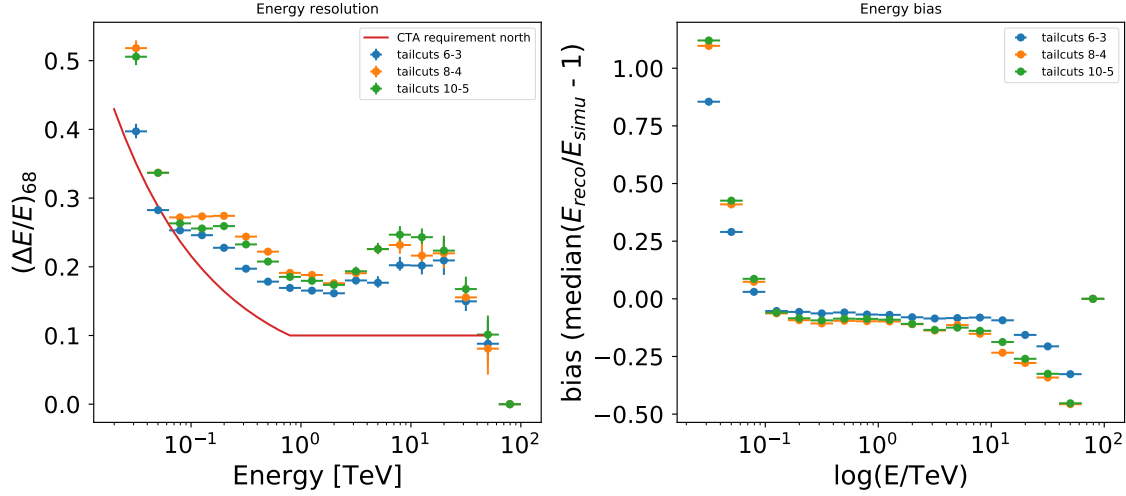


Figure 4.1: Energy resolution for the LST1 analysis applied to a MC production of point-like  $\gamma$  events, for three different sets of cleaning parameters (low level-high level threshold in number of photoelectrons). As a reference, the energy resolution requirement for CTA-north array is also shown. The energy resolution plot of the *left* has been bias corrected.

### $\gamma$ -hadron separation

The performance in  $\gamma$ -hadron separation can be studied in terms of the receiver operating characteristic (ROC) curve of the RF classifier. The ROC curve illustrates the diagnostic ability of a binary classifier as its discrimination threshold is varied. It is produced plotting the true positive rate (the rate of  $\gamma$ s correctly classified) versus the false positive rate (the rate of protons incorrectly classified as  $\gamma$ s) at several thresholds in gammaness. A value of 1 in true positive rate, while 0 in the false positive rate would mean a perfect classification. The closest of the ROC curve to a diagonal line, the more similar to a uniformly random distribution is the classification. For this result, shown in figure 4.3, a subset of protons was used to test the RF classifier together with the point-like  $\gamma$ s. The features used for the  $\gamma$ /hadron classification ordered by their importance can be seen in figure E.1.

### Sensitivity

For the calculation of the sensitivity, a subset of proton events was used as background (off) events. Apart from the general cuts in intensity, width/length and leakage<sup>2</sup> mentioned above, cuts in gammaness and  $\theta^2$  were optimized to calculate the sensitivity. Subsets of point-like  $\gamma$  and proton events were used to calculate the cuts in gammaness and  $\theta^2$  which provided the best sensitivity in each of the 20 energy bins taken. The sensitivity was calculated for 10 cuts in gammaness and 10 in  $\theta^2$  for each energy bin. The combination of cuts giving the lower sensitivity value, keeping a minimum of 10  $\gamma$  and proton events in the bin (both before and after re-weighting), was selected.

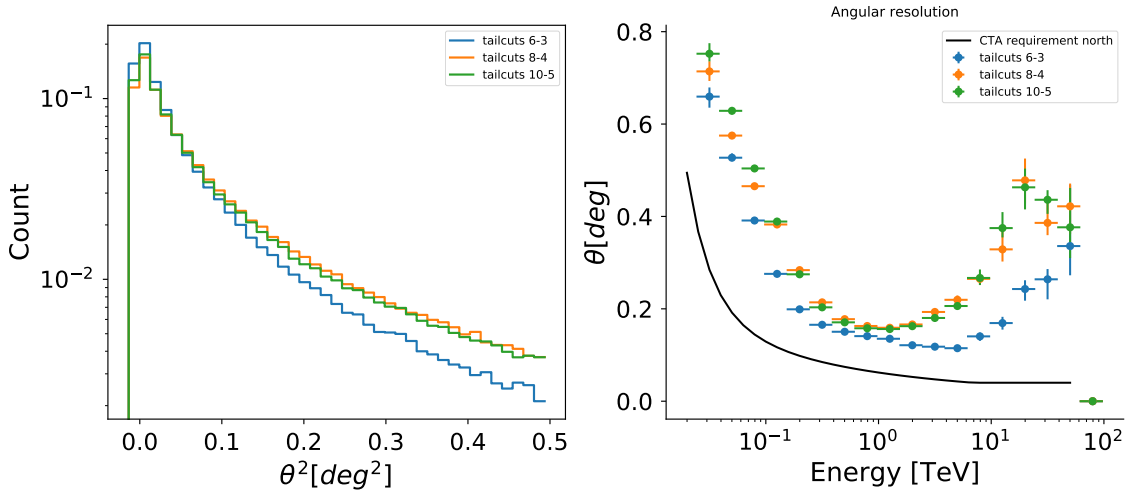


Figure 4.2: *Left:*  $\theta^2$  plot for the MC simulated  $\gamma$  point-like events, using three sets of cleaning parameters. *Right:* Angular resolution as a function of reconstructed energy.

The resulting sensitivity was then calculated for a different subset of  $\gamma$ s and protons, applying the selected cuts. The sensitivity curve is shown in picture 4.4.

## 4.4 Expectation-Maximization method for Hillas Parameters calculation without cleaning

As explained in section 4.2.2, cleaning methods often require the empirical adjustment of some parameters, to find a balance between a good enough background suppression without losing too much information from the shower. The cleaning parameters affect particularly the analysis of low energy showers. In the tailcuts method, too strong cleaning thresholds tend to eliminate many pixels of the already small low energy showers, making the task of  $\gamma$ -hadron separation much more difficult. Also, losing the ellipse shape of  $\gamma$  showers lead to wrong calculation of Hillas parameters and consequently of the disp vector.

For all these reasons, to research for new analysis methods which could improve the performance of LST, a method for image parameterization which does not require a previous cleaning has been developed in the scope of this thesis. It is based on the EM algorithm, where the light content in each pixel is recursively assigned to be part of the shower or the background. In the next sections, the basic concepts of the EM method and how it can be applied to images of showers will be summarized. Then some results comparing the EM with the classic cleaning method will be discussed.

### 4.4.1 The Expectation-Maximization algorithm

The EM algorithm [197] is an iterative method for calculating maximum likelihood estimates of model parameters, where the model depends on unobserved data or

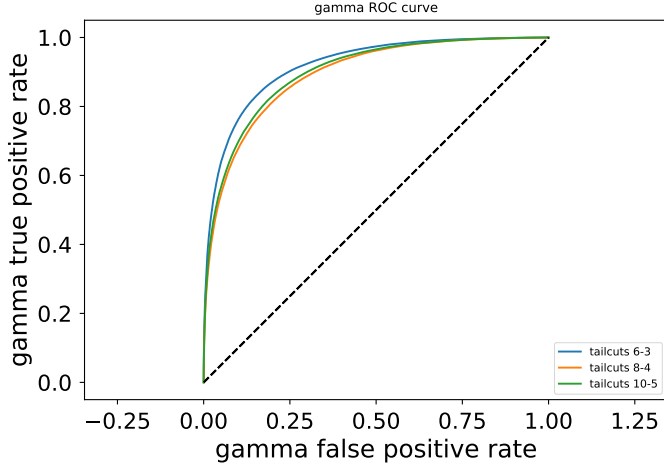


Figure 4.3: ROC curve of the RF classifier applied to point-like gamma and diffuse proton events, for three different sets of cleaning parameters.

latent variables. These latent variables would be those that cannot be observed in the data set but still can influence other random variables. The algorithm will iterate until finding the model parameters and hidden variables that converge to a maximum likelihood estimation.

Given a statistical model which has generated a set of  $X$  observed data points, which depends on a set of latent variables  $Z$  and unknown parameters  $\theta$ , the basic iteration of the EM consist on two steps:

- **Expectation:** Creates an expectation function  $Q(\theta|\theta^{(t)})$ , which is the evaluation of the log-likelihood with the current estimate of the model parameters  $\theta^{(t)}$ , meaning it calculates the latent variables  $Z$ .

$$Q(\theta|\theta^{(t)}) = E_{Z|X,\theta^{(t)}} \quad (4.16)$$

- **Maximization:** Maximizes the log-likelihood function found in the previous step to find a new set of estimated parameters.

$$\theta^{(t+1)} = \operatorname{argmax} Q(\theta|\theta^{(t)}) \quad (4.17)$$

A common problem that has been successfully solved by the EM algorithm is the mixture models problem, where there is a set of data produced by several density distribution functions, but it is impossible to know which distribution has produced each data point. This distinction between distributions would be the latent variable. This is the particular case we face with shower images. We have a distribution of light in the pixels of the camera, and we know that some photoelectrons come from Cherenkov light, and others belong to fluctuations in the NSB. We want to know the fraction of light in each pixel which belongs to each of the distributions. We assume that the Cherenkov light will follow a bi-dimensional Gaussian distribution

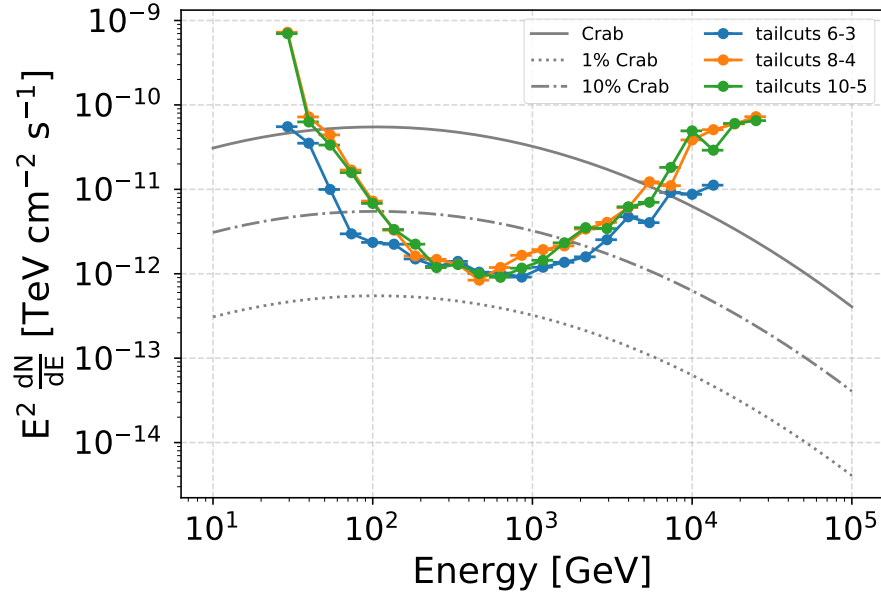


Figure 4.4: Sensitivity plot for 50h of observation of a point-like  $\gamma$ -ray source with a Crab-like spectrum, obtained by selecting the cuts in gammaness and  $\theta^2$  which provided the best differential sensitivity per energy bin. As a reference, the spectra of Crab, 10% of Crab and 1 % of Crab flux are shown.

which produces the typical elliptical shape in the image, and the background is simply a two-dimensional constant distribution. The parameters of the model will be the usual Gaussian parameters (mean and standard deviation in two dimensions)  $\{x_0, y_0, \sigma_{xx}, \sigma_{yy}, \sigma_{xy}\}$  and the latent variables will be the fraction of photoelectrons from the Cherenkov shower  $n_{Ch}/n$  and from the background  $n_{bkg}/n$  in each pixel with  $n$  total photoelectrons. The number of photoelectrons belonging to each distribution is:

$$N_i = \sum_{pixels} P(pixel/i) \cdot N \quad (4.18)$$

Where  $N_i$  is the number of photoelectrons produced by the distribution  $i$  (Cherenkov or background),  $N$  is the total number of photoelectrons in the image and  $P(pixel/i)$  is the probability of a photoelectron in the pixel to have been produced by the distribution  $i$ .

Using the Bayes theorem:

$$P(pixel/i) = \frac{P_i(pixel) \cdot P_i}{P(pixel)} \quad (4.19)$$

Where  $P_i(pixel)$  is the probability of a photoelectron produced by the distribution  $i$  to fall in the pixel,  $P_i$  is the probability of a photoelectron to be produced by the

distribution  $i$  and  $P(pixel)$  is the probability of a photoelectron to fall in the pixel. This last probability will actually be:

$$P(pixel) = \sum_i P_i \cdot P_i(pixel) \quad (4.20)$$

Where probabilities  $P_i = (P_{Ch}, P_{Bkg})$  are equal to the fraction of photoelectrons in the image belonging to the shower(background) with respect to the total number of photoelectrons. The probabilities  $P_i(pixel)$  can be written as:

$$\begin{aligned} P_{Ch}(pixel) &= BiGaus(x_0, y_0, \sigma_{xx}, \sigma_{yy}, \sigma_{xy}) \cdot A_{pixel} \\ P_{bkg}(pixel) &= A_{pixel}/A_{total} \end{aligned} \quad (4.21)$$

Where  $A_{pixel}$  is the area of the pixel and  $A_{total}$  the sum of the areas of all pixels. The loop in the EM to solve this problem will go as follows:

1. An initial assumption of the Gaussian parameters is made. Because the bi-dimensional Gaussian corresponds to the Hillas ellipse, the means of the distribution will coincide with the center of gravity of the ellipse, which will be close to the pixel with the larger number of photoelectrons. To avoid choosing an outlier pixel, we take the initial means of the Gaussian ( $x_0, y_0$ ) as the coordinates of the barycenter of the three more luminous pixels. The initial values of the standard deviations are set to arbitrary high values  $\sigma_{xx} = 20000$  mm,  $\sigma_{yy} = 20000$  mm,  $\sigma_{xy} = 0$  mm. Also we assume an initial estimation of the fraction of the light belonging to the shower and background as 50% of the total number of photoelectrons for each.
2. *Expectation:* Using the previous estimation of Gaussian parameters and fractions, equation 4.19 is solved and the new distributions of the shower and the background are obtained. For each pixel, the number of photoelectrons belonging to the shower and the background is calculated.
3. *Maximization:* Using the distributions from previous steps, the parameters of the bi-dimensional Gaussian are calculated, and also the fraction of the total photoelectrons produced by each distribution (which is simply the sum of all shower and background pixels content respectively). The new Gaussian

parameters will be:

$$\begin{aligned}
 mean_x &= \frac{1}{N} \sum_{pixels} n_{Ch} x_{pix} \\
 mean_y &= \frac{1}{N} \sum_{pixels} n_{Ch} y_{pix} \\
 \sigma_{xx} &= \frac{1}{N} \sum_{pixels} n_{Ch} x_{pix}^2 - mean_x^2 \\
 \sigma_{yy} &= \frac{1}{N} \sum_{pixels} n_{Ch} y_{pix}^2 - mean_y^2 \\
 \sigma_{xy} &= \frac{1}{N} \sum_{pixels} n_{Ch} x_{pix}^2 y_{pix}^2 - mean_x mean_y
 \end{aligned} \tag{4.22}$$

4. Steps 2 and 3 are repeated until convergence.

Once the loop has ended, the parameters of the resulting Gaussian distribution are used to calculate the Hillas parameters as the first ( $x, y, r$ ), second (width, length,  $\phi, \psi$ ) and third order (skewness, kurtosis) moments of the distribution. The intensity (number of photoelectrons) of the shower, is simply the sum of the photoelectrons assigned to the Gaussian distribution by the algorithm.

#### 4.4.2 Comparison of EM without cleaning and tailcuts cleaning

The EM method was used to calculate the Hillas parameters of the MC production described in section 4.3.3. These parameters were used to train a new set of RFs to perform the energy and direction reconstruction and the  $\gamma$ -hadron classification. The results obtained with EM have been compared to those obtained applying a two-level tailcuts cleaning (6-3) before image parameterization as of the one used in section 4.3.3. In this case, the RFs, both for EM and tailcuts were trained without including the intercept parameter (see list of features in E.3.2). The reason is that by the time this section was written, this parameter was ruled out as a valid training feature in *cta-lstchain* because there were reasons to believe it was strongly biasing the RFs results. Therefore, the performance results shown in this section regarding the tailcuts method slightly differ from the ones of section 4.3.3.

In this section, results on energy resolution, angular resolution, and  $\gamma$ -hadron separation are shown comparing the two methods, with different cuts in intensity. Cuts in gammaness  $> 0.6$  (except to produce ROC curves, where no cut in gammaness is applied), leakage  $< 0.2$ , and width/length  $> 0.1$  were also applied to the reconstructed events.

From figures 4.5 and 4.6, it appears that the performance of the EM method is worse than the tailcuts for the majority of the energy range, except for the lower

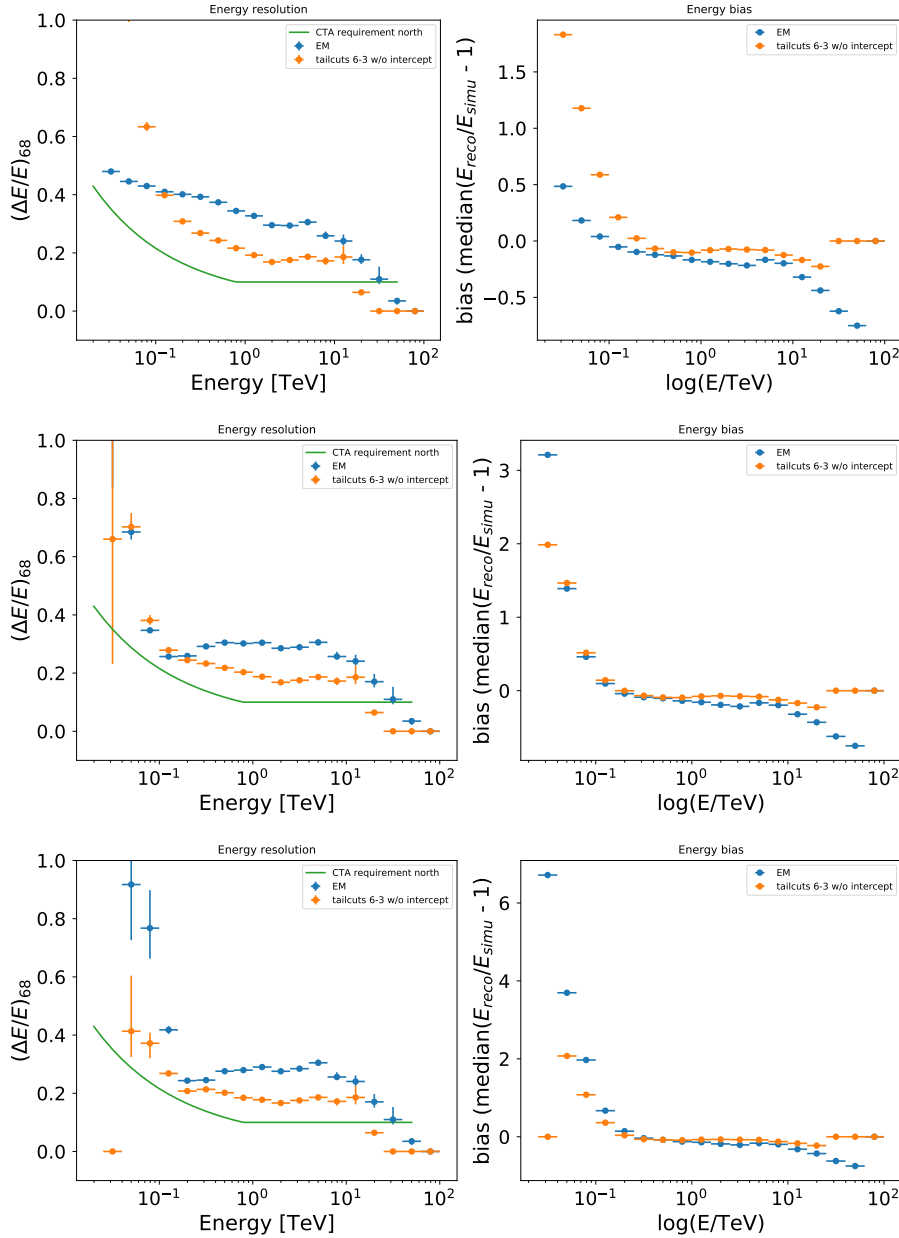


Figure 4.5: Energy resolution plots for cuts in intensity  $> 100$  phe (*top*),  $> 500$  phe (*middle*) and  $> 1000$  phe (*bottom*) comparing the EM method for Hillas parameterization and the tailcuts cleaning method.

energy bins when a small cut in intensity ( $> 100$ ) is applied. This supports the hypothesis that the tailcuts cleaning tends to lose information from showers with a low number of photoelectrons, while EM preserves the information of the full image. Despite these results, it is interesting to observe how according to the ROC curves in figure 4.7, the EM seems to perform a better classification than the tailcuts cleaning.

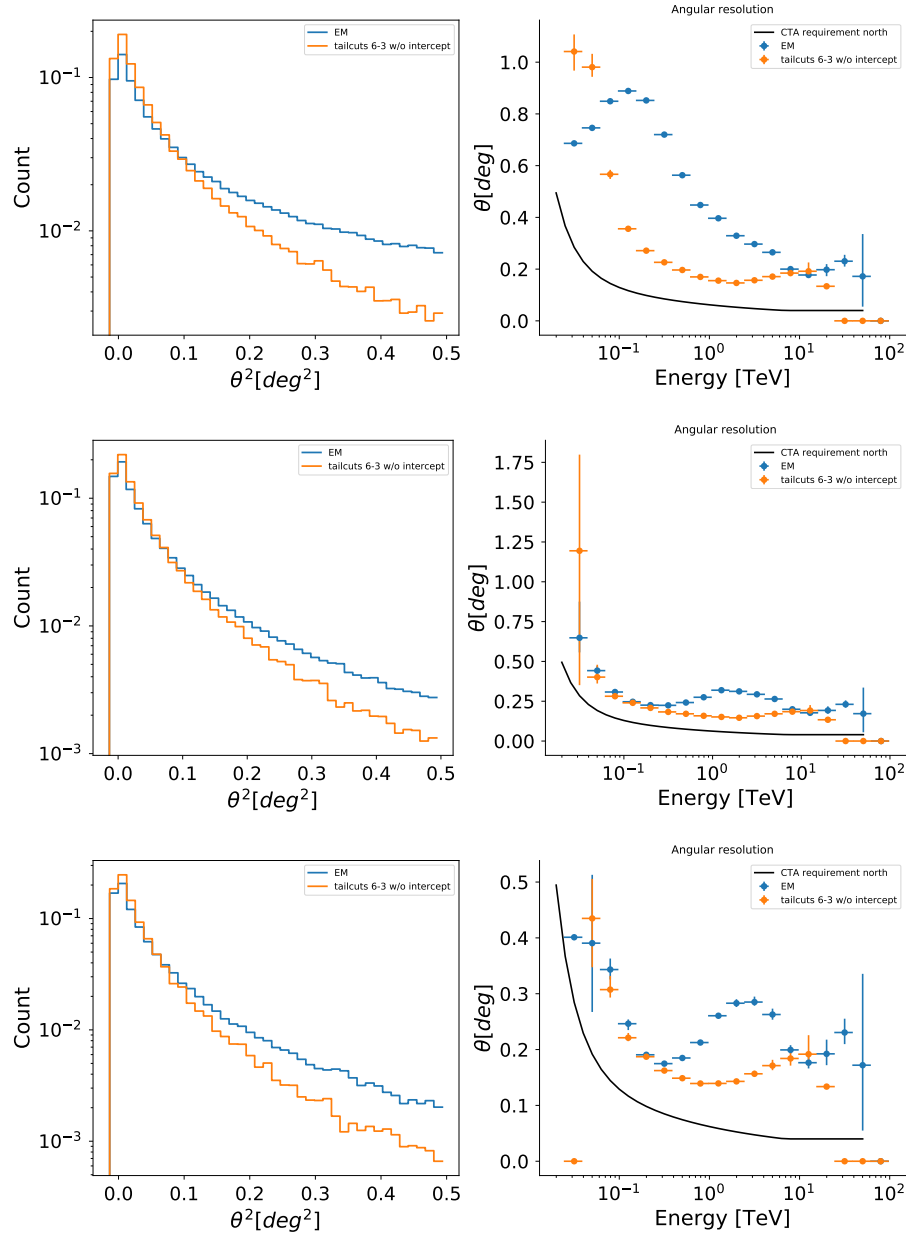


Figure 4.6: Angular resolution plots for cuts in intensity  $> 100$  phe (*top*),  $> 500$  phe (*middle*) and  $> 1000$  phe (*bottom*) comparing the EM method for Hillas parameterization and the tailcuts cleaning method.

Further discussion on this issue, which shows interesting results when applying the method to real data, is given in section 4.5.1.

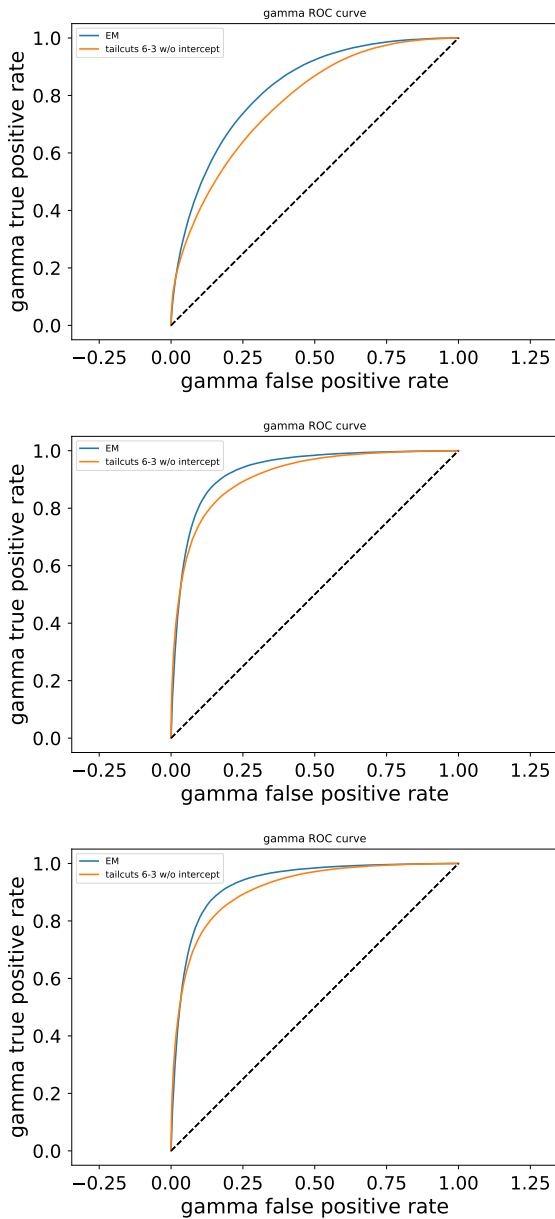


Figure 4.7: ROC curves for cuts in intensity  $> 100$  phe (*top*),  $> 500$  phe (*middle*) and  $> 1000$  phe (*bottom*) comparing the EM method for Hillas parameterization and the tailcuts cleaning method.

## 4.5 Results on real data

Since the beginning of the commissioning of the telescope, three Crab data taking campaigns have been carried on, where the Crab nebula has been observed with the LST1 during several nights, to test the performance of the whole instrument and the analysis tools.

In this section the data taken during the three Crab campaigns have been analyzed following the methods described in previous sections, deriving the final detection significance of the Crab over the total observation time of each campaign, after applying different cuts in intensity and gammaness. Telescope data is taken in several runs of a certain duration, where events are recorded and stored in fits files. Each night, four kinds of runs are taken: DRS4 calibration runs (for pedestal subtraction), camera calibration runs (see section 4.2.1) and data runs of two types: on and off runs. Data on runs are taken pointing with the telescope to the  $\gamma$ -ray source, in this case the Crab nebula. Off runs are taken pointing to a region without a  $\gamma$ -ray sources, where the Cosmic Ray (CR) background is similar to that of the on region, to extract the signal events as an excess over the background in the on.

The data runs have been calibrated and parameterized using *cta-lstchain* following the steps described in section 4.2. The signal extractor used has been the *GlobalPeak-WindowSum* and the cleaning method applied is a two-level tailcuts with  $Th_{high} = 6$  phe and  $T_{low} = 3$  phe. The RF models for energy and direction reconstruction, and  $\gamma$ /hadron separation have been trained with MC data, as described in sections 4.2.3 and 4.2.4, and applied to the on and off data for reconstruction to DL2 data level. The intercept parameter was not included among the RF features. Quality cuts in leakage  $< 0.2$  and width/length  $> 0.1$  were applied, while cuts in intensity and gammaness have been optimized to obtain the best results.

In the on region, close to the source position, an excess of events should be observed compared to the background. At further distances, the rate of events should be comparable to that of the off region, where there are only background events. The number of background events  $N_{bkg}$  in the on region can be estimated as  $N_{off}$  multiplied by a normalization factor <sup>2</sup>,  $n = N_{on}/N_{off}$  calculated at a large distance from the assumed source position (the center of the camera), which accounts for the difference in observation time of the two regions. The significance of the excess in the on region is calculated using the Li&Ma formula [194], [198] (see also section 4.3):

$$S = \sqrt{2} \left( N_{on} \cdot \ln \left( \frac{(1+n)N_{on}}{n(N_{on} + N_{off})} \right) + N_{off} \cdot \ln \left( \frac{(1+n)N_{off}}{N_{on} + N_{off}} \right) \right)^{1/2} \quad (4.23)$$

The normalization factor  $n$  has been calculated using the  $\alpha$  angle, which is defined as:

$$\alpha = \arccos \left( \frac{X_{c.o.g.} \cos(\psi) + Y_{c.o.g.} \sin(\psi)}{X_{c.o.g.}^2 + Y_{c.o.g.}^2} \right) \quad (4.24)$$

Where  $X_{c.o.g.}$  and  $Y_{c.o.g.}$  are the coordinates of the center of gravity of the Hillas ellipse of the shower image, and angle  $\psi$  is the angle between the semi-major axis

---

<sup>2</sup>This factor  $n$  is equivalent to the factor  $\alpha$  of section 4.3. In the present section the name has been changed to not be confused with the  $\alpha$  angle, described below.

of the ellipse and the line between the center of the camera and the centroid of the ellipse. The  $\alpha$  angle is a measure of how deviated is the Hillas ellipse from pointing towards the center of the camera. Events with a high  $\alpha$  angle are more likely to be background events, whereas  $\gamma$  events will point towards the same position, close to the center, having small  $\alpha$  angles. To estimate the background normalization factor  $n$ , events with  $\alpha$  angle between  $20^\circ$  and  $70^\circ$  have been used. To calculate the excess signal and sensitivity, a cut in  $\alpha < 8^\circ$  is applied.

The rate of  $\gamma$  events (number of events per minute) can be calculated dividing the number of excess events  $N_{ex} = N_{on} - nN_{off}$  by the total observation time.

The  $\alpha$  plots of the three campaigns are shown in pictures 4.12, 4.13 and 4.14, for different cuts in intensity and gammaness, to show the effect of these cuts in the significance. For the first Crab campaign, the best cuts of intensity  $> 1000$  and gammaness  $> 0.6$  resulted in a significance of  $24.38\sigma$  in 4.5 h of total observation time. For the second Crab campaign the best cuts were intensity  $> 500$  and gammaness  $> 0.6$ , giving a total significance of  $22.31\sigma$  for 7.8h of observation. The same cuts for the third Crab campaign resulted in a significance of  $15.48\sigma$  for 6.1 h of observation. During the commissioning of the telescope, several tests are performed in all the subsystems, along with updates and changes in the configuration. These activities affect the performance, making it very variable throughout the different observation nights. For that reason, it is necessary to keep track of how the performance varies from one campaign to the next. In picture 4.8 the evolution of the significance with the square root of observation time along the three campaigns can be observed. This result will be compared with the future data taking campaigns, to characterize the stability of the telescope in the commissioning phase.

#### **4.5.1 Analysis of Crab Campaigns with Expectation-Maximization method for Hillas Parameterization**

The data from the full three Crab campaigns was reduced from R0 to DL2 data level using the EM method to calculate the Hillas parameters, without applying a tailcuts cleaning to the shower images. To reconstruct the energy and direction of the primaries, and to perform the  $\gamma$ -hadron separation the RFs trained for section 4.4.2 were used. The alpha plots, computed using the same approach as described in section 4.5, for the three campaigns are shown in pictures 4.15, 4.16 and 4.17, for different cuts in gammaness and intensity.

Note that for the EM parameterized data, the higher significance is reached with a lower cut in intensity than for the tailcuts cleaning based analysis (intensity  $> 100$ ). As can be seen in picture 4.9, the majority of showers have an intensity value between 100 and 1000 photoelectrons. A cut in intensity  $> 500$ , or 1000 photoelectrons, which is required to obtain the maximum sensitivity when applying the tailcuts cleaning (see pictures 4.12, 4.13 and 4.14), suppose to discard a huge number of recorded events. Because intensity and energy are directly related, those discarded events correspond to the lower energies.

To understand this difference in the optimum intensity cuts, it is necessary to study

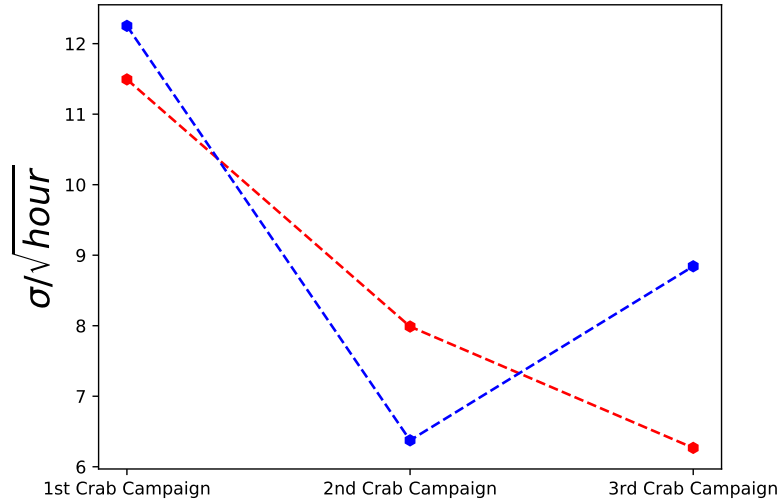


Figure 4.8: Evolution of the maximum significance per square root of time during the three Crab Campaigns. The red line shows the evolution when parameterizing the data applying a tailcuts cleaning, while the red line shows the significance obtained when using the EM method. Note that for each campaign, the maximum significance has been obtained applying different cuts in intensity and gammaness, as described in sections 4.5 and 4.5.1.

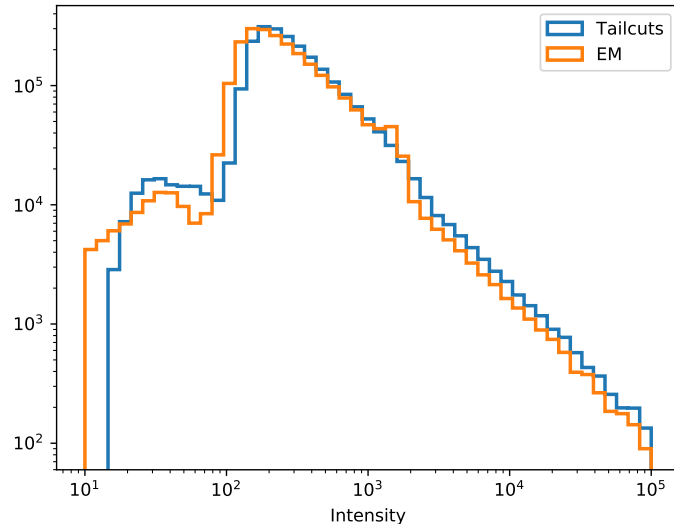


Figure 4.9: Distribution of intensity of the showers for a subset of real data events, reduced using the EM method (orange), and applying the tailcuts cleaning (blue).

how the parameterization performed with both methods is affecting the  $\gamma$ -hadron classification of the showers. The gammaness distributions of a set of MC  $\gamma$  and proton events, which were produced applying the tailcuts cleaning and the EM method are shown in figure 4.10, for two cuts in intensity (100 and 500 photoelectrons). The EM tends, in general, to give higher values of gammaness to  $\gamma$  events, even for low intensities, while when applying the tailcuts cleaning, the majority of events are classified with low values of gammaness. In figure 4.7, the ROC curves showed that the classification of the EM is better for any cut in intensity. The EM recovers a big number of  $\gamma$  events which would be classified as protons when applying the tailcuts cleaning. In figure 4.11, the fraction of the total of  $\gamma$  and proton events that are left after different cuts in gammaness are shown for the EM and tailcuts method. For a cut in intensity  $>100$  and gammaness of 0.7 (which are the optimum cuts in real data for the EM method), close to a 40% more of true  $\gamma$  events would be correctly classified as  $\gamma$ s with the EM. On the other hand, because the EM tends to assign higher values of gammaness also to proton events, the number of protons that survive the cut contributing to the background raises in a 10%. This explains the higher number of events, and higher rates in the  $\alpha$  plots computed with the EM, in comparison with the tailcuts cleaning method.

The EM recovers a large number of  $\gamma$  events that do not survive the gammaness cut when using the tailcuts method, but on the other hand, keeps a larger background of hadron events. These two effects seem to compensate in the end, resulting in a similar final significance, but lowering the intensity cut and therefore, preserving more low energy events. Keeping low energy events still having a good background rejection is fundamental to lower the energy threshold of LST1 in single telescope mode. The EM method has proven to be a potential tool to accomplish this task and its refinement and a better understanding of its effect in the reconstruction can suppose an improvement in the performance of the telescope during its commissioning phase.

## 4.6 Summary and conclusion

In this chapter, the chain for the single telescope data analysis of LST1 has been described, and successfully applied to MC simulated events, to compute the performance of the LST1. Also, it has been used to analyze the first real data taken with the instrument, obtaining the detection significance of the Crab Nebula for the three data taking campaigns carried on up to the date this thesis is being written.

About the performance estimated using MC simulations, it has been shown that the energy resolution reaches an error as low as 20% in the range from  $\sim 100$  GeV to a few TeV and the angular resolution in the same energy range is  $\sim 0.2^\circ$ . From the three sets for tailcuts parameters, the one giving the best results has been the 6-3 tailcuts. The best sensitivity of LST1 for 50 hours of observation is reached in the range between 100 GeV and 1 TeV, going below the 10% of the Crab flux.

Regarding real data, the analysis chain designed for LST1 has been successfully applied

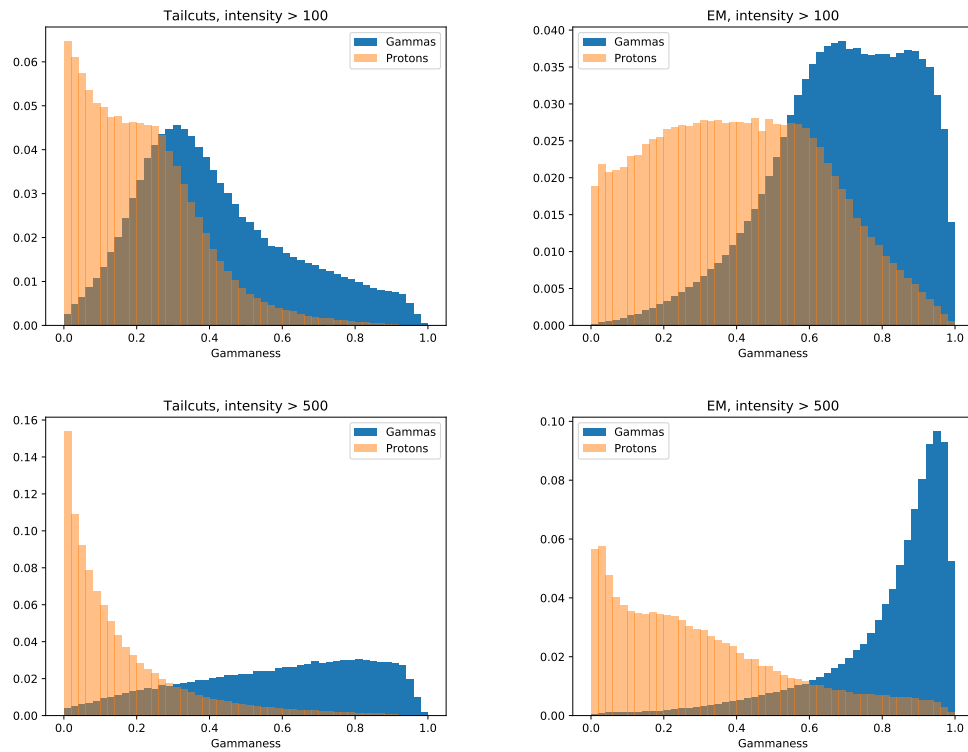


Figure 4.10: Gammaness distribution (normalized) of a subset of MC *gamma* and proton events, parameterized after applying a tailcuts method (*left*) and with the EM method without cleaning (*right*, with cuts in intensity  $> 100$  (*top*) and  $> 500$  (*bottom*) photoelectrons.

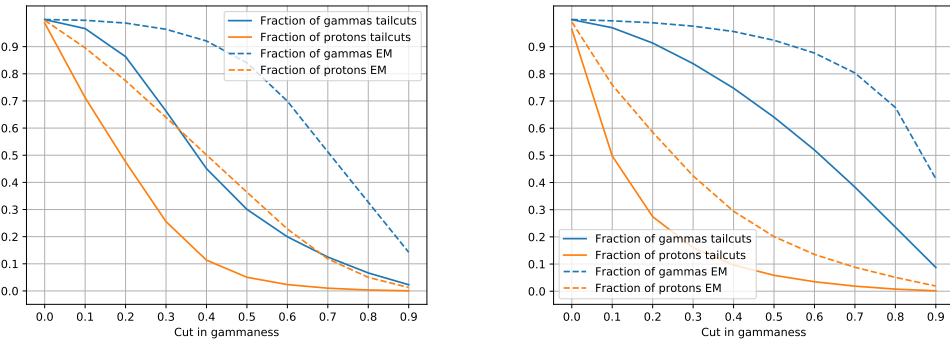


Figure 4.11: Fraction of  $\gamma$  and proton events that would be left after making different cuts in gammaness (x axis) for a cut in intensity  $> 100$  phe (*left*) and  $> 500$  phe (*right*). That is the fraction that would be classified as  $\gamma$  events. Continuous line refers to the events reduced with the tailcuts cleaning, while dashed line represent events reduced using the EM method for Hillas parameterization.

to the three Crab campaigns where Crab nebula data has been taken using the LST1 between November 2019 and February 2020. The code has allowed to reconstruct the recorded events and to calculate the significance of detection of the source in terms of the  $\alpha$  angle.

The EM method has been presented as a potential alternative for Hillas parameterization without applying a cleaning to the shower images, which avoids the necessity of adjusting the cleaning parameters. While the performance in energy and angular resolution was not as good as with the tailcuts cleaning method when compared in the same conditions, it offered an interesting result for the  $\gamma$ -hadron classification, especially improving the classification of low energy/low intensity showers. This method has also been applied to the data of the three Crab campaigns, finding a similar significance as for the tailcuts method, but allowing to keep lower intensity showers. This result implies that the EM would be more efficient in classifying low energy showers, being a potential tool to lower the energy threshold of the telescope. Further investigation of this issue, retrieving the spectral information of the recorded data would be the next step to validate the method to improve the telescope performance in a wider energy range.

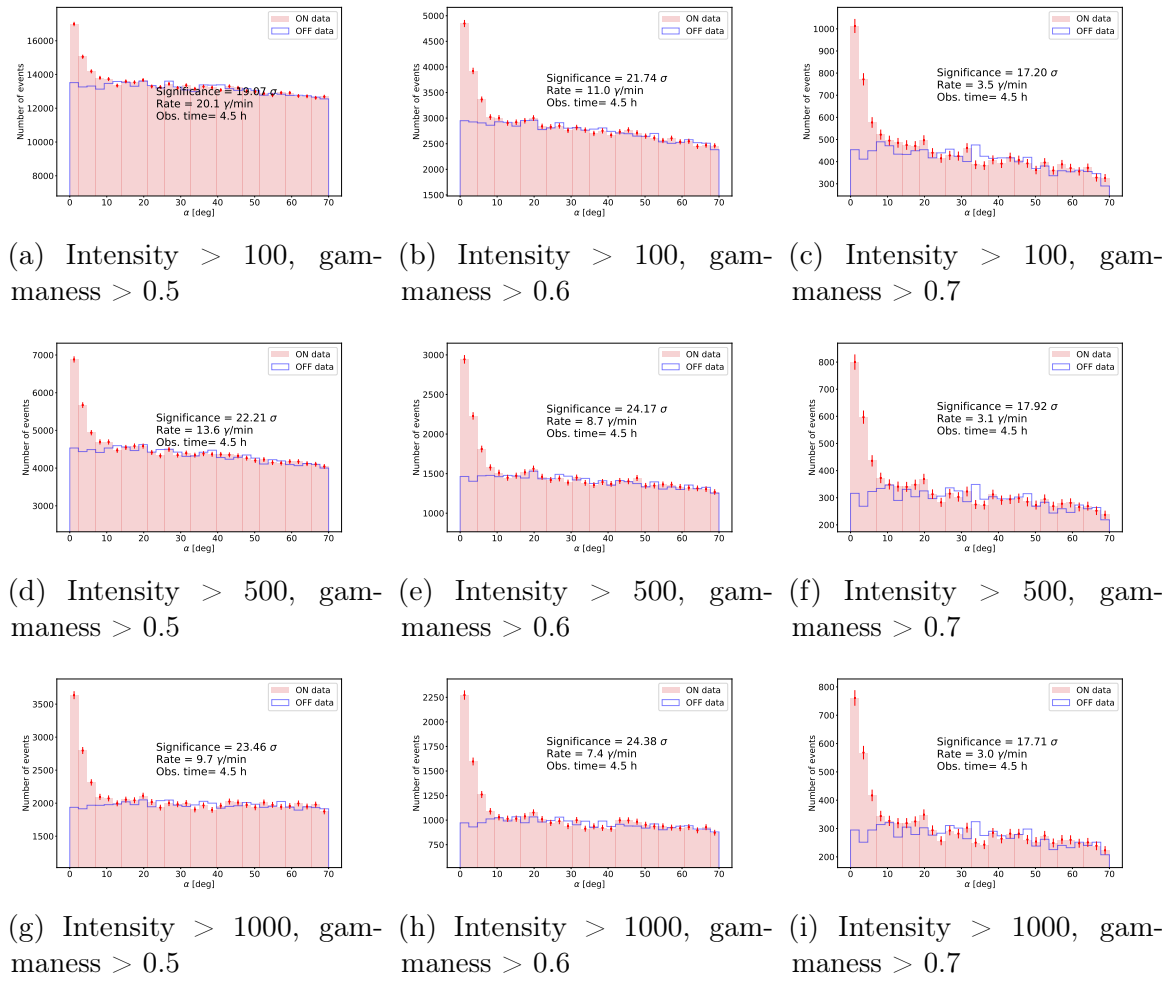


Figure 4.12: Results of  $\alpha$  plot of the First Crab Campaign of LST for different cuts in intensity and gammaness. In each plot the reached significance is shown, defined as explained in section 4.5, together with the rate of  $\gamma$ s per minute and the total observation time.

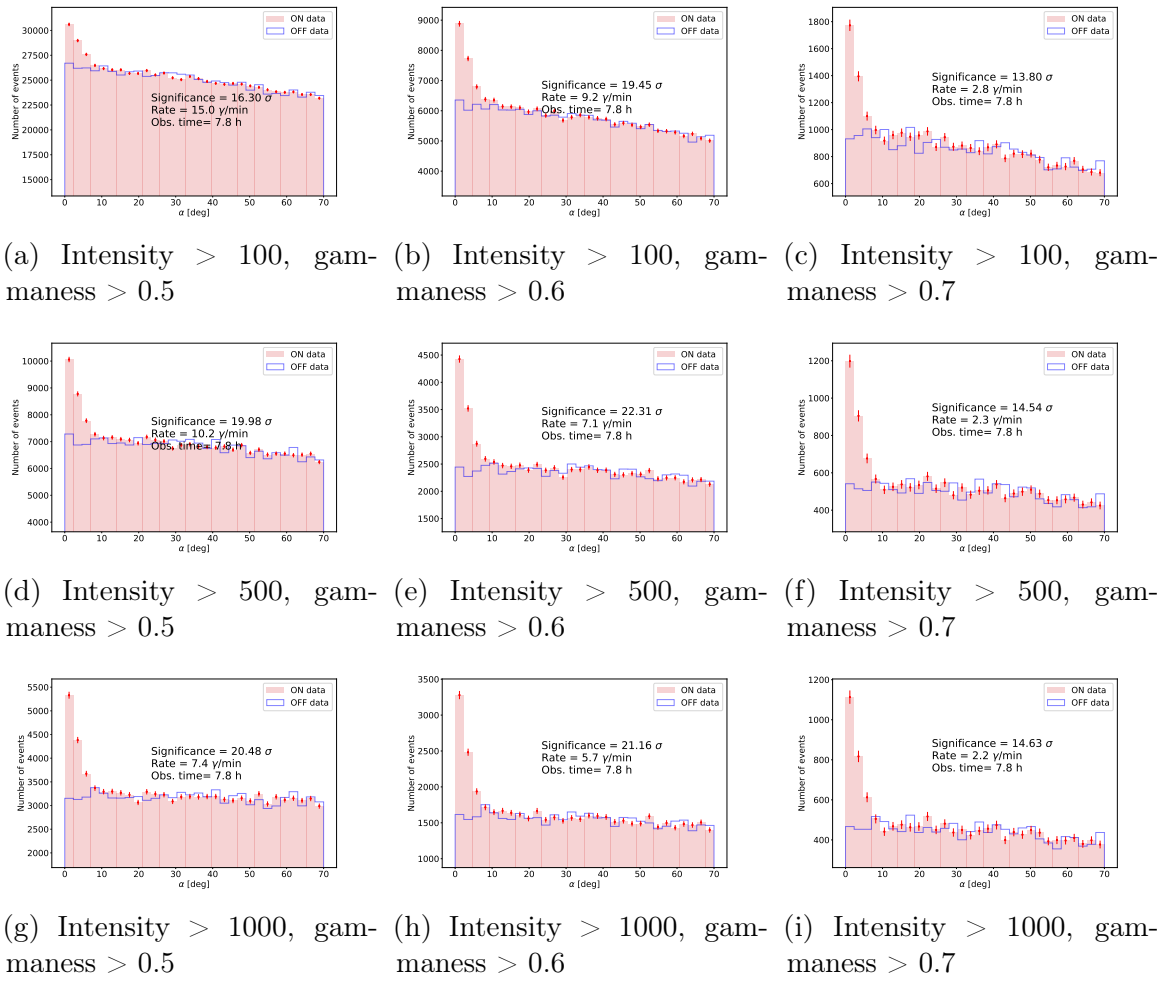


Figure 4.13: Results of  $\alpha$  plot of the Second Crab Campaign of LST for different cuts in intensity and gammaness. In each plot the reached significance is shown, defined as explained in section 4.5, together with the rate of  $\gamma$ s per minute and the total observation time.

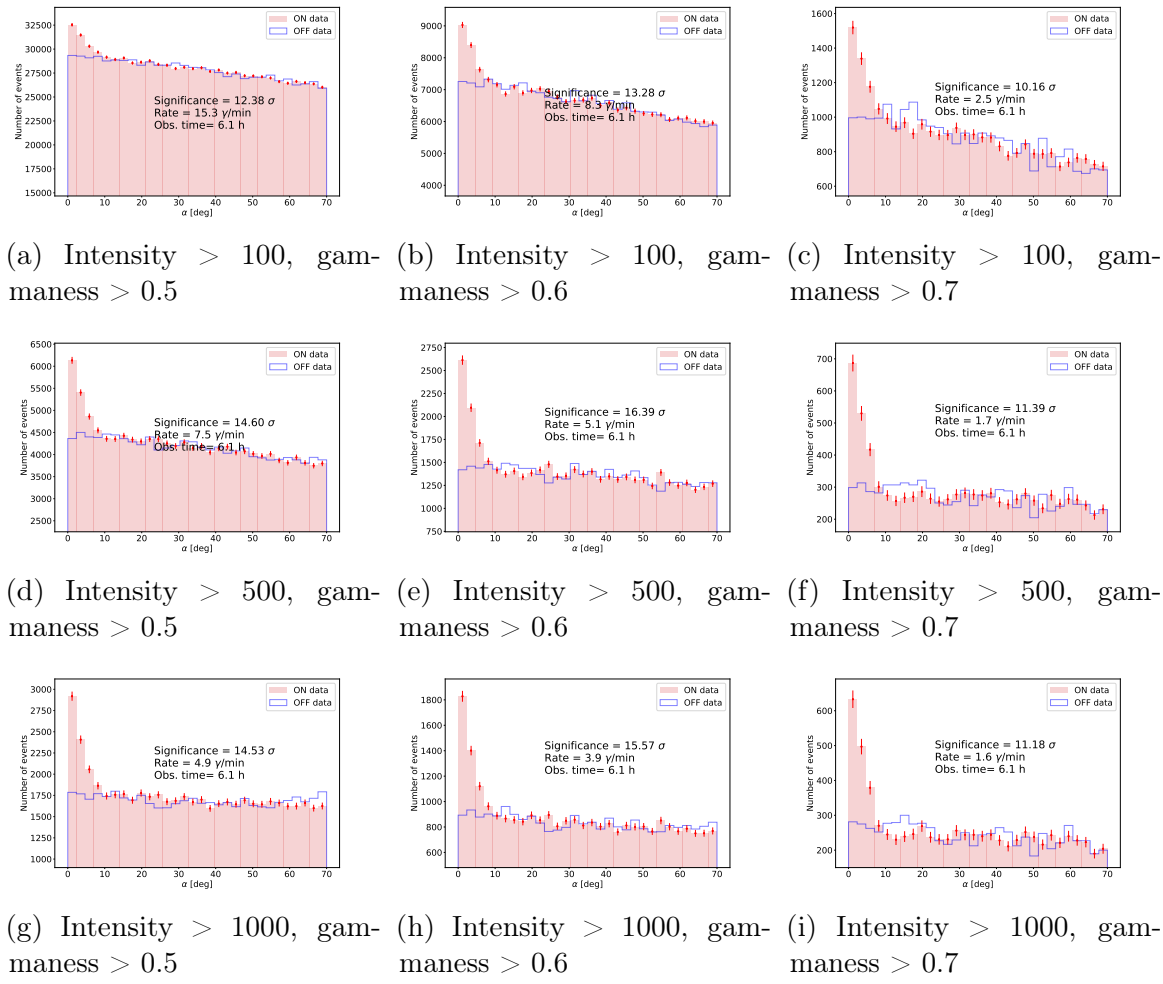


Figure 4.14: Results of  $\alpha$  plot of the Third Crab Campaign of LST for different cuts in intensity and gammaness. In each plot the reached significance is shown, defined as explained in section 4.5, together with the rate of  $\gamma$ s per minute and the total observation time.

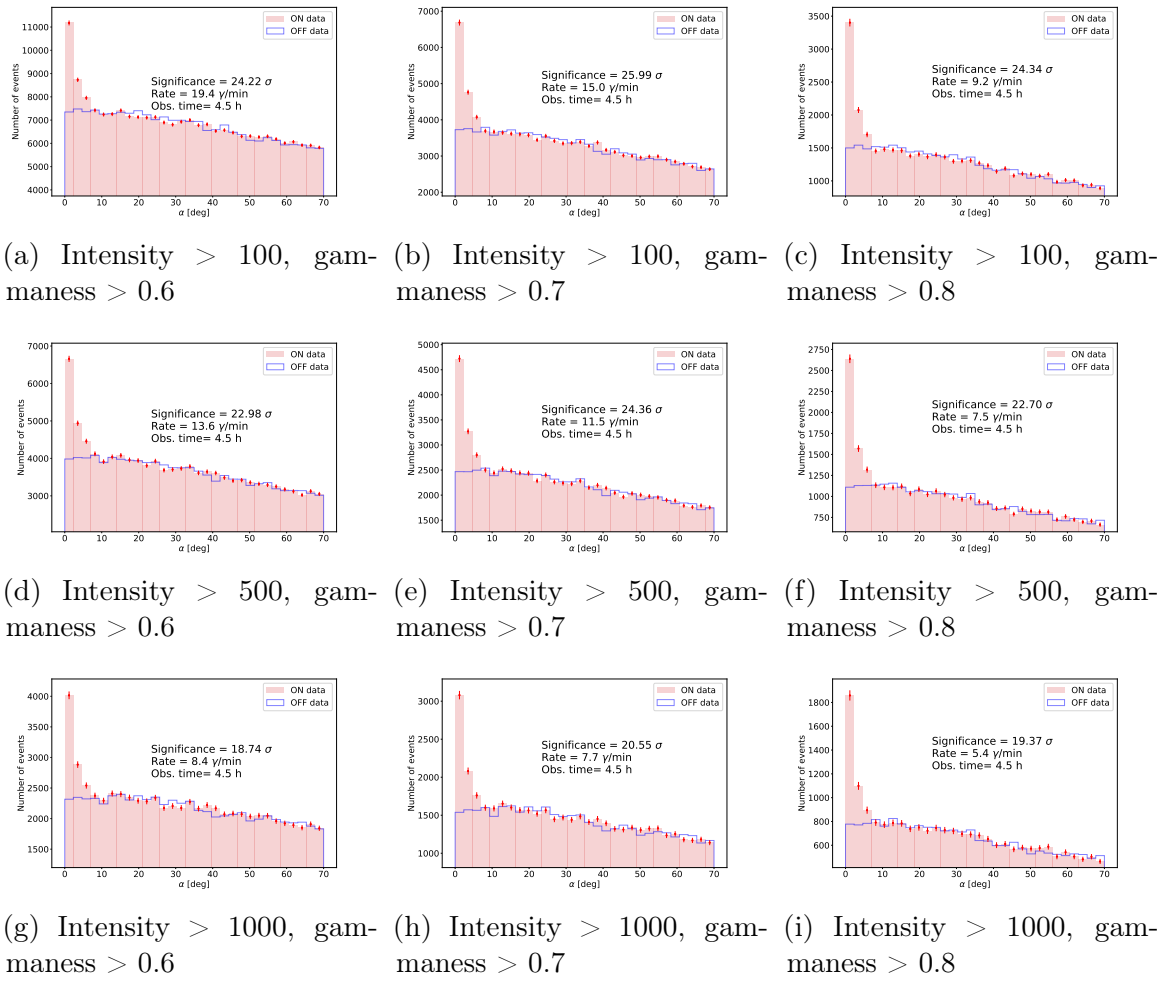


Figure 4.15: Results of  $\alpha$  plot of the First Crab Campaign of LST, analyzed using the EM method for Hillas parameterization, for different cuts in intensity and gammaness. In each plot the reached significance is shown, defined as explained in section 4.5, together with the rate of  $\gamma$ s per minute and the total observation time.

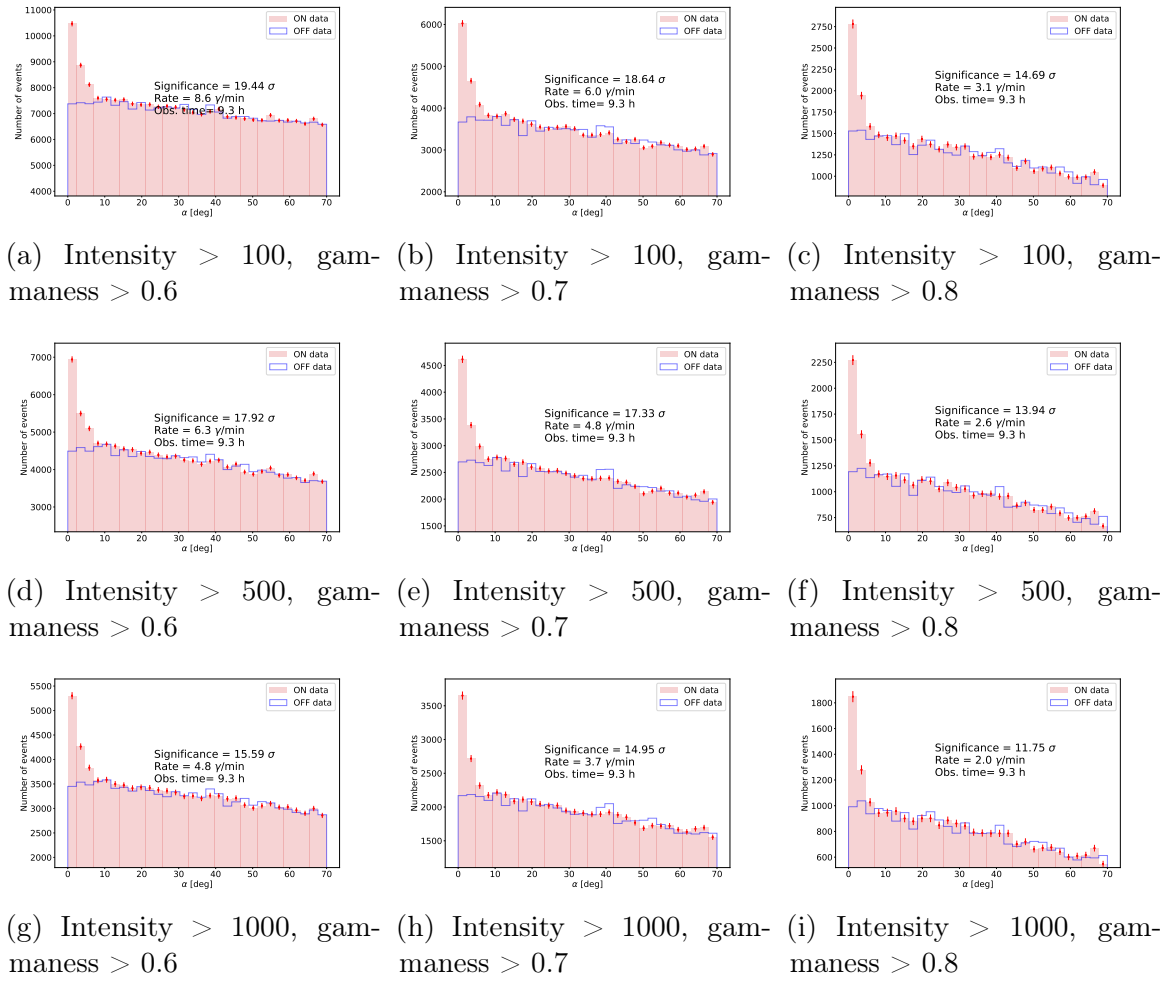


Figure 4.16: Results of  $\alpha$  plot of the Second Crab Campaign of LST, analyzed using the EM method for Hillas parameterization, for different cuts in intensity and gammaness. In each plot the reached significance is shown, defined as explained in section 4.5, together with the rate of  $\gamma$ s per minute and the total observation time.

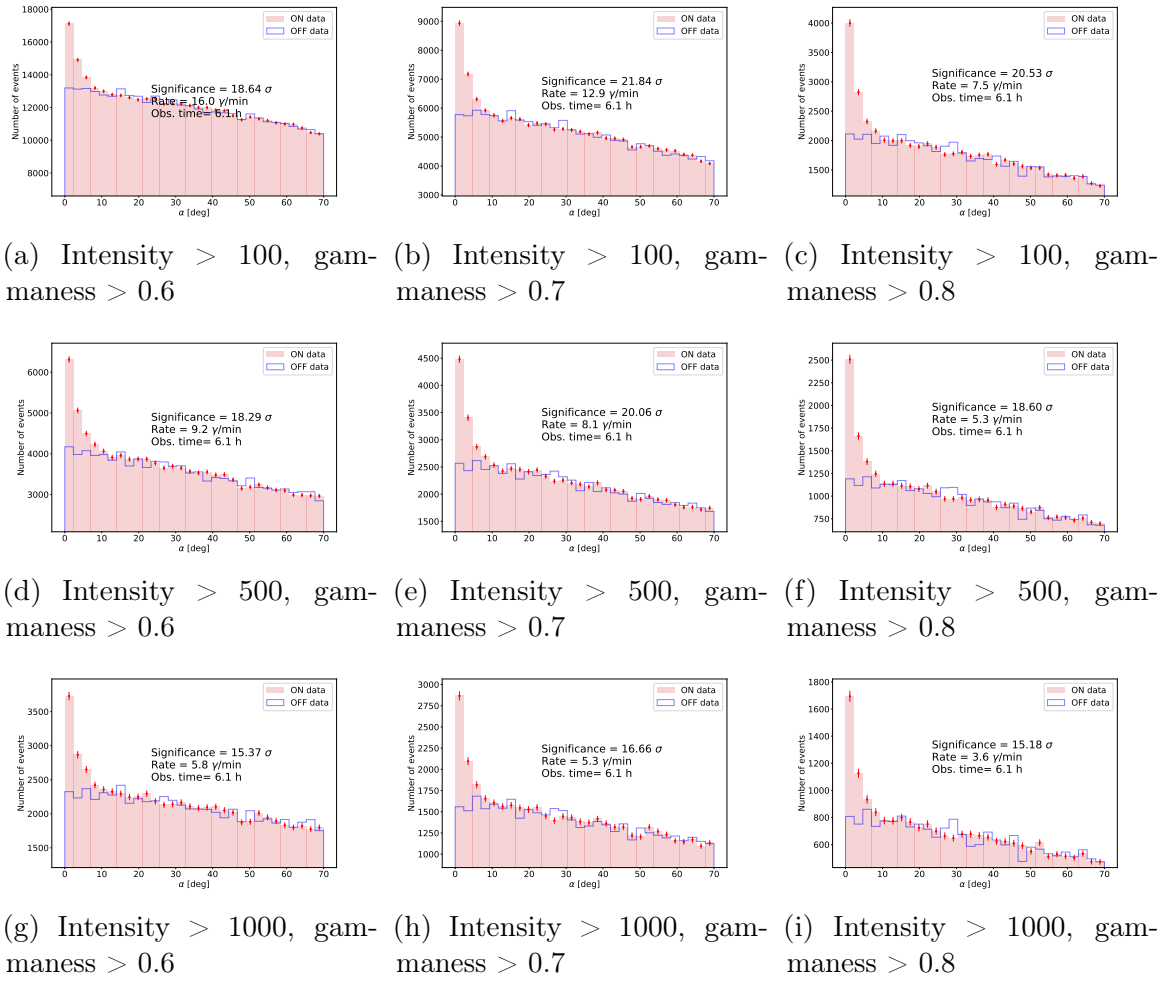


Figure 4.17: Results of  $\alpha$  plot of the Third Crab Campaign of LST, analyzed using the EM method for Hillas parameterization, for different cuts in intensity and gammaness. In each plot the reached significance is shown, defined as explained in section 4.5, together with the rate of  $\gamma$ s per minute and the total observation time.



## 5. Characterization of the Large Magellanic Cloud and prospects on Dark Matter detection for CTA

### 5.1 Introduction

The Large Magellanic Cloud (LMC) is one of the closest satellite galaxies of the Milky Way (MW) located at a distance of  $\sim 50$  kpc [199]. Thanks to its proximity, large volume and orientation angle ( $\sim 30^\circ$  [200]), it is observed as an extended object of about  $10^\circ$  diameter in the sky, which has allowed the study of its structure and individual components in great detail. Observations of the LMC in the whole electromagnetic spectrum have revealed the presence of a big number of extreme objects such as pulsars [201] [202], Supernova Remnants (SNRs) [203] [204] [205], Pulsar Wind Nebulae (PWNe) [206] [202] [207] [208] and  $\gamma$ -ray binaries [209]. Many of these objects are known to be Cosmic Ray (CR) accelerators and therefore potential  $\gamma$ -ray emitters.  $\gamma$ -ray emission up to TeV energies from several sources within the LMC has already been detected by the current generation gamma-ray experiments *Fermi*-LAT and High Energy Stereoscopic System (H.E.S.S.). In addition, *Fermi*-LAT observations of the LMC revealed a diffuse  $\gamma$ -ray emission little correlated with the large scale distribution of the gas column density of the galaxy [210]. This correlation would be observed if CRs could freely diffuse in the Interstellar Medium (ISM) as it is observed in the MW. Instead, this emission appears to be much more correlated with tracers of massive star forming regions such as the 30 Doradus region [211]. The study of the diffuse emission of CRs in the MW has the problem of line-of-sight confusion of sources, encouraging its study in other close galaxies like the LMC, which offers an unique opportunity, as it is viewed nearly face on.

Beyond the extraordinary opportunities for CR physics, the LMC offers also the possibility to help solving the fundamental problem of Dark Matter (DM). The LMC has a mass of the order of  $10^9 M_\odot$  enclosed in 8.9 kpc and more than a half is due to a dark halo [212]. Study of the rotational curves of the LMC revealed that it also could

contain a dark compact bulge with an anomalously high mass-to-luminosity ratio as large as  $\sim 20 - 50 \text{M/L}$  [213] compared of that of the MW of  $\sim 7 \text{ M/L}$  [214]. With these characteristics, LMC would be the most DM massive object after the Galactic Center (GC) offering an alternative source for indirect searches of DM signal.

Among all the theories trying to explain the nature of DM, the Weak Interacting Massive Particle (WIMP) theory is one of the most popular in the field. Under this model, DM is composed by thermal relic particles which can suffer annihilation or decay into Standard Model (SM) particles. Different channels of annihilation would produce a certain spectrum of  $\gamma$ -rays [215] which could be detected as an excess over the  $\gamma$ -ray flux produced by standard astrophysical sources. Following this scheme, *Fermi*-LAT used five years of data to search for a DM annihilation signal in  $\gamma$ -rays and placed competitive bounds on the annihilation cross section as a function of the dark matter particle mass and annihilation channel [210].

Given its strong physics cases, the Cherenkov Telescope Array (CTA) dedicates one of its Key Science Projects (KSPs) to the LMC [216], with more than 300 hours of observation time assigned to perform a survey of the full galaxy, aiming to study the strong CR accelerators in the galaxy, as SNRs and PWNe, the injection and transport of CRs and to search a DM signal.

In this chapter, a characterization of the LMC in the energy range observable by CTA is performed, in order to cast predictions on the possible results of the LMC survey. The methodology followed started by building a full emission model of the LMC, including known point sources, diffuse emission from the interaction of CRs with the interstellar medium, and a synthetic population of PWNe. A dedicated CTA software was used to perform simulations of the survey data products. Then, a maximum likelihood approach is used to calculate the detection significance of the different sources of  $\gamma$ -rays in the LMC, and to set constraints on the diffuse CR emission. In the same way, sensitivity curves for the detection of a possible DM annihilation signal are calculated. Section 5.2 is dedicated to the description of the  $\gamma$ -ray emission model of the LMC. In section 5.3 the analysis and simulation methodology is explained. Results on the detectability of ordinary sources in the LMC (not DM) are presented in section 5.4. The case, analysis and results on the possible detection of annihilation DM signal is covered in section 5.5.

## 5.2 Emission Model

The LMC has been observed by *Fermi*-LAT and H.E.S.S. in the High Energy (HE) and Very High Energy (VHE) ranges. To perform predictions on how the LMC will look like in the range of energies observable by CTA, up to hundreds of TeV, we must rely on the previous observations and make assumptions on how the emission extrapolate to higher energies. The  $\gamma$ -ray emission in the LMC can be divided in two types: emission from point-like sources and diffuse emission from CRs. The idea is to build a complete emission model of the LMC which afterwards will be convolved with CTA Instrument Response Functions (IRFs) to simulate the expected data to be obtained

from the LMC survey. The simulations have been computed using the software *ctools*, already described in chapter 3. These simulations are used to cast predictions on the detectability of the sources included in the emission model, which includes the point sources detected by previous instruments, a synthetic population of PWNe computed for this work, and CR diffuse emission from leptonic and hadronic origin. Finally, the emission model computed is also used as background for the potential detection of a DM annihilation signal. In this section, the emission model developed for the global  $\gamma$ -ray emission of the LMC is described. The baseline model consist on four already-known VHE point-like sources, galaxy-scale interstellar emission of both hadronic and leptonic origin, and a population of PWNe.

### 5.2.1 Diffuse emission

CRs are an important component of the ISM in galaxies, with energy densities comparable to that of magnetic fields. As discussed in previous chapters, the origin and propagation of CRs is still a field of study as well as their role in galaxy evolution. It is believed that they have a significant effect in star formation, acting as an extrinsic feedback source. Even the energy injection rate of CRs is negligible compared to other by-products of star formation, such as photons, winds and supernova shocks, they interact with the ISM and exchange a significant amount of momentum. Studies on starburst galaxies luminosities [217] have established that it is possible that CR winds are produced in high star formation rate regions, perturbing the hydrostatic balance and truncating star formation. On the other hand, infrared observations of Ultraluminous Infrared Galaxies (ULRIGs) suggest that CRs are able to heat gas in molecular clouds and are their main agent of temperature regulation and ionization, fundamentally altering the initial conditions for star formation [218]. The study of CRs in a star formation region such as the LMC offers a unique opportunity to throw light on how CRs interact with the medium, how are they injected and propagated. In order to prepare the material that will be needed for the analysis of the LMC survey, we must try to build a CR diffuse emission model as precise as possible.

Interstellar diffuse emission of  $\gamma$ -rays in galaxies, and particularly here in the LMC, is produced by the interaction of CRs with the ISM. Two kinds of interactions have been considered to compute the diffuse emission model: Inverse Compton (IC) scattering processes from CR electrons and pion-decay from proton interactions. The distribution of CRs in the LMC has been computed under the assumptions of steady CR injection from an ensemble of point sources, followed by diffusive transport in the ISM and interaction with simplified distributions of interstellar components (gas, photon and magnetic fields). The resulting interstellar emission model is obtained by convolving the distribution of injection sources with average emission kernels for pion-decay and IC scattering, plus a correction by the actual gas distribution for the pion-decay.

As has been discussed in chapter 1, CRs are accelerated by the power provided by winds and outflows around massive stars, supernova explosions and compact objects, which are traced by Star forming regions (HII regions). The HII regions catalog from [219] was used as template for the distribution of CR sources, taking only regions with

$H\alpha$  luminosity above  $10^{37}$  erg s $^{-1}$ , a limit below which the  $H\alpha$  luminosity functions flattens as a result of stochastic ionizing populations [220], resulting on the lost of the steady CR injection condition. The most luminous HII region in the LMC is 30 Doradus, with a luminosity of  $10^{39.66}$  erg s $^{-1}$  is not included in the injection model because its mostly populated by very young OB stars ( $< 4$  Myrs) [221] and is unlikely that many Supernovae (SNe) have exploded recently in the region. The CR injection power is assumed to be proportional to the ionizing luminosity of the HII regions and constant in time, corresponding to the release of  $E_{SN} = 10^{51}$  erg per Supernova (SN) explosion, at an estimated rate of  $r_{SN} = 0.002$  SN yr $^{-1}$  [222]. The fraction of mechanical energy trapped by CR acceleration is taken to have the typical values in the literature, given by  $\eta_p = 10^{-1}$  for protons and  $\eta_e = 10^{-3}$  for electrons. This total power is distributed among all the different star forming regions in proportion to their ionizing luminosity. A study on the impact of the variation of these values is out of the scope of this thesis, but no big variations in the results presented are expected, since the model is going to be fitted to the observations. The injection spectra is assumed to follow a power-law distribution in momentum, with an spectral index for protons(electrons) of 2.45(2.65), starting at 1 GeV/s, with an exponential cut off at 1 PeV/s.

The diffusion of CRs away from their sources is assumed to occur due to spatial diffusion and energy losses. Energy loss processes include hadronic interactions of CR protons and synchrotron, IC scattering and Bremsstrahlung radiation of CR electrons interacting with the homogeneous gas, photons and magnetic fields of the ISM model adopted. The spatial distribution of protons and electrons around a stationary source is computed by integrating the solution of the diffusion loss equation, as of [223], over an injection duration of  $T_{inj} = 100$  Myr. This accounts for the Stellar Formation History (SFH) of the LMC which was not steady over recent times and exhibits a drop in star formation 100 Myr ago [224]. Surface brightness angular profiles are computed by integrating the particle spatial distributions along the line of sight over a thickness  $2H$ , where  $H$  is the half-thickness representative of the target distribution: a 180 pc gas disk scale height for CR protons and a 1 kpc magnetic and radiation field halo for CR electrons. The result of these calculations are the emission kernels for IC and pion-decay, which were convolved with the CR source distribution. Furthermore, for the pion-decay component a nuclear enhancement factor of 1.753 is introduced to account for the contribution of helium and heavier nuclei in CRs and the ISM. This value has been computed for a 0.4 solar metallicity medium, as of [225], assuming that heavy nuclei are 40% more abundant in the MW. Also, the resulting emission cube is re-scaled by the gas column density map of the LMC, to recover the actual gas distribution structure of the galaxy.

About the ISM medium in the LMC, an average ISM model has been computed, which includes a description of the interstellar conditions in terms of gas mass and structure, and a stellar population feeding the radiation fields and magnetic field configuration. The CRs transport and subsequent  $\gamma$ -ray emission will be strongly affected by the characteristics of this ISM. For the interstellar gas, a disk having a

radius of 3.5 kpc and a scale height of  $h=0.18$  kpc has been used, where the mass of atomic, molecular and ionized hydrogen has been computed. The interstellar radiation field model has been developed following the work of [226], where the broadband infrared dust emission in the LMC is computed for typical HII regions. About the magnetic field, the total magnetic field strength in the LMC is calculated to be 4.3  $\mu\text{G}$  [227].

The final maps computed for the pion-decay component and the IC component are shown in picture 5.1 in the 1 TeV energy bin.

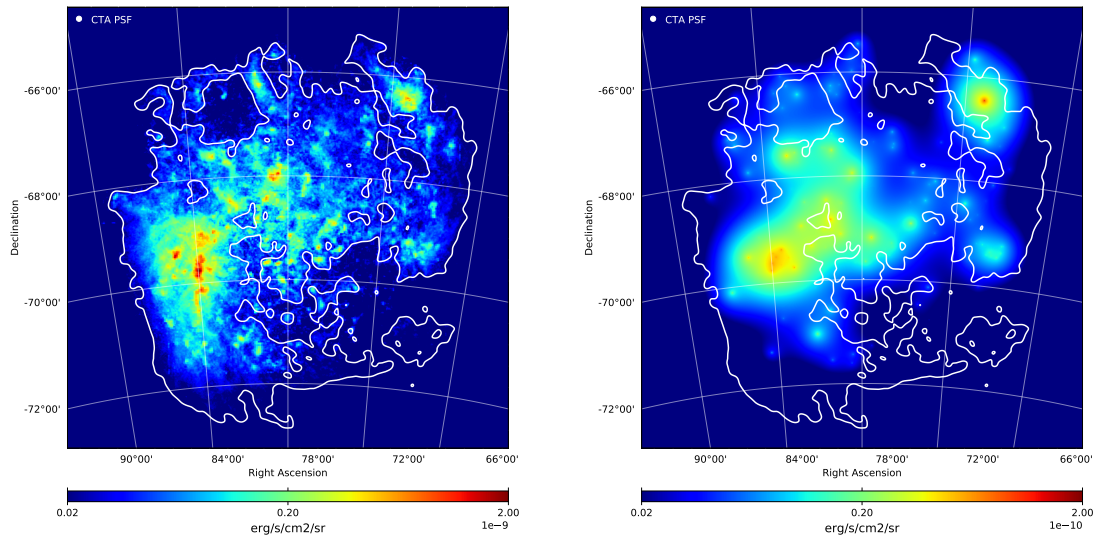


Figure 5.1: Intensity maps at 1 TeV for large-scale interstellar emission in the LMC computed as described in section 5.2.1. *Left:* Pion-decay diffuse emission. *Right:* IC diffuse emission. White contours trace the extent of the most of the gas disk.

### 5.2.2 Point Sources

Observations in  $\gamma$ -rays of the LMC have provided a catalog of powerful point-like sources of different nature, which have revealed very interesting features. For this work, we use the LMC data collected by *Fermi*-LAT [210] [202] and H.E.S.S. [228] [206] [209] to build the emission models of the sources included in this study. A description of the different point sources and their emission models is given in the next subsections.

#### Pulsar Wind Nebula N157B

A signal of  $\gamma$ -ray emission from the direction of the Pulsar Wind Nebula (PWN) N 157B associated to the pulsar PSR J053-6910 has been measured both by *Fermi*-LAT in the HE range ( $\sim 10\sigma$ ) and by H.E.S.S. in the VHE range ( $33\sigma$ ). This is the first and only PWN ever detected outside the MW in  $\gamma$ -rays [229]. PWNe are the result of a supernova explosion, where a fast-rotating, highly-magnetized central pulsar powers

a nebula of ultra-relativistic particles with its spin-down energy, i.e. the loss rate of rotational energy. The well known Crab PWN is an object of this kind, which seems to present large similarities with N157B. The central pulsar of this system, PSR J053-6910 was first discovered in X-ray energies and seems to be the most powerful pulsar known, with a spin-down power of  $\Delta E = 4.9 \cdot 10^{34}$  erg s $^{-1}$  [230]. The TeV  $\gamma$ -ray emission of this kind of objects is directly connected to their spin-down power and has its origin in the IC scattering of lower energy photons by relativistic electrons (and positrons). Thanks to its extremely high power, the emission from N157B can be detected despite its large distance ( $\sim 48\text{kpc}$  [231]) because it is embedded in the strong infrared photon-fields from nearby sources of the superbubble formed by the stellar association LH99, which serve as additional targets for IC scattering. To model this source, we follow the results from [206], where the multiwavelength data (X-rays from Chandra [232] and  $\gamma$ -rays from *Fermi*-LAT and H.E.S.S.) can only be explained with a leptonic IC model where the highest possible magnetic field should be  $45\mu\text{G}$ . The spectral model adopted for this source is shown in figure 5.2.

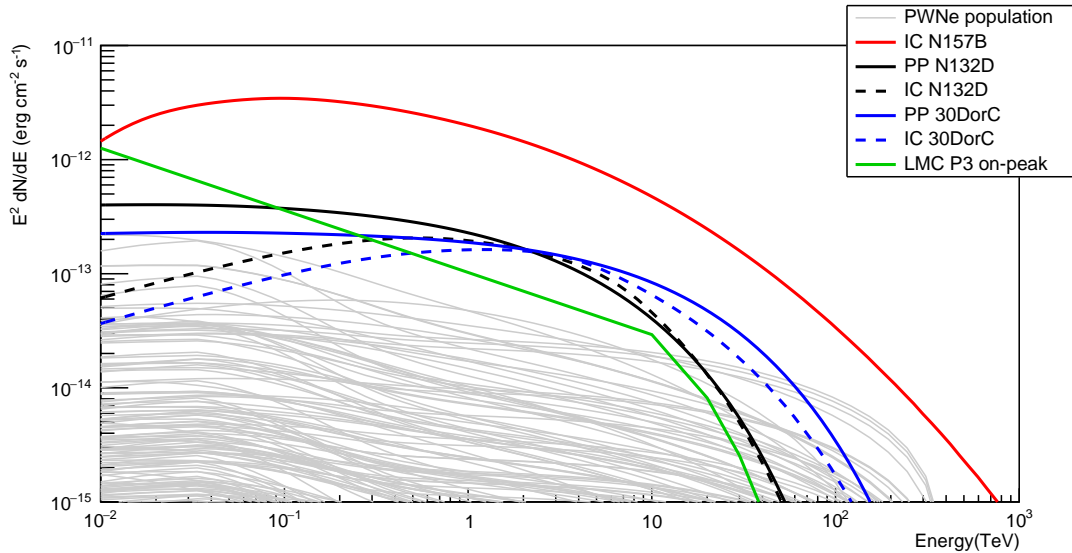


Figure 5.2: Spectral energy distribution of the point sources in the LMC. Spectra from N157B, N132D and 30DorC are extracted from [206]. Spectrum of LMC P3 is a power-law with the spectral parameters of the on-peak orbital region from [209], with an exponential cut-off at 10 TeV. Spectra from the PWNe population are derived following the baseline model described in section 5.2.3

### Supernova Remnant N132D

Both *Fermi*-LAT and H.E.S.S. have detected  $\gamma$ -ray emission with strong evidences to belong to the SNR N132D, a very bright thermal X-ray remnant. It is the brightest remnant of the LMC and belongs to a rare type of oxygen-rich remnants which show optical emission from pure heavy-element ejecta, similar to the MW SNR

Cas A [233]. The origin of this SNR, deduced by its chemical composition, is the core-collapse supernova of a massive progenitor star of mass  $> 35M_{\odot}$  [233]. The origin of the  $\gamma$ -ray emission yields on the interaction of the supernova shock with the cloud of dense material ejected by the progenitor star during its lifetime. The flux detected by H.E.S.S. [206], with a  $\gamma$ -ray luminosity in the 1-10 TeV band of  $0.9 \pm 0.2 \times 10^{35}(d/50kpc)^2$  erg/s, allows to consider the possibility of two origins of the radiation: In the hadronic scenario the flux of  $\gamma$ -rays is produced by the decay of neutral-pions, which would imply a remarkably high fraction of energy injected to CRs by the supernova explosion, or a gas density higher than the one expected from X-ray observations. Either possibility is plausible given the observations in the optical and infrared bands, which reveals a structure produced by the interaction of the remnant with shocked interstellar gas [234]. In the leptonic scenario,  $\gamma$ -rays are produced by IC scattering of low energy-photons. This model could be supported by the high synchrotron emission in radio and X-rays, however, it would require a lower magnetic field than the one inferred from radio observations ( $20\mu G$  vs.  $40\mu G$ ). The fluxes and spectral index measured by *Fermi*-LAT in [202] seem to rule out this model.

For this work, we assume the hadronic (PP) model shown in figure 5.2 based on H.E.S.S. measurements.

### **Superbubble 30 Dor C**

The Superbubble 30DorC, detected by H.E.S.S. in the VHE range, is a radiation emitting shell which stands out in X-rays, being the largest X-ray synchrotron shell known (with a radius of 47pc) [235], and also emits radio and optical radiation [236]. Its origin seems to be related to the stellar winds and supernovae of the stellar association LH 90 [237]. Both leptonic and hadronic scenario could explain the  $\gamma$ -ray flux detected by H.E.S.S. from this source as discussed in [206]. The two models are shown in figure 5.2. For this work we tested both models, given that CTA observations from 100 GeV could be able to set which is the most probable model, thanks to the slope differences up to 1 TeV.

### **Binary system LMC P3**

This object was first detected by *Fermi*-LAT at HE energies in [202], but was classified as an unidentified source in the environment of the HII regions NGC 2029/NGC2032. They measured a very soft power-law spectrum (index  $\sim 2.8$ ) but did not notice any variability down to a monthly basis. Later, emission from this object in the VHE range was detected by H.E.S.S. [209]. They discovered a variability of 10.3 days period, classifying the object as the first extragalactic  $\gamma$ -ray binary system. The position of LMC P3 is consistent with a soft X-ray source, with variability in X-ray flux. The radial velocity measured from Balmer absorption lines confirmed that it is very likely a binary system [238], [239]. From optical radial velocity measurements, it is derived that the system must be composed by a neutron star with an O5III star companion [240].  $\gamma$ -ray binaries are believed to be a brief phase of the evolution of high-mass

X-ray binaries, in which the  $\gamma$ -ray emission dominates the electromagnetic output [241].

The spectrum of LMC P3 (HESS J0536-675) was fitted by H.E.S.S. to a simple power law of the form  $\frac{dN}{dE} = \Phi_{1TeV} \left(\frac{E}{1TeV}\right)^{-\Gamma}$  with an on-peak spectral index  $\Gamma$  of 2.1, and an off-peak index of 2.4, where on-peak represents the orbit region where most of the  $\gamma$ -ray radiation is emitted. The detection of the source only achieved enough statistical significance during the on-peak period.

For simplicity in this work, we will assume the on-peak spectral parameters of the source without any temporal modulation ( $\Gamma = 2.1$ ,  $\Phi_{1TeV} = 5 \cdot 10^{-13} cm^{-2}s^{-1}TeV^{-1}$ ). The justification is that the on-peak orbital phase lasts for  $\sim 50$ h, which is way below the total observation time assigned to the LMC survey. An upper limit for the detection of the off-peak region was also calculated and results are given in section 5.4.

### 5.2.3 PWNe population in the LMC

PWNe are the predominant class of TeV emitters in our Galaxy, with more than 30 sources detected up to date [242]. If we assume that the same is true for the LMC, we can model a typical PWNe population reproducing the so called *baseline* spectral model, first introduced by [243] and revised by [244]. The model is a one-zone, time-dependent model which allows to trace the evolution of VHE lepton population and hence, radiative output of a PWN. In the model, the number of leptons with energy  $E$  residing in the nebula at time  $t + \delta t$  will be determined by the balance between the injected leptons and those cooled out in the respective energy interval:

$$\frac{dN}{dE}(E, t + \delta t) = \frac{dN_{cooled}}{dE}(E, t + \delta t) + \frac{dN_{inj}}{dE}(E, t + \delta t) \quad (5.1)$$

Where for the number of injected leptons  $dN_{inj}/dE$  a power-law spectral shape is assumed:

$$\frac{dN_{inj}}{dE}(E, t) = \Phi_0(t) \left(\frac{e}{1TeV}\right)^{-\beta} \quad (5.2)$$

with a power-law index  $\beta$ , also known as injection index. The normalization  $\Phi_0(t)$  will depend on the amount of spin-down energy converted into relativistic electrons and positrons in a time step  $t + \delta t$ . The cooling mechanisms comprise synchrotron escape and adiabatic losses, and the number of cooled leptons can be approximated by:

$$\frac{dN_{cooled}}{dE}(E, t) = \frac{dN}{dE}(E, t - \delta t) \cdot \exp\left(-\frac{\delta t}{\tau_{eff}(E, t)}\right) \quad (5.3)$$

Parameter description			Parameter values
Braking index	n		3.0
Initial spin-down power	$\dot{E}_0$	( $10^{39}$ erg s $^{-1}$ )	2.0
Initial spin-down timescale	$\tau_0$	(kyr)	0.5
Initial magnetic field strength	$B_0$	( $\mu$ G)	200
Reverse shock interaction timescale	$\tau_{rs}$	(kyr)	4.0
PWN radius at t=3kyr	$R_3$	(pc)	6.0
Adopted const. ISM magn. field strength	$B_{ISM}$	( $\mu$ G)	3.0
Lepton conversion efficiency	$\eta$		1.0
Index of magnetic field evolution	$\alpha$		0.6
Index of lepton injection spectrum	$\beta$		1.75, 2.0, 2.25
Lower bound of lepton energy distribution	$E_{min}$	(TeV)	0.03
Upper bound of lepton energy distribution	$E_{max}$	(TeV)	300

Table 5.1: Parameters used for the modelling of the PWNe population, based on table A.1 from [244].

Where  $\tau_{eff}$  is the effective cooling timescale, which will depend on the time evolution of the PWN radius and magnetic field strength.

The baseline model requires a series of parameters which are listed in table 5.1:

Three equally probable values of the injection index  $\beta$  have been considered, and the interstellar magnetic and radiation fields have been adapted to the average conditions in the LMC.

The population of PWN has been generated considering that pulsars are born at a rate of  $r_{CC} = 0.0011SNyr^{-1}$ , in agreement with the assumed rate of SNe explosion and ratio of core-collapse to thermonuclear SNe, assuming that all core-collapse SNe lead to the formation of a spinning neutron star. The lifetime for each PWN is approximated as of  $\tau_{PWN} = 200kyr$ , which yields to an average number of  $r_{CC} \times \tau_{PWN} = 220$  PWNe in the LMC if the pulsar creation is in steady state during the time  $\tau_{PWN}$ . The following steps have been carried on to generate the synthetic population of PWNe:

- (i) Draw a random number of objects from a Poisson distribution with mean  $r_{CC} \times \tau_{PWN}$ .
- (ii) Draw random ages from a uniform distribution over 0 to  $\tau_{PWN}$ .
- (iii) Random select an injection index among the three values considered, listed in table 5.1.
- (iv) From the baseline spectral model, compute the spectra of all objects given their ages and injection indices.
- (v) Distribute them spatially among the different massive star forming regions, in proportion to their ionizing luminosity.
- (vi) Add some luminosity scatter to reflect the properties of the observed PWNe population in the MW.
- (vii) Apply two cuts in the synthetic population: First, remove objects younger than 2kyr, because we already know at least two objects of that age (SN 1987A

and N158A); second, remove all objects with  $> 1\text{TeV}$  luminosity above  $2.2 \times 10^{34} \text{ erg s}^{-1}$ , because they would have been detected by H.E.S.S. already, as shown in the upper limits calculated for SN1987A in [228].

The total number of 189 PWNe have been included in the simulated model, and their spectral energy distributions are shown in figure 5.2. A mapcube of the emission of the PWNe population at 1 TeV is shown in picture 5.3.

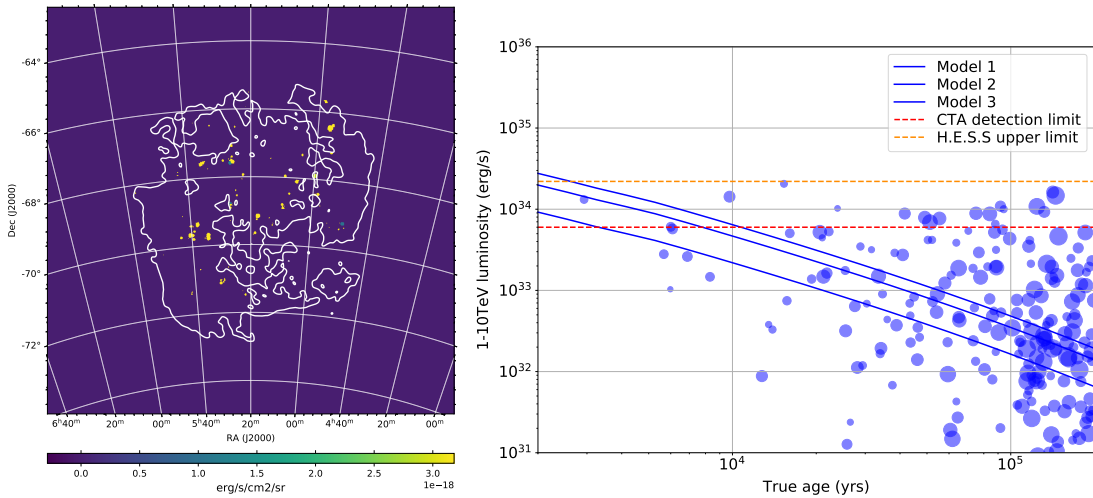


Figure 5.3: *Left:* Mapcube of the PWNe synthetic population generated as described in section 5.2.3 at 1 TeV. *Right:* Luminosity as a function of age for one random sample of our PWNe population model. Dot size is linearly proportional to PWN radius. Overlaid are the average relations for the different models from which the population was drawn (models 1 to 3, differing by the particle injection index, from 1.75 to 2.25), the upper limit on point-like emission from H.E.S.S. [Abramowski:2015], and the threshold for detection with CTA.

## 5.3 Simulations and Analysis method

### 5.3.1 Region of Interest and Observational strategy

The Region of Interest (ROI) of the LMC extends about  $10^\circ$  in the sky. In order to reach this large field of view (FoV), CTA will cover the full region by a series of slightly overlapping pointings with a FoV of  $\sim 3^\circ$  each. The total amount of hours assigned to the LMC survey is 340h plus 150h more in case the SNR 1987A is detected. For this work, different pointing patterns have been tested in order to adopt the observational strategy which will maximize the significance of detection both for point sources and extended sources. The final scheme consist on 7 pointings arranged in 3 rows with a 2-3-2 configuration centered in the coordinates  $\text{RA}=80.0^\circ$ ,  $\text{dec}=-69.0^\circ$  with a separation of  $2^\circ$  between pointings, as shown in figure 5.4. The duration of the observation in each pointing position is of  $\sim 1.75 \times 10^5$  s. For the simulations performed in this work, all telescopes planned for CTA South are involved.

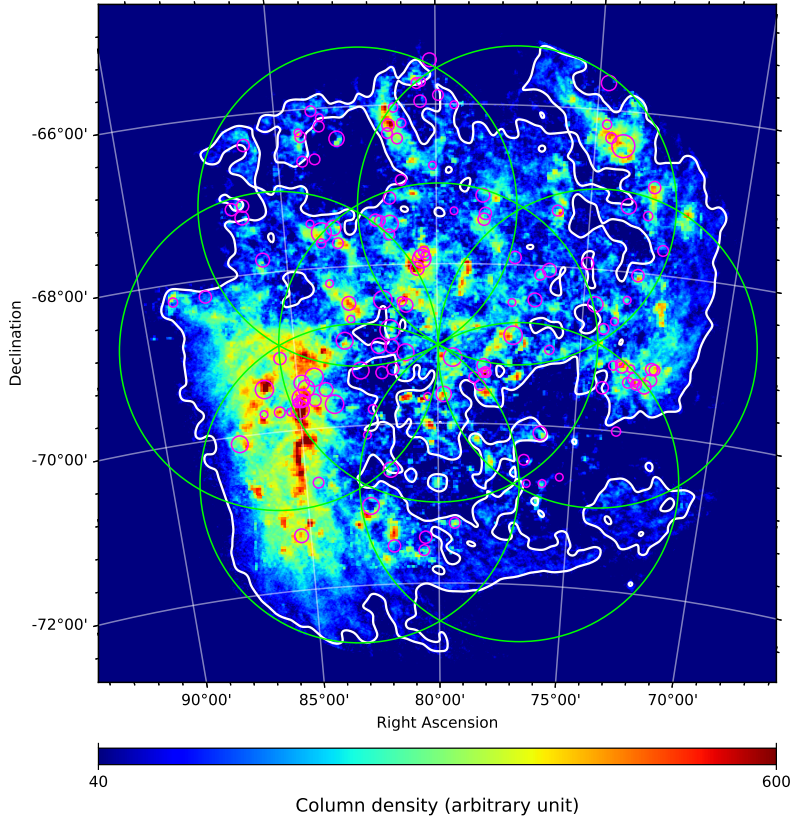


Figure 5.4: Total hydrogen gas column density map in the the region of interest of the LMC. The pointing pattern is overlapped in the shape of green circles. Magenta circles give the position of the HII regions selected as CR injection sites, with circle size proportional to the logarithm of the ionizng luminosity, used as proxy for relative CR injection power.

### 5.3.2 Simulation parameters

To calculate the predicted number of counts from a certain emission model, the CTA collaboration provides a set of IRFs [156] with information about the effective area and angular resolution of the instrument for several zenith angles. For this work we have used the IRF *South\_z40\_50h* from the production *prod3b-v2*. This IRF only accounts for the southern observatory and is optimized for zenith angles around 40° (LMC will be observed at  $\sim 46^\circ$  from the southern site) and 50 hours of observation time.

The simulations were computed using *ctools* and *gammalib* [245], a software framework for the analysis of astronomical  $\gamma$ -ray data, specifically designed for CTA (see section 3.4.3). The function *ctobssim* uses a Monte Carlo (MC) generator to recreate event lists for observations. As input, it requires a full model of the ROI, including each individual source with a spatial and spectral component, and a model of the instrumental background accounting for CR events misidentified as  $\gamma$ s. Also, *ctobssim*

requires the IRF for the observation and the energy range. Each running of *ctobssim* results in a realization of the model where the event list is generated with a random number generator. We have performed realizations of the full emission model of the LMC with the pointing pattern described before, in the energy range from 0.05 TeV to 150 TeV. *Ctobssim* is able to combine the different observations of the overlapping pointings, averaging the IRFs of each region. The resulting event lists are written into FITS files, one for each pointing, which can be combined afterwards for the analysis.

### 5.3.3 Fitting method

A binned likelihood analysis has been performed in this work, to fit the emission model to the simulated data. The event lists of the 7 pointings have been combined and then the data has been binned into 110 energy bins using the *ctools* function *ctbin*. The boundaries of the energy bins have been generated using the function *csebin*, which inspects the variation in the effective area and background template of the IRF with energy, for the specific simulations. It settles a bin boundary when the quantities change in a fraction selected by the user. To ensure a sufficiently large number of energy bins (it is recommended to have at least 30 bins per decade), the threshold for the fractional change in effective area has been settled to 0.06, and to 0.16 for background rate.

The energy range chosen for the analysis is from 100 GeV to 100 TeV. The higher lower limit, compared to the full range of CTA (which can go down to 30 GeV) comes from the limitations of performance at high zenith angles, given that LMC will be always observed at  $z > 40^\circ$ . The background model, the exposure cube and point spread function cube are precomputed using the functions *ctbkgcube*, *ctexpcube* and *ctpsfcube* respectively. The results are a series of mapcubes which will be used to calculate the maximum likelihood function.

An Asimov data set has been computed to produce the results presented in this chapter. The *Asimov* data set [246] is a representative data set which, when fitted, will retrieve the true values of the model parameters. It can be computed with *ctools* using the function *ctmodel*, and allow to give mean results for significance and upper limits without needing a large number of realizations of the simulated data.

Different slices of the Asimov dataset produced for this analysis is shown in picture 5.5.

### 3D Likelihood Analysis for $\gamma$ -ray sources

The likelihood analysis is based in the Poisson likelihood function:

$$\mathcal{L}(\mu|n) = \prod_{i,j} \frac{\mu_{ij}^{n_{ij}}}{n_{ij}!} e^{-\mu_{ij}} \quad (5.4)$$

Where  $n_{ij}$  represents the simulated counts and  $\mu_{ij}$  the model prediction for each bin in energy(i) and space (j). The model  $\mu_{ij}$  is the result of the combination of the models

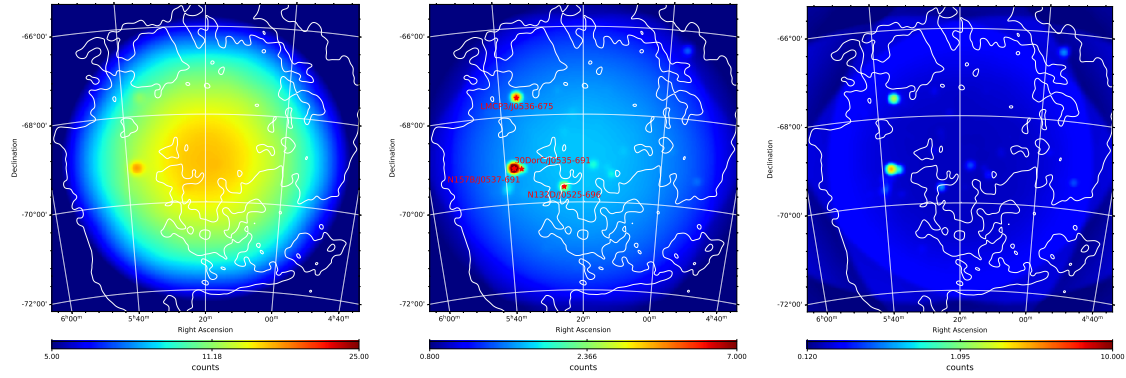


Figure 5.5: Three slices of the Asimov mapcube at 0.100 TeV, 1 TeV and 10 TeV (*left, middle, and right* respectively) produced with the full emission model of the LMC described in section 5.2. The four H.E.S.S. point sources are marked with red stars in the 1 TeV map.

for each of the  $\gamma$ -ray sources described in section 5.2. Each source model accounts for a spectral and a spatial component. For extended sources, both components are combined in one mapcube. In the likelihood fitting the only free parameter for each of these models is the spectral normalization  $A^X$ , which determine the relative weight of component  $X$ . The only exception is the point source LMC P3, whose spectral model is a power-law where the free parameters are the normalization and the spectral index. The shape of  $\mu$  is therefore:

$$\mu_{ij}(A^X) = \sum_X A^X \mu_{ij}^X + A^{LMCP3}(E)^{-\Gamma} \quad (5.5)$$

The maximum likelihood is calculated finding the normalization parameters  $A^X$  which maximize equation 5.4.

The detection significance of a source is calculated in terms of the Test Statistics:

$$TS = 2\log \frac{\mathcal{L}(\mu(A^X)|n)}{\mathcal{L}_{null}} \quad (5.6)$$

Where  $\mathcal{L}(\mu(A^X)|n)$  is the maximum likelihood function and  $\mathcal{L}_{null}$  is the value of the likelihood function of the null hypothesis for the specific source (meaning  $A^X = 0$ ). With this definition, typically a source is considered to be detected when  $TS > 25$ , equivalent to  $5\sigma$ .

The maximum likelihood analysis has been performed using the function *ctlike* from *ctools*. The inputs are the data mapcubes from the stacked analysis and the description of the emission model. For the likelihood fit the same emission model used for the simulations is given as input, meaning that the fitting results will represent the most optimistic case, where the model is perfectly describing the data.

### **Upper limits calculation**

For sources which have a flux too low to be detected ( $TS < 25$ ) we calculate upper limits on the minimum flux needed for the source to be detected with CTA. We calculate this upper limits as the flux that leads to a decrease in the likelihood that corresponds to a certain Confidence Level (CL). This is the chosen definition for upper limits in this work, as it is the one included in *ctools*, but it must be noted that other definitions exist in the literature. Using the definition of TS from 5.6, according to Wilks' theorem [247], the TS function asymptotically approaches a  $\chi^2$ -distribution with one degree of freedom under the null hypothesis, therefore to get the flux that yields to the 95% CL upper limit, we must find the normalization parameter  $A_{max}^X > A^X$  which corresponds to  $TS = 2.71$ .

This calculation is performed using the function *ctulimit* from *ctools*, which requires as input the mapcube of the simulated data and a model with all the sources, including the source for which the upper limit will be calculated. In this case, we use the model resulting from the maximum likelihood fit. The only free parameters must be again the spectral normalizations. The results from *ctulimit* are the upper limit in the differential flux for a reference energy, the integrated upper flux limit for a specific energy range and the integrated upper energy flux limit for the same range.

We have used this method to set constraints on the DM annihilation cross section  $\langle \sigma v \rangle$  as described in section 5.5.

## **5.4 Results**

### **5.4.1 Point sources**

The results for the fitting of the four point sources tested in this work in the full energy range (100 GeV to 100 TeV) are given in table 5.2. The significance of detection of the sources is given in terms of the Test Statistics described in the previous section. For LMC P3 three cases have been tested: The case of a spectrum following a power-law with the on-peak parameters from [209]; the same power-law but with an exponential cut-off at 10 TeV; and a last case where no source has been simulated, but an upper limit on the flux for a source with the off-peak spectral index has been computed in the energy range 0.1-100 TeV. Also, energy flux upper limits for three energy ranges are shown in figure 5.8.

The results show that CTA will be able to detect with high significance all the known point sources in the LMC, including the binary system LMC during the on-peak orbital region, and will be able to test the flux of the off-peak region.

### **5.4.2 Population of PWNe**

For the fitting of the PWNe population, a mapcube including all the artificially computed candidates has been used for simulation. Then, each PWN spectrum has been fitted individually, keeping all the rest of the PWNe and other model components fixed. The results show that 15 from the total of 189 simulated PWNe would be

Source name	RA( $^{\circ}$ )	Dec( $^{\circ}$ )	Normalization ( $0.1 - 100 TeV$ )	TS	Significance( $\sigma$ )
Point Sources					
N157B/HESS J0537-691	84.44	-69.18	$1 \pm 0.005$	130951.51	361.9
N132D/HESS J0525-696	81.26	-69.64	$1 \pm 0.019$	5370.19	73.3
30DorC/HESS J0535-691 (PP)	83.96	-69.2	$0.999 \pm 0.022$	4762.83	69.0
30DorC/HESS J0535-691 (IC)	83.96	-69.2	$0.999 \pm 0.022$	3919.0	62.6
LMCP3/HESS J0536-675 (on-peak, cut-off 10 TeV)	84.0	-67.59	Prefactor: $4.99 \pm 0.05 \cdot 10^{-19}$ ( $cm^{-2}s^{-1}MeV^{-1}$ ) Index: $2.1 \pm 0.01$	27353.83	165.4
LMCP3/HESS J0536-675 (on-peak)	84.0	-67.59	Prefactor: $4.99 \pm 0.05 \cdot 10^{-19}$ ( $cm^{-2}s^{-1}MeV^{-1}$ ) Index: $2.1 \pm 0.006$	48021.95	219.14
LMCP3/HESS J0536-675 (off-peak)	84.0	-67.59	Int. flux ulimit (99 % CL): $1.23 \cdot 10^{-13}$ ( $cm^{-2}s^{-1}$ )	-	-
Diffuse emission components					
LMC Pion-decay	-	-	$1 \pm 0.185$	29.06	5.39
LMC IC	-	-	Int. flux ulimit(99% CL): $7.33 \cdot 10^{-12}$ ( $cm^{-2}s^{-1}$ )	-	-

Table 5.2: Results of the fit for the point sources and diffuse components included in the emission model. For the first three sources, the normalization of the spectrum is the only free parameter to fit. For LMCP3, a power-law spectrum with exponential cut-off at 10 TeV has been fitted, accordingly with the results of [209]. For the off-peak region, the upper limit at 99% CL for the integrated flux has been calculated. From the diffuse components, only the hadronic emission could be detected at  $TS > 25$  therefore an upper limit has been computed for the leptonic IC component.

detected with  $TS > 25$ , giving an estimation of the number of new PWNe that could be discovered by CTA. Also, 12 more PWNe were fitted giving a  $TS > 9$  ( $3\sigma$  significance). It must be taken into account that this is a very optimistic result, giving that the true spectrum and position of each PWNe is being used for fitting. In reality, a totally blind search will be performed, scanning the full region in the search for excesses, and assuming a generic spectral shape. The results on the PWNe are shown in figure 5.6, showing the fitted flux compared to the true flux, and the TS value vs. the true flux.

#### 5.4.3 Diffuse Emission

The diffuse emission models for pion-decay and IC scattering have been fitted as mapcubes where the only free parameter left is the normalization. The fit in the full energy range has resulted in a positive detection for the pion-decay component, with a mean TS value of 29.06 ( $5.39\sigma$  significance). A Test Statistics (TS) map for this component has been computed, and is shown in picture 5.7, where a radial disk with a power law spectrum of 2.5 is used as test source (instead of the true model). The map shows how the regions with higher TS values are concentrated in high density gas areas. When modifying the spectrum of the pion-decay model to have a harder spectral index of 2.2 (instead of 2.7 as the baseline model), typical of starburst galaxies, the detection spreads more over the full galaxy.

Regarding the IC component, the TS obtained is 0.282, resulting in a non-detection. Upper limits for this model have been calculated instead, giving an upper limit at

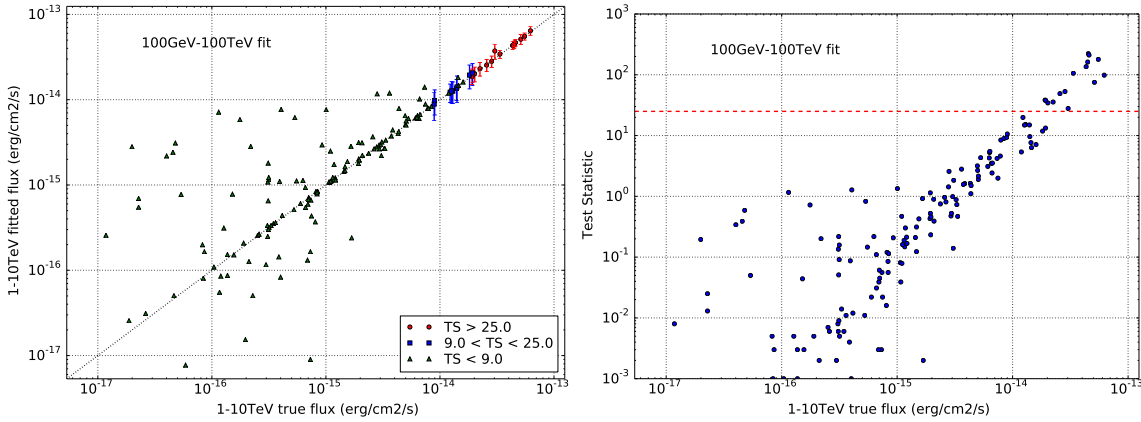


Figure 5.6: *Left:* True flux vs. fitted flux for the synthetic population of PWNe. Each PWN has been fitted individually, keeping the rest of the model components fixed. *Right:* TS value vs. true flux of the PWNe population. Red line corresponds to  $TS=25$  ( $5\sigma$  detection significance).

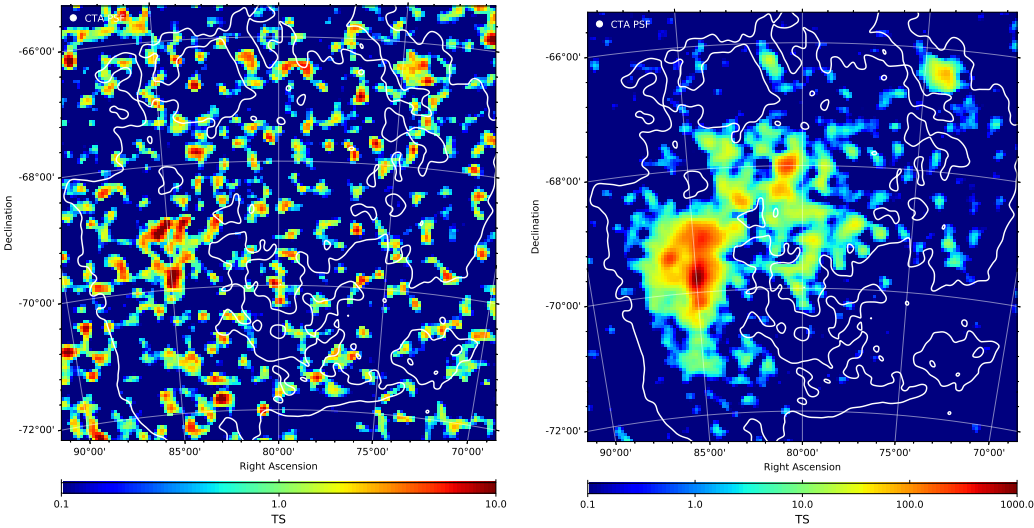


Figure 5.7: TS map for simulated observations of the large-scale pion decay emission component computed over 0.1-100 TeV. The test source used to evaluate the TS over a grid of positions is a uniform brightness disk of  $0.1^\circ$  radius having a power-law spectrum with fixed photon index 2.5. The left panel shows the TS map for the baseline pion decay model, which has photon index of  $\sim 2.7$ , and the right panel shows the TS map obtained for a harder emission model, with photon index of  $\sim 2.2$  similar to starburst galaxies.

99% confidence level in the integral flux limit of  $7.33 \cdot 10^{-12} \text{ ph cm}^{-2}\text{s}^{-1}$  in the range 100 GeV-100TeV. In figure 5.8, energy flux upper limits for three energy ranges (0.1-1

TeV, 1-10 TeV, 10-100 TeV) are shown.

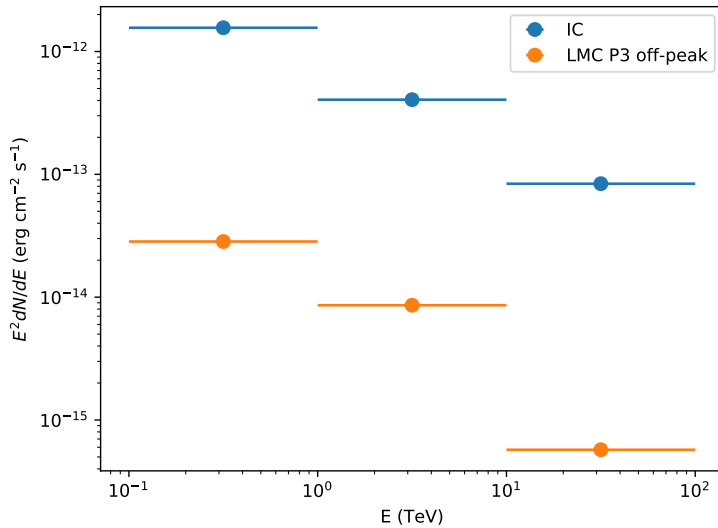


Figure 5.8: Energy flux upper limits computed for the IC diffuse component and LMC P3 off-peak model in three energy ranges.

## 5.5 Dark Matter annihilation in the LMC

In this section, an additional component of the diffuse  $\gamma$ -ray emission in the LMC, due to the annihilation of DM, is considered. The aim is to find the parameter space of models that could be probed with CTA, determining if the LMC is a good candidate to set constraints on the WIMP DM model.

The assumption is that DM is composed by stable particles which can annihilate and produce a shower of SM particles, which in turn would lead to either direct or secondary production of  $\gamma$ -rays, as explained in section 1.5. The range of energies for this process can go from a few GeV to several TeV, making it potentially observable by CTA. It must be taken into account that there exists plenty of DM candidates in the literature [248], [249], [250], but in this work only the WIMPs annihilation scenario is considered.

The flux of  $\gamma$ -rays produced by DM annihilation was presented in equation 1.23, reproduced here for convenience:

$$\frac{d\Phi}{dE} = \frac{1}{8\pi} \frac{\langle \sigma v \rangle}{m_\chi^2} \frac{dN_\gamma}{dE} \int_{\Delta\Omega} \int_{l.o.s} dl \rho^2(\vec{l}) \quad (5.7)$$

Where  $dN/dE$  is the spectrum of  $\gamma$ -rays from annihilation of a pair of dark matter particles,  $\langle \sigma v \rangle$  is the thermal velocity averaged annihilation cross section,  $m_\chi$  is the

DM particle mass and  $\rho$  is the dark matter density profile. If DM particle is not its own antiparticle, equation 5.7 should be multiplied by a factor 1/2.

Along the full analysis, the mass of the DM particle and the annihilation cross section will be considered free parameters, fixing the rest of the model features. A single annihilation spectra will be assumed where the branching ratio of the reaction is one, meaning that the entire annihilation happens in a specific channel. The results will be presented in the shape of sensitivity curves where the minimum annihilation cross section needed for detection is plotted against the mass of the DM particle for a specific annihilation channel and DM profile.

### **5.5.1 Dark Matter profile in the LMC**

The DM distribution of the LMC can be inferred by the gravitational structure of its disk, following the rotation curve method. Assuming circular orbits, the mass of a galaxy enclosed in a certain radius can be calculated thanks to the rotation velocity,  $v_{rot} = GM(<r)/r$ . Measurements of the rotation velocities of stars and gas in the LMC allow to calculate the total mass [251], and subtracting the contribution to the rotation curve of the luminous matter, the remaining DM mass can be estimated. The dark matter profiles used in this section rely on the works of [252], where the gas mass component of HI+He as a function of the radius is taken from [253]; and the stellar mass is extracted from [122]. The rotation curve of the LMC can be seen in picture 5.9.

A generalized six-parameter Hernquist-Zhao DM profile has been adopted for this work ([254], [37]), following equation 1.5 from section 1.5, reproduced here for convenience:

$$\rho(r) = \frac{2^{\frac{\beta-\gamma}{\alpha}} \times \rho_0}{\left(\frac{r}{r_s}\right)^\gamma \left[1 + \left(\frac{r}{r_s}\right)^\alpha\right]^{\frac{\beta-\gamma}{\alpha}}} \Theta(r_{max} - r) \quad (5.8)$$

Where  $\Theta$  is the Heaviside step function,  $r_s$  is the scale radius and  $\rho_0$  is the characteristic density. These two last parameters are properties of the specific DM halo. Setting  $(\alpha, \beta, \gamma) = (1, 3, 1)$  we retrieve the Navarro-Frenk-White (NFW) profile [38]<sup>1</sup>. An isothermal profile is obtained setting  $(\alpha, \beta, \gamma) = (2, 2, 0)$ . Variations of these two profiles have been tested, with their parameters shown in table 5.3 and plotted in figure 5.10. For the NFW profile, a more cuspy profile with  $\gamma = 1.5$  and a more cored profile, with  $\gamma = 0.5$  are tested. In the case of the isothermal profile, the scale radius is varied from the iso-mean profile with  $r_s = 2.4$  (kpc) to iso-max with  $r_s = 3$  (kpc) and iso-min with  $r_s = 1$  (kpc).

The DM profiles were simulated using the software *clumpy*, a code for  $\gamma$ -ray and neutrino signals from DM structures [256]. It allows to compute simulations of DM halos characterized by a series of parameters depending on the DM profile. *Clumpy*

---

<sup>1</sup>When  $\alpha = 1$  and  $\beta = 3$  the Zhao profile is typically called generalised NFW profile (gNFW) with flexible inner DM density slope  $\gamma$ .

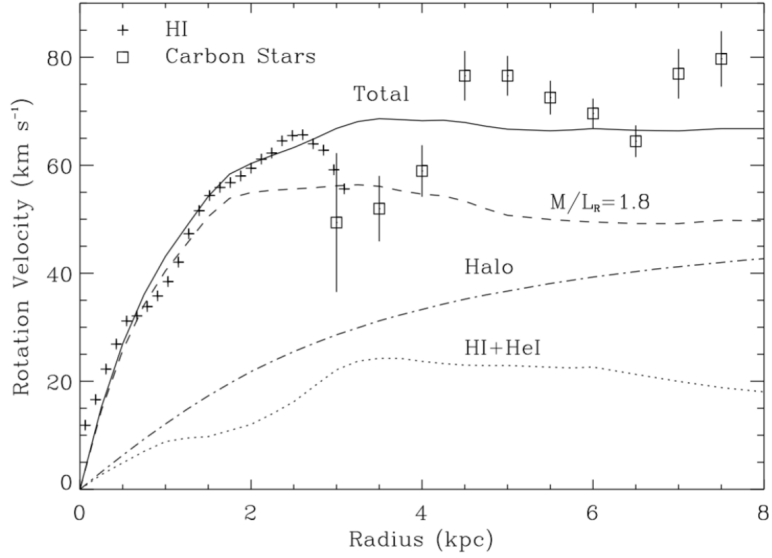


Figure 5.9: Rotation curve of the LMC, from [251]. The solid black line is the total predicted rotation curve constructed from the following components: (a) HI mass distribution from [253], and a 30% He contribution (*dotted line*). (b) R stellar light distribution based on the data from [255] and  $M/L_R = 1.8$  (*dashed line*). (c) Pseudoisothermal dark halo with core radius 2.5 kpc and central density  $0.009 M_\odot \text{pc}^{-3}$ .

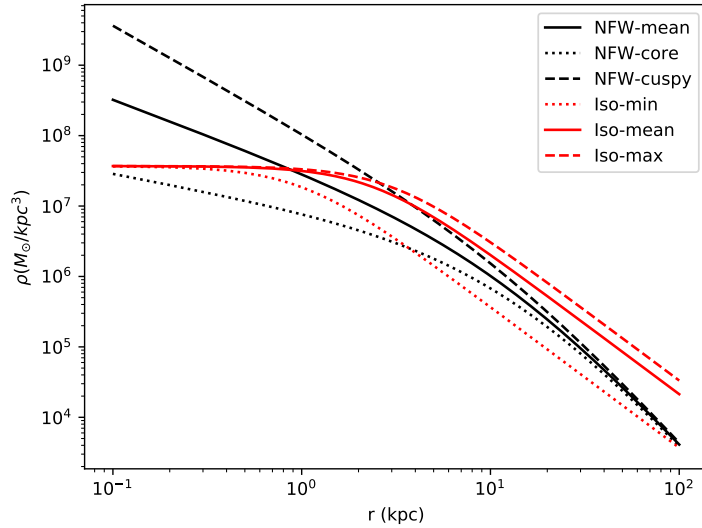


Figure 5.10: DM profiles plotted against the radius  $r$  from the LMC center, with the parameters listed in table 5.3.

was used in this work to simulate maps of the J-factor in the region of the LMC in order to create the spatial distribution of the different DM models, which afterwards

Profile	$\alpha$	$\beta$	$\gamma$	$r_S(kpc)$	$\rho_0(M_\odot/kpc^3)$	$J(10^\circ)(GeV^2/cm^5)$
NFW-mean	1	3	1	12.6	$2.6 \times 10^6$	$1.36 \times 10^{21}$
NFW-core	1	3	0.5	12.6	$2.6 \times 10^6$	$5.13 \times 10^{20}$
NFW-cuspy	1	3	1.5	12.6	$2.6 \times 10^6$	$4.22 \times 10^{22}$
Iso-min	2	2	0	1	$3.7 \times 10^7$	$8.51 \times 10^{19}$
Iso-mean	2	2	0	2.4	$3.7 \times 10^7$	$9.71 \times 10^{20}$
Iso-max	2	2	0	3	$3.7 \times 10^7$	$1.74 \times 10^{21}$

Table 5.3: Parameters of the DM profiles used in this work. Values of NFW-mean and Iso-mean profiles are the same as of [252]. The  $J$ -factors are integrated over  $10^\circ$  from the halo center.

were combined with the spectrum of several annihilation channels to reproduce the  $\gamma$ -ray flux in the LMC. The 2D J-factor of the different profiles used in this work, computed with *clumpy* can be seen in figure 5.11.

### 5.5.2 $\gamma$ -ray spectrum

For the spectral part of the DM emission model ( $dN_\gamma/dE$  in equation 1.23), the methodology from [215] was followed, where the energy spectra of  $\gamma$ -rays produced by different DM annihilation channels are provided. For this thesis, the studied channels were  $b\bar{b}$ ,  $W^+W^-$ ,  $\tau^+\tau^-$ ,  $\mu^+\mu^-$  including electro-weak corrections as computed in [257]. The annihilation spectral flux of these channels is shown in figure 5.12, computed for a set of DM particle masses.

### 5.5.3 Results on DM sensitivity curves

Using the DM profiles and spectra described in previous sections, a likelihood analysis was performed to obtain the minimum flux needed for the LMC DM component to be detectable by CTA. The Asimov data set with the astrophysical  $\gamma$ -ray sources described in section 5.2 is used for this task as a background on top of which the flux needed to be emitted by each DM model in order to be detected is calculated. To do so, the procedure for upper limits calculation described in section 5.3.3 is applied. Each DM model is included in the model as a new test source, for which the differential upper flux limit for a reference energy, the integrated upper flux limit over the energy range from 0.1 GeV to the DM particle mass, and the integrated energy limit are calculated.

From the resulting flux  $\frac{d\Phi_{ulim}}{dE}$ , replacing the value in equation 5.7, the limit on the velocity averaged annihilation cross section  $\langle \sigma v \rangle$  can be extracted. The sensitivity curves where  $\langle \sigma v \rangle$  is plotted versus DM particle masses are shown in picture 5.13. Each curve corresponds to a specific DM profile and annihilation channel. The space above the curves represent the parameter space of  $\langle \sigma v \rangle$  and DM mass that could be detected by CTA. Since the results on the Asimov dataset only provide mean

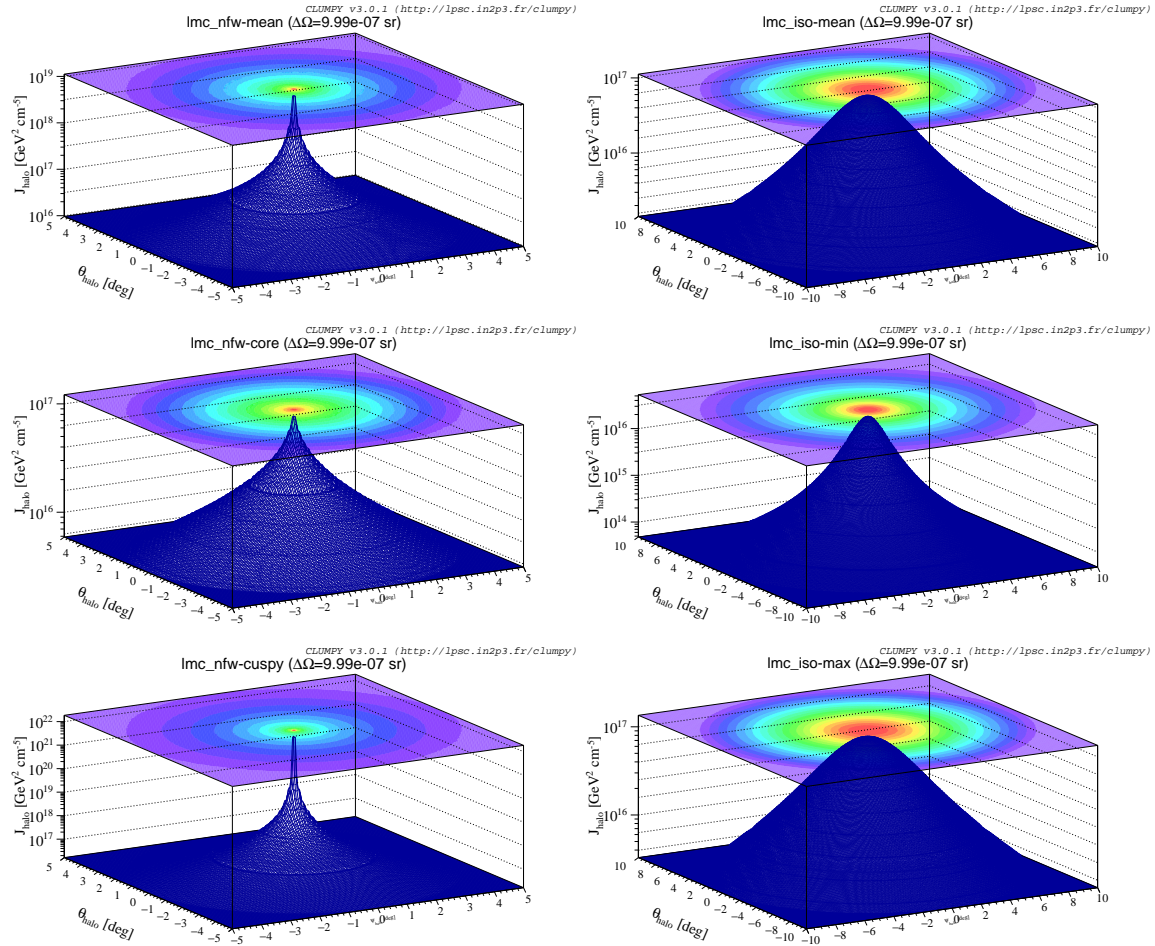


Figure 5.11: 2-D J-Factors of the LMC DM profiles probed in this work. The NFW and Isothermal profiles were computed using the same parameters as in [252].

values, it must be taken into account that these sensitivity curves are subject to uncertainties due to poissonian fluctuations of the data, and systematics. However, because the curves are several orders of magnitude above the canonical thermal cross section (which is the one supported by WIMP theory), it has not been considered necessary to perform a detailed analysis of these uncertainties, which would unlikely reach the region of the canonical thermal cross section anyway.

#### 5.5.4 Effect of the diffuse emission on the DM sensitivity curves

Since the LMC is observed as an extended object and present a particular structure in its diffuse  $\gamma$ -ray emission, it offers the unique opportunity to study the influence of this extended emission in the detection of DM. The differences in the spatial structure of the diffuse  $\gamma$ -ray emission, which is correlated with CR acceleration sources, and the DM density distribution (roughly of spherical shape), can serve as a feature to disentangle the presumably weak signal from DM annihilation, from the diffuse

## Chapter 5. Characterization of the Large Magellanic Cloud at TeV energies and prospects on Dark Matter detection for CTA

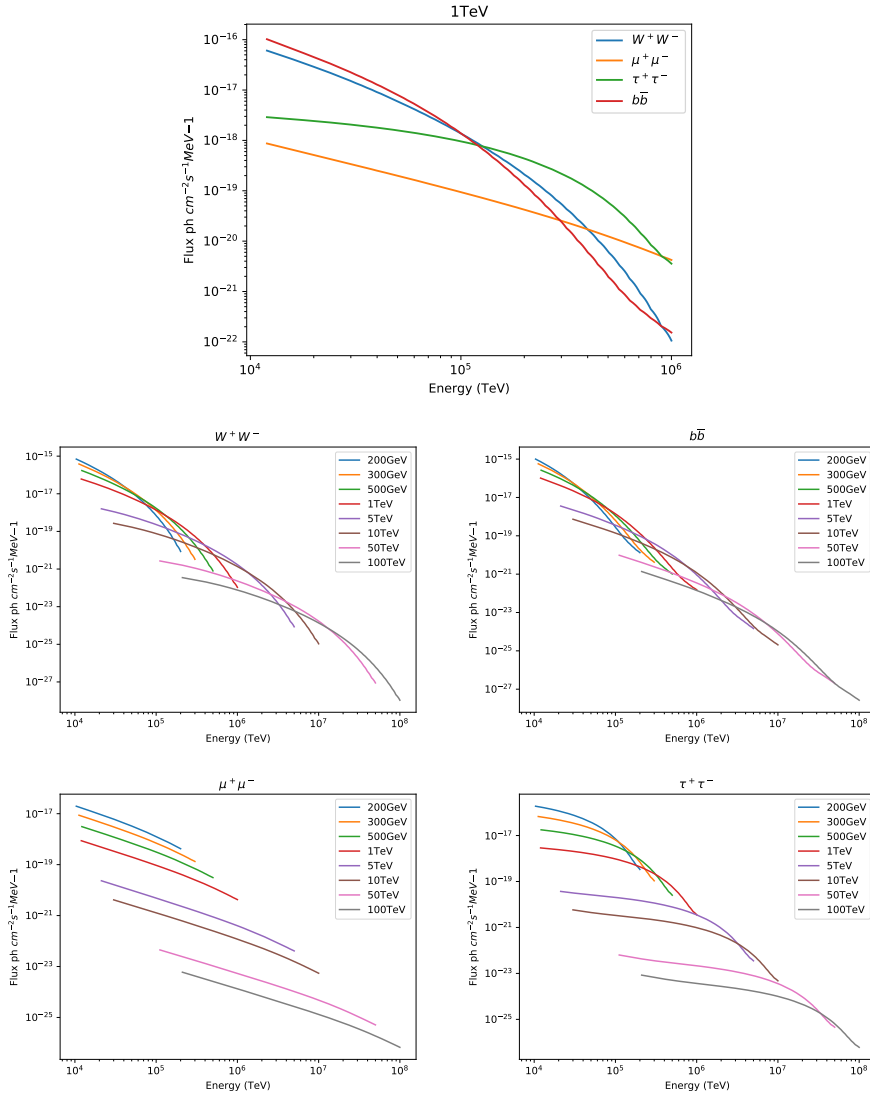


Figure 5.12: Flux of  $\gamma$ -rays produced by DM pair annihilation, for different annihilation channels and masses of the DM particle.

background. To study the effects of the diffuse emission on the DM sensitivity curves, two extra scenarios have been considered: One assuming no diffuse emission in the galaxy at all, removing the leptonic and hadronic components; and other including an enhanced model of pion-decay emission, with a harder spectral index (2.2 instead of 2.7 as the baseline model). For each scenario, sensitivity curves for the mean NFW and mean isothermal profiles, and four annihilation channels have been computed. In picture 5.14 the sensitivity curves obtained for those models are shown compared to the baseline. The effect of varying the spectrum of the large scale interstellar emission mildly affect the DM sensitivity curve, lowering it when removing the diffuse

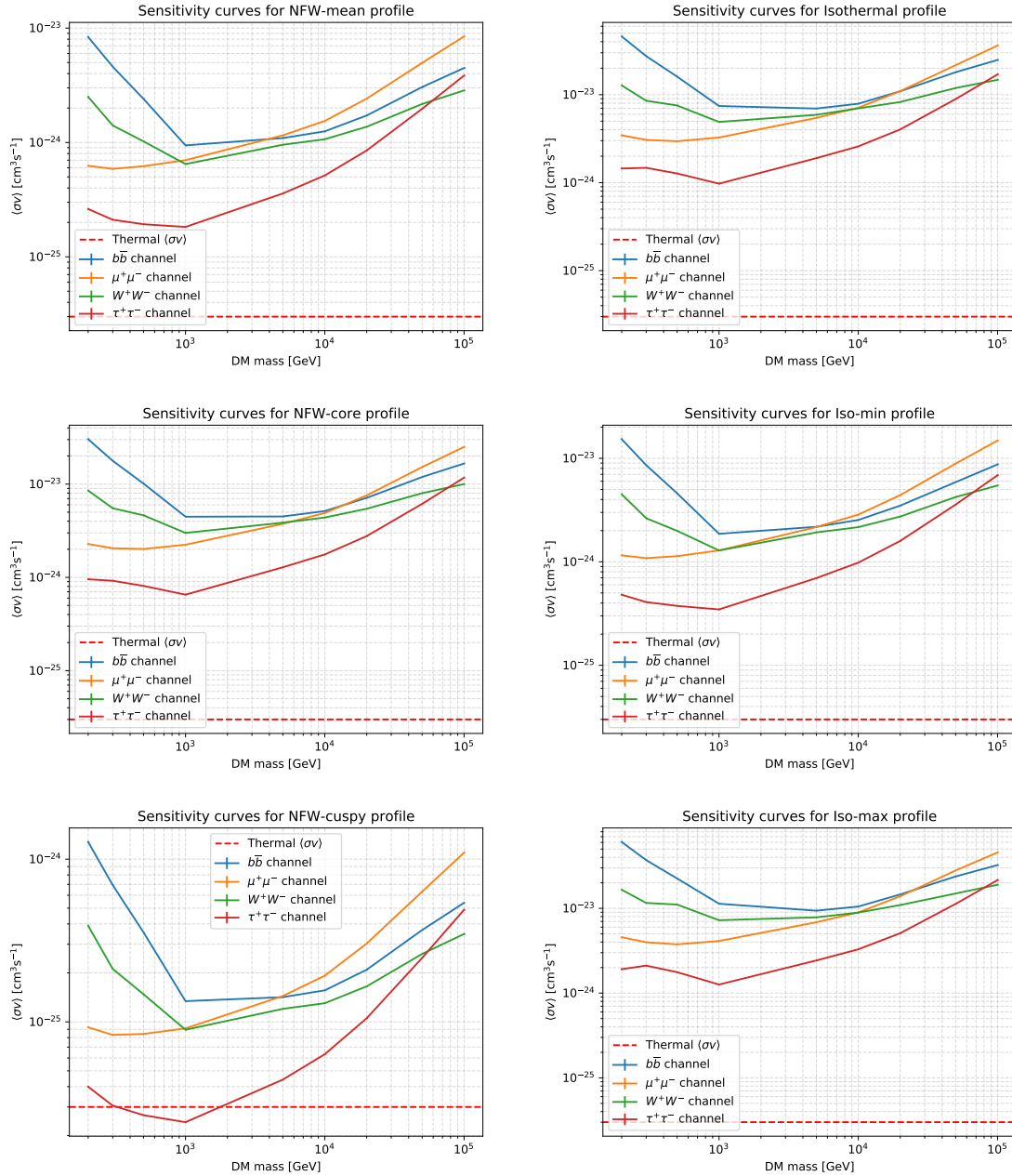


Figure 5.13: Sensitivity curves of  $\langle \sigma v \rangle$  vs. DM particle mass, resulting for the profiles listed in table 5.3, and for four annihilation channels:  $b\bar{b}$ ,  $W^+W^-$ ,  $\mu^+\mu^-$ ,  $\tau^+\tau^-$ .

component, and slightly rising it when the pion decay spectrum is harder. This result means that the DM component and the diffuse components are well separated in the model fitting, at least in the best case scenario, when the true spatial structure of the diffuse component is being fitted. Of course, in a more realistic case where the exact

shape of the diffuse emission is not known, correlations between the two components can arise, affecting the DM limits and likely uprising the sensitivity curves.

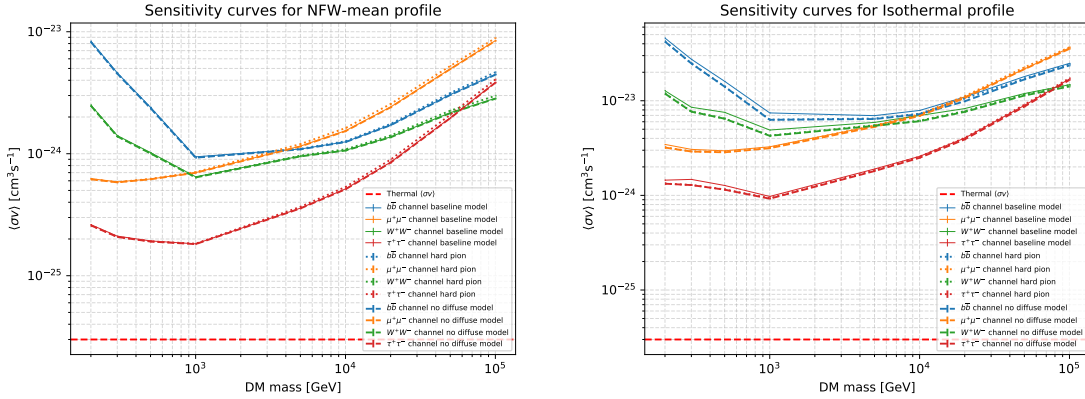


Figure 5.14: Sensitivity curves of  $\langle \sigma v \rangle$  vs. DM particle mass for the NFW-mean (*left*) and Isothermal-mean (*right*) profiles for four annihilation channels, having three different cases of diffuse interstellar emission: Baseline model (thin line), no diffuse emission (dotted line) and pion decay emission with harder spectrum (dashed line).

## 5.6 Summary and conclusions

The deep survey of the LMC will be an ambitious task which will account for many challenges, but that will potentially provide as many scientific results and new discoveries. Besides a lot of work can be done in the subject until CTA is fully available, in this work the first hints on the possible results of the survey have been studied.

Regarding the known point sources, a remarkable high significance has been obtained for all of them, meaning they will be easily detected within the survey with a binned likelihood analysis, which will allow to characterize the sources spectra in the CTA energy range, at least over 100 GeV. Given the duration of the survey ( $>300$  h), it will also be possible to study the variability of LMC-P3, for which an upper flux limit for the off-peak emission has been derived. From the artificial population of PWNe introduced in the emission model, for 15 of them a significance sufficiently large to be detected has been obtained, providing an estimation of the number of new sources that CTA will be able to detect. The computed distribution of PWNe will serve as guide for a blind search, when dealing with real data from the survey.

One of the most interesting features of the LMC is the fact that, as an extended source, it is possible to study the structure of its  $\gamma$ -ray emission, allowing to probe models of CR injection and propagation. In this work, two models of diffuse emission of CR due to leptonic IC scattering and hadronic interactions leading to pion decay have been tested. The possibility to take into account the structure and distribution of CR

sources in the LMC leads to the positive result on the detection of pion-decay emission following the model described in section 5.2.1. This is however a best-case scenario, where uncertainties in the model are not taken into account. It is still an encouraging result to make efforts on the refinement of the analysis and model computation of the diffuse emission in the LMC for the future real data. The IC component, on the other hand, has resulted in a too low significance, meaning it would be not possible to disentangle this emission component from the rest of the background. An upper flux limit has been derived for this model.

Finally, prospects on the detection of a possible  $\gamma$ -ray signal from DM annihilation have been calculated. The results have established the parameter space of DM models which will be possible to study with CTA. The main reasons to point towards the LMC were its extended nature, which allow to rely on DM spatial structure for its differentiation from the background and its relatively high J-factor, comparable to other popular DM candidates such as Dwarf Spheroidal Galaxies (DSphe). However, the big population of other  $\gamma$ -ray emitters difficult the task of extracting a  $\gamma$ -ray signal coming from DM annihilation. In the results presented in this thesis, several DM profiles, annihilation channels and DM particle masses have been tested on top of the emission model of the LMC, to compute the velocity averaged annihilation cross section needed to detect the signal. It can be seen from picture 5.13, that the majority of the models lie several orders of magnitude above the canonical thermal cross section, which is the self-annihilation cross section of WIMP DM in the case of being a thermal relic. This result predicts that CTA will unlikely be able to exclude the canonical cross section for the typical WIMP DM models, except for the most cuspy profiles (yet not very realistic) at DM masses  $\sim 1\text{TeV}$  (case of nfw-cuspy profile and  $\tau^+\tau^-$  channel).

The work performed within this thesis will serve as a starting point for the future work that can be done regarding the LMC KSP. The emission model developed will serve as a benchmark for future studies and for the analysis of real data from the LMC survey. Other topics which have been left out of the scope of this thesis, but which still will benefit from its results could be a more detailed and realistic study on the possible new discovered sources, performing a totally blind search over the PWNe population as a more realistic analysis approach. The PWNe model can also be used to study the possibilities of detecting TeV halos in the LMC, following a similar approach as [258]. Other known sources, not yet detected in the VHE range in the LMC, such as SNR 1987A can be studied on top of the emission model to predict its detectability within the LMC survey. Also, detailed studies on the spectral features which could be extracted from the detected sources can be performed, and many more science cases. On top of that, considering that the commissioning of CTA will take place in several phases, it should be useful to perform a study of possible results obtained with a reduced number of telescopes (instead of the full array as has been done here).

The results presented in this chapter have been gathered in a CTA consortium paper currently in preparation phase, from which the author of this thesis is one of the

corresponding authors.



## 6. Conclusiones

A lo largo del desarrollo de esta tesis, he contribuído a la puesta en marcha de la Red de Telescopios Cherenkov (Cherenkov Telescope Array (CTA) en inglés), aportando mi granito de arena a la astrofísica de rayos  $\gamma$  de muy alta energía.

El prototipo del telescopio grande de CTA, el Large Size Telescope (LST)1, se encuentra en fase de comisionado desde Diciembre de 2018, y desde sus inicios, me he involucrado en diferentes tareas para su puesta en marcha. La mitad del trabajo que he desarrollado durante mi tesis, ha estado destinado al desarrollo y prueba del software de análisis de datos de este telescopio, durante su operación en solitario. Este software, actualmente en una versión muy avanzada, permite tratar los datos recogidos por el telescopio, desde el más bajo nivel (R0), hasta la reconstrucción de la información de la partícula primaria (es decir, su energía, dirección y distinción entre  $\gamma$ s y hadrones, nivel DL2). La reconstrucción de los datos se realiza en varias fases. En primer lugar, los datos recogidos en cada pixel de la cámara son calibrados, de manera que es posible realizar la conversión entre cuentas del Analog to Digital Converter (ADC) y fotoelectrones. Una vez obtenida la imagen de la cascada Cherenkov en la cámara, esta es parametrizada según el método de Hillas. Estos parámetros, junto a la información del tiempo de llegada de la luz a cada pixel, son utilizados para reconstruir la energía, dirección y tipo de partícula primaria con la ayuda de técnicas de Machine Learning, los Random Forests (RFs). Mi contribución a este trabajo, ha consistido en la escritura y verificación de gran parte del código del software, especialmente en sus primeras fases de desarrollo. He utilizado la cadena de análisis, aplicada a simulaciones de Monte Carlo, para derivar el rendimiento del telescopio, que alcanza una resolución en la energía del 20 % en el rango desde  $\sim 100$  GeV hasta  $\sim 1$  TeV. Con respecto a la resolución angular, esta es de hasta  $\sim 0,2^\circ$  en el mismo rango de energías. También he derivado la sensitividad del telescopio a la detección de una fuente puntual tras 50h de observación, que se acerca al 10 % del flujo de la Nebulosa del Cangrejo en el rango

entre 100 GeV y 1 TeV. He utilizado la misma cadena de análisis para reconstruir los datos obtenidos durante las tres campañas de toma de datos llevadas cabo con el LST1, en las que se ha alcanzado una significancia de detección de la Nebulosa del Cangrejo de entre  $6\text{-}10 \sigma/\sqrt{h}$ .

Adicionalmente, he desarrollado un método alternativo para el cálculo de los parámetros de Hillas basado en un algoritmo de Esperanza-Maximización (Expectation-Maximization (EM) en inglés), que no requiere la utilización de un método de limpieza de las imágenes de las cascadas ('cleaning'). Aplicando este método, el rendimiento en resolución angular y de reconstrucción de la energía no llega a ser tan bueno como utilizando el método de tailcuts, excepto para las energías más bajas ( $<200$  GeV). Por otro lado, ha demostrado una mejor separación entre  $\gamma$ s y hadrones, sin hacer cortes en el número de fotoelectrones de las cascadas, lo que permite recuperar un gran número de eventos de baja intensidad. Al hacer el análisis con EM, y optimizar la separación de  $\gamma$ s-hadrones, se obtiene que el corte óptimo en gammaness estaría en torno a gammaness  $>0.7$ . Haciendo este corte, con el método EM se pueden recuperar hasta un 40 % de eventos de  $\gamma$ s, que serían descartados por el método tradicional haciendo el mismo corte. Por otro lado, para el mismo corte de gammaness  $>0.7$ , habría un 10 % más de protones que serían erróneamente clasificados como  $\gamma$ s, con respecto al método tradicional.

Aplicado a datos reales del LST1, el método de EM muestra que puede igualar en sensibilidad al método tradicional, sin hacer cortes en la intensidad de las cascadas, y recuperando por tanto un gran número de eventos, ya que típicamente, para obtener un buen rendimiento con el método tradicional, es necesario descartar cascadas con menos de 500 fotoelectrones. Como consecuencia, presumiblemente este método permitiría conservar un mayor número de eventos de baja energía, reduciendo el umbral de energía del telescopio.

Como segunda parte de la tesis, realizada en paralelo con la anterior, he participado en el proyecto científico de la Gran Nube de Magallanes (Large Magellanic Cloud (LMC) en inglés) de CTA. Este proyecto ha asignado más de 300 horas de observación a esta galaxia, con las que se pretende alcanzar tres principales objetivos científicos: El estudio de las potentes fuentes de rayos  $\gamma$  presentes en la LMC y descubrimiento de otras nuevas, el estudio de la inyección y propagación de rayos cósmicos en la LMC a través de la detección de una emisión difusa; y la posible detección de una señal de aniquilación de Materia Oscura en la galaxia. Para garantizar el éxito de este proyecto, ha sido necesario crear un modelo de la emisión esperada en la LMC en el rango de energías de CTA. El modelo de emisión construido comprende fuentes puntuales conocidas, emisión difusa producida por rayos cósmicos interaccionando con el medio interestelar y una población sintética de nebulosas de viento de pulsar (Pulsar Wind Nebulae (PWNe)). El modelo ha sido utilizado para realizar una simulación de observación con el software de CTA, *ctools*, que reproduce el aspecto que tendrán los datos obtenidos al completar el tiempo de observación asignado al proyecto. Con esta simulación como valores medidos, se ha realizado un ajuste al modelo de emisión, utilizando el método de máxima verosimilitud, para obtener predicciones en las posi-

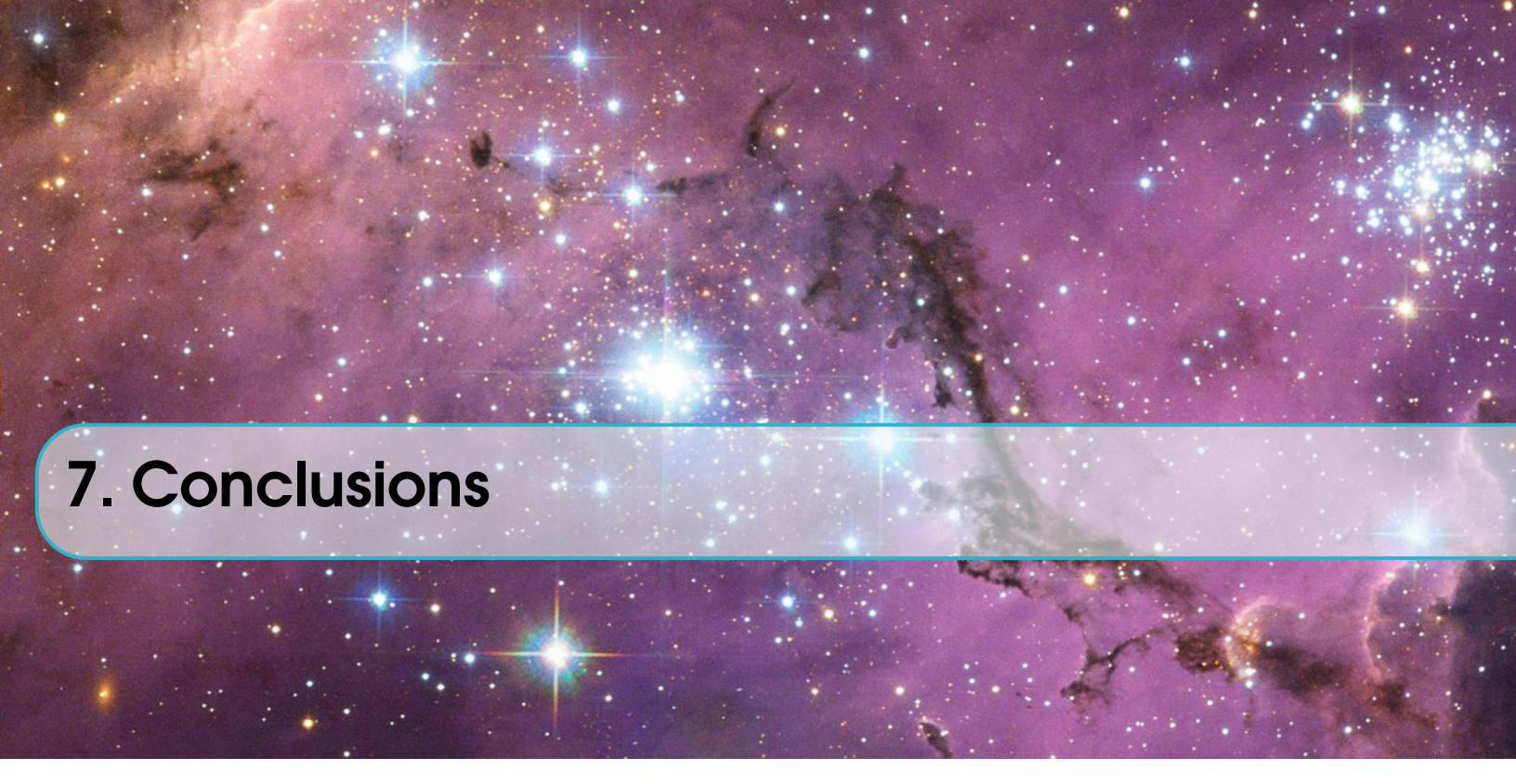
---

bilidades de CTA para detectar y estudiar las diferentes fuentes de rayos  $\gamma$  en la LMC. Los resultados muestran que las potentes fuentes puntuales conocidas serán detectadas con una gran significancia, permitiendo estudiar sus características espectrales en el rango de energías desde 100 GeV hasta 100 TeV. También, se estima que al menos una decena de nuevas fuentes del tipo de PWNe serán detectadas. Con respecto a la emisión difusa de rayos cósmicos, el modelo utilizado para recrear la componente leptónica producida por scattering Compton inverso de rayos cósmicos cargados parece demasiado débil como para poder ser distinguida del fondo instrumental en el análisis. La componente hadrónica, producida por decaimiento de piones, ofrece resultados más optimistas, pudiendo ser detectada con alta significancia, especialmente en las regiones donde hay más acumulación de gas en la galaxia.

Además del estudio de las fuentes astrofísicas, se ha utilizado el modelo de emisión creado como un fondo sobre el que estimar si CTA podría ser capaz de detectar una señal de rayos  $\gamma$  producida por la aniquilación de materia oscura formada por partículas pesadas que interaccionan débilmente (Weak Interacting Massive Particles (WIMPs)). Para ello, se han construído diferentes modelos de perfiles de materia oscura en la LMC, combinados con diferentes canales de aniquilación, comúnmente utilizados en la literatura, para estudiar el espacio de parámetros entre sección eficaz de aniquilación y masa de la partícula de Materia Oscura que podría ser estudiado por CTA. Los resultados de este análisis muestran que, salvo en los modelos en los que la materia oscura está muy concentrada en un volumen muy pequeño (modelos, por otro lado, poco realistas), CTA no sería capaz de descartar el modelo típico de WIMPs con la sección eficaz canónica.

Este trabajo servirá como base para el proyecto de la LMC dentro de CTA, y abre el camino para la realización de análisis más realistas y que se acercaría más a los resultados con datos reales. Los próximos pasos serían hacer un análisis ‘ciego’ de las fuentes puntuales, estudiar en detalle las características que se podrán derivar de las fuentes conocidas, incluir en el modelo el remanente de supernova SNR1987A, incluir una población desconocida de remanentes de supernova, etcétera. Los resultados de este trabajo han dado como fruto un artículo dentro del consorcio CTA que se encuentra actualmente en fase de preparación, y del cual soy una de las principales autoras.





## 7. Conclusions

Along the scope of this thesis, I have contributed to the commissioning of the Cherenkov Telescope Array (CTA), playing my small part to the very high energy  $\gamma$ -ray astrophysics field.

The prototype of the Large Size Telescope (LST) is currently in its commissioning phase since December 2018, and since its beginning I have participated in several activities related to it. Half of the work done during this thesis has been destined to the development and verification of the software for the analysis of LST1 data during single telescope operation. This software, currently in a very advanced version, allow to reduce the data taken by the telescope, from the raw level (R0), to the reconstruction of the primary particle information (energy, direction and distinction between  $\gamma$ s and hadrons, level DL2). The data reconstruction is made in several phases. In first place, the data recorded in each pixel is calibrated, doing the conversion between Analog to Digital Converter (ADC) counts and photoelectrons. Once the image of the Cherenkov shower is extracted, it is parameterized followig the Hillas method. These parameters, together with the arrival time of the light to each pixel, are used to reconstruct the energy, direction and type of particle making use of a set of Random Forests (RFs), a machine learning method. My personal contribution to this task, has consisted in the writing and verification of the code for the analysis, specially in its initial versions. I have used the analysis chain, applied to Monte Carlo simulations, to obtain the performance of the telescope, which reaches an energy resolution of 20% in the range from  $\sim 100$  GeV to  $\sim 1$  TeV. About the angular resolution, it goes down to  $\sim 0.2^\circ$  in the same energy range. I have also computed the sensitivity of the telescope to the detection of a point source in 50 hours of observation time, which goes close to the 10% of the Crab Nebula flux in the range from 100 GeV to 1 TeV. I have applied the same analysis chain to reconstruct real data recorded with the telescope during the three data taking campaigns, where a significance of  $6\text{-}10\sigma/\sqrt{h}$  has been reached

for the detection of the Crab Nebula.

In addition, I have developed an alternative method for the calculation of the Hillas parameters based the Expectation-Maximization (EM) algorithm, which do not require the application of a cleaning to the shower images, and therefore no tuning of cleaning parameters is needed. Using this method, the performance obtained regarding energy and angular resolution is in general, not as good as when applying the traditional tailcuts cleaning, except for the lower energies (below 200 GeV). On the other hand, it has shown a better performance in  $\gamma$ -hadron separation, even without making strong cuts in the intensity of the showers, which allow to recover a large number of low intensity  $\gamma$  events. Performing the data reconstruction with EM and optimizing the  $\gamma$ -hadron separation, the best cut in gammaness is  $> 0.7$ . With this cut, it is possible to recover up to a 40% of  $\gamma$  events, which with the traditional tailcuts cleaning method would be discarded. On the other hand, it has the caveat of missclassify 10% more of hadrons for the same cut in gammaness, relative to the traditional method. Applying this method to the real data of the three Crab campaigns of LST1 provided similar values of maximum detection significance as of the method with tailcuts cleaning, but applying a lower cut in intensity which allow to preserve more events, and reach higher  $\gamma$  rates. Typically to obtain a good performance with the tailcuts cleaning method, it is required to discard showers with less than 500 or 1000 photoelectrons. As a consequence, the EM allows to preserve more showers with low energy, and therefore, lower the energy threshold of the telescope.

As a second part of the thesis, in which I have worked in parallel with the previous, I have participated in the Key Science Project (KSP) of the Large Magellanic Cloud (LMC) for CTA. This project has more than 300 hours of observation assigned to a full galaxy survey, which pursues three main scientific goals: The study of the powerful  $\gamma$ -ray sources of the LMC and the discovering of new ones, the study of cosmic-ray injection and propagation by the detection of the  $\gamma$ -ray diffuse emission in the LMC; and the possible detection of a Dark Matter (DM) annihilation signal in the galaxy. For this project, it has been necessary to create a model of the expected  $\gamma$ -ray emission from the LMC in the energy range of CTA. The model computed includes four known point sources detected by current  $\gamma$ -ray telescopes, diffuse emission produced by Cosmic Rays (CRs) interacting with the Interstellar Medium (ISM), and a synthetic population of Pulsar Wind Nebulae (PWNe). The model has been given as input for a simulation of the data that would be obtained from the CTA LMC survey, using the CTA software *ctools*. This simulation has been then used to perform a binned likelihood analysis, fitting the simulated values to the model, in order to foresee the possibilities of CTA to detect and study the different  $\gamma$ -ray sources of the LMC. The results show that the powerful known point sources will be detected with high significance, allowing to study their spectral features on the energy range from 100 GeV to 100 TeV. Also, at least around a ten of new sources of the Pulsar Wind Nebula (PWN) type will be discovered by CTA. About the diffuse emission from CRs, the model built to reproduce the leptonic component, as a result of Inverse Compton (IC) scattering of charged CRs, seems to be too faint to be disentangled from the

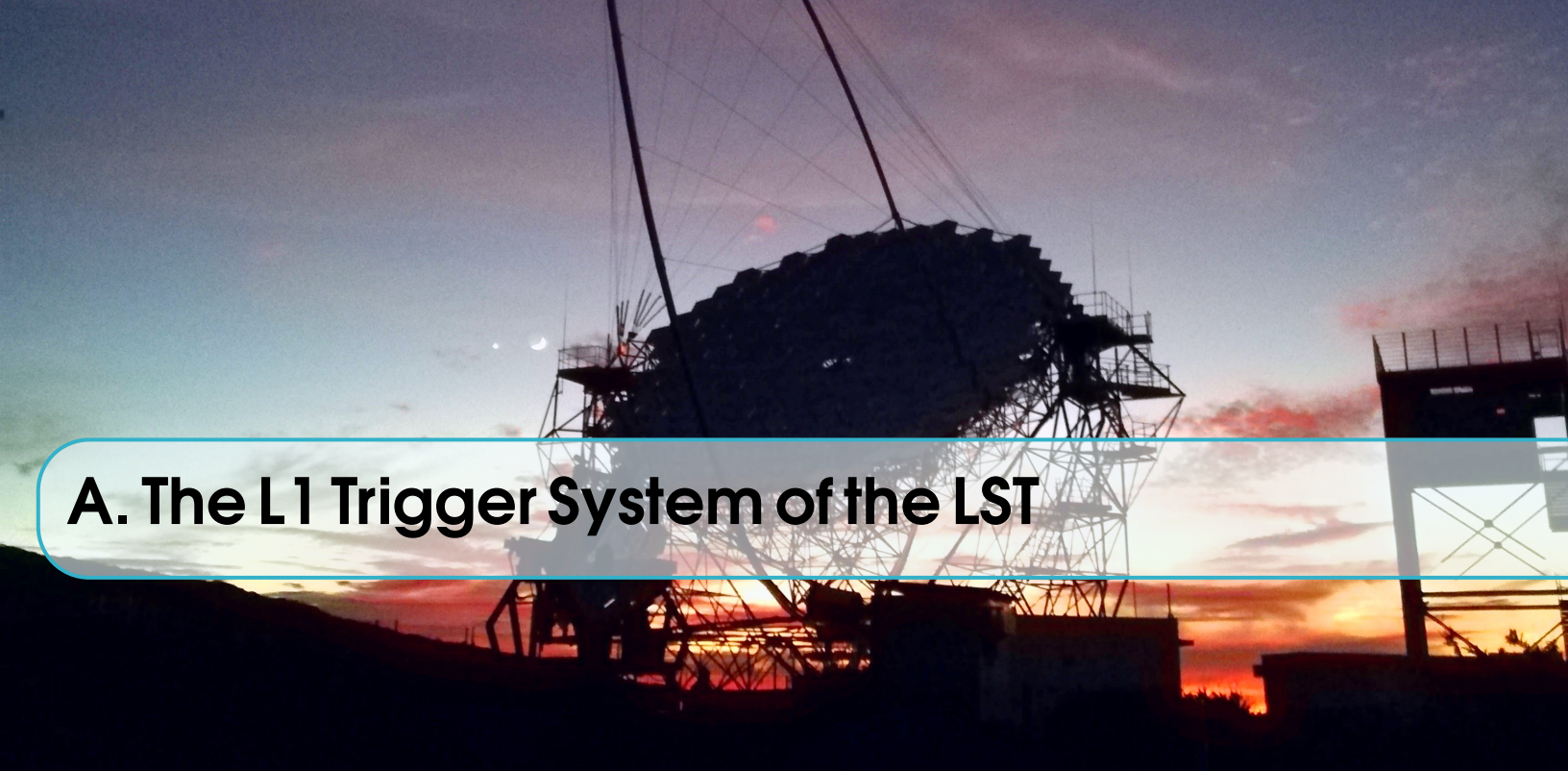
instrumental background. On the other hand, the hadronic component, produced by pion-decay, offers more optimistic results, with high significance values specially in regions with high gas density.

Besides the study of the astrophysical sources, the emission model and the results from the previously described analysis, have been used as background over which to study the possibilities of CTA to detect a signal from the annihilation of DM composed by Weak Interacting Massive Particles (WIMPs). To do so, different models of DM profiles in the LMC have been tested, together with a set of different annihilation channels, typically used in the literature, to study the parameter space of annihilation cross section and DM particle masses which could be probed by CTA. The results from this analysis show that, except for the models with very cuspy DM profiles (yet unrealistic ones), CTA will not be able to rule out the typical WIMP model of the canonical thermal cross section.

This work will serve as a baseline for the LMC KSP, opening the path for more detailed and realistic analysis. The next steps would be to perform a blind analysis of the point sources, with a detailed study of the spectral features which could be derived, include in the model the Supernova Remnant (SNR) 1987A, include a synthetic population of SNRs, etc.

The results from this work have been gathered in a CTA consortium paper, currently in preparation, for which I am one of the corresponding authors.





## A. The L1 Trigger System of the LST

### A.1 Introduction

Imaging Atmospheric Cherenkov Telescopes (IACTs) work detecting the Cherenkov light produced by the interaction of  $\gamma$ -rays and other particles in the atmosphere. These Cherenkov photons must be distinguished from those of the Night Sky Background (NSB) that fill the atmosphere, and constantly reach the telescopes. An efficient trigger system is necessary to decide whether the light reaching the camera must be stored as a Cherenkov event, or discarded as background. Typically this task is accomplished by recognizing a concentration of signal from several pixels both in space and time which would belong to a shower, while NSB light is randomly distributed over the entire camera.

Two possible approaches for the detection of coincident light are used in IACTs, known as *majority trigger* and *sum trigger*. In majority trigger the light of each pixel is compared to a certain threshold. If the signal of most pixels in a certain region exceeds the threshold in a short time, the trigger is fired. This approach presents a disadvantage when detecting low energy photon showers, as happens in Large Size Telescope (LST). The problem is that as the pixels must overcome the threshold individually, therefore, if the signal is too low, it is possible that not enough of them exceed the threshold and therefore the event would be interpreted as NSB. On the other hand, the sum trigger approach takes into account the total signal coming to a group of several pixels. The light arriving at each pixel of the group is added and this sum is compared to a threshold to fire the trigger. If several close groups of pixels surpass the threshold at a given time window, then the event is recorded as a shower event.

In the LST, a multilevel trigger system is implemented, that guarantees the rejection of the majority of the NSB. The pixels in the LST camera are distributed in 265

hexagonal modules of 7 pixels, that are connected to each of its 6 neighbors. The first trigger level (L0) sums the signal of the pixels in each module, and if it is higher than the configured threshold, it sends the L0 signal to the neighboring modules. In the second trigger level (L1), each module takes the trigger signal coming from its neighbors and compares it to another threshold to decide if the camera trigger is fired. Finally, the third level compares the camera trigger of several telescopes and if two or more telescopes have triggered in a certain time window, the event is recorded. A scheme of the trigger system of LST is shown in picture A.1. In the next sections, a detailed description of the three trigger levels is given.

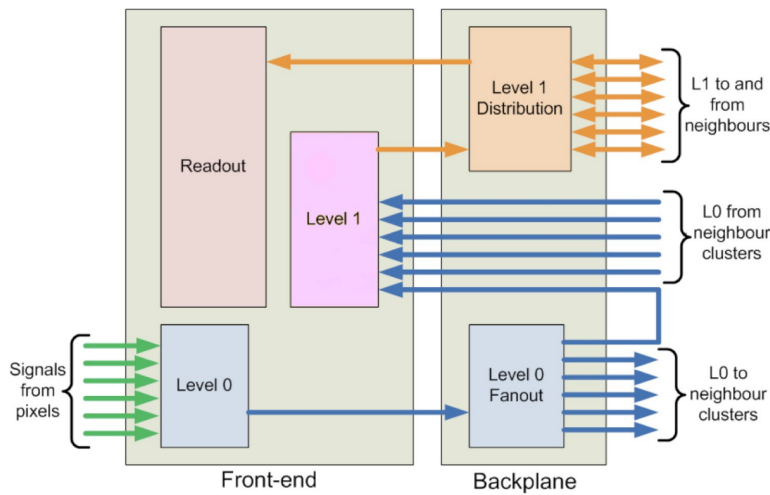


Figure A.1: Architecture of the analog trigger system of the LST.

## A.2 Pixel Level: L0 trigger decision

The pixel-level trigger, known as L0, takes into account the signals from the pixels in one module or cluster. If the trigger is fired, the signal is replicated and distributed by the L0 fan out to the local L1 and the neighboring modules. Both, the majority and sum trigger approaches have been implemented in LST.

### A.2.1 Majority trigger

The majority approach counts the number of pixels in a module that have a signal over a certain threshold voltage, generating a digital signal. The signal from all the pixels is added, with a resulting amplitude proportional to the number of activated pixels, that goes to the local L1 trigger system, and the neighboring modules. This approach does not account for the number of photoelectrons that activated each pixel, only for the number of pixels that have surpassed the threshold. This means that even if a large number of pixels in a region receive a flash of light but in each pixel

the amount of photoelectrons is not over the threshold, the event will not be recorded, possibly losing very low energy events.

### A.2.2 Sum trigger

The sum trigger adds the signal received in each pixel of the module and the resulting signal is compared with a threshold voltage. If the threshold is surpassed, the signal is sent to local L1 and neighboring modules. This way makes it possible to take into account the photoelectron contribution of all pixels of the module, raising the sensitivity to low energy events while still rejecting NSB events. After adding the signals of all pixels, a clipping is applied to overcome afterpulse effects in the photomultipliers. Afterpulses are sometimes produced after a real pulse in the photosensors, due to the ionization of residual gases, and can contribute with a very high amplitude to the sum.

### A.2.3 Camera Level: L1 trigger decision

Camera level trigger decision system, known as L1, analogically adds the resulting signals of L0 trigger from neighboring modules and compares the result with a threshold voltage. If the analog sum is over the configured threshold, a signal is sent through the L1 distribution system to trigger the whole camera. Each module can combine the L0 fan-out signals from six neighbors, plus the local L1. To ensure that all modules are participating in the trigger efficiently, it is possible to configure by slow-control different modes of adding configurations. In figure A.2 the three possible modes are shown. These configurations make it possible, through combinations of two, three, or four modules, to evaluate any trigger region.

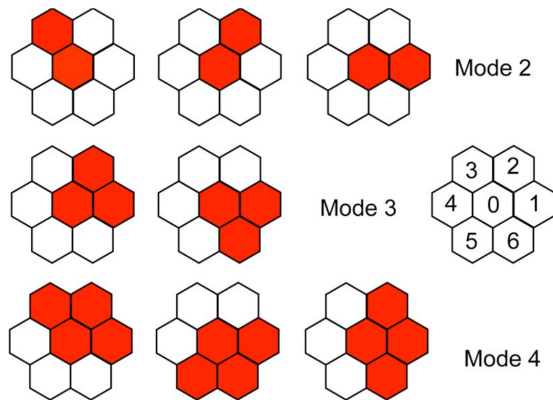


Figure A.2: Illustration of the three possible modes for adding signals of neighbouring modules. Each hexagon represents a group of seven photomultipliers.

The threshold voltages for each module should be calibrated to find the threshold level which produces a trigger signal at a rate of 50%. The calibration algorithm developed for LST camera is described in appendix C.

### **L1 Trigger Distribution**

The L1 trigger distribution system allows the L1 signal to reach the data acquisition systems of all the modules and start the digitalizing process. Every module can propagate the L1 signal to each of its six neighbors, being aware of its position in the camera. This way, when a module receives an L1 signal, it can be delayed depending on its position in the camera, and be sent to the appropriate neighbors following the preconfigured paths (See figure A.3). The distribution paths are firmware configurable and they can automatically be reconfigured to go through the full camera, even if one module is malfunctioning or deactivated. The algorithm developed for the time delay calibration of the L1 signal is described in appendix D.

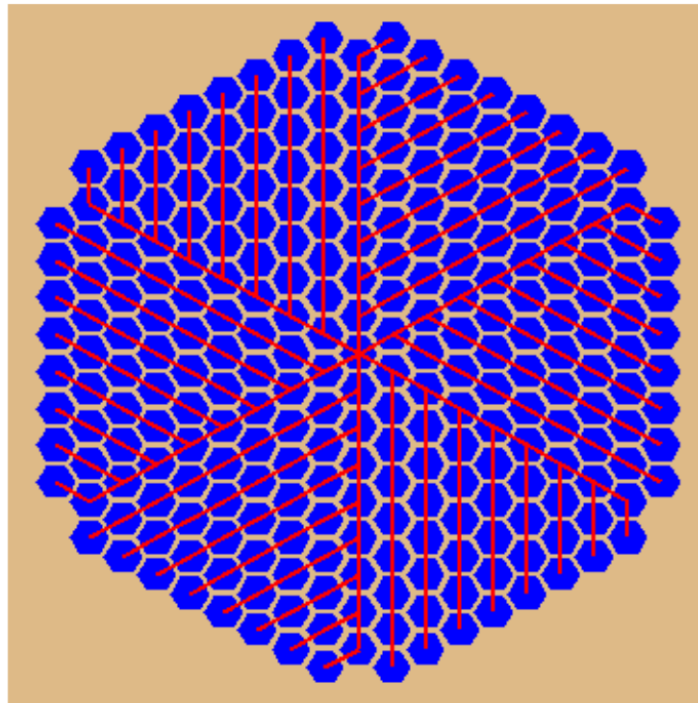


Figure A.3: Paths for trigger distribution over the entire camera.

#### **A.2.4 Array Level trigger decision**

Array level trigger looks for coincidences in events recorded by several telescopes. If more than one telescope produces a camera trigger in a certain time window, the light is likely produced by a Cherenkov shower, so the event will be stored. This level rejects the majority of NSB events that have overcome the lower level triggers.



## B. Characterization of analogue ASIC for L1 trigger decision

### B.1 Introduction

The implementation of the analog L1 Trigger System in the Large Size Telescope (LST) cameras has been made using a dedicated Application-Specific Integrated Circuit (ASIC) [259]. The function of the ASIC is to collect the analog signals from the L0 fan-out, add them in three different configurations, and discriminate the resulting voltage to produce digital trigger output signals. The ASIC was designed to accomplish several specifications needed to ensure the required performance for Cherenkov Telescope Array (CTA): it must be flexible to work with the two L0 trigger modes (sum and majority) and to configure the three L1 trigger modes from picture A.2. The noise must be lower than 0.2 photoelectrons per added channel. The range of the signals processed must be between 0.2 and 100 phe. The gain of the ASIC must be such that it will avoid saturation if the entire signal is concentrated in one channel. Bandwidth must be greater than 500MHz to avoid Night Sky Background (NSB) pulses being added with the signals. Because all the electronics are installed inside the camera box, the ASIC must be compact and have a low power consumption ( $< 150mW/ch$ ). The scheme of ASIC is shown in picture B.1.

There are seven input differential analog channels and two output differential digital channels in the ASIC. The seven signals arriving at the input channels are replicated three times and sent to three analog adders (named A, B, and C). The signals in each adder are selected by a set of switches, corresponding to the different configurations of the three trigger modes. The output of the adders is sent to two discriminators, which make the comparison of the added signal with a threshold voltage. The two discriminators have different and independent threshold voltages, low and high-level, generated by differential Digital to Analog Converters (DACs). The discriminator outputs are connected to two OR gates which are in turn connected

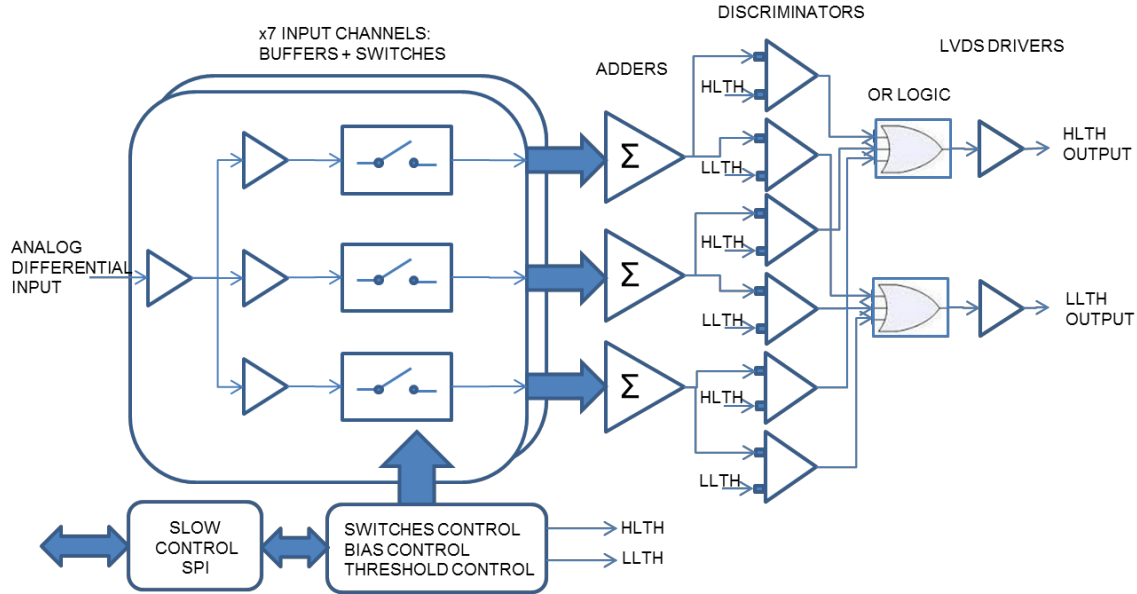


Figure B.1: L1 ASIC Block diagram

to Low-Voltage Differential Signalling (LVDS) transmitters that provide the trigger signal.

About 400 ASICs were produced at CIEMAT, subject to quality control tests to validate their performance. The tests probed several characteristics of the ASICs, such as gain, noise, and offset, for all the channels, adders, and discriminators. From all the ASICs tested, 389 surpassed the quality control test, and the results were analyzed to characterize the general behavior of the ASIC. The result is an overall view of the features that a default ASIC would have, shown in table B.2. In this appendix, the results of the characterization of the L1 ASICs produced at CIEMAT are summarized, using the data from the quality control tests.

## B.2 Quality control test

The quality control test consisted of several steps to qualify the behavior of the ASIC in its different parts (seven input channels, three adders, and two LVDS outputs). The quality control provided a datasheet for each individual ASIC with the results of the tests. Each combination of channel (7), adder (3), and discriminator(2) is tested separately, having a proper gain, offset, and noise. This procedure allows the detection of a defect in any part of the ASIC. The quality control tests provided direct measures of offset and noise, but gain must be calculated from the rate scan results in the test voltage. This procedure also offers another way of measuring the offset. The computation of gain and offset from the rate scan, described in section B.2.2, was performed considering a linear behavior of the input voltage vs. threshold voltage for the 50% trigger rate. From a linear fit, the gain and offset are obtained. In the next

sections, the different steps of the quality control test are described.

### B.2.1 Test DAC

Measurement of the maximum and minimum voltage of the DAC was taken directly from the output pin of the ASIC by a multimeter. Each DAC set is composed by 2 DACs of 9 bits to get a final resolution of 10 bits (positive and negative parts). The measurement is made setting the code in the register with the maximum and minimum values for both positive and negative parts.

### B.2.2 Voltage Test: Rate scan

The Voltage test measured the gain of all seven input single channels and the two outputs for 10 different voltages (from 100 mV to 1000 mV) using a rate scan methodology, consisting on the comparison of the input trigger rate from a generator on the evaluation setup and the ASIC trigger output rate. This computation is performed with scalers implemented in the FPGA board.

### B.2.3 Test Adder Channels

The gain of different sum combinations was obtained by the same rate scan methodology. There are three different methods, combining different channels of different adders.

### B.2.4 Analog Offset test

The Analog offset test consisted of the measurement of the offset in the Analog Adder Output test, which is the output of a multiplexor that selects among the available analog output adders, plus a buffer for the output pins. The measurement is made directly from the differential output pin of the ASIC by a Multimeter.

### B.2.5 Digital Offset test

The Digital offset test procedure measures the offset in the LVDS digital outputs, by the evaluation of the output status as a function of the threshold. The methodology consists in increasing the threshold from 0 Volts using the DAC values until finding the minimum value where the output goes from 1 to 0, and the maximum for which it goes from 0 to 1. The voltage difference between these two points is the noise of the digital output, and the mean point is the offset. Setting the Threshold to 0, three possible behaviors are observed:

- If the status of the digital output is a logic '1' (tagged as type 'Pos') it is possible to measure the minimum and the maximum points and therefore it is possible to calculate the offset and the noise.
- If the status of the digital output is a logic '0' (tagged as type 'Neg'), it is not possible to measure neither the minimum nor the maximum point, and then a value of zero is assigned by the program both to the noise and the offset.

- If the status of the digital output is switching (tagged as type 'Com'), it is only possible to measure the maximum value, and the other is assigned to 0. In this case the noise is underestimated and the threshold is overestimated.

## B.3 Characterization of the ASIC

In this section, the results from the quality control tests for all ASICs are analyzed and discussed.

### B.3.1 Rate Scan Fit

For the calculation of the gain, the output of the Voltage test is used to perform a linear fit. If we assume a linear model, the relation between the input voltage and the rate scan result should be:

$$V_{rs} = Gain * V_{input} + Offset \quad (\text{B.1})$$

Where  $V_{rs}$  represents the threshold voltage that gives a rate of 50% trigger, and  $V_{input}$  is the input voltage. The use of this method has the advantage of obtaining not only the gain but also the offset of the ASIC without having to measure it with a multimeter. Since linearity seems to depend on the input voltage, it is necessary to consider a range for the fitting where the linearity is better. To do so, several ranges were fitted and the offset obtained was compared to the offset measured with the multimeter in the analog offset test. The range where the difference between the two offsets was lower was selected as the best range to fit the linear model. The resulting range was from 0 to 300 V and so this range was used to calculate the gain and offset for every path of each ASIC. In figure B.2 the rate scan result versus ten input voltages for a certain path (channel, adder, discriminator) of one ASIC is shown. The linearity can be easily appreciated, especially for low input voltages (under 500 mV).

### B.3.2 Gain

The gain was calculated with the model fitting described in the previous section. Figure B.3 shows the distribution of gain values over the paths of the 389 ASICs. A clear gaussian profile is observed, centered in the characteristic gain of 0.87, the expected result according to the design specifications. Some outliers were identified as having gain values that are too low for the requisites, which could mean a malfunctioning in the ASIC. Fitting the distribution to a gaussian, it is possible to see that the probability of an ASIC to have a gain lower than 0.7 in any of its paths is lower than 0.025%. There are some outliers with higher gain values, but the probability of any entry to have a gain over 1.05 is lower than 0.007%. The outliers are identified in image B.3 by their ASIC number.

Cleaning the outliers from the sample, the characteristic gain is  $0.87 \pm 0.038$ , obtained from the gaussian fit. This is an average of all the possible paths of channel,

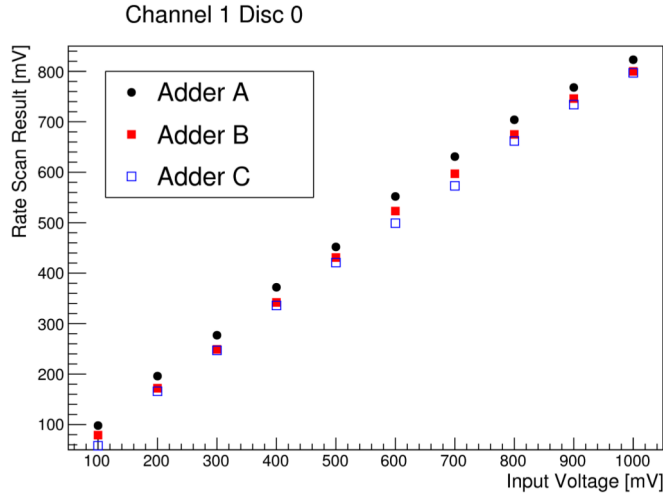


Figure B.2: Rate scan result from one of the voltage tests for ASIC #61. It can be observed a linear tendency which deteriorates at high voltages. Similar plots where obtained from the rest of channel-adder-discriminator combinations.

Channel	Mean Gain	RMS
1	0.871	0.035
2	0.839	0.036
3	0.880	0.036
4	0.873	0.036
5	0.876	0.036
6	0.873	0.036
7	0.878	0.036

Table B.1: Mean gains for the seven channels, averaged to the sample of all asics, without the outliers.

adder, and discriminator in the ASICS analyzed. A single path characterization is given in table B.2, each entry averaged to all ASICS. When having the average gain for each channel separately in table B.1 and in image B.4, it can be observed that the second channel has a slightly lower gain than the others, and the third one a slightly higher gain. This effect comes out from the configuration used during the quality control tests. The third channel was connected directly to the pulse generator, while the second channel had to be fed with a cable of a different length than the others.

To find if any part of the ASIC is dominating the fluctuations of the gain, correlation plots between channels, adders, and discriminators were studied. A remarkable correlation is not observed in any of the elements of the ASIC, so we can conclude that all parts contribute to the final value of the gain similarly.

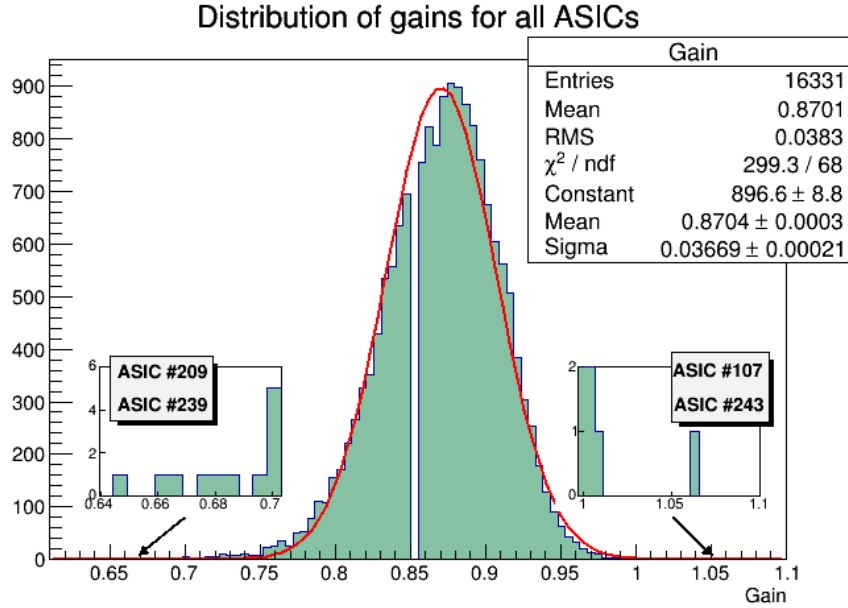


Figure B.3: Distribution of gains for all ASICs. Each entry represents the gain of one possible path (a combination of channel-adder-discriminator). The red line represents a gaussian fit with mean 0,8704 and sigma 0,3669. The zoom-ins show several outliers with gains very deviated from the average.

### B.3.3 Offset

The offset has been measured in three different ways. In the tests, the analog offset was directly measured with a multimeter, the digital offset was measured using the procedure described in section B.2.5, and finally, from equation B.1 an offset value that will be called fit offset was calculated. In figure B.5 the distributions of the analog and digital offsets are shown. It must be noted that it was not possible to measure the digital offset for all the configurations, only the ones with an output status tagged as ‘Pos’, so it’s not possible to measure negative values of digital offset. Some outliers were detected, with digital offset values very deviated from the mean, which has been removed from the sample at the final characterizaton. Those outiers correspond to ASICs 110, 209, 248 and 437.

The average value of the analog offset is  $-6.138$  mV with RMS of  $13.01$  mV while for the digital offset the mean is  $8.41$  mV with RMS of  $6.17$  mV. Plotting the correlation between the two measured offsets( B.6 it can be seen that there is a correlation between the two ways of measuring the offset.

Regarding the fit offset, the distribution of the obtained values is shown in figure B.7. To check the validity of this method of obtaining the offset value, the difference between the fit offset and the analog offset has been studied. The averaged value of the fit offset is  $0.1334$  mV with RMS  $13.75$  mV. The mean difference between the analog offset and the fit offset is of  $5.55$  mV with RMS  $8.06$  mV. Checking the

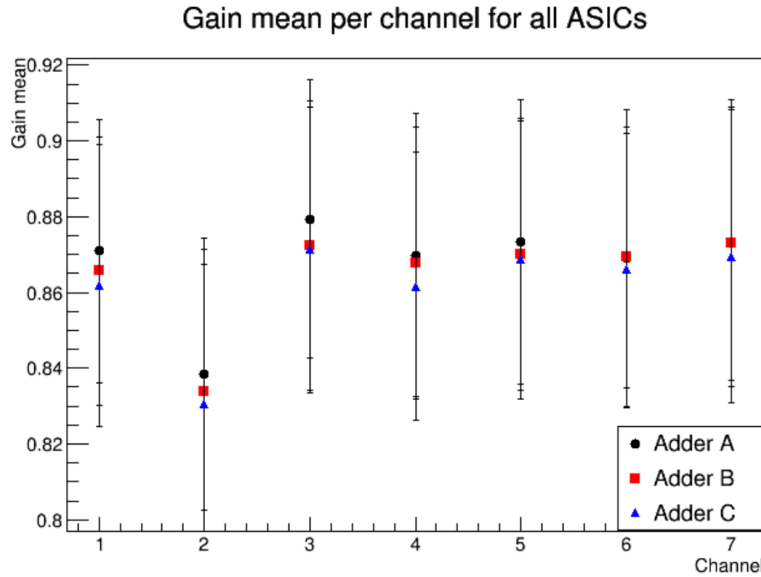


Figure B.4: Gain mean of all ASICs per channel, for the three adders. Vertical bars represent the RMS of the distribution in each channel.

correlation between the two offset values (fig B.6) it can be observed that even there is a clear correlation between them, the fit offset is underestimating the analog offset measured. In figure B.8 the averaged offsets to all ASICs, separated by channels and adders are plotted. In general the offset takes similar values for all the channels and adders, without any remarkable outlier. In table B.2 the average offsets to all ASICs in every single path are shown.

To find out which part of the ASIC is responsible for the offset, correlation plots between channels, adders, and discriminators were studied. Channels and discriminators show a clear correlation between pairs of them, but for adders, a real correlation is not observed. This implies that the offset does not depend on the channels or discriminators, but it is introduced by the adders. This result was expected from the original specifications of the ASIC.

#### B.3.4 Noise

The noise in the ASIC was measured during the Digital Offset test described in section B.2.5. The noise again can only be measured when the output status is tagged as ‘Pos’. In figure B.9 the total distribution of noise values is shown, having an average noise of 5.186 mV with RMS of 2.878 mV. Several outliers were spotted and are marked in the plot, with noises very deviated from the mean. If we fit a gaussian profile to the distribution, the probability of having an outlier with noise over 40 mV is 0% and over 10 mV is less than 1%. These outliers have been excluded from the general characterization.

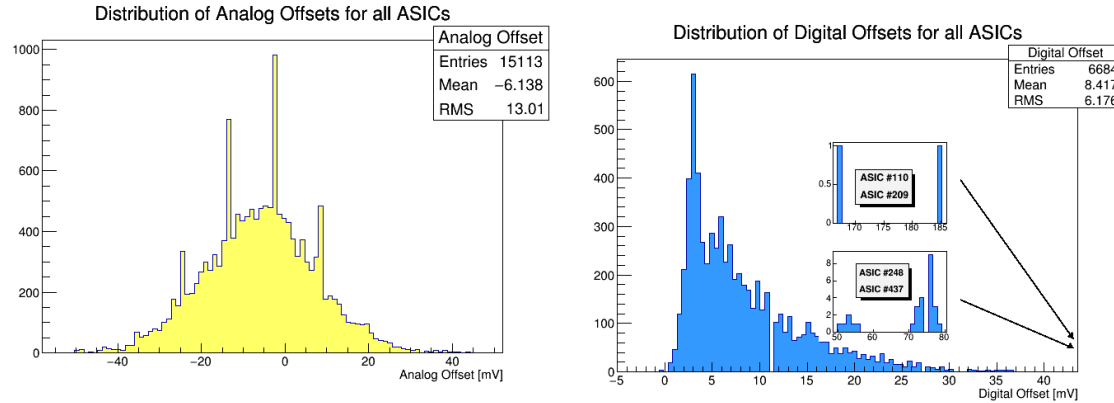


Figure B.5: Distribution of offsets for all ASICs. Each entry represents the offset of one possible path (combination of channel-adder-discriminator). *Top:* Analog offset. *Bottom:* Digital offset. The zoom-ins represent outliers in the digital offset.

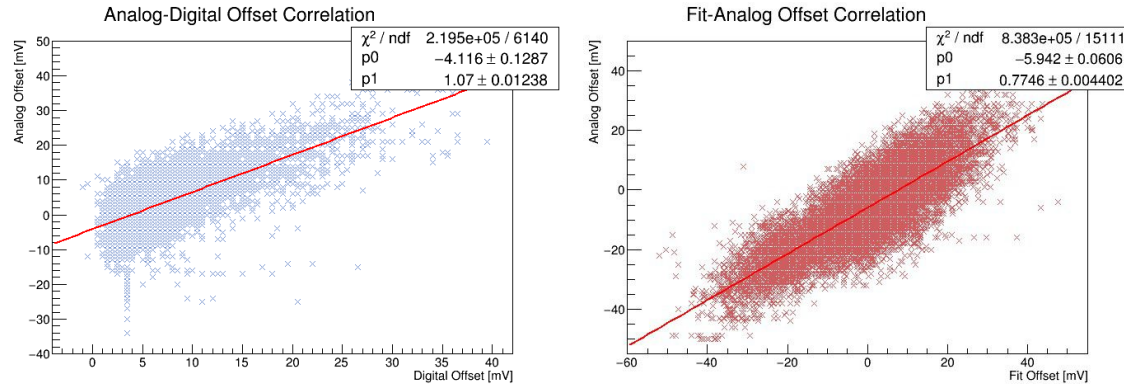


Figure B.6: *Left:* Correlation between analog offset and digital offset. *Right:* Correlation between analog offset and fit offset.

No correlation of the noise between pairs of channels, adders or discriminators have been observed, so the noise is being introduced in each part of the ASIC in a similar way. In figure B.9 the average noise value separated by channels and adders shows that its value is mostly uniform.

## B.4 Characterization: Summary and discussion

The gain measured in the ASIC has a typical value of about  $0.87 \pm 0.038$ , having two channels that slightly differ from the rest. Is the case of the channels 2 and 3, that for all ASICs seem to have a deviation from the general mean. This effect is explainable by the setup configuration of the rate scan test. There are two ASICs where the gain has a very low value, under 0.7, in several of their channels. Relative to the correlation study, there is not a strong correlation for the gain in any part of

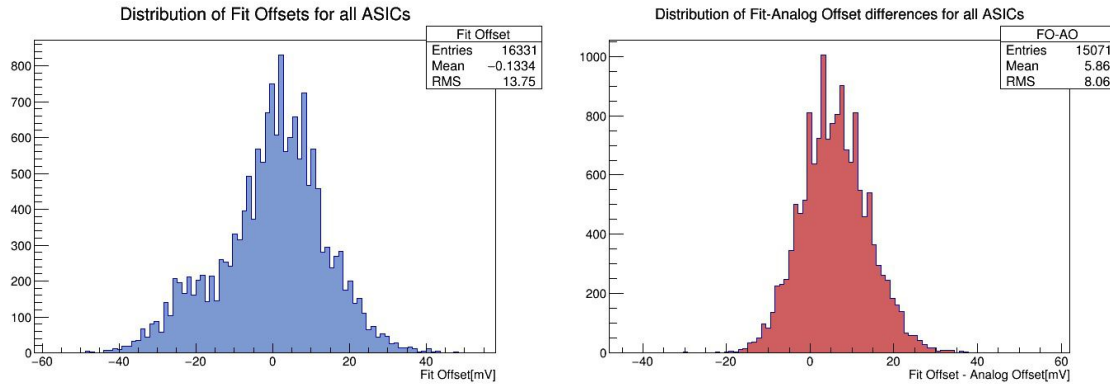


Figure B.7: *Left:* Distribution of offset calculated from the rate scan fitting. *Right:* Distribution of the difference between the analog offset and the fit offset.

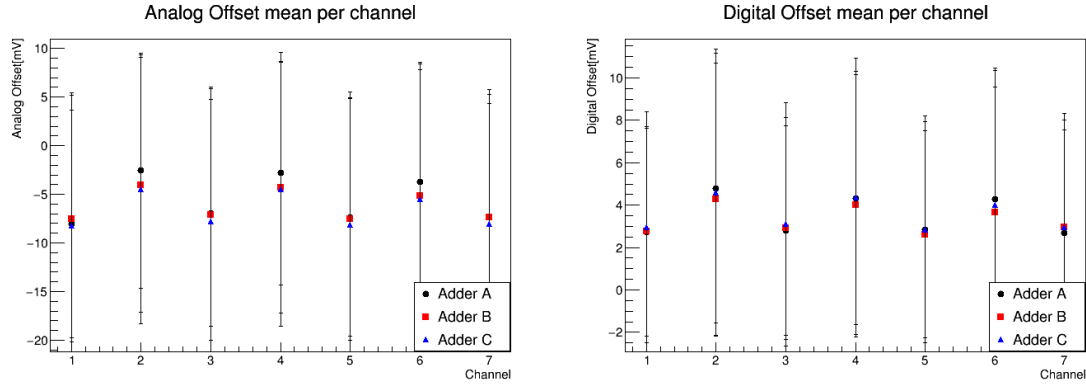


Figure B.8: *Left:* Analog offset averaged to all ASICs separated by channel and adder. *Right:* Digital offset averaged to all ASICs separated by channel and adder. Vertical lines represent the RMS of the distribution in each channel.

the ASICs, having all of them a correlation coefficient below 0,5.

The analog offsets measured in the test have a negative mean value, while the digital offset, as the rate scan can only measure positive offsets, gives a positive mean value. In the correlation plots for the analog offset, it can be observed a positive correlation between channels, with correlation coefficients  $\sim 0,8$ . For the adders however, no significant correlation is observed, concluding that in the adders, the offset measured is independent of each other, so they are the part of the ASIC where the offset is introduced. In the case of the digital offset, no correlation is observed at all, with coefficients very close to 0. It is needed to take into account that the data of the digital offset is biased by the rate scan conditions. From the correlation plot of digital and analog offset, we can say that both offsets have a correspondence and we are measuring the same feature, having a linear correlation with slope  $\sim 1$ . In summary, the offset expected from a typical ASIC would be of  $-6 \pm 13$  mV.

A method to calculate the offset of the ASIC in an indirect way was applied assuming

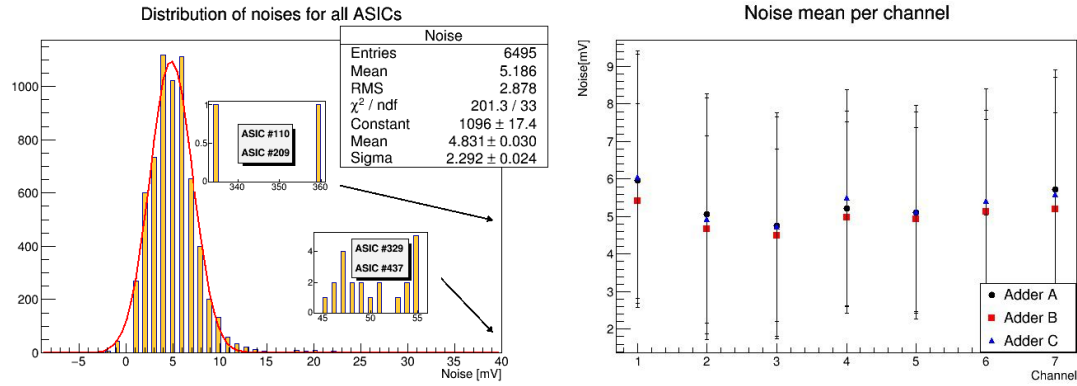


Figure B.9: *Left:* Distribution of noises measured for all ASICs. Each entry represent the noise in a certain path (channel-adder-discriminator combination). The zoom-ins show the outliers. *Right:* Noise averaged to all ASICs separated by channel and adder. Vertical lines represent the RMS of the distribution in each channel.

a model where the input signal and the rate scan result have a linear relation. The offset calculated by this method have in average, a difference with the analog offset of  $5.86 \pm 8$  mV. The correlation between the fit offset and the analog offset showed that they have a linear correlation by a factor of 0.774. The study of the fit offset in the different parts of the ASICs supported the idea that the adders are responsible for introducing the offset in the ASIC.

Finally, the values of gain, offset, and noise averaged to all the ASICs studied are shown in table B.2. These values represent the typical values that should be expected from a correctly functional ASIC. If deviations from these numbers are observed, it might point to a defect in the ASIC, meaning a bad performance that will not fit the specifications.

Disc.	Ch.	Add.	Gain	RMS	Analog Offset[mV]	RMS[mV]	Digital Offset[mV]	RMS[mV]	Fit Offset[mV]	RMS[mV]	Noise[mV]	RMS[mV]
0	1	0	0.870941	0.0347202	-8.04178	11.7013	7.6831	5.41629	0.237361	12.2547	5.86861	3.00563
0	1	1	0.865733	0.0354431	-2.56825	12.0754	9.26942	6.00255	5.42159	13.151	4.73869	2.65657
0	1	2	0.861889	0.0372319	-6.90529	11.6572	7.38961	5.61574	0.459297	13.2761	4.40559	2.48136
0	2	0	0.838466	0.035875	-2.82682	11.5199	8.88718	5.92886	4.81186	12.0241	5.08421	2.35825
0	2	1	0.833886	0.0374605	-7.35196	12.2333	7.90845	5.88134	0.506872	13.5916	5	2.55973
0	2	2	0.830387	0.0369065	-3.70752	12.1045	8.92932	6.18108	3.99229	12.8837	4.79679	2.44105
0	3	0	0.879369	0.0367518	-7.35933	11.7325	7.87132	5.64872	0.784061	13.1786	5.64662	3.484
0	3	1	0.872314	0.0381587	-7.52089	12.7001	7.58562	5.68263	-0.450728	13.1254	5.22917	2.54056
0	3	2	0.871234	0.0377928	-4.04735	13.1041	9.25946	6.80006	3.55013	14.3746	4.32	2.18838
0	4	0	0.869755	0.0373787	-7.07521	12.9157	8.36331	6.00024	0.205656	13.5603	4.19231	2.25012
0	4	1	0.867655	0.0359559	-4.30168	12.8884	8.9435	6.38963	2.65292	13.278	4.65497	2.18266
0	4	2	0.861649	0.0354134	-7.55153	12.4649	7.70956	5.78174	0.0951152	13.1499	4.81395	2.60223
0	5	0	0.873273	0.0374989	-5.17827	12.9837	8.79697	6.41468	1.78835	13.7437	4.80921	2.19069
0	5	1	0.870116	0.0359688	-7.37604	12.6522	8.36525	5.49044	-0.487576	13.7508	5.05839	2.46957
0	5	2	0.868586	0.0368392	-8.2312	13.7086	8.84926	6.51816	-0.999143	14.8268	5.9771	3.5693
0	6	0	0.86892	0.0393618	-4.48189	13.8268	9.7963	7.14917	3.15424	15.5242	4.8895	3.11456
0	6	1	0.869291	0.0343526	-7.76602	13.8442	8.83929	6.63897	-0.61611	14.7812	4.48462	2.61721
0	6	2	0.866015	0.0360581	-4.48324	14.1144	9.44624	6.93439	3.11168	14.9143	5.3587	2.9565
0	7	0	0.873033	0.0379731	-8.15042	13.6576	8.28777	6.33279	-0.973436	14.9387	4.92537	2.75526
0	7	1	0.872879	0.0360707	-5.50418	14.0574	9.41124	7.01801	1.49357	14.6893	5.28402	3.06379
0	7	2	0.869562	0.0386874	-8.07242	13.8974	8.32168	6.35307	-0.732647	14.9372	5.6383	2.63978
1	1	0	0.881697	0.0341451	-8.04178	11.7013	7.4927	5.56054	-3.03256	12.605	6.04444	3.70158
1	1	1	0.876093	0.0328864	-2.56825	12.0754	9	6.24797	2.56555	12.6045	5.40816	3.62626
1	1	2	0.872108	0.0318161	-6.90529	11.6572	7.15753	5.46745	-2.59383	12.1416	5.12057	3.43424
1	2	0	0.847899	0.0314701	-2.82682	11.5199	8.46073	5.71851	1.5189	11.4802	5.34737	2.79574
1	2	1	0.845232	0.0323591	-7.34819	12.2164	7.43103	5.58897	-3.17824	13.3383	5.1958	2.79425
1	2	2	0.838856	0.0329706	-3.70752	12.1045	8.5582	5.93878	0.9006	12.3124	5.41711	2.95009
1	3	0	0.890874	0.0358411	-7.35933	11.7325	7.37132	5.31715	-3.06684	12.7281	5.78195	2.88199
1	3	1	0.884409	0.0339822	-7.52089	12.7001	7.07483	5.47237	-3.13453	13.5406	5.6069	2.64522
1	3	2	0.883612	0.0325719	-4.04735	13.1041	8.89503	6.50563	0.259641	13.9549	5.01156	2.73066
1	4	0	0.882881	0.034909	-7.07521	12.9157	7.51034	5.7519	-2.88689	13.3739	4.77698	2.30121
1	4	1	0.878196	0.0336269	-4.30168	12.8884	8.66384	6.19265	-0.0876289	13.5648	5.28977	2.82262
1	4	2	0.875941	0.0309881	-7.55153	12.4649	7.20438	5.55088	-3.23393	13.001	5.03759	2.28893
1	5	0	0.887686	0.034171	-5.17827	12.9837	8.5122	6.00304	-0.83976	12.6118	5.41718	2.66956
1	5	1	0.881864	0.0329572	-7.37604	12.6522	7.61986	5.27637	-3.32048	12.9181	5.34028	2.65666
1	5	2	0.877262	0.0327925	-8.2312	13.7086	7.81071	5.98285	-3.39332	14.0924	6.13971	3.1557
1	6	0	0.880771	0.0354957	-4.48189	13.8268	9.3288	6.61699	0.871464	14.3059	4.99444	3.31913
1	6	1	0.878608	0.0332089	-7.76602	13.8442	8.63603	6.52525	-3.29734	13.35	4.96296	3.16791
1	6	2	0.87653	0.031666	-4.48324	14.1144	9.18362	6.59579	-0.118557	13.5596	5.63793	2.83065
1	7	0	0.887339	0.0345601	-8.15042	13.6576	7.87037	6.10918	-3.0437	13.7544	5.31579	2.9389
1	7	1	0.88383	0.033284	-5.50418	14.0574	8.97059	6.77424	-0.674379	13.6534	5.5503	2.8985
1	7	2	0.881967	0.0317656	-8.07242	13.8974	7.93478	5.91143	-3.7892	14.0832	5.56115	3.54846

Table B.2: Values of the gain, offset (measured by three different methods) and noise for the different parts of the typical ASIC, obtained averaging to all the ASICs tested.





## C. Calibration method for the L1 analog trigger system of LST camera

### C.1 Introduction

During the year 2016, a connectivity test took place at CIEMAT involving 35 modules of the Large Size Telescope (LST)1 camera, to evaluate the integration of the electronics and mechanical structure. As explained in chapter 3, the modules of the LST are designed to be manipulated individually, allowing easy removal and substitution in the case of malfunctioning modules. The goals of the C35 test were to evaluate the interface between cluster mechanics and the cluster holder, check the possible interference of modules during assembly, establish an assembly procedure, find potential problems during assembly, and test assembly time. Also, it was dedicated to checking the interfaces between the different parts of the electronics such as the Dragon boards and mezzanines, and the connection between the clusters and the backplanes. During this test, 35 modules were assembled in the camera plate in different configurations, and several connectivity tests were performed, such as tests on the clock, PPS, camera trigger and busy signals, power supply, trigger distribution along the camera, and time delays configuration.

Within the scope of the C35 test, it was necessary to design a calibration method for the L1 transfer function, to find the threshold voltage which produces a trigger rate of 50%, depending on the input signal. In the next sections the calibration algorithm developed for this task is described and results on the calibration are commented. This is the calibration method currently implemented in the telescope.

### C.2 L1 transfer function calibration

A method for the calibration of the L1 analog trigger system was developed and tested, based on a rate scan methodology. The goal of the calibration is to find the threshold

voltage needed in each module to obtain a trigger rate of 50%. The calibration needs to be performed for each one of the three adders and two discriminators of the L1 Application-Specific Integrated Circuit (ASIC). The 50% trigger rate threshold is obtained for several input signals to plot a curve that allows retrieving the gain and offset of the circuit and compare them with the characterization of the ASICs.

The setup for the calibration consists of one module where a pulse with fixed amplitude and frequency can be injected in each of its seven pixels by the Slow Control Board (SCB). Increasing signal voltages are generated by adding the pulses injected in each of the seven channels of the module, meaning that in total it is possible to obtain up to 6 points for the calibration curve. An algorithm based in a bisection method is applied to each input signal to calculate the 50% trigger rate threshold.

### C.2.1 Calibration algorithm

The algorithm for this calibration has been implemented using a scripting language specially designed for the C35 test. It proceeds by configuring a fixed gain and frequency pulse in the SCB, in a fixed number of pixel lines. This way, the amplitude of the input pulse can be modified by adding more pixels. Once the initial pulse is configured, a bisection method is used to find the 50% trigger rate threshold. The threshold voltage in the ASIC is configured through a Digital to Analog Converter (DAC) with 8 bits, which can provide up to 255 different voltages from 0 to 1.2 V in steps of 4.8 mV. The algorithm initiates setting the threshold at the maximum voltage (setting the 8 bits to 1) and runs bit by bit, from the most significant bit, changing 1 to 0. If the new threshold voltage provides a trigger rate that is less than the target rate (in this case the target is 50%) then that threshold voltage is stored and the algorithm goes to the next bit. This way, only 8 steps are necessary to find the required threshold voltage. A diagram describing the algorithm is shown in figure C.1.

Once the loop is finished, the 50% trigger rate threshold is calculated following the formula:

$$50TH = \frac{(TargetRate - Baseline)}{(Baseline - Rate[CurrentThreshold - 1])} + CurrentThreshold \quad (C.1)$$

Being baseline the rate at the current threshold, say the last threshold that was stored in the loop.

### C.2.2 Calibration result

When the full algorithm ends and runs over the 6 possible input signals, the obtained 50% threshold can be plotted against the number of pixels added to see the calibration curve (see figure C.2).

If the initial pulse injected by the SCB is known and assuming that the adding is correct, the amplitude of each pulse is simply the multiplication of the initial pulse by

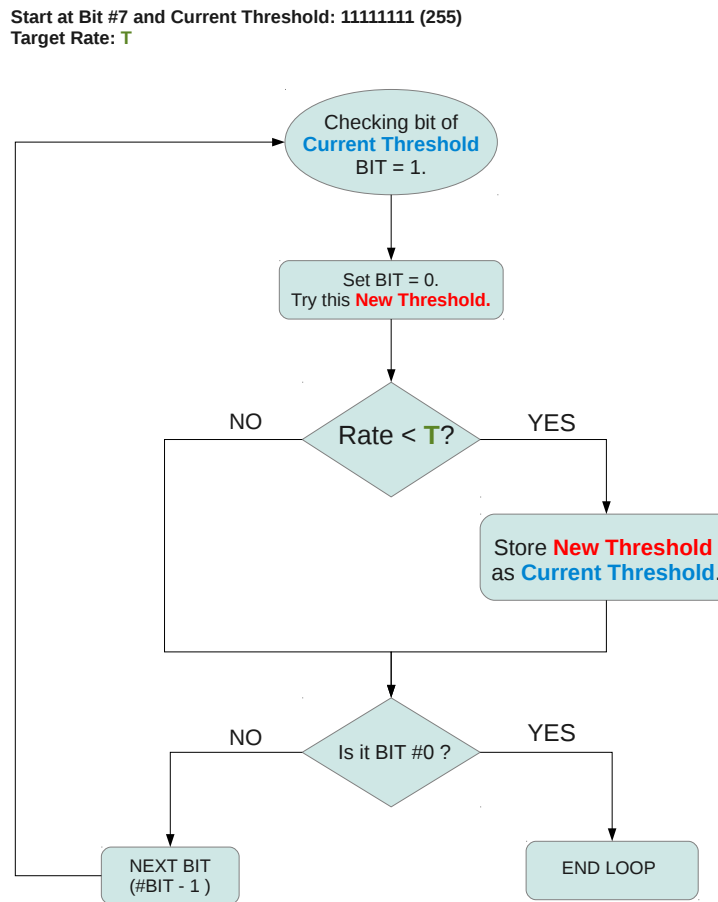


Figure C.1: Flux diagram of the calibration algorithm.

the number of pixels added. This way, it is possible to obtain the gain and offset of the ASIC.

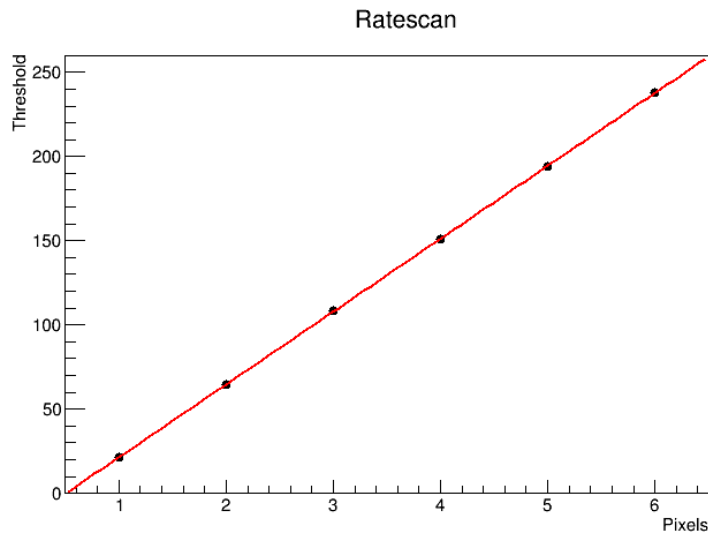


Figure C.2: Result of the rate scan for Adder A of one module.



## D. Time calibration for implementation of the trigger distribution in the backplane network of LST camera

### D.1 Introduction

In the Large Size Telescope (LST), the L1 trigger signal time must be equalized throughout the whole camera. An L0 trigger signal which is transmitted from one module will be propagated backplane to backplane from the center to the outer modules. To ensure that the L1 trigger time is the same in the whole camera, a series of delays must be applied in the backplanes, which depend on the distance of each module to the one propagating the signal. The requirement is that the time difference between all the camera modules must be lower than 300 ps. An algorithm for the time calibration was developed and tested at CIEMAT. A description of the time calibration procedure, algorithm, and results on the tests carried on is included in this appendix.

### D.2 Time calibration procedure

The time calibration is performed in cycles, where one module named the ‘reference’ distributes the signal (also known as the ‘pulser’), and another module, the ‘victim’, receives the signal and must adjust a delay to be equalized with the previous module. The goal of the calibration is to set an outgoing delay ( $oD^V$ ) and ingoing ( $iD^V$ ) delay, in a way that the time for a signal to be transmitted from the central module to the victim ( $t_C$ ), and from the victim to the center ( $t_{L1}$ ) is the same as for the reference module. The scheme of the cycle is shown in picture D.1.

The delays are calculated determining the time difference between the L1 signal leaving the backplane, and the camera trigger signal returning to the backplane. These times are read from the difference between the TDC3 and TDC0 (time-to-digital converters) from the backplane. The calibration is separated into two phases, the

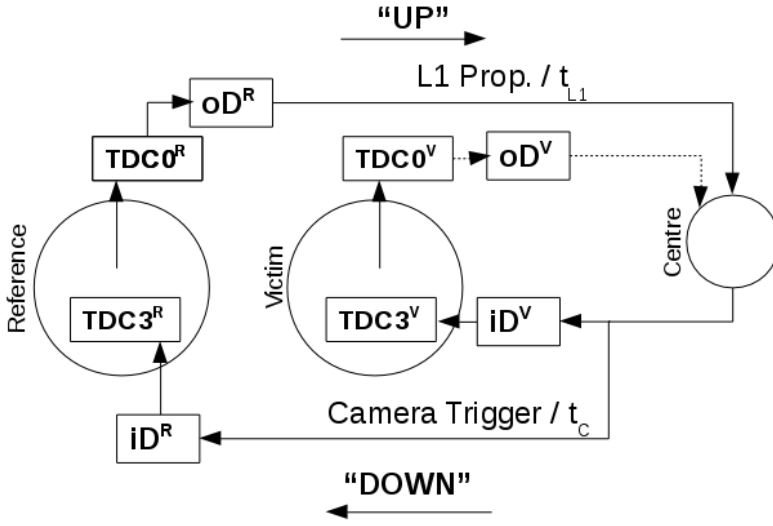


Figure D.1: Flux diagram of the calibration algorithm.

‘down’ calibration and the ‘up’ calibration, as shown in picture D.1.

- For the down calibration, the L1 signal distribution of the victim is deactivated, so the camera trigger signal is only triggered by the L1 of the reference. Because reference and victim are triggered by the same L0, the time at TDC0 for both modules will be the same. The difference  $TDC3 - TDC0 = \Delta$  can be measured both in the reference and victim modules, therefore the incoming delay is simply:

$$iD_V = (TDC3 - TDC0)^r - (TDC3 - TDC0)^V = \Delta^R - \Delta^V \quad (\text{D.1})$$

Once the required delay value is calculated, it is set in two steps: a coarse delay in steps of 10ns and a fine delay in steps of 36 ps.

- For the up calibration, the L1 signal distribution of the victim is activated, and the reference is deactivated. The goal of the up calibration is to set the outgoing delay in a way that the difference  $(TDC3 - TDC0)^V$ , which is the total time the signal needs to go from the victim module to the center and back to the victim, is the same as for the reference. The delay therefore is:

$$oD^V = L - (TDC3 - TDC0)^V = L - \Delta^V \quad (\text{D.2})$$

Where  $L$  is the latency and corresponds to the  $\Delta^R$  measured in the down calibration.

At the end of the cycle, the times  $t_C$  and  $t_{L1}$  will be the same both for reference and victim. At the start of the new cycle, the victim will be the new reference and another module is chosen as the victim.

The calibration algorithm was implemented in a scripting language specifically designed for the communication with the different backplane registers.

### D.3 Time calibration setup and tests

Two time calibration setups were configured at CIEMAT. At first, four modules were set as shown in picture D.2, allowing to run three time calibration cycles as described in the previous section. The test consisted in setting initial default values in the delays, given by the position of the modules, and running the calibration several times for different initial values to ensure the reliability of the procedure. An example of the results obtained in the first set-up is shown in table D.1. This first test allowed to fix a bug in the calibration algorithm regarding the neighbor assignment to the center module, which resulted in a drop in the TDC between the second and third module. After the success of the first implementation, a second setup was prepared involving eight modules. The calibration procedure was performed several times, to check the stability of the final TDC values and that the deviations with every backplane were in the allowed range of 300 ps. The results for six of these runs are shown in table D.2 as an example. It can be seen that the differences between TDC values of the eight modules after the calibration is less than the required 300 ps, verifying the calibration method.

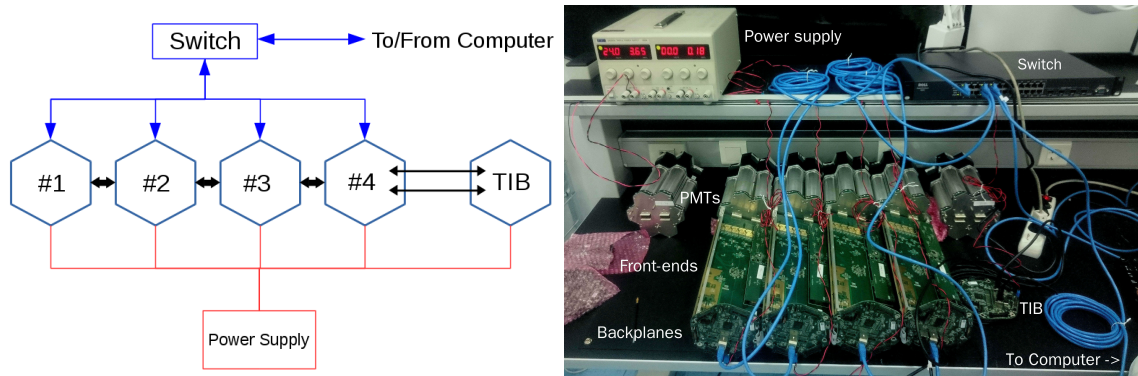


Figure D.2: *Left:* Diagram of the four modules setup. *Right:* Picture of the actual setup at CIEMAT clean room.

The time calibration algorithm was then adapted to perform the calibration of the full camera, following the predefined paths of signal distribution as shown in picture A.3. This time calibration procedure is currently being used in the commissioning of the LST1 and must be run at last once every night of operation of the telescope.

Initial Delays				TDC of bp. no. (ps)			
Coarse up	Coarse down	Fine up	Fine down	#1	#2	#3	#4
8	15	202	254	211619	211615	211085	211061
8	15	194	250	211361	211343	210733	210709
7	15	202	254	202125	202196	201684	201671
7	15	194	254	201848	201881	201326	201417

Table D.1: TDC measurements in the four backplanes of first set up for different initial delays. As can be seen, there is a drop in the TDC values between the second and the third backplanes. This problem was an issue regarding the assignment of the neighbors of the center module, which was solved for the second test.

Module no.	TDC(ps)					
	Run 1	Run 2	Run 3	Run 4	Run 5	Run 6
1	254723	254940	255040	254951	255047	254988
2	254771	254983	255047	254968	255136	255003
3	254846	254960	255082	255143	255117	255031
4	254804	255042	255103	255090	255132	255047
5	254739	255119	255039	255079	255110	254975
6	254741	254948	255052	255099	255110	254923
7	254779	254962	255112	255162	255177	254989
8	254794	254999	255202	255225	255234	254931
Average	254775	254973	255067	255095	255125	254984

Table D.2: TDC measurements for six calibration runs performed in the second set up. The differences in TDC values for the eight backplanes are well within the 300 ps required margin.



## E. Random Forests

### E.1 Introduction

A Random Forest (RF) is a supervised learning algorithm that uses an ensemble of several decision trees [181]. Decision trees are flow-chart-like structures where each internal node denotes a test on a selected feature. The result is a split in the dataset depending on the value of that feature. The best splitting criterion for regression is typically calculated using the mean squared error (MSE). For each node, the MSE of the two subsets is calculated for each feature and for each possible cut on that feature, until a minimum is reached. This step is repeated at each node until a condition is reached, typically that the MSE of the remaining data sample is below a threshold, or it has too few events to keep splitting. The termination nodes are also known as *leaves*. For classification, the splitting criterion is based on the gini index, described in section E.2. In the RF, several decision trees are trained using a randomly selected subset of the train data ('bootstrapping') and the prediction of all the trees is averaged to reach the final result. Also, the features are always randomly permuted at each split. These two sources of randomness in the RF prevent the typical problem of over-fitting from too complicated decision trees.

### E.2 Gini Index

The gini index or gini impurity is a measure of how often a randomly chosen event would be incorrectly classified if it was classified randomly following the distribution of classes. The formula for the Gini index  $I_G$  calculated for a set of events with J

classes is:

$$I_G(p) = 1 - \sum_{i=1}^J p_i^2 \quad (\text{E.1})$$

Where  $p_i$  is the probability of an event belonging to the class  $i$  to be correctly classified. The Gini index goes from 0 to 1, where 0 means that all the events of a subset have been classified into one class, and 1 that the events of the subset are randomly distributed along with all the possible classes. The splitting decision will be made minimizing the value of the Gini index.

## E.3 Random Forests in cta-lstchain

### E.3.1 Random Forest parameters

The RFs applied in this thesis for the analysis performed in chapter ?? were implemented using the python package *scikit-learn* [193]. Several configurable parameters can be tuned to improve the performance of the RFs. The parameters used in this thesis are summarized in table E.1.

Parameter name	Value for regression	Value for classification	Description
n_estimators	150	100	Number of trees in the forest
criterion	mse	gini	Function to measure the quality of a split
max_depth	50	100	Maximum depth of the tree
min_samples_split	2	2	Minimum number of samples required to split an internal node
min_samples_leaf	2	2	Minimum number of samples to be at a leaf node
max_features	all	all	Number of features to consider when looking for the best split
random_state	42	42	Control the randomness of the bootstrapping and the sampling of features
n_jobs	4	4	Number of jobs to run in parallel

Table E.1: Some parameters that can be configured for *RandomForestRegressor* and *RandomForestClassifier* classes, with the values used in *cta-lstchain* for the training of the RFs used in this thesis.

### E.3.2 Random Forest features

The features used for the splitting of the tree nodes are  $\log_{10}(\text{intensity})$ ,  $\text{width}$ ,  $\text{length}$ ,  $x$ ,  $y$ ,  $\psi$ ,  $\phi$ ,  $\text{width}/\text{length}$ ,  $\text{skewness}$ ,  $\text{kurtosis}$ ,  $r$ ,  $\text{time gradient}$ ,  $\text{intercept}$ <sup>1</sup>,  $\text{leakage2}$  and  $\text{number of islands}$ , where  $x$ ,  $y$ , and  $r$  are the coordinates and module of the vector from the center of gravity of the Hillas ellipse to the center of the camera. These quantities can be ordered based on their importance for the regression, as shown in figure E.1, which is calculated based on the *Gini* index (see section E.2). It can be seen for example that for direction reconstruction there are two features, time gradient and angle  $\psi$ , which are the best candidates to make a good splitting, while for  $\gamma$ -hadron separation all features supply with a similar amount of information.

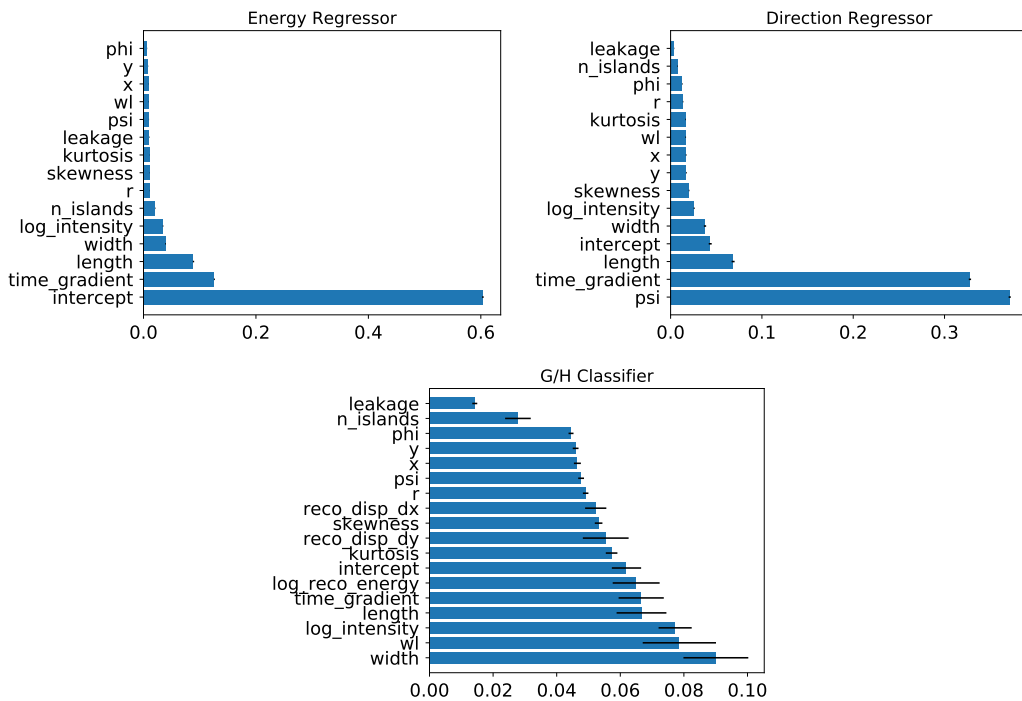


Figure E.1: Parameters importance for the trained RF used in the analysis of Monte Carlo (MC) simulated Large Size Telescope (LST)1 data. The higher the importance value, the more relevant is the feature for the regression/classification.

<sup>1</sup>Intercept has been considered a controversial parameter because it does not have a physical meaning, but still is taken by the RF as a very important parameter for the regression. In the latest versions of *cta-lstchain* this parameter has been removed from the list of features, reaching an even better performance of the RFs.





## F. Evolution of LST1 camera uniformity

### F.1 Introduction

During the commissioning phase of the Large Size Telescope (LST) 1, one of the objectives is to test the uniformity of the camera and perform the necessary adjustments to ensure it. The non-uniformity along all the pixels of the camera translates in some pixels or modules to be more probable to trigger than others, biasing the results of the data analysis shown in chapter 4. To have an idea of the uniformity of the camera during the three Crab campaigns, and spot possible problems in the data, the distribution of the centroids of the Hillas ellipses in the camera has been plotted for each day of observation. This way, anisotropies can be observed, pointing to pixels that are triggered with a different frequency than the mean.

### F.2 Distribution of centroids of Hillas ellipses for standard analysis

In this section, the centroids calculated using the standard LST1 analysis, as described in section 4.2, are shown in pictures F.1, F.2 and F.3.

### F.3 Distribution of centroids of Hillas ellipses for Expectation-Maximization analysis

In this section, the centroids calculated using the Expectation-Maximization (EM) method for Hillas parameterization, as described in section 4.4.1, are shown in pictures F.4, F.5 and F.6.

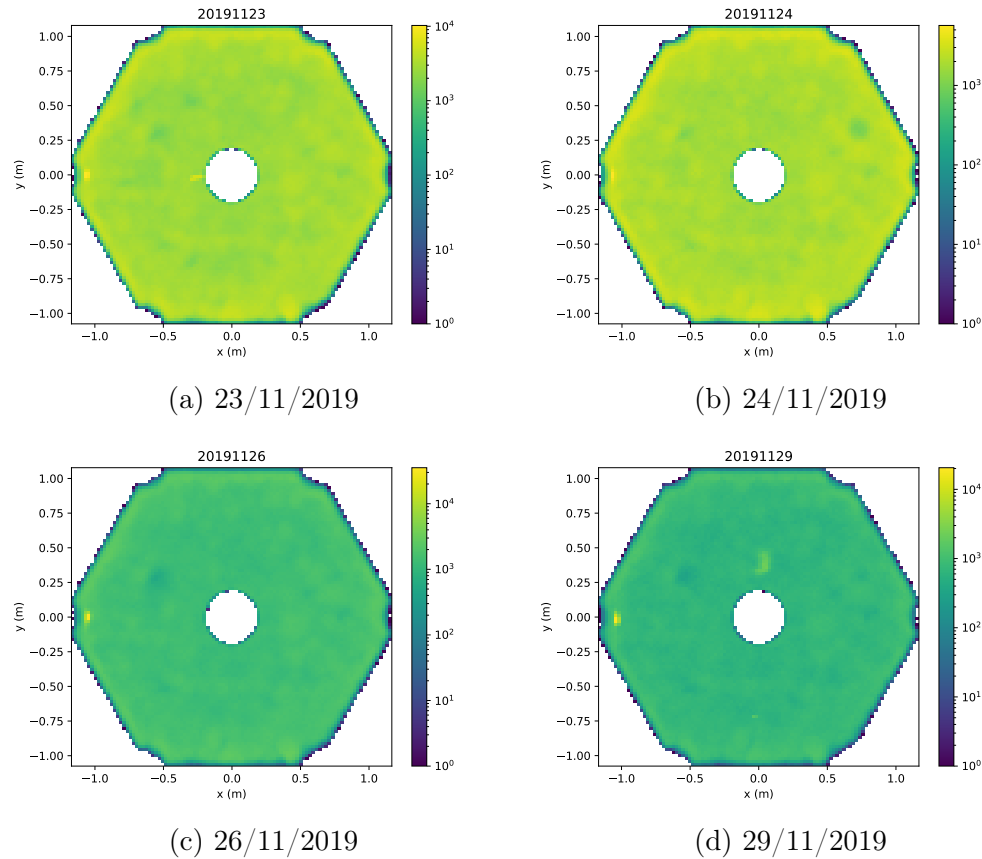


Figure F.1: Distribution of the positions in the camera of the center of gravity of Hillas ellipses for the data taken during the different days of the First Crab Campaign.

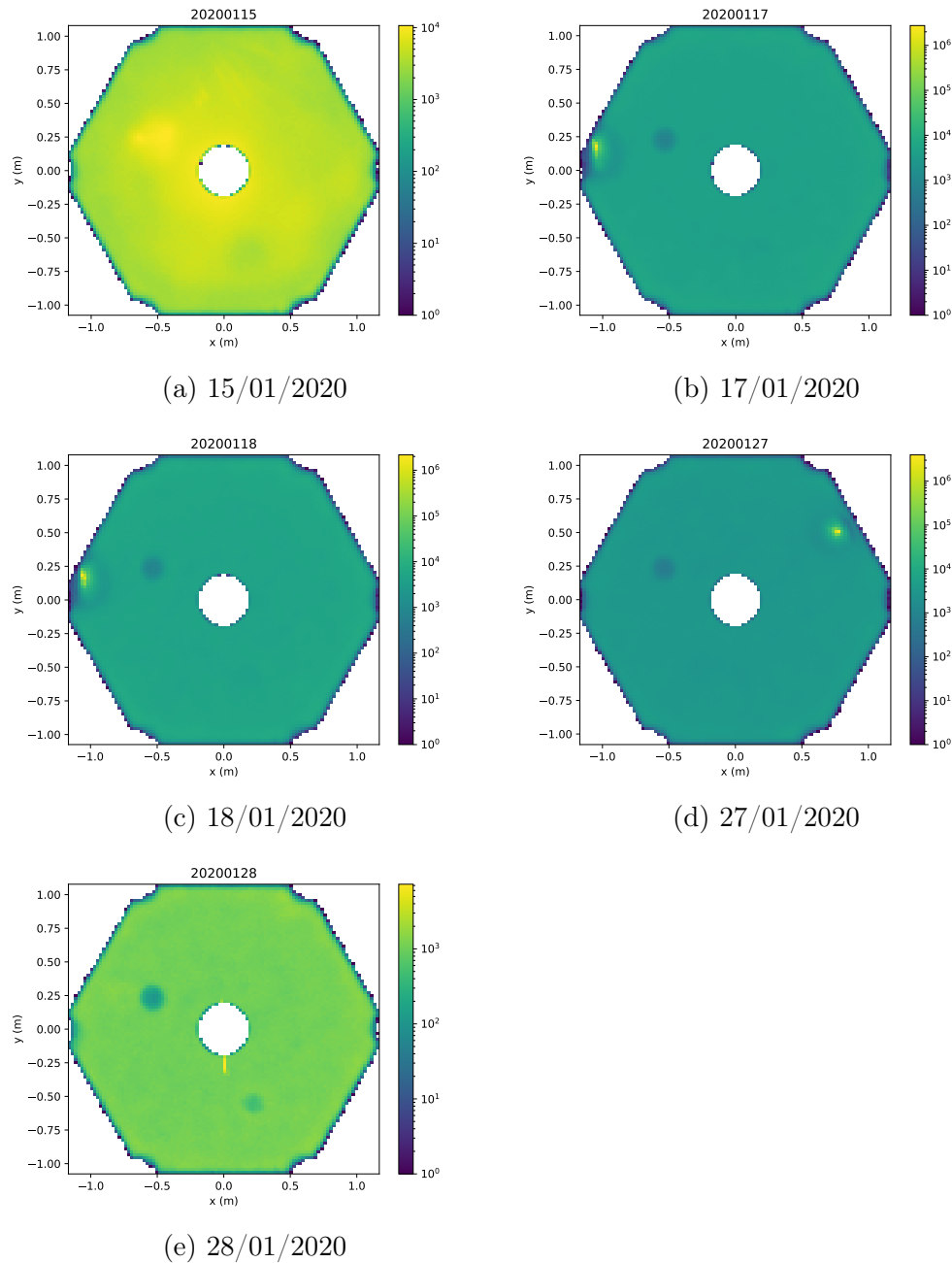


Figure F.2: Distribution of the positions in the camera of the center of gravity of Hillas ellipses for the data taken during the different days of the Second Crab Campaign.

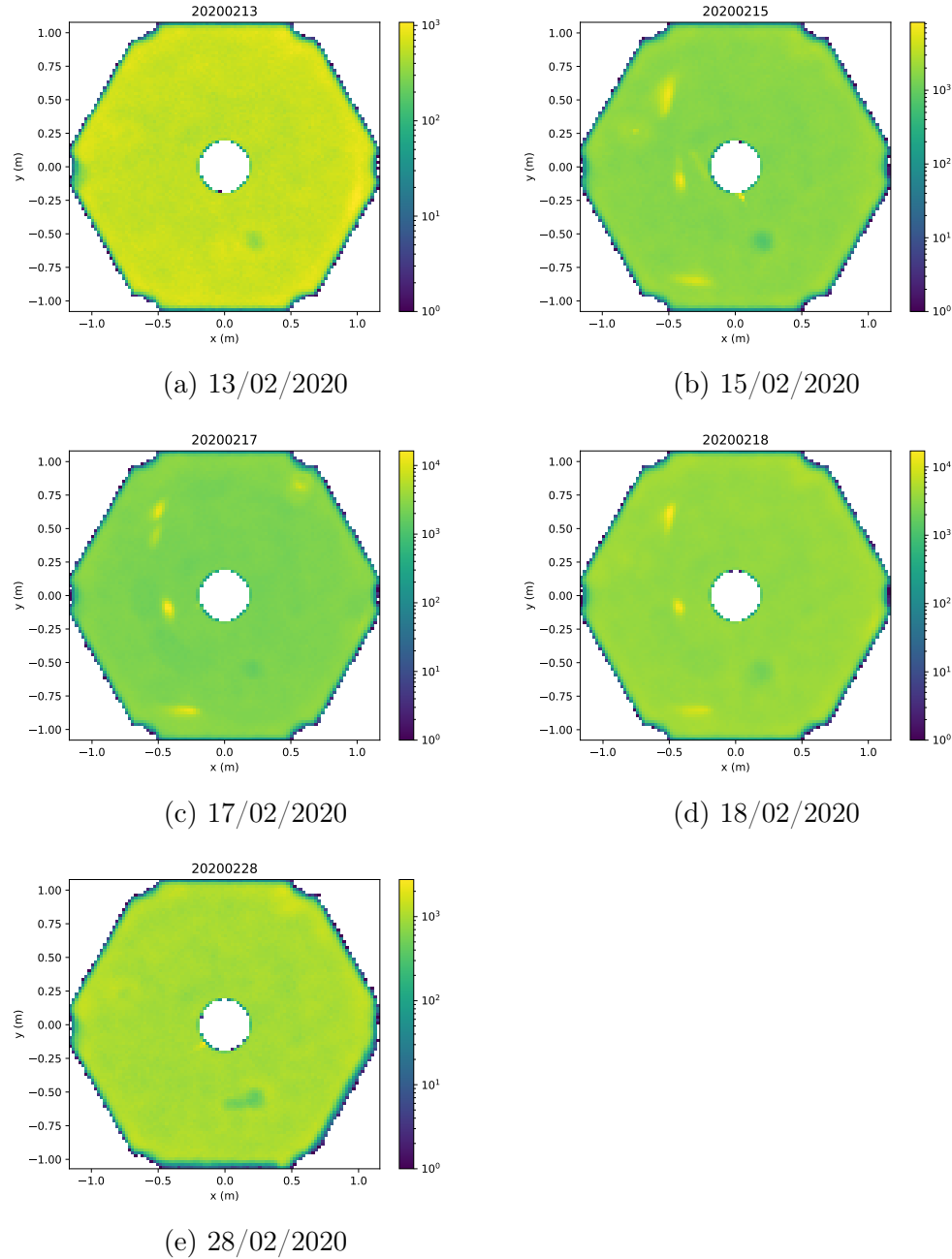


Figure F.3: Distribution of the positions in the camera of the center of gravity of Hillas ellipses for the data taken during the different days of the Third Crab Campaign.

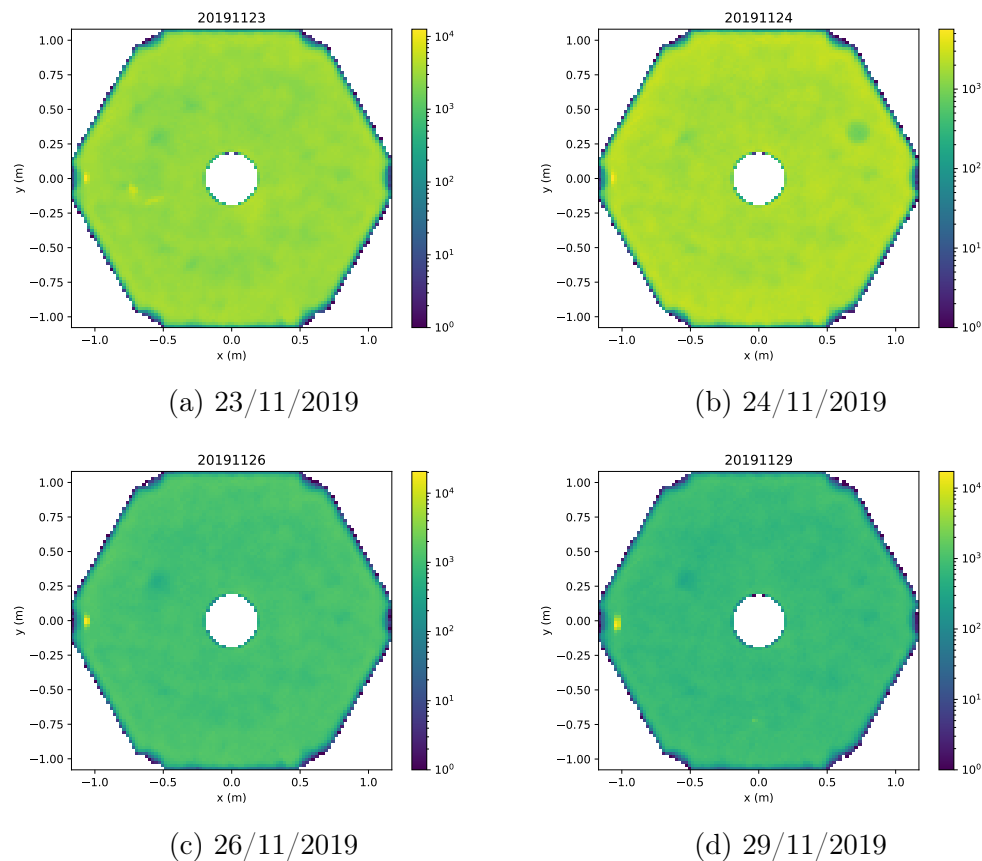


Figure F.4: Distribution of the positions in the camera of the center of gravity of Hillas ellipses for the data taken during the different days of the First Crab Campaign, using the EM method for Hillas parameterization.

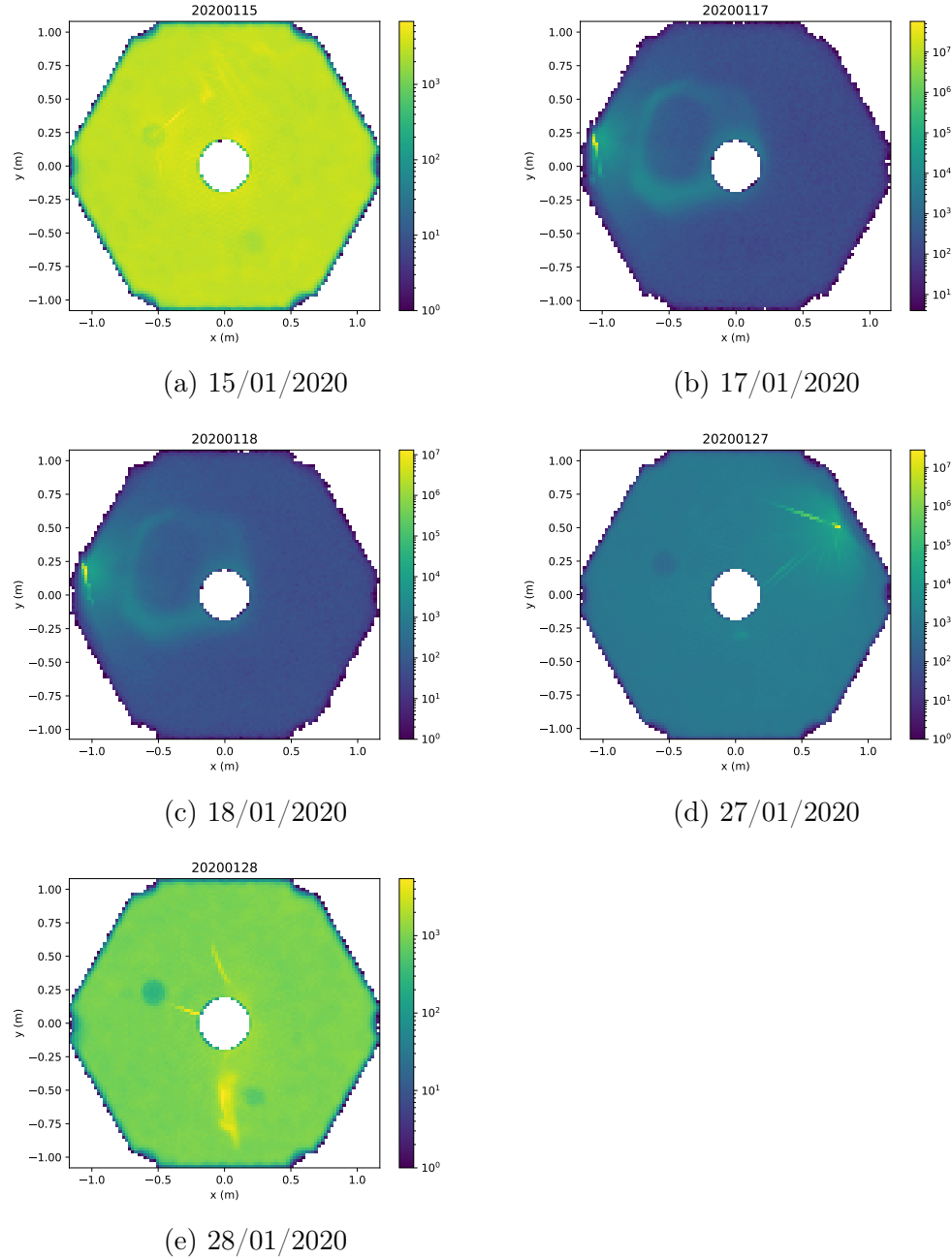


Figure F.5: Distribution of the positions in the camera of the center of gravity of Hillas ellipses for the data taken during the different days of the Second Crab Campaign, using the EM method for Hillas parameterization. .

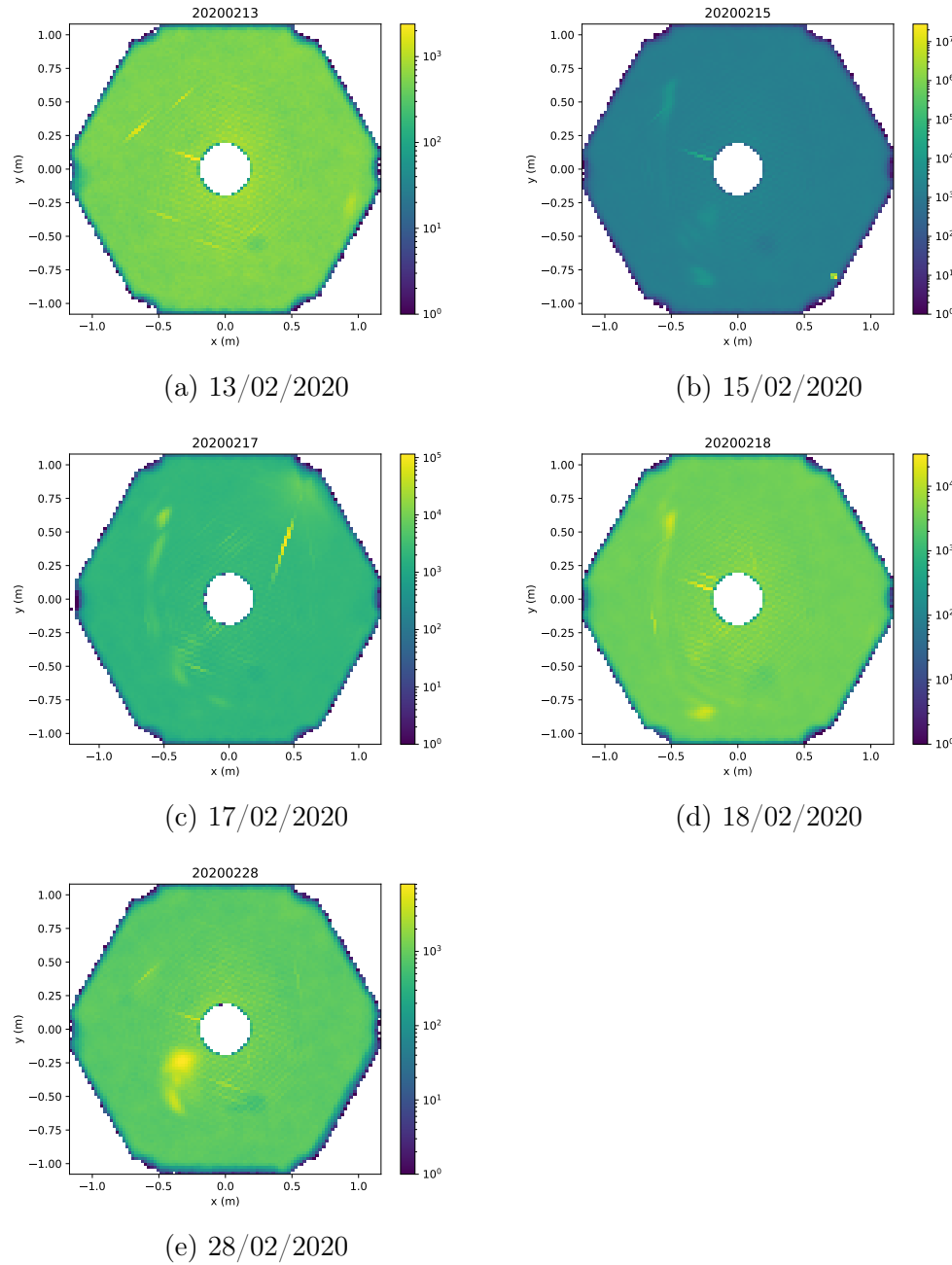


Figure F.6: Distribution of the positions in the camera of the center of gravity of Hillas ellipses for the data taken during the different days of the Third Crab Campaign, using the EM method for Hillas parameterization.



# Bibliography

1. Berezhko, E. G. Origin of Galactic Cosmic Rays from Supernova Remnants. *Nuclear Physics B Proceedings Supplements* **256**, 23–35 (Nov. 2014).
2. Gozzini, S. R., Carmona, E., Jankowski, F., Krause, J. & and, I. R. The supernova remnant W51C: a plausible source of galactic cosmic rays? *Journal of Physics: Conference Series* **409**, 012116 (Feb. 2013).
3. Thoudam, S. & Hörandel, J. R. Nearby supernova remnants and the cosmic ray spectral hardening at high energies. *Monthly Notices of the Royal Astronomical Society* **421**, 1209–1214. ISSN: 0035-8711 (Mar. 2012).
4. Thoudam, S. *et al.* Cosmic-ray energy spectrum and composition up to the ankle: the case for a second Galactic component. *A&A* **595**, A33 (Oct. 2016).
5. Bazilevskaya, G. A. Once again about origin of the solar cosmic rays. *Journal of Physics: Conference Series* **798**, 012034 (Jan. 2017).
6. Podgorny, A. I., Podgorny, I. M., Balabin, Y. V., Meshalkina, N. S. & Vashenyuk. The spectrum of solar relativistic cosmic ray measurements and numerical simulation. *Journal of Physics: Conference Series* **798**, 012027 (Jan. 2017).
7. Castellina, A. & Donato, F. in *Planets, Stars and Stellar Systems: Volume 5: Galactic Structure and Stellar Populations* (eds Oswalt, T. D. & Gilmore, G.) 725–788 (Springer Netherlands, Dordrecht, 2013). doi:10.1007/978-94-007-5612-0\_14. <[https://doi.org/10.1007/978-94-007-5612-0\\_14](https://doi.org/10.1007/978-94-007-5612-0_14)>.
8. Alves Batista, R. *et al.* Open Questions in Cosmic-Ray Research at Ultrahigh Energies. *Frontiers in Astronomy and Space Sciences* **6**, 23. ISSN: 2296-987X (2019).
9. Hanlon, W. F. *Updated cosmic ray spectrum 2015*. <<http://www.physics.utah.edu/~whanlon/spectrum.html>>.
10. Hillas, A. M. The Origin of Ultra-High-Energy Cosmic Rays. *Annual Review of Astronomy and Astrophysics* **22**, 425–444 (1984).
11. Perkins, D. H. *Particle Astrophysics* 2nd ed. (Oxford University Press, 2009).
12. Tatischeff, V. & Gabici, S. Particle Acceleration by Supernova Shocks and Spallogenic Nucleosynthesis of Light Elements. *Annual Review of Nuclear and Particle Science* **68**, 377–404 (Oct. 2018).

13. Hillas, A. M. The Origin of Ultrahigh-Energy Cosmic Rays. *Ann. Rev. Astron. Astrophys.* **22**, 425–444 (1984).
14. Petrosian, V. & Bykov, A. M. Particle Acceleration Mechanisms. *Space Sci. Rev.* **134**, 207–227 (Feb. 2008).
15. Melrose, D. B. Acceleration Mechanisms. *arXiv e-prints*, arXiv:0902.1803 (Feb. 2009).
16. Fermi, E. in, 238–252 (Dec. 1972). ISBN: 9780080167244. doi:10.1016/B978-0-08-016724-4.50024-0.
17. Longair, M. S. *High Energy Astrophysics* 3rd ed. (Cambridge University Press, 2011).
18. Lagage, P. O. & Cesarsky, C. J. The maximum energy of cosmic rays accelerated by supernova shocks. *A&A* **125**, 249–257 (Sept. 1983).
19. Ramana Murthy, P. V. & Wolfendale, A. W. *Gamma-ray Astronomy* 273 (Apr. 1993).
20. Weekes, T. *Very High Energy Gamma-Ray Astronomy* ISBN: 9781420033199. <<https://books.google.com.ua/books?id=wSTOBgAAQBAJ>> (CRC Press, 2003).
21. Maoz, D. *Astrophysics in a nutshell* <<https://cds.cern.ch/record/1142636>> (Princeton Univ. Press, Princeton, NJ, 2007).
22. Oya Vallejo, I. *Observations of Active Galactic Nuclei with the MAGIC Telescope* PhD thesis (UCM, Madrid, Dept. Phys., 2010). <<https://magiccoll.mpp.mpg.de/publications/theses/I0ya.pdf>>.
23. Harwit, M. *Astrophysical Concepts. Fourth edition* <<https://www.springer.com/gp/book/9781475720198>> (Springer Science and Business Media, 2006).
24. Ruderman, M. A. & Sutherland, P. G. Theory of pulsars - Polar caps, sparks, and coherent microwave radiation. *Astrophysical Journal* **196**, 51–72 (Feb. 1975).
25. Aharonian, F. A. *Very high energy cosmic gamma radiation : a crucial window on the extreme Universe* doi:10.1142/4657 (2004).
26. Stecker, F. W. The Production of Cosmic Gamma Rays in Interstellar and Intergalactic Cosmic-Ray Collisions. Iv: Gamma-Ray Production from Cosmic Proton-Antiproton Interactions. *SAO Special Report* **261** (Dec. 1967).
27. Domínguez, A. *et al.* Extragalactic background light inferred from AEGIS galaxy-SED-type fractions. *Monthly Notices of the RAS* **410**, 2556–2578 (Feb. 2011).
28. Franceschini, A. & Rodighiero, G. The extragalactic background light revisited and the cosmic photon-photon opacity. *Astronomy and Astrophysics* **603**, A34 (July 2017).

29. Moralejo, A. *et al.* Measurement of the EBL through a combined likelihood analysis of gamma-ray observations of blazars with the MAGIC telescopes in 35th International Cosmic Ray Conference (ICRC2017) **301** (Jan. 2017), 604. arXiv: 1709.02238 [astro-ph.HE].
30. Andernach, H. & Zwicky, F. English and Spanish Translation of Zwicky's (1933) The Redshift of Extragalactic Nebulae. *arXiv e-prints*, arXiv:1711.01693 (Nov. 2017).
31. Rubin, V. C., Ford, W. K. Jr. & Thonnard, N. Extended rotation curves of high-luminosity spiral galaxies. IV - Systematic dynamical properties, SA through SC. *Astrophysical Journal* **225**, L107–L111 (Nov. 1978).
32. Planck Collaboration *et al.* Planck 2013 results. XVI. Cosmological parameters. *Astronomy and Astrophysics* **571**, A16 (Nov. 2014).
33. Olive, K. A. TASI Lectures on Dark Matter. *arXiv e-prints*, astro-ph/0301505 (Jan. 2003).
34. Lisanti, M. *Lectures on Dark Matter Physics* in *New Frontiers in Fields and Strings (TASI 2015)* (Jan. 2017), 399–446. doi:10.1142/9789813149441\_0007. arXiv: 1603.03797 [hep-ph].
35. Kravtsov, A. V., Klypin, A. A., Bullock, J. S. & Primack, J. R. The Cores of Dark Matter-dominated Galaxies: Theory versus Observations. *Astrophysical Journal* **502**, 48–58 (July 1998).
36. Hernquist, L. An analytical model for spherical galaxies and bulges. *Astrophysical Journal* **356**, 359–364 (June 1990).
37. Zhao, H. Analytical models for galactic nuclei. *Monthly Notices of the RAS* **278**, 488–496 (Jan. 1996).
38. Navarro, J. F., Frenk, C. S. & White, S. D. M. The Structure of Cold Dark Matter Halos. *Astrophysical Journal* **462**, 563 (May 1996).
39. Einasto, J. On the Construction of a Composite Model for the Galaxy and on the Determination of the System of Galactic Parameters. *Trudy Astrofizicheskogo Instituta Alma-Ata* **5**, 87–100 (Jan. 1965).
40. Wakely, S. P. & Horan, D. TeVCat: An online catalog for Very High Energy Gamma-Ray Astronomy. *International Cosmic Ray Conference* **3**, 1341–1344 (2008).
41. Aliu, E. *et al.* Observation of Pulsed  $\gamma$ -Rays Above 25 GeV from the Crab Pulsar with MAGIC. *Science* **322**, 1221 (Nov. 2008).
42. Kuiper, L. *et al.* The Crab pulsar in the 0.75–30 MeV range as seen by CGRO COMPTEL. A coherent high-energy picture from soft X-rays up to high-energy gamma-rays. *Astronomy and Astrophysics* **378**, 918–935 (Nov. 2001).
43. McCann, A. Observations of the Crab Pulsar with VERITAS. *arXiv e-prints*, arXiv:1303.0275 (Mar. 2013).

44. Abdo, A. A. *et al.* Fermi Large Area Telescope Observations of the Crab Pulsar And Nebula. *ApJ* **708**, 1254–1267 (Jan. 2010).
45. Hirotani, K. High Energy Emission from Rotation-Powered Pulsars: Outer-gap vs. Slot-gap Models. *arXiv e-prints*, arXiv:0809.1283 (Sept. 2008).
46. Gajdus, M. *The Vela pulsar in very high energy gamma-rays with H.E.S.S. II* PhD thesis (Humboldt-Universität zu Berlin, Mathematisch-Naturwissenschaftliche Fakultät, 2016). doi:<http://dx.doi.org/10.18452/17610>.
47. Chandrasekhar, S. The Maximum Mass of Ideal White Dwarfs. *Astrophysical Journal* **74**, 81 (July 1931).
48. Osterbrock, D. E. & Ferland, G. J. *Astrophysics of gaseous nebulae and active galactic nuclei* (2006).
49. Weiler, K. W. & Sramek, R. A. Supernovae and supernova remnants. *Annual Review of Astron and Astrophys* **26**, 295–341 (Jan. 1988).
50. Becker Tjus, J., Eichmann, B., Kroll, M. & Nierstenhöfer, N. Gamma-ray emitting supernova remnants as the origin of Galactic cosmic rays? *Astroparticle Physics* **81**, 1–11 (Aug. 2016).
51. Cristofari, P., Gabici, S., Terrier, R. & Humensky, T. B. On the search for Galactic supernova remnant PeVatrons with current TeV instruments. *MNRAS* **479**, 3415–3421 (Sept. 2018).
52. Gaensler, B. M. & Slane, P. O. The Evolution and Structure of Pulsar Wind Nebulae. *Annual Review of Astron and Astrophys* **44**, 17–47 (Sept. 2006).
53. H. E. S. S. Collaboration *et al.* HESS J1818-154, a new composite supernova remnant discovered in TeV gamma rays and X-rays. *A&A* **562**, A40 (Feb. 2014).
54. Hewitt, J. W. & Lemoine-Goumard, M. Observations of supernova remnants and pulsar wind nebulae at gamma-ray energies. *Comptes Rendus Physique* **16**, 674–685 (Aug. 2015).
55. Dubus, G., Guillard, N., Petrucci, P.-O. & Martin, P. Sizing up the population of gamma-ray binaries. *A&A* **608**, A59 (Dec. 2017).
56. Dubus, G. Gamma-ray binaries and related systems. *Astronomy and Astrophysics Reviews* **21**, 64 (Aug. 2013).
57. *Classical Novae* 2nd ed. doi:10.1017/CBO9780511536168 (Cambridge University Press, 2008).
58. Abdo, A. A., Ackermann, M., Ajello, M., Atwood & Fermi LAT Collaboration. Gamma-Ray Emission Concurrent with the Nova in the Symbiotic Binary V407 Cygni. *Science* **329**, 817–821 (Aug. 2010).
59. Ackermann, M. *et al.* Fermi establishes classical novae as a distinct class of gamma-ray sources. *Science* **345**, 554–558 (Aug. 2014).

60. Sitarek, J. & Bednarek, W. GeV-TeV gamma rays and neutrinos from the Nova V407 Cygni. *Physical Review D* **86**, 063011 (Sept. 2012).
61. Albert, J. *et al.* Observation of Gamma Rays from the Galactic Center with the MAGIC Telescope. *ApJ* **638**, L101–L104 (Feb. 2006).
62. H. E. S. S. Collaboration *et al.* The H.E.S.S. Galactic plane survey. *A&A* **612**, A1 (Apr. 2018).
63. Archer, A. *et al.* TeV Gamma-Ray Observations of the Galactic Center Ridge by VERITAS. *ApJ* **821**, 129 (Apr. 2016).
64. Goldwurm, A. *An Overview of the High-Energy Emission from the Galactic Center in The Galactic Center: a Window to the Nuclear Environment of Disk Galaxies* (eds Morris, M. R., Wang, Q. D. & Yuan, F.) **439** (May 2011), 391. arXiv: 1007.4174 [astro-ph.HE].
65. Goldwurm, A. High energy activity of the super-massive black hole at the Galactic Center. *Comptes Rendus Physique* **8**, 35–44 (Jan. 2007).
66. Su, M., Slatyer, T. R. & Finkbeiner, D. P. Giant Gamma-ray Bubbles from Fermi-LAT: Active Galactic Nucleus Activity or Bipolar Galactic Wind? *Astrophysical Journal* **724**, 1044–1082 (Dec. 2010).
67. Ackermann, M. *et al.* The Spectrum and Morphology of the Fermi Bubbles. *Astrophysical Journal* **793**, 64 (Sept. 2014).
68. Abdo, A. A. *et al.* A population of gamma-ray emitting globular clusters seen with the Fermi Large Area Telescope. *Astronomy and Astrophysics* **524**, A75 (Dec. 2010).
69. H. E. S. S. Collaboration *et al.* Search for very-high-energy  $\gamma$ -ray emission from Galactic globular clusters with H.E.S.S. *Astronomy and Astrophysics* **551**, A26 (Mar. 2013).
70. Freire, P. C. C. *et al.* Fermi Detection of a Luminous -Ray Pulsar in a Globular Cluster. *Science* **334**, 1107–1110. ISSN: 0036-8075 (2011).
71. Wu, J. H. K. *et al.* SEARCH FOR PULSED  $\gamma$ -RAY EMISSION FROM GLOBULAR CLUSTER M28. *The Astrophysical Journal* **765**, L47 (Feb. 2013).
72. Tam, P.-H. T., Hui, C. Y. & Kong, A. K. H. Gamma-ray Emission from Globular Clusters. *Journal of Astronomy and Space Sciences* **33**, 1–11 (Mar. 2016).
73. Urry, C. M. & Padovani, P. Unified Schemes for Radio-Loud Active Galactic Nuclei. *Publications of the Astronomical Society of the Pacific* **107**, 803 (Sept. 1995).
74. Dermer, C. D. & Giebels, B. Active galactic nuclei at gamma-ray energies. *Comptes Rendus Physique* **17**, 594–616 (June 2016).
75. Madejski, G. G. & Sikora, M. Gamma-Ray Observations of Active Galactic Nuclei. *ARA&A* **54**, 725–760 (Sept. 2016).

76. Wilson, A. S. & Colbert, E. J. M. The Difference between Radio-loud and Radio-quiet Active Galaxies. *ApJ* **438**, 62 (Jan. 1995).
77. Urry, C. M. & Padovani, P. Unified Schemes for Radio-Loud Active Galactic Nuclei. *PASP* **107**, 803 (Sept. 1995).
78. Piran, T. The physics of gamma-ray bursts. *Reviews of Modern Physics* **76**, 1143–1210 (Oct. 2004).
79. Kouveliotou, C. *et al.* Identification of two classes of gamma-ray bursts. *Astrophysical Journal* **413**, L101–L104 (Aug. 1993).
80. Piran, T. Gamma-ray bursts and the fireball model. *Physics Reports* **314**, 575–667 (June 1999).
81. Ghirlanda, G., Bernardini, M., Calderone, G. & D’Avanzo, P. Are short Gamma Ray Bursts similar to long ones? *Journal of High Energy Astrophysics* **7**. Swift 10 Years of Discovery, a novel approach to Time Domain Astronomy, 81 –89. ISSN: 2214-4048 (2015).
82. .
83. Ajello, M. *et al.* Fermi-LAT Observations of LIGO/Virgo Event GW170817. *ApJ* **861**, 85 (July 2018).
84. Mirzoyan, R. First time detection of a GRB at sub-TeV energies; MAGIC detects the GRB 190114C. *The Astronomer’s Telegram* **12390** (Jan. 2019).
85. Ohm, S. Starburst galaxies as seen by gamma-ray telescopes. *Comptes Rendus Physique* **17**, 585–593 (June 2016).
86. Acero, F. *et al.* Detection of Gamma Rays from a Starburst Galaxy. *Science* **326**, 1080 (Nov. 2009).
87. VERITAS Collaboration *et al.* A connection between star formation activity and cosmic rays in the starburst galaxy M82. *Nature* **462**, 770–772 (Dec. 2009).
88. Abdo, A. A. *et al.* Detection of Gamma-Ray Emission from the Starburst Galaxies M82 and NGC 253 with the Large Area Telescope on Fermi. *Astrophysical Journal* **709**, L152–L157 (Feb. 2010).
89. Brunetti, G. Gamma rays from galaxy clusters. *AIP Conference Proceedings* **1792**, 020009 (2017).
90. Brunetti, G. & Jones, T. W. Cosmic Rays in Galaxy Clusters and Their Nonthermal Emission. *International Journal of Modern Physics D* **23**, 1430007–98 (Mar. 2014).
91. Ackermann, M. *et al.* GeV Gamma-ray Flux Upper Limits from Clusters of Galaxies. *Astrophysical Journal* **717**, L71–L78 (July 2010).
92. Aleksić, J. *et al.* Constraining cosmic rays and magnetic fields in the Perseus galaxy cluster with TeV observations by the MAGIC telescopes. *Astronomy and Astrophysics* **541**, A99 (May 2012).

93. Xi, S.-Q. *et al.* Detection of gamma-ray emission from the Coma cluster with Fermi Large Area Telescope and tentative evidence for an extended spatial structure. *Physical Review D* **98**, 063006 (Sept. 2018).
94. Czerny, B. *et al.* Astronomical Distance Determination in the Space Age. Secondary Distance Indicators. *Space Science Reviews* **214**, 32 (Feb. 2018).
95. Rezaeikh, S., Javadi, A., Khosroshahi, H. & van Loon, J. T. The star formation history of the Magellanic Clouds derived from long-period variable star counts. *Monthly Notices of the RAS* **445**, 2214–2222 (Dec. 2014).
96. Robitaille, T. P. & Whitney, B. A. The Present-Day Star Formation Rate of the Milky Way Determined from Spitzer-Detected Young Stellar Objects. *Astrophysical Journal* **710**, L11–L15 (Feb. 2010).
97. Sreekumar, P. *et al.* Observations of the Large Magellanic Cloud in High-Energy Gamma Rays. *Astrophysical Journal* **400**, L67 (Dec. 1992).
98. Abdo, A. A. *et al.* Detection of the Small Magellanic Cloud in gamma-rays with Fermi/LAT. *Astronomy and Astrophysics* **523**, A46 (Nov. 2010).
99. Abdo, A. A. *et al.* Observations of the Large Magellanic Cloud with Fermi. *Astronomy and Astrophysics* **512**, A7 (Mar. 2010).
100. Ackermann, M. *et al.* Deep view of the Large Magellanic Cloud with six years of Fermi-LAT observations. *Astronomy and Astrophysics* **586**, A71 (Feb. 2016).
101. Corbet, R. H. D. *et al.* A Luminous Gamma-ray Binary in the Large Magellanic Cloud. *Astrophysical Journal* **829**, 105 (Oct. 2016).
102. H. E. S. S. Collaboration *et al.* The exceptionally powerful TeV  $\gamma$ -ray emitters in the Large Magellanic Cloud. *Science* **347**, 406–412 (Jan. 2015).
103. Komin, N. *et al.* H.E.S.S. observations of the Large Magellanic Cloud. *arXiv e-prints*, arXiv:1201.0639 (Jan. 2012).
104. Ackermann, M. *et al.* Observations of M31 and M33 with the Fermi Large Area Telescope: A Galactic Center Excess in Andromeda? *Astrophysical Journal* **836**, 208 (Feb. 2017).
105. Navarro, J. F. The Structure of Cold Dark Matter Halos. *Symposium - International Astronomical Union* **171**, 255–258 (1996).
106. Cherenkov Telescope Array Consortium *et al.* *Science with the Cherenkov Telescope Array* doi:10.1142/10986 (2019).
107. Abramowski, A. *et al.* Search for a Dark Matter Annihilation Signal from the Galactic Center Halo with H.E.S.S. *Physical Review Letters* **106**, 161301 (Apr. 2011).
108. Aharonian, F. *et al.* HESS Observations of the Galactic Center Region and Their Possible Dark Matter Interpretation. *Physical Review Letters* **97**, 221102 (Dec. 2006).

109. Ackermann, M. *et al.* The Fermi Galactic Center GeV Excess and Implications for Dark Matter. *Astrophysical Journal* **840**, 43 (May 2017).
110. Kuhlen, M., Diemand, J., Madau, P. & Zemp, M. The Via Lactea INCITE simulation: galactic dark matter substructure at high resolution. *Journal of Physics: Conference Series* **125**, 012008 (July 2008).
111. Simon, J. D. & Geha, M. The Kinematics of the Ultra-faint Milky Way Satellites: Solving the Missing Satellite Problem. *Astrophysical Journal* **670**, 313–331 (Nov. 2007).
112. Abdo, A. A. *et al.* Observations of Milky Way Dwarf Spheroidal Galaxies with the Fermi-Large Area Telescope Detector and Constraints on Dark Matter Models. *Astrophysical Journal* **712**, 147–158 (Mar. 2010).
113. Abramowski, A. *et al.* Search for dark matter annihilation signatures in H.E.S.S. observations of dwarf spheroidal galaxies. *Physical Review D* **90**, 112012 (Dec. 2014).
114. Ahnen, M. L. *et al.* Indirect dark matter searches in the dwarf satellite galaxy Ursa Major II with the MAGIC telescopes. *Journal of Cosmology and Astroparticle Physics* **2018**, 009 (Mar. 2018).
115. Archambault, S. *et al.* Dark matter constraints from a joint analysis of dwarf Spheroidal galaxy observations with VERITAS. *Physical Review D* **95**, 082001 (Apr. 2017).
116. Oakes, L. *Combined Dark Matter Searches Towards Dwarf Spheroidal Galaxies with Fermi-LAT, HAWC, HESS, MAGIC and VERITAS* in *36th International Cosmic Ray Conference (ICRC2019)* **36** (July 2019), 539. arXiv: 1909.06310 [astro-ph.HE].
117. Cirelli, M., Moulin, E., Panci, P., Serpico, P. D. & Viana, A. Gamma ray constraints on decaying dark matter. *Physical Review D* **86**, 083506 (Oct. 2012).
118. Huang, X., Vertongen, G. & Weniger, C. Probing dark matter decay and annihilation with Fermi LAT observations of nearby galaxy clusters. *Journal of Cosmology and Astroparticle Physics* **2012**, 042 (Jan. 2012).
119. Ackermann, M. *et al.* Constraints on dark matter annihilation in clusters of galaxies with the Fermi large area telescope. *Journal of Cosmology and Astroparticle Physics* **2010**, 025 (May 2010).
120. Abramowski, A. *et al.* Search for Dark Matter Annihilation Signals from the Fornax Galaxy Cluster with H.E.S.S. *Astrophysical Journal* **750**, 123 (May 2012).
121. Acciari, V. A. *et al.* Constraining dark matter lifetime with a deep gamma-ray survey of the Perseus galaxy cluster with MAGIC. *Physics of the Dark Universe* **22**, 38–47 (Dec. 2018).

122. van der Marel, R. P. *The Large Magellanic Cloud: structure and kinematics* in *The Local Group as an Astrophysical Laboratory* (eds Livio, M. & Brown, T. M.) **17** (Jan. 2006), 47–71. arXiv: astro-ph/0404192 [astro-ph].
123. Sofue, Y. Dark Bulge, Exponential Disk, and Massive Halo in the Large Magellanic Cloud. *Publications of the Astronomical Society of Japan* **51**, 445–448. ISSN: 0004-6264 (Aug. 1999).
124. Buckley, M. R. *et al.* Search for gamma-ray emission from dark matter annihilation in the large magellanic cloud with the fermi large area telescope. *Physical Review D* **91**, 102001 (May 2015).
125. *IBIS homepage* <https://www.cosmos.esa.int/web/integral/instruments-ibis>.
126. *INTEGRAL homepage* <https://sci.esa.int/web/integral/home>.
127. Atwood, W. B. *et al.* The Large Area Telescope on the Fermi Gamma-Ray Space Telescope Mission. *ApJ* **697**, 1071–1102 (June 2009).
128. Ackermann, M. *et al.* Detection of the Characteristic Pion-Decay Signature in Supernova Remnants. *Science* **339**, 807–811 (Feb. 2013).
129. Ackermann, M. *et al.* Fermi-LAT Observations of the Gamma-Ray Burst GRB 130427A. *Science* **343**, 42–47 (Jan. 2014).
130. Goldstein, A. *et al.* An Ordinary Short Gamma-Ray Burst with Extraordinary Implications: Fermi-GBM Detection of GRB 170817A. *The Astrophysical Journal* **848**, L14 (Oct. 2017).
131. Heitler, W. *Quantum theory of radiation* (1954).
132. Rossi, B. & Greisen, K. Cosmic-Ray Theory. *Rev. Mod. Phys.* **13**, 240–309 (4 Oct. 1941).
133. Vallejo, I. O. *Observation of active galactic [sic] nuclei with the Magic telescope* Tesis de la Universidad Complutense de Madrid, Facultad de Ciencias Físicas, Departamento de Física Atómica, Molecular y Nuclear, leída el 23-06-2010. PhD thesis (Madrid, Oct. 2010). <<https://eprints.ucm.es/11431/>>.
134. Collado, T. H. *Sensitivity studies for the Cherenkov Telescope Array* Tesis inédita de la Universidad Complutense de Madrid, Facultad de Ciencias Físicas, Departamento de Física Atómica, Molecular y Nuclear, leída el 28-09-2015. Madrid, Jan. 2016. <<https://eprints.ucm.es/35143/>>.
135. Gaisser, T. K., Engel, R. & Resconi, E. *Cosmic Rays and Particle Physics* (June 2016).
136. Jelley, J. *Čerenkov radiation, and its applications* <<https://books.google.es/books?id=uzZRAAAAMAAJ>> (Pergamon Press, 1958).
137. Borione, A. *et al.* CASA-MIA: A precision” EAS detector. [Cyg X-3; Her X-1; M1; NGC 1952; PSR 0531+21]. doi:10.1063/1.43832 (June 1993).

138. Di Sciascio, G. & LHAASO Collaboration. The LHAASO experiment: From Gamma-Ray Astronomy to Cosmic Rays. *Nuclear and Particle Physics Proceedings* **279**, 166–173 (Oct. 2016).
139. Huo, X. A. *et al.* *Tibet-AS  $\gamma$  Experiment* in *International Cosmic Ray Conference* **2** (Jan. 1990), 427.
140. Fonseca, V. The HEGRA experiment (High Energy Gamma Ray Array). *Nuclear Physics B - Proceedings Supplements* **28**, 409 –412. ISSN: 0920-5632 (1992).
141. Di Sciascio, G. A.-Y. C. *Latest results from the ARGO-YBJ experiment* in *Journal of Physics Conference Series* **632** (Aug. 2015), 012089. doi:10.1088/1742-6596/632/1/012089. arXiv: 1503.09102 [astro-ph.HE].
142. Mostafá, M. A. The High-Altitude Water Cherenkov Observatory. *Brazilian Journal of Physics* **44**, 571–580 (Oct. 2014).
143. Arqueros, F. *et al.* The Wide Angle Air Cherenkov Detector AIROBICC at La Palma (Aug. 1996).
144. Hillas, A. M. *Cerenkov light images of EAS produced by primary gamma* in *19th International Cosmic Ray Conference (ICRC19), Volume 3* (ed Jones, F. C.) **3** (Aug. 1985).
145. de Naurois, M. Analysis methods for Atmospheric Cerenkov Telescopes. *arXiv e-prints*, astro-ph/0607247 (July 2006).
146. de Naurois, M. & Mazin, D. Ground-based detectors in very-high-energy gamma-ray astronomy. *Comptes Rendus Physique* **16**, 610–627 (Aug. 2015).
147. Kildea, J. *et al.* The Whipple Observatory 10 m gamma-ray telescope, 1997-2006. English (US). *Astroparticle Physics* **28**, 182–195. ISSN: 0927-6505 (Oct. 2007).
148. Cortina, J. *Highlights of the MAGIC telescopes* in *International Cosmic Ray Conference* **11** (Jan. 2011), 147. doi:10.7529/ICRC2011/V12/H12. arXiv: 1110.4747 [astro-ph.HE].
149. Pühlhofer, G. H.E.S.S. highlights. *arXiv e-prints*, arXiv:1801.06074 (Jan. 2018).
150. Furniss, A. *Recent Highlights from the VERITAS Gamma-ray Observatory* in *American Astronomical Society Meeting Abstracts #233* **233** (Jan. 2019), 433.04.
151. *MAGIC homepage* <https://magic.mpp.mpg.de/>.
152. *CTA Observatory site* <https://www.cta-observatory.org/>.
153. Acharya, B. *et al.* Introducing the CTA concept. *Astroparticle Physics* **43**. Seeing the High-Energy Universe with the Cherenkov Telescope Array - The Science Explored with the CTA, 3 –18. ISSN: 0927-6505 (2013).
154. Bernlöhr, K. *et al.* Monte Carlo design studies for the Cherenkov Telescope Array. *Astroparticle Physics* **43**, 171–188 (Mar. 2013).

155. Hassan, T. *et al.* Monte Carlo performance studies for the site selection of the Cherenkov Telescope Array. *Astroparticle Physics* **93**, 76–85 (July 2017).
156. *CTA Performance* <https://www.cta-observatory.org/science/cta-performance/>.
157. Maier, G. *et al.* *Performance of the Cherenkov Telescope Array* in *35th International Cosmic Ray Conference (ICRC2017)* **301** (Jan. 2017), 846. arXiv: 1709.01381 [astro-ph.IM].
158. Ambrosi, G. *et al.* The Cherenkov Telescope Array Large Size Telescope. *arXiv e-prints*, arXiv:1307.4565 (July 2013).
159. Mazin, D., Cortina, J. & Teshima, M. *Large size telescope report* in *6th International Symposium on High Energy Gamma-Ray Astronomy* **1792** (Jan. 2017), 080001. doi:10.1063/1.4969022. arXiv: 1610.04403 [astro-ph.IM].
160. Ritt, S. *Design and performance of the 6 GHz waveform digitizing chip DRS4* in *2008 IEEE Nuclear Science Symposium Conference Record* (2008), 1512–1515.
161. Delgado, C. *et al.* Mechanics and cooling system for the camera of the Large Size Telescopes of the Cherenkov Telescope Array (CTA). *arXiv e-prints*, arXiv:1307.4540 (July 2013).
162. Nieto, D. *et al.* Prototype 9.7 m Schwarzschild-Couder telescope for the Cherenkov Telescope Array: status of the optical system. *arXiv e-prints*, arXiv:1709.06324 (Sept. 2017).
163. Glicenstein, J. F. *Status of the Davies Cotton and Schwarzschild-Coude Medium Sized Telescopes for the Cherenkov Telescope Array* in *36th International Cosmic Ray Conference (ICRC2019)* **36** (July 2019), 269. arXiv: 1907.08455 [astro-ph.IM].
164. Garczarczyk, M., Schlenstedt, S., Oakes, L., Schwanke, U. & the MST Team. Status of the Medium-Sized Telescope for the Cherenkov Telescope Array. *arXiv e-prints*, arXiv:1509.01361 (Sept. 2015).
165. Barrio, J. Status of the large size telescopes and medium size telescopes for the Cherenkov Telescope Array observatory. *Nuclear Instruments and Methods in Physics Research Section A: Accelerators, Spectrometers, Detectors and Associated Equipment*. ISSN: 0168-9002. doi:<https://doi.org/10.1016/j.nima.2018.11.047>. <<http://www.sciencedirect.com/science/article/pii/S016890021831622X>> (2018).
166. Pareschi, G. *et al.* The dual-mirror Small Size Telescope for the Cherenkov Telescope Array. *arXiv e-prints*, arXiv:1307.4962 (July 2013).
167. White, R. & Schoorlemmer, H. A Compact High Energy Camera (CHEC) for the Gamma-ray Cherenkov Telescope of the Cherenkov Telescope Array. *arXiv e-prints*, arXiv:1709.05799 (Sept. 2017).

168. Maccarone, M. C. & Astri Project, C. *ASTRI for the Cherenkov Telescope Array* in *35th International Cosmic Ray Conference (ICRC2017)* **301** (Jan. 2017), 855. arXiv: 1709.03078 [astro-ph.IM].
169. Funk, S. *et al.* *TARGET: A digitizing and trigger ASIC for the Cherenkov telescope array* in *6th International Symposium on High Energy Gamma-Ray Astronomy* **1792** (Jan. 2017), 080012. doi:10.1063/1.4969033. arXiv: 1610.01536 [astro-ph.IM].
170. Heck, D., Knapp, J., Capdevielle, J. N., Schatz, G. & Thouw, T. *CORSIKA: a Monte Carlo code to simulate extensive air showers.* (1998).
171. Klages, H. *et al.* The Kascade experiment. *Nuclear Physics B - Proceedings Supplements* **52**, 92 –102. ISSN: 0920-5632 (1997).
172. Ostapchenko, S. QGSJET-II: towards reliable description of very high energy hadronic interactions. *Nuclear Physics B Proceedings Supplements* **151**, 143–146 (2006).
173. Schmidt, F. & Knapp, J. *CORSIKA Shower Images*
174. Bernlöhr, K. Simulation of imaging atmospheric Cherenkov telescopes with CORSIKA and sim\\_telarray. *Astroparticle Physics* **30**, 149–158 (Oct. 2008).
175. *EventIO data format* [https://www.mpi-hd.mpg.de/hfm/~bernloehr/sim\\_telarray/Documentation/eventio\\_en.pdf](https://www.mpi-hd.mpg.de/hfm/~bernloehr/sim_telarray/Documentation/eventio_en.pdf).
176. *Ctapipe webpage* <https://cta-observatory.github.io/ctapipe/index.html>.
177. Contreras, J. L. *et al.* *Data model issues in the Cherenkov Telescope Array project* in *34th International Cosmic Ray Conference (ICRC2015)* **34** (2015), 960. arXiv: 1508.07584 [astro-ph.IM].
178. Knöldlseder, J. *et al.* GammaLib and ctools. A software framework for the analysis of astronomical gamma-ray data. *A&A* **593**, A1 (2016).
179. Pence, W., Seaman, R. & White, R. L. A Tiled-Table Convention for Compressing FITS Binary Tables. arXiv: 1201.1340 [astro-ph.IM] (Jan. 2012).
180. The HDF Group. *Hierarchical data format version 5* <<http://www.hdfgroup.org/HDF5>> (2000-2010).
181. Breiman, L. Random Forests. English. *Machine Learning* **45**, 5–32. ISSN: 0885-6125 (2001).
182. *Ctapipe: Image Extraction* [https://cta-observatory.github.io/ctapipe/ctapipe\\_api/image/extractor.html?highlight=extractor](https://cta-observatory.github.io/ctapipe/ctapipe_api/image/extractor.html?highlight=extractor).
183. Iori, M. *et al.* Design of a prototype device to calibrate the Large Size Telescope camera of the Cherenkov Telescope Array. *arXiv e-prints*, arXiv:1508.06752 (Aug. 2015).

184. Palatiello, M., Iori, M., Cassol, F., Cauz, D. & Ferrarotto, F. Performance of the INFN Camera calibration device of the first Large Size Telescope in the Cherenkov Telescope Array. *arXiv e-prints*, arXiv:1909.08475 (Sept. 2019).
185. Mirzoyan, R. *On the Calibration Accuracy of Light Sensors in Atmospheric Cherenkov Fluorescence and Neutrino Experiments in International Cosmic Ray Conference* **7** (Jan. 1997), 265.
186. Parsons, R. D. & Ohm, S. Background Rejection in Atmospheric Cherenkov Telescopes using Recurrent Convolutional Neural Networks. *arXiv e-prints*, arXiv:1910.09435 (Oct. 2019).
187. Shayduk, M. & Consortium, C. *Optimized Next-neighbour Image Cleaning Method for Cherenkov Telescopes in International Cosmic Ray Conference* **33** (2013), 3000. arXiv: 1307.4939 [astro-ph.IM].
188. Shayduk, M., Hengstebeck, T., Kalekin, O. R., Pavel, N. A. & Schweizer, T. *A New Image Cleaning Method for the MAGIC Telescope* in (2005).
189. Lessard, R., Cayón, L., Sembroski, G. & Gaidos, J. Wavelet Imaging Cleaning Method for Atmospheric Cherenkov Telescopes. *Astroparticle Physics* **17**. doi:10.1016/S0927-6505(01)00173-6 (Oct. 2001).
190. HEGRA Collaboration: A. Daum. First Results on the Performance of the HEGRA IACT Array. *arXiv e-prints*, astro-ph/9704098 (Apr. 1997).
191. Fomin, V. P. *et al.* New methods of atmospheric Cherenkov imaging for gamma-ray astronomy. I. The false source method. *Astroparticle Physics* **2**, 137–150 (May 1994).
192. Domingo-Santamaria, E. *The DISP analysis method for point-like or extended gamma source searches/studies with the MAGIC Telescope* in (2005).
193. Pedregosa, F. *et al.* Scikit-learn: Machine Learning in Python. *Journal of Machine Learning Research* **12**, 2825–2830 (2011).
194. Li, T. P. & Ma, Y. Q. Analysis methods for results in gamma-ray astronomy. *ApJ* **272**, 317–324 (Sept. 1983).
195. Aharonian, F. *et al.* The Crab Nebula and Pulsar between 500 GeV and 80 TeV: Observations with the HEGRA Stereoscopic Air Cerenkov Telescopes. *ApJ* **614**, 897–913 (Oct. 2004).
196. Sanuki, T. *et al.* Precise Measurement of Cosmic-Ray Proton and Helium Spectra with the BESS Spectrometer. *ApJ* **545**, 1135–1142 (Dec. 2000).
197. Dempster, A. P., Laird, N. M. & Rubin, D. B. Maximum Likelihood from Incomplete Data via the EM Algorithm. *Journal of the Royal Statistical Society. Series B (Methodological)* **39**, 1–38. ISSN: 00359246 (1977).
198. Gillessen, S. & Harney, H. L. Significance in gamma-ray astronomy - the Li & Ma problem in Bayesian statistics. *A&A* **430**, 355–362 (Jan. 2005).

199. Pietrzyński, G. *et al.* An eclipsing-binary distance to the Large Magellanic Cloud accurate to two per cent. *Nature* **495**, 76–79 (Mar. 2013).
200. Nikolaev, S. *et al.* Geometry of the Large Magellanic Cloud Disk: Results from MACHO and the Two Micron All Sky Survey. *ApJ* **601**, 260–276 (Jan. 2004).
201. Ridley, J. P. *et al.* Eight new radio pulsars in the Large Magellanic Cloud. *MNRAS* **433**, 138–146 (July 2013).
202. Ackermann, M. *et al.* Deep view of the Large Magellanic Cloud with six years of Fermi-LAT observations. *A&A* **586**, A71 (Feb. 2016).
203. Reid, W. A., Stupar, M., Bozzetto, L. M., Parker, Q. A. & Filipović, M. D. Optical discovery and multiwavelength investigation of supernova remnant MCSNR J0512- 6707 in the Large Magellanic Cloud. *MNRAS* **454**, 991–999 (Nov. 2015).
204. Maggi, P., Haberl, F., Sturm, R. & Dewey, D. XMM-Newton observations of SNR 1987A. II. The still increasing X-ray light curve and the properties of Fe K lines. *A&A* **548**, L3 (Dec. 2012).
205. Maggi, P. *et al.* The population of X-ray supernova remnants in the Large Magellanic Cloud. *A&A* **585**, A162 (Jan. 2016).
206. H. E. S. S. Collaboration *et al.* The exceptionally powerful TeV  $\gamma$ -ray emitters in the Large Magellanic Cloud. *Science* **347**, 406–412 (Jan. 2015).
207. Gaensler, B. M., Hendrick, S. P., Reynolds, S. P. & Borkowski, K. J. Discovery of a New Pulsar Wind Nebula in the Large Magellanic Cloud. *ApJ* **594**, L111–L114 (Sept. 2003).
208. Campana, R. *et al.* X-ray observations of the Large Magellanic Cloud pulsar PSR B0540-69 and its pulsar wind nebula. *MNRAS* **389**, 691–700 (Sept. 2008).
209. Komin, N., Haupt, M. & H. E. S. S. Collaboration. *Discovery of VHE Gamma-Ray Emission from the Binary System LMC P3 in 35th International Cosmic Ray Conference (ICRC2017)* **301** (Jan. 2017), 730. arXiv: 1708.03171 [astro-ph.HE].
210. Abdo, A. A. *et al.* Observations of the Large Magellanic Cloud with Fermi. *A&A* **512**, A7 (Mar. 2010).
211. Murphy, E. J., Porter, T. A., Moskalenko, I. V., Helou, G. & Strong, A. W. CHARACTERIZING COSMIC-RAY PROPAGATION IN MASSIVE STAR-FORMING REGIONS: THE CASE OF 30 DORADUS AND THE LARGE MAGELLANIC CLOUD. *The Astrophysical Journal* **750**, 126 (Apr. 2012).
212. van der Marel, R. P., Alves, D. R., Hardy, E. & Suntzeff, N. B. New Understanding of Large Magellanic Cloud Structure, Dynamics, and Orbit from Carbon Star Kinematics. *AJ* **124**, 2639–2663 (Nov. 2002).
213. Sofue, Y. Dark Bulge, Exponential Disk, and Massive Halo in the Large Magellanic Cloud. *PASJ* **51**, 445–448 (Aug. 1999).

214. Sofue, Y. in *Planets, Stars and Stellar Systems Vol. 5, by Oswalt, Terry D.; Gilmore, Gerard, ISBN 978-94-007-5611-3. Springer Science+Business Media Dordrecht, 2013*, p. 985 (eds Oswalt, T. D. & Gilmore, G.) 985 (2013). doi:10.1007/978-94-007-5612-0\_19.
215. Cirelli, M. *et al.* PPPC 4 DM ID: a poor particle physicist cookbook for dark matter indirect detection. *J. Cosmology Astropart. Phys.* **2011**, 051 (Mar. 2011).
216. Cherenkov Telescope Array Consortium *et al.* *Science with the Cherenkov Telescope Array* doi:10.1142/10986 (2019).
217. Socrates, A., Davis, S. W. & Ramirez-Ruiz, E. The Eddington Limit in Cosmic Rays: An Explanation for the Observed Faintness of Starbursting Galaxies. *The Astrophysical Journal* **687**, 202–215 (Nov. 2008).
218. Papadopoulos, P. P. A Cosmic-Ray dominated interstellar medium in ultra luminous infrared galaxies: New initial conditions for star formation. *The Astrophysical Journal* **720**, 226–232 (Aug. 2010).
219. Pellegrini, E. W. *et al.* THE OPTICAL DEPTH OF H II REGIONS IN THE MAGELLANIC CLOUDS. *The Astrophysical Journal* **755**, 40 (July 2012).
220. Bradley, T., Knapen, J., Beckman, J. & Folkes, S. A composite HII region luminosity function in H alpha of unprecedented statistical weight. *Astronomy & Astrophysics - ASTRON ASTROPHYS* **459**. doi:10.1051/0004-6361:20066151 (Nov. 2006).
221. De Marchi, G. *et al.* Star Formation in 30 Doradus. *ApJ* **739**, 27 (Sept. 2011).
222. Bergh, S. V. D. Supernova rates: A progress report. *Physics Reports* **204**. doi:10.1016/0370-1573(91)90034-j (6 1991).
223. Berezhinsky, V. & Gazizov, A. Z. Diffusion of Cosmic Rays in the Expanding Universe. I. *ApJ* **643**, 8–13 (May 2006).
224. Harris, J. & Zaritsky, D. The Star Formation History of the Large Magellanic Cloud. *AJ* **138**, 1243–1260 (Nov. 2009).
225. Mori, M. Nuclear enhancement factor in calculation of Galactic diffuse gamma-rays: A new estimate with DPMJET-3. *Astroparticle Physics* **31**, 341–343 (June 2009).
226. Stephens, I. W. *et al.* Spitzer Observations of Dust Emission from H II Regions in the Large Magellanic Cloud. *ApJ* **784**, 147 (Apr. 2014).
227. Gaensler, B. M. *et al.* The Magnetic Field of the Large Magellanic Cloud Revealed Through Faraday Rotation. *Science* **307**, 1610–1612 (2005).
228. Komin, N. *et al.* H.E.S.S. observations of the Large Magellanic Cloud. *arXiv e-prints*, arXiv:1201.0639 (Jan. 2012).

229. H. E. S. S. Collaboration *et al.* Discovery of gamma-ray emission from the extragalactic pulsar wind nebula N 157B with H.E.S.S. *A&A* **545**, L2 (Sept. 2012).
230. Marshall, F. E., Gotthelf, E. V., Zhang, W., Middleditch, J. & Wang, Q. D. Discovery of an Ultrafast X-Ray Pulsar in the Supernova Remnant N157B. *ApJ* **499**, L179–L182 (June 1998).
231. Macri, L. M., Stanek, K. Z., Bersier, D., Greenhill, L. J. & Reid, M. J. A New Cepheid Distance to the Maser-Host Galaxy NGC 4258 and Its Implications for the Hubble Constant. *ApJ* **652**, 1133–1149 (Dec. 2006).
232. Wang, Q. D., Gotthelf, E. V., Chu, Y. H. & Dickel, J. R. Detection of an X-Ray Pulsar Wind Nebula and Tail in SNR N157B. *ApJ* **559**, 275–281 (Sept. 2001).
233. Borkowski, K. J., Hendrick, S. P. & Reynolds, S. P. X-Ray-Emitting Ejecta of Supernova Remnant N132D. *ApJ* **671**, L45–L48 (Dec. 2007).
234. Tappe, A., Rho, J. & Reach, W. T. Shock Processing of Interstellar Dust and Polycyclic Aromatic Hydrocarbons in the Supernova Remnant N132D. *ApJ* **653**, 267–279 (Dec. 2006).
235. Bamba, A., Ueno, M., Nakajima, H. & Koyama, K. Thermal and Nonthermal X-Rays from the Large Magellanic Cloud Superbubble 30 Doradus C. *The Astrophysical Journal* **602**, 257–263 (Feb. 2004).
236. Mathewson, D. S. *et al.* Supernova remnants in the Magellanic Clouds. III. *ApJS* **58**, 197–200 (June 1985).
237. Lorette, M. C. & Testor, G. Optical observations of the bubble nebula N 157C (=0536.6-6914) and the tight clusters in the association LH 90 in LMC. *A&A* **139**, 330–340 (Oct. 1984).
238. Long, K. S., Helfand, D. J. & Grabelsky, D. A. A soft X-ray study of the Large Magellanic Cloud. *ApJ* **248**, 925–944 (Sept. 1981).
239. Seward, F. D. *et al.* DEM L241, A SUPERNOVA REMNANT CONTAINING A HIGH-MASS X-RAY BINARY. *The Astrophysical Journal* **759**, 123 (Oct. 2012).
240. Corbet, R. H. D. *et al.* A LUMINOUS GAMMA-RAY BINARY IN THE LARGE MAGELLANIC CLOUD. *The Astrophysical Journal* **829**, 105 (Sept. 2016).
241. Meurs, E. J. A. & van den Heuvel, E. P. J. The number of evolved early-type close binaries in the galaxy. *A&A* **226**, 88–107 (Dec. 1989).
242. Hinton, J. A. & Hofmann, W. Teraelectronvolt Astronomy. *ARA&A* **47**, 523–565 (Sept. 2009).
243. Mayer, M. *et al.* Predicting the X-ray flux of evolved pulsar wind nebulae based on VHE gamma-ray observations. *arXiv e-prints*, arXiv:1202.1455 (Feb. 2012).

244. H. E. S. S. Collaboration *et al.* The population of TeV pulsar wind nebulae in the H.E.S.S. Galactic Plane Survey. *A&A* **612**, A2 (Apr. 2018).
245. Knödlseder, J. *et al.* GammaLib and ctools. A software framework for the analysis of astronomical gamma-ray data. *A&A* **593**, A1 (Aug. 2016).
246. Cowan, G., Cranmer, K., Gross, E. & Vitells, O. Asymptotic formulae for likelihood-based tests of new physics. *European Physical Journal C* **71**, 1554 (Feb. 2011).
247. Wilks, S. S. The Large-Sample Distribution of the Likelihood Ratio for Testing Composite Hypotheses. *Ann. Math. Statist.* **9**, 60–62 (Mar. 1938).
248. Baltz, E. A. Dark Matter Candidates. *arXiv e-prints*, astro-ph/0412170 (Dec. 2004).
249. Bertone, G., Hooper, D. & Silk, J. Particle dark matter: evidence, candidates and constraints. *Phys. Rep.* **405**, 279–390 (Jan. 2005).
250. Bergström, L. Dark matter candidates. *New Journal of Physics* **11**, 105006 (Oct. 2009).
251. Kim, S. *et al.* An HiAperture Synthesis Mosaic of the Large Magellanic Cloud. *The Astrophysical Journal* **503**, 674–688 (Aug. 1998).
252. Buckley, M. R. *et al.* Search for gamma-ray emission from dark matter annihilation in the large magellanic cloud with the fermi large area telescope. *Phys. Rev. D* **91**, 102001 (May 2015).
253. LUKE, K T; ROHLFS. Structure and kinematics of neutral hydrogen gas in the Large Magellanic Cloud. English. *Astronomy and astrophysics (Berlin. Print)*. ISSN: 0004-6361 (1992).
254. Hernquist, L. An Analytical Model for Spherical Galaxies and Bulges. *ApJ* **356**, 359 (June 1990).
255. de Vaucouleurs, G. & de Vaucouleurs, A. An analysis of the composite spectrum of the Large Magellanic Cloud. *AJ* **63**, 304 (Feb. 1958).
256. Hütten, M., Combet, C. & Maurin, D. CLUMPY v3:  $\gamma$ -ray and  $\nu$  signals from dark matter at all scales. *Computer Physics Communications* **235**, 336–345 (Feb. 2019).
257. Ciafaloni, P. *et al.* Weak corrections are relevant for dark matter indirect detection. *J. Cosmology Astropart. Phys.* **2011**, 019 (Mar. 2011).
258. Sudoh, T., Linden, T. & Beacom, J. F. TeV halos are everywhere: Prospects for new discoveries. *Phys. Rev. D* **100**, 043016 (Aug. 2019).
259. Abel Barrio, J. *et al.* Analogue Sum ASIC for L1 Trigger Decision in Cherenkov Telescope Cameras. *arXiv e-prints*, arXiv:1410.8526 (Oct. 2014).